

University of Warwick institutional repository: <http://go.warwick.ac.uk/wrap>

**A Thesis Submitted for the Degree of PhD at the University of Warwick**

<http://go.warwick.ac.uk/wrap/66903>

This thesis is made available online and is protected by original copyright.

Please scroll down to view the document itself.

Please refer to the repository record for this item for information to help you to cite it. Our policy information is available from the repository home page.

**Cyclic behaviour of external diaphragm  
joint between steel I-section beam and  
circular hollow section column**

**by**

**Majd Khador**

A thesis submitted in fulfilment of the requirements for the  
degree of  
Doctor of Philosophy in Engineering

University of Warwick, School of Engineering

January 2015

*This Thesis is dedicated to my home country  
Syria  
My ultimate pride and pain  
& to Syrians who still admire life in spite of all the death surrounding them  
awaiting the day she rises again like a phoenix from the ashes*

# Contents

<i>Dedication</i> .....	2
<i>Contents</i> .....	3
<i>List of figures</i> .....	8
<i>List of tables</i> .....	13
<i>Acknowledgments</i> .....	15
<i>Declaration</i> .....	17
<i>Summary</i> .....	18
<i>Symbols</i> .....	19
<i>Abbreviations</i> .....	29

## ***Chapter 1 – Introduction***

1.1. <i>Advantages of hollow sections</i> .....	32
1.2. <i>Aims and objectives of this project</i> .....	35
1.3. <i>Outline of thesis</i> .....	36

## ***Chapter 2 – Literature Review***

2.1. <i>Introduction</i> .....	38
2.2. <i>Moment joints to tubular columns</i> .....	39
2.3. <i>Externally stiffened joints to tubular columns</i> .....	44
2.3.1. <i>T-stiffeners</i> .....	44
2.3.2. <i>Channel stiffeners</i> .....	46

2.3.3. External diaphragm stiffeners .....	47
2.4. Concluding remarks .....	60

### **Chapter 3 – Joint Design Development**

3.1. Introduction.....	62
3.2. Joint design philosophy.....	63
3.3. Details of the joint arrangement .....	64
3.4. Design calculations of the joint components .....	73
3.4.1. Tapered cover plates (TCPs).....	74
3.4.1.1. Geometric properties.....	74
3.4.1.2. Material properties.....	75
3.4.1.3. Design tension resistance .....	75
3.4.2. I-section beam - UKB 203×133×30 .....	77
3.4.2.1. Geometric properties.....	77
3.4.2.2. Material properties.....	78
3.4.2.3. Cross section classification .....	78
3.4.2.4. Design bending resistance.....	79
3.4.2.5. Design shear resistance.....	82
3.4.2.6. Shear buckling check.....	83
3.4.3. The connection between a TCP and an I-beam flange .....	84
3.4.3.1. Geometric properties.....	84
3.4.3.2. Material properties.....	85
3.4.3.3. Local buckling checks .....	85
3.4.3.4. Design shear resistance of the M22 bolt .....	86
3.4.3.5. Design bearing resistance of the M22 bolt in the TCP .....	86
3.4.3.6. Design bearing resistance of the M22 bolt in the I-beam .....	87
3.4.3.7. Design resistance of the TCP-beam connection.....	87
3.4.3.8. Design slip resistance of the TCP-beam connection.....	88
3.4.4. Diaphragm plates .....	89
3.4.4.1. Geometric properties.....	90
3.4.4.2. Material properties.....	91
3.4.4.3. Design tension resistance of the rectangular part of the DP .....	91

3.4.4.4.	<i>Design tension resistance of the DP section at the column face.....</i>	92
3.4.4.5.	<i>Design tension resistance of the DP ring section.....</i>	93
3.4.4.6.	<i>Local buckling check for the ring cross section.....</i>	94
3.4.5.	<i>The connection between a TCP and a DP.....</i>	94
3.4.5.1.	<i>Geometric properties.....</i>	94
3.4.5.2.	<i>Material properties.....</i>	95
3.4.5.3.	<i>Design shear resistance of the M22 bolt.....</i>	95
3.4.5.4.	<i>Design bearing resistance of the M22 bolt in the TCP.....</i>	95
3.4.5.5.	<i>Design bearing resistance of the M22 bolt in the DP.....</i>	95
3.4.5.6.	<i>Design resistance of the TCP-DP connection.....</i>	95
3.4.5.7.	<i>Design slip resistance of the TCP-DP connection.....</i>	96
3.4.6.	<i>Web stub.....</i>	96
3.4.6.1.	<i>Geometric properties.....</i>	97
3.4.6.2.	<i>Material properties.....</i>	97
3.4.6.3.	<i>Design shear resistance of the web plate.....</i>	97
3.4.6.4.	<i>Design block tearing resistance of the web plate.....</i>	99
3.4.6.5.	<i>Design bending resistance of the web plate.....</i>	100
3.4.7.	<i>The connection between the I-beam web and the web stub.....</i>	100
3.4.7.1.	<i>Geometric properties.....</i>	101
3.4.7.2.	<i>Material properties.....</i>	102
3.4.7.3.	<i>Design shear resistance of the M16 bolt.....</i>	102
3.4.7.4.	<i>Design bearing resistance of the M16 bolt in the I-beam web.....</i>	102
3.4.7.5.	<i>Design bearing resistance of the M16 bolt in the web stub.....</i>	102
3.4.7.6.	<i>Design resistance of the web connection.....</i>	102
3.4.7.7.	<i>Design slip resistance of the web connection.....</i>	103
3.4.8.	<i>CHS column.....</i>	104
3.4.8.1.	<i>Geometric properties.....</i>	104
3.4.8.2.	<i>Material properties.....</i>	104
3.4.8.3.	<i>Cross section classification.....</i>	104
3.4.8.4.	<i>Design bending resistance.....</i>	105
3.4.8.5.	<i>Design shear resistance.....</i>	105
3.4.9.	<i>Design of weld.....</i>	106
3.4.9.1.	<i>Geometric properties.....</i>	106

3.4.9.2.	<i>Material properties</i> .....	107
3.4.9.3.	<i>Design resistance of the weld subject to shear</i> .....	107
3.4.9.4.	<i>Design resistance of the weld to combined shear and bending</i> .....	108
3.5.	<i>Concluding remarks</i> .....	109

## **Chapter 4 – Tensile Coupon Tests**

4.1.	<i>Introduction</i> .....	110
4.2.	<i>Tensile coupons preparation</i> .....	111
4.3.	<i>Instrumentation of the tensile coupon tests</i> .....	116
4.4.	<i>TC test procedure</i> .....	118
4.5.	<i>TC test results</i> .....	120
4.6.	<i>Concluding remarks</i> .....	123

## **Chapter 5 – Experimental Set-up**

5.1.	<i>Introduction</i> .....	124
5.2.	<i>Preparation of test specimens</i> .....	125
5.3.	<i>Test rig</i> .....	131
5.4.	<i>Geometry measurements</i> .....	137
5.5.	<i>Geometry imperfection measurements</i> .....	142
5.6.	<i>Loading protocol</i> .....	146
5.7.	<i>Test instrumentation</i> .....	148
5.7.1.	<i>Actuator</i> .....	148
5.7.2.	<i>Strain gauges</i> .....	149
5.7.3.	<i>Inclinometers</i> .....	158
5.7.4.	<i>Displacement transducers</i> .....	164
5.7.5.	<i>Test-data logging</i> .....	171
5.8.	<i>Concluding remarks</i> .....	173

## **Chapter 6 – Experimental Results and Discussion**

6.1.	<i>Introduction</i> .....	174
------	---------------------------	-----

6.2.	<i>Tests results</i> .....	175
6.2.1.	<i>Strain levels in the joint components</i> .....	175
6.2.1.1.	<i>Column web panel</i> .....	176
6.2.1.2.	<i>Web stub</i> .....	180
6.2.1.3.	<i>I-section beam</i> .....	181
6.2.1.4.	<i>Diaphragm plates</i> .....	186
6.2.1.5.	<i>Tapered cover plates</i> .....	189
6.2.2.	<i>Failure modes</i> .....	192
6.2.3.	<i>Hysteretic response</i> .....	193
6.2.4.	<i>Initial rotational stiffness of the joint</i> .....	199
6.2.5.	<i>Energy dissipation</i> .....	200
6.3.	<i>Analysis and comparison of the tests results</i> .....	202
6.3.1.	<i>Steel grade comparison</i> .....	203
6.3.2.	<i>Use of stiffeners comparison</i> .....	207
6.3.3.	<i>Size of bolt holes comparison</i> .....	211
6.3.4.	<i>Bolt preloading force comparison</i> .....	216
6.4.	<i>Concluding remarks</i> .....	220

## **Chapter 7 – Conclusions**

7.1.	<i>Research summary</i> .....	222
7.2.	<i>Key findings of the research</i> .....	225
7.3.	<i>Limitations of this project</i> .....	227
7.4.	<i>Suggestions for future work</i> .....	228
7.5.	<i>Scientific outcomes</i> .....	229

<b>References</b> .....	231
-------------------------	-----

<b>Appendix A – LabVIEW Graphical Codes</b> .....	246
---	-----

<b>Appendix B – Rotation of The Column Hinges</b> .....	251
---	-----

<b>Appendix C – Elastic Deformation of The I-beam</b> .....	254
---	-----

<b>Appendix D – Connection Slip Measurements</b> .....	256
--	-----

<b>Appendix E – EuroSteel-2014 Conference Paper</b> .....	260
---	-----



# List of Figures

Fig 1.1.	<i>Ripshorster Bridge, Germany</i> .....	33
Fig 1.2.	<i>Kansai International Airport in Osaka, Japan</i> .....	33
Fig 1.3.	<i>University House at the University of Warwick, UK</i> .....	33
Fig 1.4.	<i>An under-construction frame composed of steel I-beams connected to circular CFT columns with external diaphragm plates</i> .....	35
Fig 2.1.	<i>Internal diaphragm joint</i> .....	41
Fig 2.2.	<i>Through diaphragm joint</i> .....	41
Fig 2.3.	<i>External diaphragm joint</i> .....	41
Fig 2.4.	<i>Type-I joint with flared plates</i> .....	48
Fig 2.5.	<i>Type-II joint with external diaphragms</i> .....	48
Fig 2.6.	<i>Side view of the failure of joint Type-I: weld and flange fracture</i> .....	50
Fig 2.7.	<i>Top view of the failure of joint Type-II: diaphragm and column wall fractures</i> .....	50
Fig 2.8.	<i>Front view of the failure mode of joints made with RBS beams</i> .....	54
Fig 2.9.	<i>Front view of the failure mode of joints made with the minimum width ring</i> .....	54
Fig 2.10.	<i>Top view of the exterior 3D joint to CHS column stiffened with external diaphragms</i> .....	55
Fig 2.11.	<i>Front view of the exterior 3D joint to CHS column stiffened with external diaphragms</i> .....	55
Fig 2.12.	<i>Failure modes of specimens tested in the work of Wang et al. (2011)</i> .....	56

Fig 3.1.	<i>The components of the beam to column joint before assembly</i> .....	65
Fig 3.2.	<i>The beam to column joint after assembly</i> .....	65
Fig 3.3.	<i>Moment of the joint in relation to the beam moment</i> .....	81
Fig 3.4.	<i>Widths of different sections in the DP</i> .....	90
Fig 3.5.	<i>Design assumption for the DP ring according to Wang et al. (2011)</i> .....	93
Fig 3.6.	<i>Web stub subject to shear force</i> .....	96
Fig 3.7.	<i>Block tearing of the web plate</i> .....	99
Fig 4.1.	<i>General shape and geometry of the tensile coupons</i> .....	114
Fig 4.2.	<i>Attachments of the displacement transducer to a tensile coupon</i> .....	117
Fig 4.3.	<i>Instrumentation of tensile coupon tests</i> .....	117
Fig 4.4.	<i>A tensile coupon test using the DARTEC 9500 testing facility</i> .....	119
Fig 4.5.	<i>A tensile coupon before and after testing</i> .....	120
Fig 4.6.	<i>Average engineering stress-strain curves of the joint components</i> .....	121
Fig 5.1.	<i>The column assembly</i> .....	125
Fig 5.2.	<i>Photographs of the weld work in the column assembly</i> .....	126
Fig 5.3.	<i>Details of the fillet welds in the column assembly</i> .....	126
Fig 5.4.	<i>Details of the FPB welds in the column assembly</i> .....	127
Fig 5.5.	<i>Details of the fillet welds in the beam assembly</i> .....	128
Fig 5.6.	<i>Geometry of the beam stiffener</i> .....	128
Fig 5.7.	<i>A photograph of the weld work in the beam assembly</i> .....	128
Fig 5.8.	<i>A tapered cover plate assembly and its weld details</i> .....	129
Fig 5.9.	<i>Bolt tightening process</i> .....	130
Fig 5.10.	<i>Test specimen assembled inside the test rig</i> .....	130
Fig 5.11.	<i>3D illustration of the swivel hinges and their components</i> .....	131
Fig 5.12.	<i>Function of the swivel hinges</i> .....	132
Fig 5.13.	<i>Schematic arrangement of the test rig</i> .....	133
Fig 5.14.	<i>Schematic arrangement of the lateral supports for the I-beam</i> .....	134
Fig 5.15.	<i>Photographs of the lateral support arrangement for the I-beam</i> .....	134
Fig 5.16.	<i>The column bottom hinge assembly and its components</i> .....	135

Fig 5.17. Photograph of the column bottom hinge .....	136
Fig 5.18. The digital calliper .....	137
Fig 5.19. The Ball-Micrometer .....	137
Fig 5.20. Geometry measurements of the I-section beam .....	138
Fig 5.21. Geometry measurements of a diaphragm plate .....	141
Fig 5.22. Geometry imperfection measurements of the I-beam .....	142
Fig 5.23. Geometry imperfection measurements of the I-beam top flange .....	143
Fig 5.24. Calculation of the actuator displacements for the loading protocol .....	146
Fig 5.25. Displacement-controlled loading cycles.....	147
Fig 5.26. Calibration of the actuator load cell in tension.....	149
Fig 5.27. Sketch of the column web panel zone and its strain gauges .....	151
Fig 5.28. Location of strain gauges on the column web panel zone .....	151
Fig 5.29. Sketch of the two diaphragm plates and their strain gauges .....	152
Fig 5.30. Location of strain gauges on the top diaphragm plate .....	153
Fig 5.31. Location of strain gauges on the bottom diaphragm plate .....	154
Fig 5.32. Sketch of two unstiffened TCPs and their strain gauges .....	154
Fig 5.33. Location of strain gauges on a top unstiffened TCP .....	155
Fig 5.34. Location of strain gauges on a bottom unstiffened TCP .....	155
Fig 5.35. Top and 3D views of two stiffened TCPs and their SGs .....	156
Fig 5.36. Location of strain gauges on top and bottom TCP stiffeners .....	156
Fig 5.37. Location of strain gauges on a top stiffened TCP .....	157
Fig 5.38. Location of strain gauges on a bottom stiffened TCP .....	157
Fig 5.39. Location of strain gauges on the I-section beam.....	157
Fig 5.40. Sketch of the test specimen detailing the location of INCs.....	158
Fig 5.41. Fixing arrangement of INC-1 to the column web panel .....	159
Fig 5.42. Fixing arrangements of INC-2 and INC-4 to the specimen front face ...	160
Fig 5.43. Fixing arrangement of INC-3 to the back face of the beam web .....	161
Fig 5.44. Calibration of inclinometers .....	163
Fig 5.45. Location of displacement transducers (DTs) on a test specimen .....	164
Fig 5.46. Fixing arrangements of DT-1 and DT-4 .....	166
Fig 5.47. Fixing arrangement of DT-2 and DT-3 viewed from different angles ...	166
Fig 5.48. Locations of DT-5, DT-6, DT-7 and DT-8 on a test specimen.....	168
Fig 5.49. Top view of the fixing arrangement of DT-7.....	168

Fig 5.50. Calibration of displacement transducers.....	170
Fig 5.51. The measurement hardware modules from National Instruments.....	172
Fig 5.52. The front panel of the testing program .....	173
Fig 6.1. Load–strain curves of the column web panel in Tests 1–9.....	177
Fig 6.2. Local deformation of the column web panel in Tests 1–9 .....	179
Fig 6.3. Local deformation of the web stub in Tests 1–9 .....	181
Fig 6.4. Load–strain curves of the I-beam critical section in Tests 1–9.....	183
Fig 6.5. Moment-rotation curves of the I-beam in Tests 1–9.....	186
Fig 6.6. Load–strain curves of the diaphragm plates in Tests 1–9.....	189
Fig 6.7. Load–strain curves of the tapered cover plates in Tests 1–9 .....	191
Fig 6.8. Buckling of the top TCP in Test–6: S235-NSH-NS-FP .....	192
Fig 6.9. Normalised moment-rotation curves of the joint in Tests 1–9.....	195
Fig 6.10. Normalised moment-rotation curves of the plastic hinge region .....	197
Fig 6.11. Stiffness classification of the joint in Tests 1–9 .....	200
Fig 6.12. Accumulated energy dissipation in Tests 1–9.....	201
Fig 6.13. Accumulated energy dissipation beyond the 25 <sup>th</sup> cycle in Tests 1–9.....	202
Fig 6.14. Steel grade comparison between the results of Test–1 and Test–4 .....	204
Fig 6.15. Steel grade comparison between the results of Test–2 and Test–5 .....	205
Fig 6.16. Steel grade comparison between the results of Test–6 and Test–7 .....	206
Fig 6.17. Use of stiffeners comparison between the results of Test–1 and 2 .....	208
Fig 6.18. Use of stiffeners comparison between the results of Test–6 and 3 .....	209
Fig 6.19. Use of stiffeners comparison between the results of Test–4 and 5 .....	211
Fig 6.20. Size of holes comparison between the results of Test–1 and 6 .....	212
Fig 6.21. Size of holes comparison between the results of Test–2 and 3 .....	213
Fig 6.22. Size of holes comparison between the results of Test–4 and 7 .....	215
Fig 6.23. Preloading force comparison between the results of Test–1 and 8.....	217
Fig 6.24. Preloading force comparison between the results of Test–5 and 9.....	219
Fig A.1. Block diagram of the main joint-test programme in LabVIEW .....	247
Fig A.2. Block diagram of the sub-programme “Calibration” in LabVIEW .....	248

Fig A.3.	<i>Block diagram detail – Data acquisition function</i> .....	248
Fig A.4.	<i>Block diagram detail – Recalling the sub-programme “Calibration”</i> ...	249
Fig A.5.	<i>Block diagram detail – Producing a plot in LabVIEW</i> .....	249
Fig A.6.	<i>Block diagram detail – Saving calibrated measurements to a file</i> .....	250
Fig B.1.	<i>Moment-rotation curves of the column hinges in Tests 1–9</i> .....	253
Fig C.1.	<i>Elastic rotation of a cantilever at a given section</i> .....	255
Fig D.1.	<i>Load–displacement curves for the DTs (5, 6, 7 and 8) in Tests 1–9</i> .....	259

# List of Tables

Table 3.1.	<i>Geometry and properties of the joint components</i> .....	69
Table 3.2.	<i>Tests label according to the type of TCPs used in the test specimens</i> ....	72
Table 3.3.	<i>Design tension resistance of the TCPs</i> .....	76
Table 3.4.	<i>The joint moment at full plasticity of the TCPs middle sections</i> .....	80
Table 3.5.	<i>Spacing, end and edge distances for the TCP to the beam connection</i> ..	85
Table 3.6.	<i>Spacing, end and edge distances for the TCP to the DP connection</i> .....	95
Table 3.7.	<i>Spacing, end and edge distances for the web connection</i> .....	101
Table 4.1.	<i>Number and cut location of the tensile coupons</i> .....	112
Table 4.2.	<i>Detailed dimensions of the tensile coupons</i> .....	115
Table 4.3.	<i>Strain rates and crossheads separation velocities for the TC tests</i> .....	119
Table 4.4.	<i>Key results from the tensile coupon tests</i> .....	122
Table 5.1.	<i>Geometry measurements of UKB 203×133×30</i> .....	138
Table 5.2.	<i>Tolerance on the measured dimensions of UKB 203×133×30</i> .....	139
Table 5.3.	<i>Geometry measurements of the CHS column</i> .....	140
Table 5.4.	<i>Geometry measurements of the diaphragm plates</i> .....	140
Table 5.5.	<i>Geometry measurements of the web stub</i> .....	141
Table 5.6.	<i>The I-beam out-of-squareness measurements</i> .....	144
Table 5.7.	<i>The major-axis out-of-straightness measurements of the I-beam</i> .....	145
Table 5.8.	<i>The loading protocol used for the joint tests</i> .....	147

Table 5.9.	<i>Instruments connections to the NI hardware modules.....</i>	<i>172</i>
Table 6.1.	<i>The number of completed loading cycles for the nine joint tests.....</i>	<i>175</i>
Table 6.2.	<i>The main response parameters obtained from the nine joint tests .....</i>	<i>193</i>
Table 6.3.	<i>Maximum rotation of the plastic hinge region in the nine joint tests ...</i>	<i>198</i>
Table 6.4.	<i>Initial rotational stiffness of the joint in Tests 1-9.....</i>	<i>199</i>
Table 6.5.	<i>Accumulated energy dissipation in Tests 1-9.....</i>	<i>201</i>

# *Acknowledgments*

This research was carried out under the supervision of Dr Tak-Ming Chan whose great knowledge, patience and motivation have guided me throughout the course of my research until the completion of this doctoral thesis. I would like to express my sincere gratitude and appreciation to Dr Tak-Ming Chan for all the support he has given me on both the academic and personal levels during this journey. This work would have not been completed without his invaluable advice and great expertise.

I would like also to thank Dr Ken Mao for being my supervisor during the last few months of my PhD course. I had the privilege to do my Master's degree under his supervision a few years ago and I am very thankful for having had another chance to benefit from his invaluable support and advice.

I am very thankful to Prof Toby Mottram and Prof Leroy Gardner who examined my PhD viva and gave me their honest and invaluable feedback. I would also like to thank Prof Mottram for allowing me to benefit from his great knowledge and technical expertise whenever I approached him with a question during my PhD course.

I am indeed grateful to Damascus University in Syria for their financial support, which covered a substantial period of my doctoral course. I am also grateful to the



School of Engineering at the University of Warwick for their financial awards. The technical support from the Structures Laboratory at the University of Warwick is gratefully acknowledged. I would like to thank in particular Mr Juan Munoz Leal who put a lot of time and effort into the preparation and conducting of the project laboratory experiments, and has been also a great friend I am very lucky to have met.

Beyond Engineering, I would like to thank all my close friends who had sometimes to tolerate my mood swings and never stopped being supportive or amazing. I would like to thank Dr Sotiris Paraschas for the great times we have had together; Selina Moutia for being so supportive, loving and caring; Dr Ahmad Issa for always being there for me; Dr Lena Al Khudairy for being my best friend and confidante; Kahtan Almahmoud for the great friendship we have had together since our childhood; and to Marcus Cross, I doubt there will be enough words to express how thankful I am for all the support you have given me, for believing in me and sharing with me my best and worst moments.

Last but not least, I would like to thank my family without whom I would not be where I am today. To my mother Wafaa Sulaiman and my father Sami Al Khadour, I lose words in front of your unconditional love and support. I hope I can keep you always proud of me and give back to you some of the endless kindness you have shown me. To My brother Dr Ebrahim Al'Khadour, thank you for being my backbone and making me a stronger person. To my sister Dr Sarah Khadour, thank you for being a caring sister and a faithful friend; and to my beautiful princess and little sister, Leen Al'Khadour, I am so proud of being your brother, thank you for drawing a smile on my face at all times.

Majd Khador

August 2014

# *Declaration*

This thesis is submitted to the University of Warwick in support of my application for the degree of Doctor of Philosophy in Structural Engineering. It has been composed by myself and has not been submitted in any previous application for any degree.

The work presented (including data generated and data analysis) was carried out all by myself unless otherwise stated. The theoretical planning of the joint design, test loading protocol and instrumentation were derived from collaborative work with Dr Alireza Bagheri Sabbagh during his employment as a Research Fellow at the School of Engineering, University of Warwick.

The parts of the thesis, which have been published (or submitted for publication) by me as a first author during the period of my study for this degree, are detailed in the “Scientific Outcomes” section in the “Conclusions” Chapter of this thesis.

Majd Khador

August 2014

# *Summary*

Tubular columns own many structural and architectural advantages that, in certain cases, make them more favourable than open-section columns in steel moment-resisting frames. These advantages are sometimes underexploited due to the relative lack of design guidance on their moment joints to open-section beams, in particular on semi-rigid joints with special detailing for seismic actions. Different configurations of I-beam to tubular column joints have been investigated in the past, including through, internal and external diaphragm joints. This project investigates experimentally the cyclic behaviour of an external diaphragm joint between a steel I-beam and a circular hollow section column. The proposed joint includes two diaphragm plates (DPs) welded to the outer circumference of the column and bolted to the I-beam flanges with two tapered cover plates (TCPs). A web stub is welded to the column face and bolted to the I-beam web. Full-scale laboratory experiments were conducted to investigate the hysteretic response and energy dissipative performance of the proposed joint under cyclic loading. TCPs were integrated in the joint to act as replaceable sacrificial components that dissipate most of the energy whilst the rest of the joint components remain elastic to minimise the post-seismic repair. The test specimens were identical except their TCPs that had the same geometry but differed in steel grade, size of bolt-holes, use of stiffeners or bolt preloading force. The use of higher grades of steel for the TCPs and stiffening them imposed higher strain demands in the beam and DPs and dissipated less energy than the joints with lower grades and unstiffened TCPs, respectively. The results confirmed that the main energy dissipation fuse in these joints was yielding in the TCPs while the other components remained elastic. Connection slippage created a second fuse for energy dissipation when the bolt preloading force was properly controlled, and the rotation of the plastic hinge region exceeded the minimum threshold of 25mrad for medium ductility class structures.

# *Symbols*

$a$	<i>Effective throat thickness of fillet weld</i>
$A$	<i>Percentage elongation after fracture for a tensile-testing piece</i>
$a_0$	<i>Original thickness of a tensile-testing piece</i>
$A_b$	<i>Gross cross section area of a bolt</i>
$A_{\text{beam}}$	<i>Area of the I-beam cross section</i>
$A_c$	<i>Area of the CHS column cross section</i>
$A_{\text{DP,cf}}$	<i>Area of the DP cross section at the column face</i>
$A_{\text{DP,r}}$	<i>Area of the cross section of the DP ring</i>
$A_{\text{DP,rec}}$	<i>Area of the DP rectangular cross section</i>
$A_f$	<i>Area of the I-beam flange</i>
$A_{\text{gr}}$	<i>Area of the gross section</i>
$A_{\text{net}}$	<i>Area of the net cross-section at holes for bolts</i>
$A_{\text{nt}}$	<i>Net area subject to tension</i>
$A_{\text{nv}}$	<i>Net area subject to shear</i>
$A_{\text{red}}$	<i>Area of the reduced section of the TCP</i>
$A_s$	<i>Tensile stress area of a bolt</i>
$A_v$	<i>Shear area of the I-beam</i>
$A_{\text{vc}}$	<i>Shear area of the column</i>

$A_w$	<i>Area of the I-beam web</i>
$A_{wpl}$	<i>Area of the web plate cross section</i>
$b$	<i>Width of the I-beam cross section</i>
$B$	<i>Width of a tensile-testing piece</i>
$b_0$	<i>Original width of the parallel length of a tensile-testing piece</i>
$c$	<i>Width or depth of a part of a cross section</i>
$d$	<i>Nominal bolt diameter</i>
$d_0$	<i>Bolt-hole diameter</i>
$D_0$	<i>External diameter of the CHS column</i>
$d_{0,bw}$	<i>Bolt-hole diameter in the I-beam web</i>
$d_{0,wpl}$	<i>Bolt-hole diameter in the web plate</i>
$d_a$	<i>Vertical displacement of the actuator</i>
$E$	<i>Modulus of elasticity</i>
$e_1$	<i>End distance from the bolt hole centre to the adjacent end of the connected part in a line in the direction of load transfer</i>
$e_2$	<i>Edge distance from the bolt hole centre to the adjacent edge of the connected part measured in a line perpendicular to the load transfer direction</i>
$E_{beam}$	<i>Modulus of elasticity of the I-beam steel</i>
$e_{M1}$	<i>Eccentricity of the design shear force of the web connection with respect to the web plate edge</i>
$e_{M2}$	<i>Eccentricity of the design shear force of the web connection with respect to the column face</i>
$F_{b,Rd,min}$	<i>Minimum design bearing resistance of an individual bolt</i>
$F_{bf,b,Rd}$	<i>Design bearing resistance of a single bolt in the I-beam flange</i>

$F_{bf,end,b,Rd}$	<i>Design bearing resistance of an end bolt in the I-beam flange</i>
$F_{bf,inner,b,Rd}$	<i>Design bearing resistance of an inner bolt in the I-beam flange</i>
$F_{bw,end,b,Rd}$	<i>Design bearing resistance of an end bolt in the I-beam web</i>
$F_{bw,inner,b,Rd}$	<i>Design bearing resistance of an inner bolt in the I-beam web</i>
$F_{DP,end,b,Rd}$	<i>Design bearing resistance of an end bolt in the DPs</i>
$F_{DP,inner,b,Rd}$	<i>Design bearing resistance of an inner bolt in the DPs</i>
$F_{p,Cd}$	<i>Preload force of a bolt</i>
$F_{Rd,min}$	<i>Minimum design resistance of an individual bolt</i>
$F_{s,Rd}$	<i>Design slip resistance of a connection</i>
$F_{TCP,b,Rd}$	<i>Design bearing resistance of a single bolt in the TCPs</i>
$F_{TCP,end,b,Rd}$	<i>Design bearing resistance of an end bolt in the TCPs</i>
$F_{TCP,inner,b,Rd}$	<i>Design bearing resistance of an inner bolt in the TCPs</i>
$f_u$	<i>Ultimate strength</i>
$f_{u,beam}$	<i>Ultimate strength of the I-beam steel</i>
$f_{u,c}$	<i>Ultimate strength of the CHS column steel</i>
$f_{u,DP}$	<i>Ultimate strength of the diaphragm plate steel</i>
$f_{u,TCP}$	<i>Ultimate strength of the TCP steel</i>
$f_{u,w}$	<i>Ultimate strength of the fillet weld</i>
$f_{u,ws}$	<i>Ultimate strength of the web stub steel</i>
$f_{ub}$	<i>Ultimate tensile strength of a bolt</i>
$F_{v,Rd}$	<i>Design shear resistance of a single bolt</i>
$f_{vw,d}$	<i>Design shear strength of weld</i>
$F_{w,Ed}$	<i>Design value of the weld force per unit length</i>
$F_{w,Rd}$	<i>Design weld resistance per unit length</i>
$F_{ws,end,b,Rd}$	<i>Design bearing resistance of an end bolt in the web stub plate</i>

$F_{ws,inner,b,Rd}$	<i>Design bearing resistance of an inner bolt in the web stub plate</i>
$f_y$	<i>Yield strength</i>
$f_{y,beam}$	<i>Yield strength of the I-beam steel</i>
$f_{y,c}$	<i>Yield strength of the CHS column steel</i>
$f_{y,DP}$	<i>Yield strength of the diaphragm plate steel</i>
$f_{y,TCP}$	<i>Yield strength of the TCP steel</i>
$f_{y,wp}$	<i>Yield strength of the column web panel steel</i>
$f_{y,ws}$	<i>Yield strength of the web stub steel</i>
$f_{yb}$	<i>Yield strength of a bolt</i>
$h$	<i>Depth of the I-beam cross section</i>
$h_s$	<i>Height of the TCP stiffener</i>
$h_w$	<i>Depth of the I-beam web</i>
$h_{wpl}$	<i>Height of the web plate</i>
$h_{ws}$	<i>Height of the gross section of the web stub</i>
$I_{wpl}$	<i>Second moment of area of the web plate cross section about its major axis</i>
$I_y$	<i>Second moment of area about the major axis of a cross section</i>
$k$	<i>Out-of-squareness of the I-beam bottom flange</i>
$k'$	<i>Out-of-squareness of the I-beam top flange</i>
$k_s$	<i>Factor depending on bolt hole size</i>
$L_0$	<i>Original gauge length of a tensile-testing piece</i>
$L_c$	<i>Length of the parallel reduced section of a tensile-testing piece</i>
$L_{cc}$	<i>Distance between the loading point and the column centre</i>
$L_{cf}$	<i>Distance between the loading point and the column face</i>

$L_{cr}$	<i>Length of the I-beam between the centre of the loading application area and the beam critical section</i>
$L_{DP,rec}$	<i>Distance between the loading point and the critical cross section of the rectangular part of the DP</i>
$L_e$	<i>Initial displacement transducer gauge length</i>
$L_{eff}$	<i>Effective length of the I-beam between the centre of the loading application area and the beam connected end</i>
$L_t$	<i>Total length of a tensile-testing piece</i>
$L_u$	<i>Length between gauge length marks on a tensile-testing piece after rupture</i>
$L_w$	<i>Total length of fillet weld</i>
$L_{w,eff}$	<i>Effective length of fillet weld</i>
$M_2$	<i>Moment calculated at the location of INC-2</i>
$M_4$	<i>Moment calculated at the location of INC-4</i>
$M_5$	<i>Moment calculated at the location of INC-5</i>
$M_{b,el,y,Rd}$	<i>Design elastic bending resistance of the I-beam cross section</i>
$M_{b,pl,y,Rd}$	<i>Design plastic bending resistance of the I-beam cross section</i>
$M_{c,el,y,Rd}$	<i>Design elastic bending resistance of the CHS column cross section</i>
$M_{cc,ED}$	<i>Design bending value at the column centre</i>
$M_{cf}$	<i>Moment at the column face</i>
$M_j$	<i>Moment of joint</i>
$M_{j,b,el}$	<i>Joint moment when the beam critical section reaches its design elastic bending resistance</i>
$M_{j,b,pl}$	<i>Joint moment when the beam critical section reaches its design plastic bending resistance</i>



$M_{j,max}$	<i>Maximum moment of the joint calculated at the connected end of the I-beam</i>
$M_{j,pl}$	<i>Joint moment when the reduced section areas of the TCPs (and their stiffeners when applicable) reach full plasticity</i>
$M_{w,ED}$	<i>Design bending value at the fillet weld cross section</i>
$M_{wpl,ED}$	<i>Design bending value in the web plate</i>
$M_{wpl,el,Rd}$	<i>Design elastic bending resistance of the web plate cross section</i>
$n$	<i>Number of friction planes</i>
$N$	<i>Number of bolts in a connection</i>
$N_{DP,cf,t,Ed}$	<i>Design tension value in the DP cross section at the column face</i>
$N_{DP,cf,t,Rd}$	<i>Design tension resistance of the DP cross section at the column face</i>
$N_{DP,r,t,Rd}$	<i>Design tension resistance of the cross section of the DP ring</i>
$N_{DP,rec,t,Ed}$	<i>Design tension value in the DP rectangular cross section</i>
$N_{DP,rec,t,Rd}$	<i>Design tension resistance of the DP rectangular cross section</i>
$N_{pl,Rd}$	<i>Design plastic resistance of the gross section</i>
$N_{red,pl,Rd}$	<i>Design plastic resistance of the reduced cross section of the TCP</i>
$N_{TCP,t,Rd}$	<i>Design tension resistance of the TCP cross section</i>
$N_{u,Rd}$	<i>Design ultimate resistance of the net cross-section at holes for bolts</i>
$N_w$	<i>Number of fillet weld lines</i>
$P$	<i>Vertical load acting on the free end of a cantilever</i>
$P_1$	<i>Spacing between centres of bolt holes in a line in the direction of load transfer</i>
$P_2$	<i>Spacing between centres of bolt holes in a line perpendicular to the load transfer direction</i>
$q_{yy}$	<i>Major-axis out-of-straightness of the I-beam</i>

$r$	<i>Root radius</i>
$S$	<i>Leg size of fillet weld</i>
$S_0$	<i>Original cross-section area of the parallel length of a tensile-testing piece</i>
$S_{j,ini}$	<i>Initial rotational stiffness of a joint</i>
$S_{wpl}$	<i>First moment of area of the web plate section above its major axis</i>
$t_c$	<i>Thickness of the CHS column wall</i>
$t_{DP}$	<i>Thickness of the diaphragm plate</i>
$t_f$	<i>Thickness of the I-beam flange</i>
$t_s$	<i>Thickness of the TCP stiffener</i>
$t_{TCP}$	<i>Thickness of the TCP</i>
$t_w$	<i>Thickness of the I-beam web</i>
$t_{ws}$	<i>Thickness of the web stub</i>
$V_{bw-ws,Rd}$	<i>Design resistance of the web connection</i>
$V_{Ed}$	<i>Design shear value</i>
$V_{eff,1,Rd}$	<i>Design block tearing resistance</i>
$V_{el,Ed}$	<i>Design shear value in the I-beam at yield onset in its critical section</i>
$V_{el,Rd}$	<i>Design elastic shear resistance</i>
$V_{pl,Rd}$	<i>Design plastic shear resistance</i>
$V_{TCP-bf,Rd}$	<i>Design resistance of the TCP-beam connection</i>
$V_{TCP-bf,v,Ed}$	<i>Design shear value in the TCP-beam connection</i>
$V_{TCP-bf,v,Rd}$	<i>Design shear resistance of the TCP-beam connection</i>
$V_{TCP-DP,Rd}$	<i>Design resistance of the TCP-DP connection</i>
$V_{TCP-DP,v,Ed}$	<i>Design shear value in the TCP-DP connection</i>
$V_{u,Rd}$	<i>Design ultimate resistance of the net cross-section at holes for bolts</i>

$V_{wp,Ed}$	<i>Design shear value in the column web panel</i>
$V_{wp,Rd}$	<i>Design plastic shear resistance of the column web panel</i>
$V_{wp1,el,Rd}$	<i>Design elastic shear resistance of the web plate cross section</i>
$V_{wp1,pl,Rd}$	<i>Design plastic shear resistance of the web plate cross section</i>
$W_{c,el,y}$	<i>Elastic section modulus of the CHS column cross section about its major axis</i>
$W_{c,pl,y}$	<i>Plastic section modulus of the CHS column cross section about its major axis</i>
$W_{DP,cf}$	<i>Width of the diaphragm plate at the column face</i>
$W_{DP,fe}$	<i>Width of the diaphragm plate flat end</i>
$W_{DP,r}$	<i>Width of the diaphragm plate ring</i>
$W_{el,y}$	<i>Elastic section modulus about the major axis</i>
$W_{pl,y}$	<i>Plastic section modulus about the major axis</i>
$W_{red}$	<i>Width of the reduced section area of the TCP</i>
$W_{TCP}$	<i>Width of the TCP</i>
$W_{w,el,y}$	<i>Elastic section modulus of the fillet weld cross section about its major axis</i>
$W_{wp1,el,y}$	<i>Elastic section modulus of the web plate cross section about its major axis</i>
y-y	<i>Major axis</i>
$z_1$	<i>Lever arm between the coupling forces acting on the centroids of the top and bottom TCPs cross sections</i>
$z_2$	<i>Lever arm between the coupling forces acting in the shear planes of the top and bottom TCP-beam connections</i>

$z_3$	<i>Lever arm between the coupling forces acting on the top and bottom DPs cross sections</i>
$\alpha_{b,end}$	<i>Factor <math>\alpha_b</math> for an end bolt</i>
$\alpha_{b,inner}$	<i>Factor <math>\alpha_b</math> for an inner bolt</i>
$\beta_w$	<i>Correlation factor for fillet welds</i>
$\gamma_{M0}$	<i>Partial safety factor</i>
$\gamma_{M2}$	<i>Partial safety factor</i>
$\gamma_{M3,ser}$	<i>Partial safety factor for serviceability limit state</i>
$\gamma_{ov}$	<i>Material overstrength factor</i>
$\varepsilon$	<i>Factor depending on <math>f_y</math></i>
$\varepsilon_{beam}$	<i>Strain in the beam</i>
$\varepsilon_c$	<i>Strain in the column</i>
$\varepsilon_{DP}$	<i>Strain in the diaphragm plate</i>
$\varepsilon_{max,beam}$	<i>Maximum strain observed in the I-beam during a test</i>
$\varepsilon_{max,DP}$	<i>Maximum strain observed in the diaphragm plates during a test</i>
$\varepsilon_{sh}$	<i>Work-hardening strain</i>
$\varepsilon_{TCP}$	<i>Strain in the tapered cover plate</i>
$\varepsilon_u$	<i>Ultimate strain</i>
$\varepsilon_y$	<i>Yield strain</i>
$\varepsilon_{y,beam}$	<i>Yield strain of the I-beam steel</i>
$\varepsilon_{y,c}$	<i>Yield strain of the CHS column steel</i>
$\varepsilon_{y,DP}$	<i>Yield strain of the diaphragm plates steel</i>
$\varepsilon_{y,TCP}$	<i>Yield strain of the tapered cover plates steel</i>
$\eta$	<i>Factor for shear area</i>
$\theta$	<i>Angle of rotation</i>

$\theta_1$	<i>Rotation measurement from INC-1</i>
$\theta_2$	<i>Rotation measurement from INC-2</i>
$\theta_3$	<i>Rotation measurement from INC-3</i>
$\theta_4$	<i>Rotation measurement from INC-4</i>
$\theta_5$	<i>Rotation measurement from INC-5</i>
$\theta_b$	<i>Rotation at the beam section located 200mm from the connection end</i>
$\theta_{b,crit}$	<i>Rotation at the beam critical section (at the connection end)</i>
$\theta_{c,h}$	<i>Rotation of the column end hinges</i>
$\theta_{dr}$	<i>Interstory drift angle</i>
$\theta_{el}$	<i>Angle of elastic rotation of the beam</i>
$\theta_p$	<i>Rotation of the plastic hinge region</i>
$\theta_{p,DCM}$	<i>Minimum rotation capacity of the plastic hinge region for structures of medium ductility class (DCM)</i>
$\theta_{p,max}$	<i>Maximum rotation of the plastic hinge region</i>
$\theta_{wp}$	<i>Rotation of the web panel</i>
$\theta_{ws}$	<i>Rotation of the web stub</i>
$\mu$	<i>Slip factor</i>
$\sigma_{\perp}$	<i>Normal stress perpendicular to the fillet weld throat</i>
$\tau_{\parallel}$	<i>Shear stress in the plane of the fillet weld throat and parallel to the axis of the weld</i>
$\tau_{\perp}$	<i>Shear stress in the plane of the fillet weld throat and perpendicular to the axis of the weld</i>
$\tau_{Ed}$	<i>Design value of the local shear stress</i>
$\phi$	<i>Rotation of joint</i>

# *Abbreviations*

2D	<i>Two-dimensional</i>
3D	<i>Three-dimensional</i>
AIJ	<i>Architectural Institute of Japan</i>
AISC	<i>The American Institute of Steel Construction</i>
BSI	<i>British Standards Institution</i>
CFT	<i>Concrete filled tube</i>
CHS	<i>Circular hollow section</i>
CJP	<i>Complete joint penetration weld</i>
COV	<i>Coefficient of Variation</i>
DCH	<i>High ductility class</i>
DCM	<i>Medium ductility class</i>
DP	<i>Diaphragm plate</i>
DT	<i>Strain gauge displacement transducer</i>
EC	<i>Eurocode</i>
ECCS	<i>The European Convention for Constructional Steelwork</i>
FE	<i>Finite element</i>
FEMA	<i>Federal Emergency Management Agency</i>
FP	<i>Bolts are fully preloaded in line with Eurocode 3: Part 1–8</i>

FPB	<i>Full <b>p</b>enetration <b>b</b>utt weld</i>
HP	<i>Bolts are <b>p</b>reloaded to <b>h</b>alf the value in Eurocode 3: Part 1–8</i>
HSFB	<i>High strength friction <b>b</b>olt</i>
INC	<i><b>I</b>nclinometer</i>
LSP	<i>Lateral support <b>p</b>late</i>
NI	<i>National <b>I</b>nstruments corporation</i>
NS	<i>No stiffeners for the tapered cover plates</i>
NSH	<i>Normal-size <b>h</b>oles</i>
OSH	<i><b>O</b>versized <b>h</b>oles</i>
PTFE	<i>Polytetrafluoroethylene – a synthetic material that has a very low coefficient of friction</i>
RBS	<i>Reduced <b>b</b>eam section</i>
SG	<i>Strain gauge</i>
SLS	<i>Serviceability <b>L</b>imit State</i>
SMF	<i>Special <b>m</b>oment frame</i>
SSoW	<i>Safe system of work</i>
TC	<i>Tensile <b>c</b>oupon</i>
TCP	<i>Tapered cover <b>p</b>late</i>
VS	<i>Vertical stiffener</i>
WS	<i>Web stub <u>Or</u> TCPs equipped with-stiffeners</i>

# *Chapter 1*

## *Introduction*

This chapter presents an overview of the advantages of hollow sections, the aims and objectives of this research and the outline of the thesis. The definitions of connections and joints in this thesis follow those given in Clauses 1.4.2 and 1.4.4 in BS EN 1993-1-8: 2005, where a single-sided beam-to-column joint consists of the beam-to-column connection and the column web panel.



### *1.1. Advantages of hollow sections*

Structural hollow (tubular) sections possess many structural and architectural advantages due to their closed geometry. Their aesthetically pleasing profiles have offered architects a great alternative to use in structures with visible steel sections. In structures where steel sections are exposed to high humidity and aggressive atmosphere, those made with tubular sections require less protection against corrosion and have a longer corrosion protection life than comparable structures made with open sections. This is due to the round corners of hollow sections, the absence of sharp edges and having smaller surfaces exposed to corrosion than those in comparable open sections {Mesquita *et al.* (2009); Wardenier *et al.* (2010)}.

Furthermore, tubular sections, especially circular hollow sections, are favoured in offshore structures because of their lower drag coefficients in comparison to open sections. Another advantage of structural tubular sections is that their internal void may be used to incorporate ventilation systems or to be filled with concrete. Concrete filled tubes (CFT) have higher compression resistance and enhanced fire resistance duration than their hollow counterparts {Wardenier *et al.* (2010)}. Tubular sections have been used in various structural applications; such as buildings, bridges, halls and offshore structures. Figures 1.1 to 1.3 show a few examples of structures made with hollow sections {Wardenier *et al.* (2008) and (2010)}.

Circular, square and rectangular hollow sections (CHS, SHS and RHS respectively) have been the most common tubular sections in structural applications. New tubular shapes are becoming more popular recently such as elliptical hollow sections (EHS), especially after the advances in determining their structural design rules that have

emerged from recent research studies such as {Ruiz-Teran and Gardner (2008); Chan and Gardner (2010); Gardner *et al.* (2011)}.



**Figure 1.1:** *Ripshorster Bridge, Germany*



**Figure 1.2:** *Kansai International Airport in Osaka, Japan*



**Figure 1.3:** *University House at the University of Warwick, UK*

In terms of design resistances, hollow sections are very efficient with respect to their torsional stiffness and bending in both directions because of their relatively high moment of area and section modulus about the minor axis in comparison to their open-section counterparts, {Kurobane *et al.* (2004); Chan and Gardner (2008); Málaga-Chuquitaype and Elghazouli (2010); Wardenier *et al.* (2010)}.

The use of structural hollow sections in columns has many other advantages over open sections of the same section size, such as higher compression resistance {Mesquita *et al.* (2009)}. This is because the radius of gyration about the minor axis is higher for hollow sections and subsequently their slenderness ratio is lower than that of a similar size and similar effective length open section column. In addition to that, residual stresses resulting from the manufacturing process are usually distributed in hot-rolled hollow sections in a more favourable way than that in open sections due to the geometrical characteristics of the former {Kurobane *et al.* (2004)}. Finally, structural hollow sections are generally produced in long lengths, up to 20m, that enable, where applicable, the use of one length per column for the total height of a building {Kurobane *et al.* (2004)}.

Overall, open sections are more economical than hollow sections when they are subject to bending about the major axis because the unit material of tubular columns is more expensive than that of open sections. However, in cases when the design bending resistance of the section is largely reduced by lateral buckling or when bending about both axes is present, hollow sections offer a better weight-to-strength ratio than open sections. Hence, through proper design, the use of hollow sections could result in more cost effective moment frames {Kurobane *et al.* (2004); Elghazouli *et al.* (2009); Wardenier *et al.* (2010)}.

These structural and architectural advantages of tubular columns are sometimes underexploited due to the relative lack of design guidance on moment joints between open-section beams and tubular columns, and in particular the design of semi-rigid joints with special detailing for seismic actions. Figure 1.4 shows a composite frame under construction in China. The frame composes circular CFT columns and steel I-

beams joined together by external diaphragm connections. More details about previous research on moment joints to tubular columns are presented in Chapter 2.

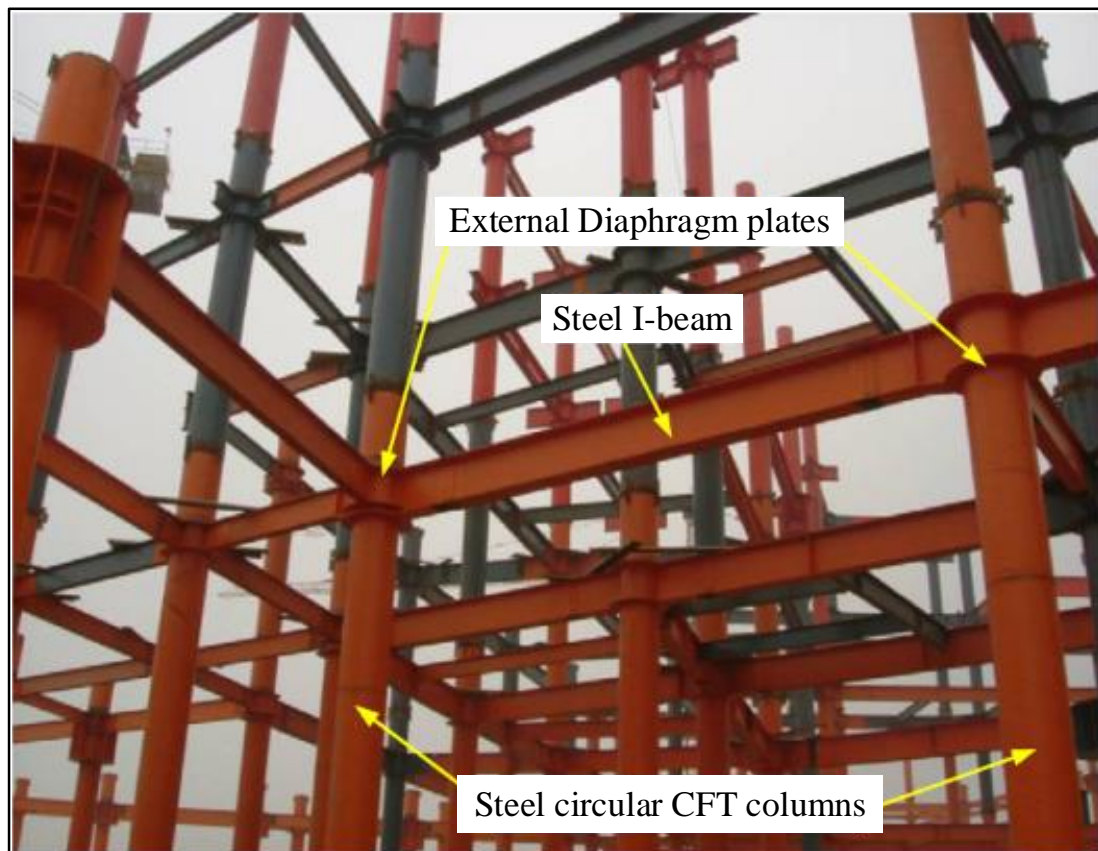


**Figure 1.4:** *An under-construction frame composed of steel I-beams connected to circular CFT columns with external diaphragm plates {Han et al. (2011)}*

## *1.2. Aims and objectives of this project*

The main aim of this project is to develop an I-beam to CHS column joint that is architecturally appealing, practical for construction and most importantly achieves the required structural performance and ductility under seismic loading for dissipative structures (moment resisting frames for this project). Furthermore, the joint should enable having no permanent deformations in the primary members of the moment-resisting frame to minimise the operations and time of repair for post-seismic damages of the structure.

The Federal Emergency Management Agency (FEMA) in the United States of America published the FEMA-356 (2000) report, prepared by the American Society of Civil Engineers, on the seismic rehabilitation of buildings. In this report, the structural performance of buildings was classified according to post-earthquake damages into four different levels and two intermediate ranges. The structural performance of buildings in FEMA-356 report ranges from the level of immediate reoccupancy of the structure after a seismic event, to the collapse prevention level, at which the building continues to support gravity loads but is not safe for reoccupancy and the required repair of the damages may not be practical nor economical because the structure is on the verge of partial or total collapse.

This project aims at designing joint detailing that allows the investigated moment-resisting frame to be classified in the Damage Control Structural Performance range, in which the post-seismic repair operations are required, yet are minimal to provide quick reoccupancy of the building. To achieve this, the proposed joint incorporates built-in replaceable links that dissipate most of the seismic energy and act as sacrificial components to be easily replaced after a seismic event, whilst the rest of the joint components remain elastic. Different types of the replaceable links were investigated in the experimental programme because of their influence on the overall seismic performance of the joint.

### *1.3. Outline of thesis*

This thesis contains seven chapters with the main contents as follows;

- Chapter 1 gives a brief introduction on the advantages of hollow sections, the aims and objectives of this project and an overview of the whole thesis.

- Chapter 2 is a review of relevant literature with a particular focus on steel joints made with external diaphragm plates.
- Chapter 3 presents the design philosophy adopted at the design stage of the project, the details of the proposed joint and the design calculations for the joint components.
- Chapter 4 reports the tensile coupon tests conducted to characterise the different joint components and the key results.
- Chapter 5 presents all the preparations that were carried out in the Structures Laboratory for the full-scale experimental program. It scopes the preparation of the test specimens, the test rig, the geometry and geometry imperfection measurements, the loading protocol and the instrumentation plan.
- Chapter 6 presents in its first section the tests results obtained from the full-scale laboratory experiments. The second section of the chapter covers a detailed parametric comparison study between the different tests results.
- Chapter 7 is used to summarise the research and present the key findings and limitations. Suggestions for future work and the scientific outcomes of the PhD studies are highlighted too.

# *Chapter 2*

## *Literature Review*

### *2.1. Introduction*

This chapter presents a review of relevant literature on the subject of joints to tubular columns in moment-resisting frames with additional emphasis on frames having CHS columns with external diaphragm joints designed for seismic loadings. Firstly, a brief overview of different configurations of moment joints to tubular columns is presented. Then, a more focused review of experimental, numerical and analytical investigations conducted on externally-stiffened joints to tubular columns is detailed.

## 2.2. *Moment joints to tubular columns*

In steel moment-resisting frames, open I-section beams are the most commonly used due to their efficiency in resisting bending about their major axis, while the columns can have either open or tubular sections. As mentioned in the Chapter 1, tubular columns have many structural and architectural advantages over open-section columns. Nonetheless, these advantages are sometimes underexploited due to the relative lack of design guidance on moment joints between open-section beams and tubular columns, and in particular the design of semi-rigid joints with special detailing for seismic actions.

Research studies on moment joints to hollow section columns have varied depending on the column shape and desired performance of the joint. There seems to be relatively fewer studies on moment joints to circular hollow section columns in comparison to their square and rectangular counterparts. This could be due to facing more difficulties in detailing joints to the curved surface of CHS columns than that to the flat faces of SHS or RHS columns.

Moreover, most of these studies have focused on joints to concrete filled tubes (CFT) rather than joints to unfilled hollow section columns. CFT columns combine the advantages of ductile steel and stiff concrete. The concrete restrains local buckling of the steel tube, while the steel tube eliminates the need of construction framework, acts as longitudinal reinforcement to the concrete and provides its lateral confinement {Bergmann *et al.* (1995); Alostaz and Schneider (1996); Fukumoto and Morita (2005); Wu *et al.* (2007); Shin *et al.* (2008)}. References to previous studies on joints to CFT columns are only for those configurations that can be applied to empty steel tubes as well.



Conventional configurations of semi-rigid bolted joints to open-section columns were examined for tubular columns as well. The closed geometry of hollow sections limits access to their outer walls only, and hence fastening techniques that do not require access to the columns inner wall were crucial to the fabrication of such joints. Connections made using the flowdrill system, which is a thermal drilling technique used for the extrusion of holes in a tubular column wall, were investigated by France *et al.* (1999) and (1999a). The blind-bolting system, which involves the use of modern bolts provided with a built-in interlock mechanism that activates when they are tightened, is another technique employed in recent years to join open-beams to tubular/CFT columns using bolted angle, flush end plate or extended end plate connections {Elghazouli *et al.* (2009); Mesquita *et al.* (2009) and (2010); Wang *et al.* (2013)}. Reverse channel connections, in which a reverse channel is welded to the column skin and bolted to the beam with angles or an end plate, were proposed in the work of Liu and Wang (2009) and Málaga-Chuquitaype and Elghazouli (2010) as a practical and cost-effective alternative for joining I-section beams to SHS/CHS columns in moment resisting frames.

The width of an open-section beam that frames into a tubular column is usually less than the column width. Previous research studies revealed that joints made by welding open-section beams directly to the outer skin of tubular columns without the use of any stiffeners were not suitable for seismic applications because they exhibited, under cyclic loading, unfavourable stiffness and strength characteristics and significant distortions of the tube wall, which prevented plastic hinging of the beam and led to brittle failures of the weld and the beam flanges {Alostaz and Schneider (1997)}.

Reinforcing the column at the levels of the beam flanges with stiffeners, which act similarly to continuity plates in open-section columns, was, when properly designed, found to increase the shear resistance of the column web panel and transfer the axial forces from the beam flanges to the column more efficiently {Kurobane *et al.* (2004); Wang *et al.* (2011)}. Figures 2.1 to 2.3, taken from the Foolad Machine company website, show the general details of three conventional joints to tubular columns employing internal, through and external stiffeners (diaphragm plates) respectively. These joints have been used in the design of moment-resisting frames mainly in Japan and some other Asian countries such as China and Korea.

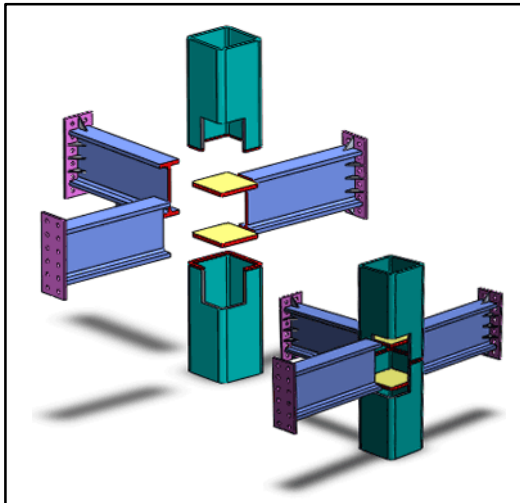


**Figure 2.1:** Internal diaphragm joint, taken from Foolad-Machine company website [www.fooladmachine.com](http://www.fooladmachine.com)

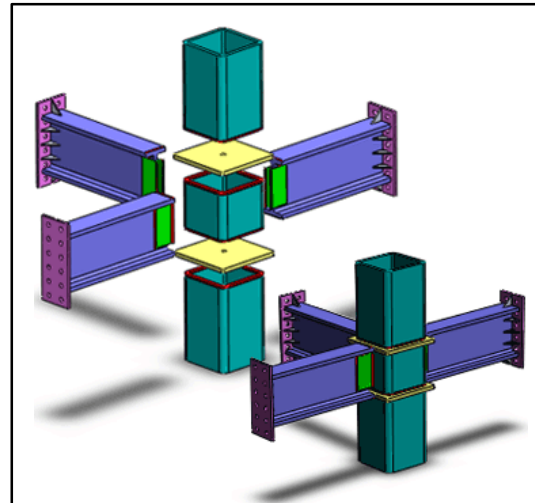


**Figure 2.2:** Through diaphragm joint, taken from Foolad-Machine company website [www.fooladmachine.com](http://www.fooladmachine.com)

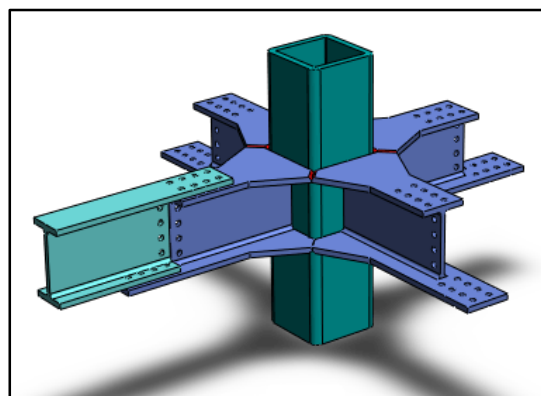


**Figure 2.3:** External diaphragm joint, taken from Foolad-Machine company website [www.fooladmachine.com](http://www.fooladmachine.com)

Internal diaphragm joints, in which the tube is usually cut in one location and continuity plates are welded around its inside wall at the position of beam flanges, have been investigated by many researchers {Chen *et al.* (2004); Ricles *et al.* (2004); Cheng *et al.* (2007); Wang *et al.* (2014)}. The fabrication of such arrangement is not simple nor cost effective because it requires extensive welding work and skilled welders to eliminate frequently detected weld defects of these joints {Alostaz *et al.* (1997); Ricles *et al.* (2004); Kurobane *et al.* (2004)}.

Through diaphragm joints, in which the tube is cut in two locations and its three pieces are welded to two diaphragm plates that themselves are welded or bolted to the beam flanges, were also investigated {Nakashima *et al.* (1998); Cheng and Chung (2003); Nishiyama *et al.* (2004); Kurobane *et al.* (2004); Jiao *et al.* (2011); Qin *et al.* (2014)}. The use of through diaphragm plates was found to transfer axial loads from the beam flanges into the column web in a simple manner and increase the strength and stiffness of the joint. Nevertheless, this arrangement discontinues the column and requires a lot of welding work that results in higher risks of weld defects. Furthermore, this arrangement is not practical when the beams framing into a column are of different depths. In spite of these weaknesses, the use of welding robots and other suitable production resources have made through diaphragm joints the most popular arrangement for joining I-beams to tubular columns in Japan {Kurobane *et al.* (2004); Wang *et al.* (2011)}.

The difficulties and risks associated with internal and through stiffening of tubular columns increased the necessity of finding efficient designs of external stiffeners. Different shapes of outer stiffeners and external diaphragm plates have been examined during the last two decades. The use of external diaphragm plates allows the hollow section column to continue through the joint, they reduce the fabrication

costs and provide structural integrity between the beam and the column {Alostaz and Schneider (1997); Kurobane *et al.* (2004); Wang *et al.* (2011)}. Joints made with either external diaphragm plates or other forms of external stiffeners are discussed in more detail in Section 2.3.

Overall, there have been relatively more research studies in Japan than anywhere else on stiffened joints to empty or concrete filled tubular columns, but most of these studies are written in Japanese. Kurobane *et al.* (2004) reviewed many of the Japanese studies in the CIDECT design guide number 9. They presented the design formulae that were established for through and external diaphragm joints in the Japanese Codes {AIJ (1990) and (2001)}. Kurobane *et al.* (2004) made a few amendments to these formulae to follow the ultimate limit state design format and take into account later studies that helped to enhance their reliability and validity range. These formulae enable design calculations for the ultimate resistance of the stiffened joint, assuming a rigid full-strength joint between the beam and the column.

Morino and Tsuda (2003) and Fukumoto (2005a) reviewed the most common configurations of moment joints between steel beams and square/circular CFT columns in Japan. These included internal, through and external diaphragm joints, and reported on their elasto-plastic behaviour. Fukumoto (2005a) reported that for through and external diaphragm joints, decreasing the width-to-thickness ratio of the tube column increased its resistance to tensile forces from the beam flanges due to an increased out-of-plane resistance. Moreover, increasing the beam-to-column width ratio resulted in higher resistances in the column wall and the diaphragm plates. Morino and Tsuda (2003) stated that there were no significant differences found in either the energy dissipation capacity or the elasto-plastic behaviour between steel frames and CFT frames as long as plastic hinging occurred mainly in the beams.

### 2.3. Externally stiffened joints to tubular columns

This section presents relevant published literature on the subject of externally stiffened joints to tubular columns in moment-resisting frames. Previous research studies on the use of T-stiffeners, channel stiffeners and external diaphragm stiffeners in tubular column joints are covered in this section. Because this project investigates an external diaphragm joint to a tubular column, previous studies on the use of external diaphragm plates are well-detailed in Subsection 2.3.3.

#### 2.3.1. T-stiffeners

Ting *et al.* (1991) inspected numerically the monotonic response of moment joints between steel I-beams and square hollow section columns using different arrangements of external stiffeners. These externally stiffened joint arrangements were studied experimentally under monotonic and cyclic loading scenarios in the work of Lee *et al.* (1993) and Shanmugam and Ting (1995). Flat triangular stiffener plates welded to the I-beam flanges and to the column face were examined first. Their results showed better distribution of stresses in the column web panel zone than that in directly-welded beam to column joints, especially when the combined width of each beam flange and its stiffeners matched the full width of the column wall. Parametric studies revealed that by having a 25° angle, or less, between the stiffener outer edge and the beam flange enhanced the flow of stresses from the flanges to the column wall. However, high stress concentrations were still found to exist at the location of welds between the stiffeners and the column wall corners. Ting *et al.* (1991) examined the influence of using angle stiffeners instead of flat triangular ones and found that stress concentrations were still present at the same locations.

The use of T-stiffeners, made of horizontal triangular and vertical rectangular plates, was reported to be the most efficient among the arrangements characterised. This is because they relatively enhanced the stiffness, strength and ductility of the joint and reduced stress concentrations at the weld region, by shifting them into the column webs, {Ting *et al.* (1991); Lee *et al.* (1993); Shanmugam and Ting (1995)}. Nevertheless, these joints failed by fracture of the beam flanges and their welding to the column. Recommendations of the optimum design and length of T-stiffeners to distribute stresses in the joint more evenly were given by Ting *et al.* (1991) and Lee *et al.* (1993). Further numerical and experimental studies on joints reinforced by external T-stiffeners between steel open-section beams and square CFT columns were conducted by Kang *et al.* (2001) and Shin *et al.* (2004), and their results showed that the use of properly designed T-stiffeners enhanced the moment-rotation characteristics of the joint, which then failed, mostly, in a brittle manner by fracture of the stiffeners welds.

Shin *et al.* (2008) and Kim *et al.* (2008) investigated the influence of using improved designs of T-stiffeners on the seismic performance of joints with square CFT columns. The use of T-stiffeners with tapered horizontal plates led to a gradual stress flow from the beam flanges to the stiffeners and reduced stress concentrations at the beginning of their junctions. A similar observation was presented in the work of Ricles *et al.* (2004). Another suggested improvement to the design of T-stiffeners was adding a hole into their horizontal plates, being near to their tips to reduce stress concentrations in that region. This technique was not effective for all the specimens on which it was tried and further research on the optimum location and size of these holes was suggested.

Shin *et al.* (2008) and Kim *et al.* (2008) examined a strategy for combining T-stiffeners with a reduced (dog-bone-shaped) beam section (RBS) to shift the location of the beam plastic hinge and beam flange buckling further away from the stiffeners ends. This development was an attempt to reduce the possibility of weld fracture between the stiffeners horizontal plates and the beam flanges. However, a specimen that was designed using this strategy failed by premature fracture of the weld between the stiffener vertical plate and the column. Shin *et al.* (2008) suggested increasing the design safety margin in such joints by adopting a strain hardening factor higher than the one recommended in the AISC seismic provisions {ANSI/AISC 341-10 (2010)} to allow for the full development of a plastic hinge in the RBS before the occurrence of any other failure.

### 2.3.2. *Channel stiffeners*

Kumar and Rao (2006) investigated numerically and experimentally a joint between RHS column and beam under cyclic loading. The joint incorporated two channel sections of uniform thickness welded to the column wall and bolted from their webs to the beam flanges to transfer forces from the latter to the column webs without the need of internal column stiffeners. A rectangular opening with rounded corners was made in the RHS beam web to help install the bolts between the beam flanges and the two channels. A doubler plate was welded to the column web to avoid shear yielding of the column web panel. Different channel sizes were examined and it was found that using high strength channels resulted in stable hysteretic response of the joint and sufficient ductility and energy dissipation capacities. Failure initiated as a crack in the beam net section, away from the column face, leading to its rupture. Rao and Kumar (2006) conducted a parametric study on the same joint and proposed a

guideline for determining its main characteristics based on the geometrical and material properties of the channels, the column and the beam.

### 2.3.3. *External diaphragm stiffeners*

Several research studies were conducted in the past two decades on external diaphragm joints to tubular columns, with most having CFT columns rather than empty tubes {Alostaz and Schneider (1996); Zhang *et al.* (2012)}. A non-linear 3D finite element (FE) study was conducted by Alostaz and Schneider (1997) on various single-sided joint details between an open-section beam (wide-flange beam) and a CFT column under monotonic loading. This computational study was conducted in conjunction with an experimental investigation by Schneider and Alostaz (1998) on the cyclic response of 2/3-scale T-shaped specimens having selected joint details. The sizes of the beam and the column were kept constant for the different joint details to enable comparison between their results. The column thickness was changed as it was one of the parameters investigated. A beam stub was shop-welded to the outside skin of the column wall and field-welded/bolted to the beam for all the joint details.

The weld work was done under sufficient quality control to address some of the problems that caused brittle failures of welded connections in the 1994 Northridge and 1995 Kobe earthquakes at a very low level of plastic demand or during the elastic response in some cases {Tremblay *et al.* (1995); Alostaz and Schneider (1997); Miller (1998); Mahin (1998); Nakashima *et al.* (1998); Azuma *et al.* (2000); FEMA-353 (2000); FEMA-355D (2000); FEMA-355E (2000); Miura *et al.* (2001); Kim *et al.* (2004); Kurobane *et al.* (2004)}. One of the key aims of Alostaz and Schneider (1997) study was to achieve a joint that could develop the design plastic



bending strength of the beam. Figures 2.4 and 2.5 illustrate two of the joint details (Types I and II) investigated in the work of Alostaz and Schneider (1997) and Schneider and Alostaz (1998).

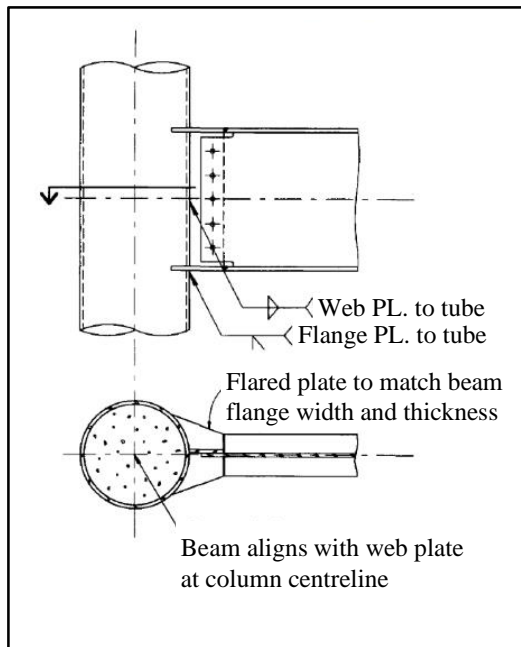


**Figure 2.4:** Type-I joint with flared plates  
{Alostaz and Schneider (1997)}

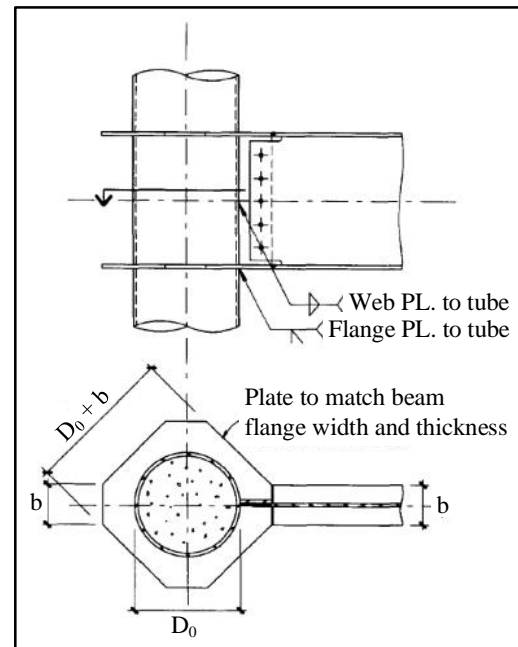


**Figure 2.5:** Type-II joint with external diaphragms  
{Alostaz and Schneider (1997)}

In Type-I detailing, the beam stub included two flared flange plates that matched the width and thickness of the beam flanges they were field-welded to. For the tube wall to have adequate through-thickness shear strength to resist the full tensile force of the beam flanges, the sections of the flared plates at the CFT column face were designed so that the arc lengths of the tube adjacent to them provided the required shear area of the tube wall {Schneider and Alostaz (1998) and Schneider *et al.* (2004)}. The numerical monotonic results of this specimen indicated high shear demand imposed on the tube wall resulting in excessive local distortions of its part adjacent to the tension flange. These deformations were noted on a greater scale in the experimental cyclic results and were accompanied by a significant deterioration of the joint strength in one load direction. The joint failed by flange and flange weld

fracture, as shown in Figure 2.6, followed by tube wall tearing and eventually a separation of the shear tab from the tube wall skin {Schneider and Alostaz (1998); Azizinamini and Schneider (2004)}.

The moment-rotation characteristics of this joint showed that its initial stiffness decreased by 50% when the beam moment exceeded 25% of its design plastic bending strength, and it sustained a drift of only 1.5% before the flange fractured, making it unsuitable for moment-resisting frames in regions of moderate to high seismic risks. In another test, increasing the column thickness by approximately 30%, ignoring the uneconomical impact of this approach, was found to have almost negligible benefit as the joint reached of about 5% higher strength before the tube wall exhibited severe local distortions.

To relieve the excessive deformations noted in the tube wall in Type-I detailing, the beam stub flanges were designed as square diaphragm plates in the detailing of Type-II to transfer the beam flange forces around the CFT column more uniformly and efficiently. The Diaphragm Plates (DPs) had similar thickness to the beam flanges, and their total width was equal to the column diameter plus the beam flange width so that the diaphragms and the beam flanges had equal cross sections. The diaphragms were field-welded to the beam flanges at their corners after cutting them to have a width equal to that of the beam flanges, as illustrated in Figure 2.5.

The numerical monotonic results of this joint indicated column wall distortion that prevented gradual flow of stresses from the beam flanges into the diaphragm plates and caused stress concentrations in the latter. As a result, the joint was not able to develop the full plastic bending strength of the beam and showed almost similar initial elastic stiffness to Type-I joint.

The experimental cyclic results indicated high local stress and strain levels at the re-entrant corners adjacent to weld. These stress concentrations resulted in fractures in both diaphragm plates, and the fractures propagated through the plates into the column wall as shown in Figure 2.7. This progressive failure caused the joint strength and stiffness to deteriorate rapidly for rotations beyond 0.01 rad. Eventually, a fracture initiated in the weld between the DPs and the beam flanges, and spread across the mid-width of the latter {Schneider and Alostaz (1998); Azizinamini and Schneider (2004)}.

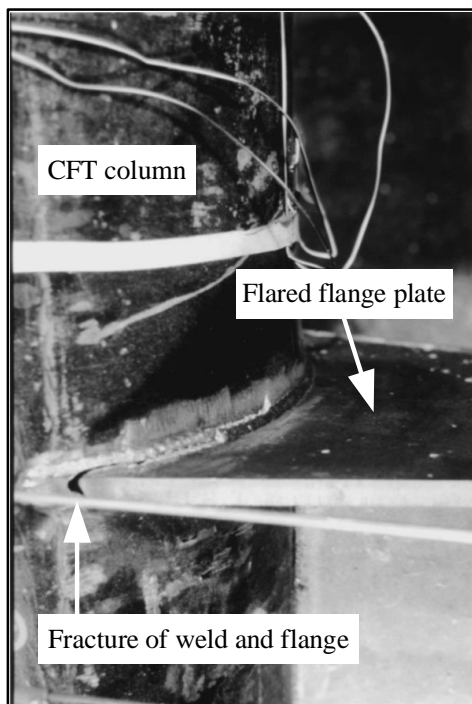


**Figure 2.6:** Side view of the failure of joint Type-I: weld and flange fractures {Schneider and Alostaz (1998)}

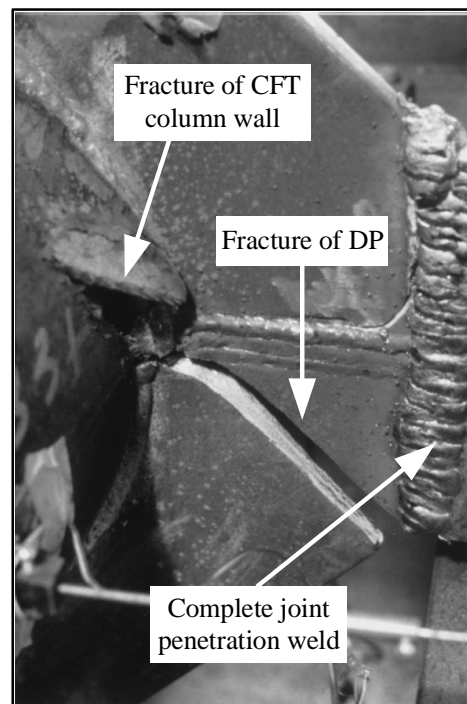


**Figure 2.7:** Top view of the failure of joint Type-II: diaphragm and column wall fractures {Schneider and Alostaz (1998)}

In an iteration to remove the structural deficiencies identified in Type-II detailing, the beam was moved further away from the column surface by reducing the angle of the diaphragm plate about its top edge from  $45^\circ$  to  $30^\circ$ . This resulted in increasing the distance between the beam connected end and the column centre from  $0.7D_0$  to  $1.1D_0$ ; where  $D_0$  is the external diameter of the tube. This reduced the sharpness of

the re-entrant corners between the DPs and the beam, allowed for better stress distribution in the diaphragm plates and better stress flow around the CFT column, and resulted in less distortion of the plates around the steel tube.

Subsequently, the joint exhibited higher stiffness and strength than the previous one and developed almost the full plastic bending strength of the beam. It was concluded that the use of properly designed diaphragm plates and locating the beam at a distance not less than  $D_0$  from the column centre allowed large strains to remain within the beam flanges, improved significantly the joint elastic and inelastic performance and developed the plastic hinge in the beam as intended in the design {Alostaz and Schneider (1996) and (1997); Schneider and Alostaz (1998)}.

Chiew *et al.* (2001) carried out an intensive numerical parametrical study and an experimental programme on both stiffened and unstiffened joints between steel I-beams and circular CFT columns under monotonic loading. External ring-shaped diaphragm plates and flared flange cover plates were some of the stiffening details examined in the study of Chiew *et al.* (2001). Most of the tested specimens failed by tube tearing at the junction with the beam flange. The exception was for the joint made with external rings. The failure mode was found to be local buckling of the beam flange.

Chiew *et al.* (2001) highlighted that the thickness of the column wall was one of the most influential parameters on joint strength, and hence it was recommended to either stiffen the joint with properly designed external diaphragm plates or increase the thickness of the column wall locally (in the column web panel region) as increasing the thickness along the full height of the column is not an economic option. Chiew *et al.* (2001) confirmed the findings of other researchers by

recommending to improve the boundary conditions at the interface of the column-beam and move the failure cross section away from the column face to avoid stress concentrations that could lead to weld fracture.

Park *et al.* (2005) investigated experimentally the cyclic performance of seven full-scale exterior joints stiffened with external diaphragm plates between steel open-section beams and square CFT columns. The external diaphragm plates were made of either four rectangular stiffener-plates joined together with fillet welds that aligned with the column flanges, or with two U-shaped stiffener-plates joined together with fillet welds that aligned with the column cross section major axis. The diaphragm plates were placed at the beam flanges levels and welded to them using complete joint penetration groove welds. A bolted shear tab was used to connect the beam web to the column face.

Different diaphragm plate widths, ranging from  $0.6b_f$  to  $0.9b_f$ , were examined; where  $b_f$  is the beam flange width. It was found that increasing the width of the diaphragm plates increased the strength and stiffness of the joint, but reduced its rotational capacity. The joint that showed the best hysteretic response, ductility and failure mode amongst the tested joints was the one made with  $0.7b_f$ -width diaphragm plates and for which the fillet welds between the stiffener-plates aligned with the column cross section major axis. Yielding of the diaphragm plates was reported as the main energy dissipation fuse, and minimum inelastic deformation occurred outside them up to 0.04 total rotation of the joint. This is the minimum storey drift angle that a joint is required to accommodate in special moment frames (SMF) according to ANSI/AISC 341-10 (2010), and hence Park *et al.* (2005) proposed that such joints could be used in high-risk seismic areas and may be repaired by replacing the diaphragm plates only after severe earthquakes.

A group of numerical and experimental parametric studies were conducted on interior frames of CFT columns connected to steel I-beams with external diaphragm plates {Han *et al.* (2008) and (2011); Wang *et al.* (2009)}. Square and circular CFT columns were considered, and the shape of the external diaphragm plates matched that of the CFT columns that they were welded to. The width of the DPs was calculated according to the recommendations of the Japanese Code AIJ (1997). The geometrical transition from the beam flanges to the diaphragm plates was gradual to avoid having abrupt geometry that could lead to undesirable stress concentrations. Based on the results of these parametric studies, simplified models for the hysteretic lateral load versus lateral displacement of these frames were developed and proposed {Wang *et al.* (2009); Han *et al.* (2011)}.

Wang *et al.* (2008) examined experimentally the seismic performance of joints between steel I-beams and CFT columns using external diaphragms. Eight internal joint specimens were tested. The geometrical and material properties of the CFT columns and the I-beams were similar in all the tests, except for three of them in which reduced section beams (RBS) were used. This was to allow for a comparison between the performance of joints fabricated with full section beams and those made with RBS beams. The width of the diaphragm plate ring was another parameter investigated in this research. The ring width was taken equal to either the full design value recommended in the Japanese Code AIJ (1997), two-thirds or one third of it. The thickness of the DPs was taken equal to that of the beam flanges. The DPs and the I-beam web were welded to the column wall.

It was found that the RBS joints exhibited strong-column-weak-beam failure with plastic hinge development at the reduced section of the beam and beam buckling (as shown in Figure 2.8). The full-section-beam joints failed in a weak-column-strong-

beam manner as the failure was limited to the column panel without significant beam deformations. However, for the joint fabricated with the minimum width ring, having 1/3 of the AIJ recommended value, failure is seen in Figure 2.9 and occurred in the diaphragm plates in the form of local buckling. The weld between the DPs and the column remained sound with no observed fractures.

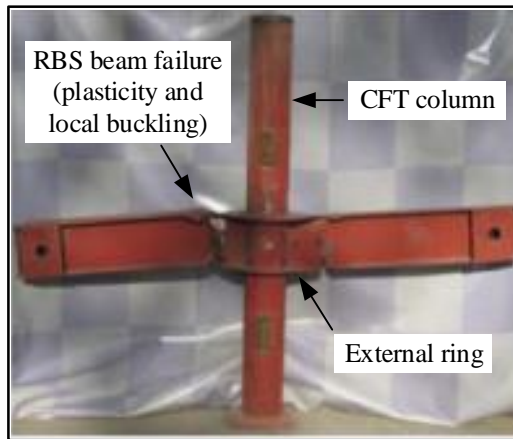


**Figure 2.8:** Front view of the failure mode of joints made with RBS beams {Wang *et al.* (2008)}

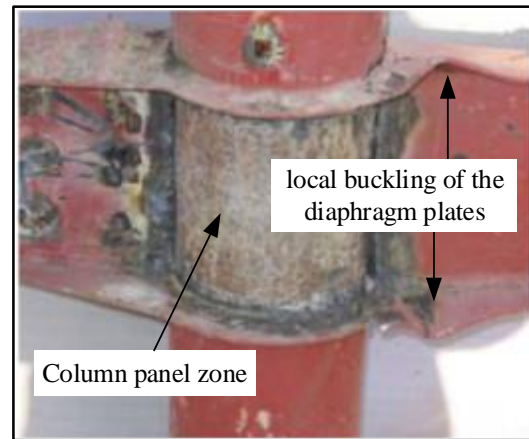


**Figure 2.9:** Front view of the failure mode of joints made with the minimum width ring {Wang *et al.* (2008)}

The hysteretic response of the RBS joints demonstrated good seismic performance and ductility with a slight reduction in their ultimate strength in comparison with the full-section-beam joints. Wang *et al.* (2008) added that reducing the width of the diaphragm plates had a negative impact on the ultimate strength, and that using DPs of a relatively small width resulted in unfavourable shifting of the failure from the beam to the diaphragm plates.

Wang *et al.* (2011) carried out an experimental investigation on the seismic behaviour of joints between steel I-beam and circular hollow section columns stiffened by external diaphragm plates. Different joint configurations, including two-dimensional (2D) and three-dimensional (3D) interior joints and a 3D exterior joint, were tested. The joints were subjected to unidirectional and bidirectional cyclic

loadings accordingly. Figures 2.10 and 2.11 illustrate top and front views respectively of the 3D exterior joint investigated by Wang *et al.* (2011). Beam stubs, each consisting of two diaphragm plates and a web plate, were shop-welded to the outside surface of the column wall.

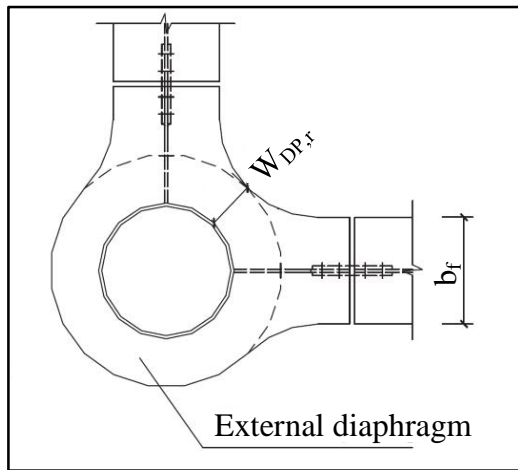


**Figure 2.10:** Top view of the exterior 3D joint to CHS column stiffened with external diaphragms {Wang *et al.* (2011)}

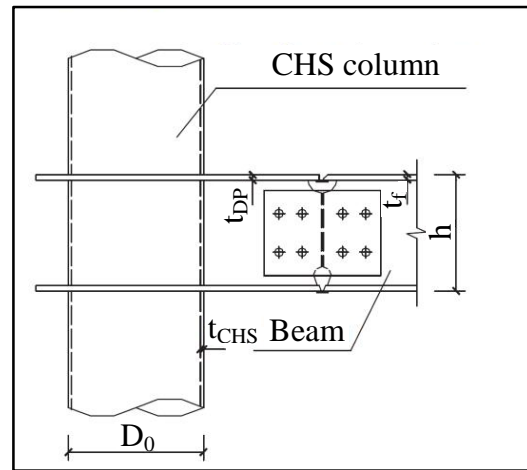


**Figure 2.11:** Front view of the exterior 3D joint to CHS column stiffened with external diaphragms {Wang *et al.* (2011)}

The web of the beam stub was bolted to the I-beam web and the diaphragm plates were field-welded to the I-beam flanges. The sections and material properties of the CHS column and the I-beam were carefully chosen to have a weak-column-strong-beam system in some tests and a strong-column-weak-beam system in the other tests. This was to compare the energy dissipation ratios, failure modes and seismic performance between the results of both joint/member systems.

The edges of the DPs were rounded to avoid stress concentrations and to allow for a smooth stress flow from the beam to the diaphragms and into the column. The width of the external edge of the diaphragm plates was made equal to the I-beam flanges width ( $b_f$ ). The thickness of the DPs ( $t_{DP}$ ) was equal to that of the I-beam flanges ( $t_f$ ) in all tests. However, the minimum width of the DPs ring ( $W_{DP,r}$ ) varied in the tests in a range from  $0.2b_f$  to  $0.7b_f$ . Some of the other parameters investigated in this



experimental programme were the diameter-to-thickness ratio of the CHS column and the type of weld between the column and the DPs, which was either a Complete Joint Penetration (CJP) weld or a fillet weld.

The results from the weak-column-strong-beam specimens revealed that yielding started either in the column web panel or in the diaphragm plates, depending on the size of the latter. Then, yielding spread to the column wall adjacent to the panel zone, while no yield was detected in the I-beam. Failure modes in these specimens are illustrated in Figures 2.12(a) and 2.12(b) and included excessive shear deformation in the column web panel, local buckling in the column wall, shear buckling in the column panel zone, local distortion in the external diaphragm plates, and cracks in the weld between the CHS column and the DPs.

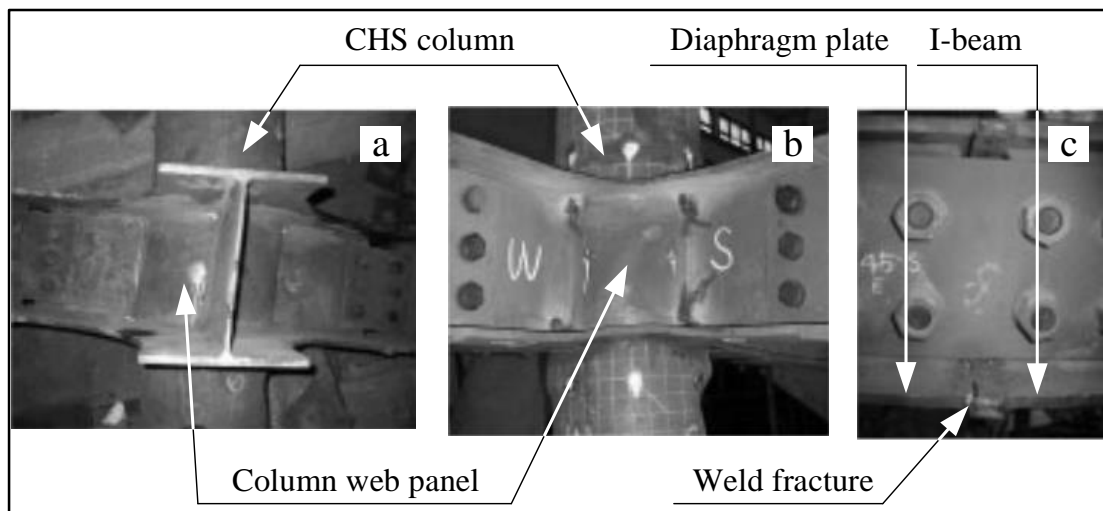


**Figure 2.12:** Failure modes of specimens tested in the work of Wang et al. (2011); a) excessive plastic shear deformation of the column web panel in a 2D interior joint; b) local buckling of the column wall, shear buckling of the column web panel and local distortion of the external diaphragm in a 3D interior joint; c) fracture of weld between the diaphragm plate and I-beam flange in the 3D exterior joint

For the strong-column-weak-beam specimens, yield occurred in the diaphragm plates and the I-beam, and a plastic hinge formed in the beam without observing any shear deformations of the column panel zone. The main failure mode of these specimens

was fracture of the weld between the I-beam flange and the DP, as shown in Figure 2.12(c).

Similar results were observed for joints made with fillet-welding the DPs to the column wall and those made with CJP welds. Based on this observation and because fillet welds are favoured to CJP welds by construction companies, Wang *et al.* (2011) recommended the use of fillet welds to connect external diaphragms to CHS columns in strong-column-weak-beam joints as there was no distortions of the panel zone or the diaphragm plates in the joint tests. Kurobane *et al.* (2004) reported similar recommendations from several Japanese studies, but added that when the required size of fillet welds becomes too large CJP welds should be used.

The hysteretic response of the different tested joints by Wang *et al.* (2011) revealed that they all met the ductility criteria for seismic resistant joints without any significant deterioration in their strength. However, weak-column joints had better dynamic energy dissipation ratios than the joints with weak beams. Wang *et al.* (2011) suggested that a design philosophy based on allowing the panel zone to yield in shear before yield onset in the I-beam could lead to higher ductility and seismic energy dissipation of the joint in spite of the high deformation demands imposed on the weld between the CHS column and the DPs as a result of excessive shear deformations of the panel zone. Wang *et al.* (2011) added that the stiffening effect of the diaphragm plates allowed for achieving high levels of ductility for weak-column joints without a significant reduction in their strength.

Although the tested joints exhibited mostly higher strength and ductility for bigger widths of the diaphragm plates ring, the results of the strong-column-weak-beam joints revealed the possibility of using small widths of the DPs to satisfy

architectural demands whilst meeting high seismic ductility criteria. This was because the axial forces of the I-beam flanges were resisted by both the DPs and the column, and the failure occurred in the I-beam before the development of full plastic deformation in the DPs. However, Wang *et al.* (2011) indicated the need of further research to determine the optimum width of DPs ring and highlighted the importance of moving the beam further away from the column face for such joints to avoid weld premature fracture. Similar recommendations regarding the reduction of stress concentrations around weld areas were given by Shen *et al.* (2010).

A numerical parametric study on a single-sided I-beam to CHS column joint under monotonic and cyclic loadings was carried out by Sabbagh *et al.* (2013) to establish joint details that eliminate the structural deficiencies identified in the work of Alostaz and Schneider (1997) and Schneider and Alostaz (1998). Sabbagh *et al.* (2013) investigated two different joint arrangements using rounded external diaphragm plates rather than chamfered ones to allow for a smooth stress flow from the beam into the column. The DPs were welded to the outer circumference of the CHS column, and their dimensions were designed for the full strength of the I-beam flanges.

In the first joint arrangement, the DPs were spaced to accommodate the beam height, and the beam was passed between the two plates and bolted to their inner surfaces. The beam web was bolted to a shear tap plate welded to the column face. Different width values of the DPs were numerically investigated while keeping their thickness and steel grade constant. It was found that the width, which conforms to the design formula given in the CIDECT design guide number 9 by Kurobane *et al.* (2004) for the joint peak moment, resulted in large areas of yielding inside and outside the column web panel. Doubling the width value, which satisfied the design criterion

suggested by Wang *et al.* (2011), was found to eliminate column web panel distortion and resulted in minimal yielding in this region.

The failure modes were computed to be local flange and web buckling in the I-beam section next to the connection zone. High post-yield stress concentrations, which could lead to unwanted modes of failures, were noted in the compressive DP in the region adjacent to the column face when the joint was subjected to monotonic loading. Sabbagh *et al.* (2013) explained that this stress concentration was a result of the relatively low out-of-plane stiffness of the DP. Hence, increasing its thickness or steel strength would not effectively eliminate it. The use of appropriately designed triangular vertical stiffeners welded to the outer surfaces of the horizontal DPs was found to eliminate the stress concentrations without impacting on the rotation capacity significantly.

To avoid fracture in the I-beam compressive flanges due to local buckling failure and to protect the primary members under severe seismic actions, a further improvement to the previous joint details was proposed by Sabbagh *et al.* (2013) in a second joint arrangement. This arrangement involved moving the beam end further away from the column face following the recommendations of Alostaz and Schneider (1997), using cover plates to connect the I-beam flanges to the DPs, and bolting the I-beam web to a single-sided web stub plate welded to the column face. The middle section of a cover plate was reduced to create a weak section for plastic hinging. The Tapered Cover Plates (TCPs) were designed to reach full plasticity before the I-beam reaches its design plastic bending resistance to create a multi-fuse energy dissipative mechanism in the joint under seismic actions. Bolt holes in the web stub plate were oversized with the maximum practical clearance and the bolts were appropriately

preloaded to allow slippage in the web connection after the onset of the inelastic response. This was to avoid web distortion and localise the failure in the TCPs.

The use of rectangular stiffeners welded longitudinally to the full length of the TCPs was also investigated to avoid premature unrestrained buckling failure of these plates, and several dimensions of the TCPs and their stiffeners were varied in parametric finite element analyses. The refined details produced a joint in which the failure modes were gross plasticity and buckling of the TCPs and their stiffeners. Yielding in the TCPs was the main energy dissipation fuse accompanied by bolts slippage in their oversized holes and yielding in the beam section located next to the connection zone as two extra energy dissipation fuses.

Sabbagh *et al.* (2013) proposed one last design refinement that was the use of a stronger beam in the joint to limit the inelastic deformations and buckling failure to the TCPs and their stiffeners, and hence turn them into replaceable links in the joint whilst keeping the rest of the components elastic for the purpose of a speed and cost-effective post-seismic repair.

#### *2.4. Concluding remarks*

This chapter presents a review of relevant literature on the subject of moment joints to tubular columns. Previous research studies revealed that joints made by welding open-section beams directly to the outer skin of tubular columns without the use of any stiffeners were not suitable for seismic applications. The difficulties and risks associated with internal and through stiffening of tubular columns increased the necessity of finding efficient designs of external stiffeners. Most of the research studies on external diaphragm joints have been done on joints to concrete filled tubes (CFT) rather than joints to unfilled hollow section columns.

Previous studies emphasised the need to avoid abrupt geometry changes at the beam-DPs junction. Gradual geometrical changes in the DPs were found necessary for the smoothest uniform stress flow around the tube. Moreover, moving the beam end further away from the column face for a distance not less than the tube external diameter was found to improve the joint elastic and inelastic performance significantly by allowing large strains to remain within the beam flanges in order to develop the plastic hinge within the beam away from the column face. Similarly, the use of RBS beams in joints to tubular columns allowed the desirable development of a plastic hinge in the reduced section of the beam. For joints made with field welding the DPs to the beam flanges, sufficient quality control and skilled welders were highly emphasised to avoid weld defects that could lead to brittle fractures similar to those in the Kobe earthquake of 1995. Field-bolting the DPs to the I-beam flanges, with cover plates, instead of welding them was found to reduce the risk of brittle fractures when the joint is subjected to severe seismic actions. In addition to that, reducing the middle section of the cover plates, which connect the beam to the diaphragm plates, showed the possibility of achieving excellent seismic performance of the joint through developing a multi-fuse energy dissipation mechanism.

The second joint arrangement proposed by Sabbagh *et al.* (2013) satisfied many of the recommendations mentioned above. In this project, the work of Sabbagh *et al.* (2013) is extended to investigate experimentally the structural performance of their second joint arrangement under cyclic loading. Nine full-scale laboratory experiments of the external diaphragm joint were conducted in the Structures Laboratory at the School of Engineering, University of Warwick. The next chapter presents the details, design philosophy and calculations of the proposed external diaphragm joint.

# *Chapter 3*

## *Joint Design Development*

### *3.1. Introduction*

This chapter presents the design philosophy and details of the external diaphragm joint between steel I-section beam and CHS column, which was investigated in this research experimentally to assess its seismic behaviour. This joint arrangement was proposed and investigated numerically in the FE work by Sabbagh *et al.* (2013). Furthermore, this chapter summarises the most important calculations carried out at the design stage. The purpose of these calculations was to verify that the proposed design would allow the achievement of the desired joint performance under cyclic loading, in line with the recommendations of BS EN 1998-1: 2004.

BS EN 1998-1: 2004 specifies in Clause 6.2 (2)P that the material distribution in the structure should allow the formation of dissipative zones under cyclic loading where they are intended to in the design, and these dissipative zones should have sufficient ductility and resistance. Clause 6.5.2 (5)P states that when the dissipative zones are

designed to form within the joint, as in this design, then the connected members should have adequate overstrength to allow the development of cyclic yielding in the joint. Furthermore, For joints in dissipative moment resisting frames, BS EN 1998-1: 2004 specifies in Clause 6.6.4 (3) that the joint design should be that the rotation capacity of the plastic hinge region exceeds 35mrad for high ductility class (DCH) structures and 25mrad for medium ductility class (DCM) structures. This should be satisfied under cyclic loading without degradation of strength and stiffness greater than 20%. Other recommendations of BS EN 1998-1: 2004 for dissipative moment resisting frames were followed and listed in this thesis where appropriate.

All the calculations listed in this chapter were done according to the standards specified in BS EN 1993-1-1: 2005, BS EN 1993-1-8: 2005, BS EN 1998-1: 2004 and their UK National Annexes, unless otherwise stated.

### *3.2. Joint design philosophy*

The design philosophy was based on attaining a joint that is architecturally appealing, practical for construction and most importantly achieves the required structural performance and ductility under seismic loading for dissipative structures. The proposed joint is for an I-section beam and a circular hollow section column in a moment-resisting frame.

Sabbagh *et al.* (2013) investigated numerically a joint that meets the criteria mentioned above and discussed the possibility of providing built-in replaceable links that can act as the main seismic energy dissipation fuse. This project investigated the seismic performance of the same joint through nine full-scale laboratory experiments and examined the influence of certain parameters on its overall hysteretic response and energy dissipation.



The joint was designed to be partial strength, and its strength was governed by the properties of the joint built-in replaceable links as detailed in Section 3.3. Efficient choice of the geometry and material properties of the different joint components is crucial so that, under cyclic loading, the dissipative zones would form where they are intended to, which is in the replaceable links, and the rest of the joint components are to have sufficient overstrength to remain elastic and allow for the development of cyclic yielding in the dissipative zones, as recommended in BS EN 1998-1: 2004.

This design philosophy was applied through the calculations listed in Section 3.4 and assessed through the laboratory experiments detailed in Chapters 5 and 6.

### *3.3. Details of the joint arrangement*

The arrangement and components of the joint before and after assembly are illustrated in Figures 3.1 and 3.2 respectively. Table 3.1 lists all the components of the joint with their nominal material properties, geometry and number per specimen.

The proposed single-sided joint includes two collar DPs, which have a 90mm-wide ring, welded to the outer circumference of a 244.5×10 CHS column and connected to the flanges of UKB 203×133×30 beam with two tapered (dog-bone shaped) cover plates (TCPs) using 24×M22 bolts of Class 10.9. A web stub (WS) plate was welded to the face of the CHS column and bolted to the I-beam web with three M16 bolts of Class 10.9.

To the point of loading, the beam was taken to be 2m long to represent the distance between the connection and the inflection point near the mid-span of a 4m beam in a moment-resisting frame. The boundary conditions of the 2m column were assumed to be hinges to represent the inflection points at the mid-height of columns in a

moment frame. The choice of the overall dimensions was governed by the available facilities in the testing laboratory.

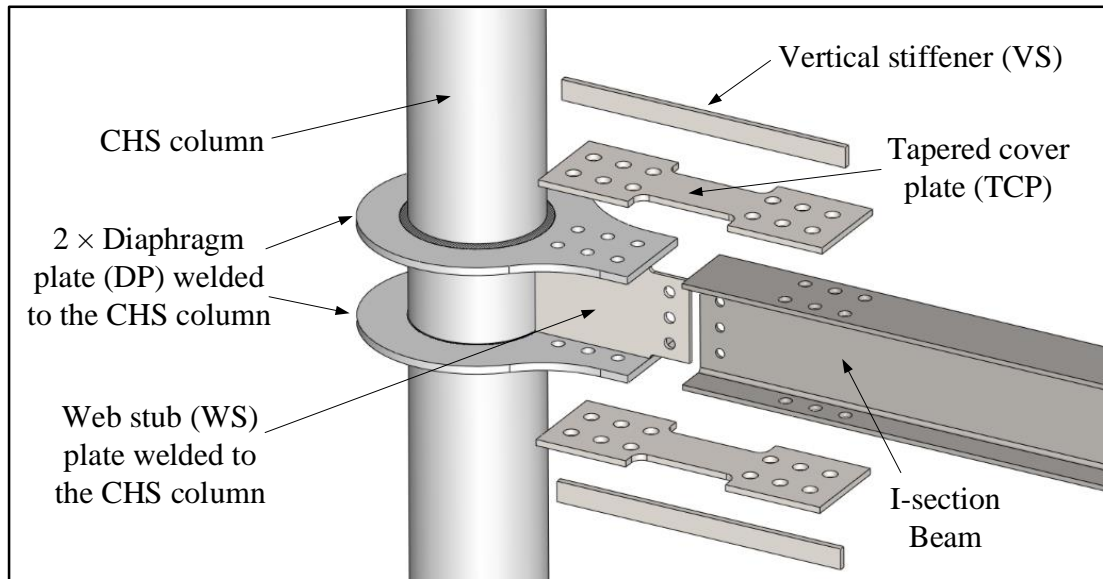


**Figure 3.1:** The components of the beam to column joint before assembly

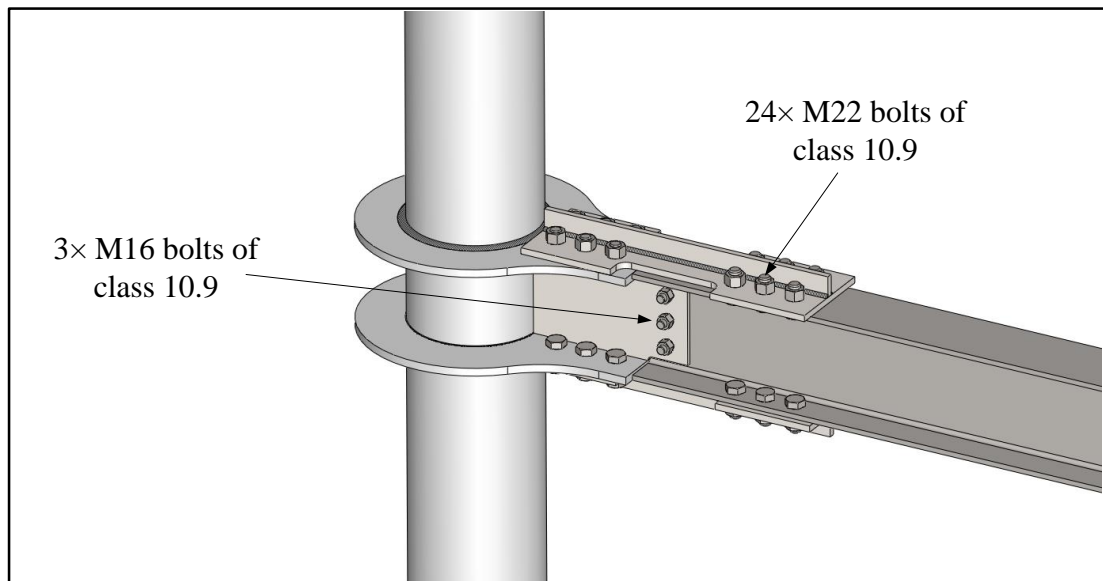


**Figure 3.2:** The beam to column joint after assembly

In the experimental work, a 3m beam was cut and the connection holes were drilled in its flanges and web from both ends so that it could be connected to the diaphragm plates from either end. The load application point was 2m from the connected end of the beam. Hereafter, the 2m length of the beam is referred to as the effective length

( $L_{eff}$ ). This arrangement led to having a more practical beam than the one cut to have the exact required length of 2m, because if there was any distortion or permanent deformation at the connected end of the 3m beam as a result of testing then the beam could still be used in testing by connecting its undeformed end. This is interpreted in the beam geometry presented in Table 3.1.

The diaphragm plates geometry was chosen in line with the recommendations of Wang *et al.* (2011) and Sabbagh *et al.* (2013) to eliminate any stress concentration in them, which could lead to weld fracture, and allow for a smooth stress flow around and into the CHS column to avoid distortion in the column web panel. The web connection was designed to transfer shear forces from the I-beam to the column face efficiently. Bolts of the web connection were appropriately preloaded and their holes in the web stub were oversized with 6mm clearance in accordance with ANSI/AISC 360-10 (2010) to avoid web distortion as recommended by Sabbagh *et al.* (2013).

The TCPs were designed, similar in principle to the flange plates utilised in the work of McMullin and Astaneh-Asl (2003), to act as the main seismic energy dissipation fuse and be the replaceable components of the joint whilst the rest of the components remained elastic. The TCPs bolted connections to the I-beam and the DPs were designed to be slip resistant at the Serviceability Limit State (SLS), which is Category B connection according to BS EN 1993-1-8: 2005. This ensures the activation of connection slippage beyond the serviceability limit to provide a second seismic energy dissipation fuse. Bolts of the connection conformed to the requirements given in 1.2.4 Reference Standards for high strength structural bolting for preloading with controlled tightening in accordance with the requirements in 1.2.7 Reference Standards in BS EN 1993-1-8: 2005, unless otherwise stated.

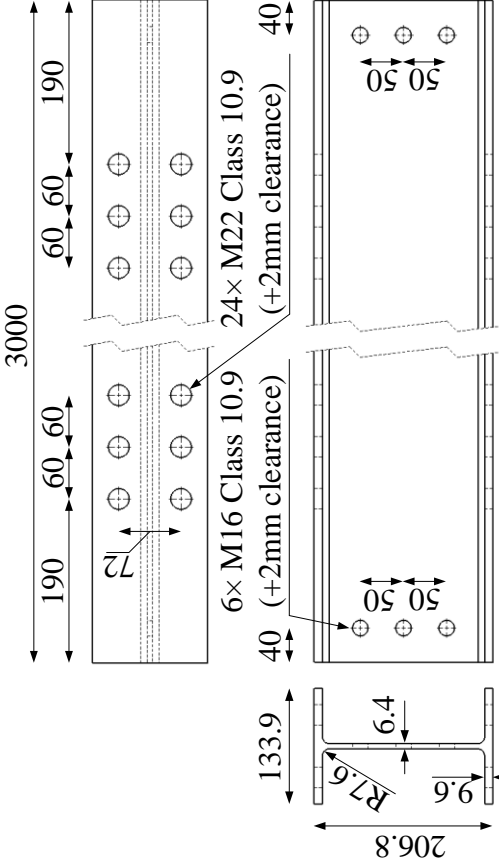
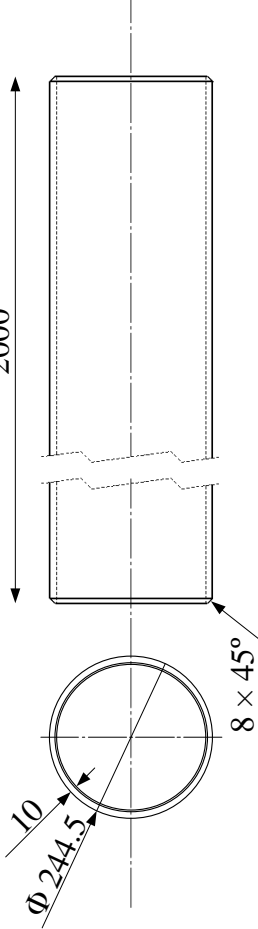
Since TCPs were the proposed replaceable components of the joint, it was crucial to understand the effect of using different types of TCPs on the overall cyclic performance. Nine full-scale laboratory experiments of the proposed joint were conducted in the Structures Laboratory at the University of Warwick. The geometry and steel grade of each joint component, except the TCPs, were identical in the nine tests. The pairs of TCPs used had the same geometry but differed from each other via one or more of the following four parameters;

- Grade of steel was either S235 or S355;
- The bolt-holes were either normal/standard round holes of size ( $d_0 = d + 2\text{mm} = 24\text{mm}$ ) as defined in BS EN 1993-1-8: 2005, or Oversized round holes of size ( $d_0 = d + 6\text{mm} = 28\text{mm}$ ). The clearance of oversized holes was chosen to be 6mm in accordance with ANSI/AISC 360-10 (2010) to show the effect of bolts slip on the overall performance of the joint;
- TCPs were either stiffened along their longitudinal axis or not;
- Value of the preloading force ( $F_{p,Cd}$ ) acting on the M22 bolts, which connected the TCPs to both the I-section beam and the diaphragm plates, was either in line with BS EN 1993-1-8: 2005 for slip-resistant connections or half that value. The full preloading force is  $F_{p,Cd} = 0.7 \times f_{ub} \times A_s$  while the half-preloaded bolts had  $F_{p,Cd} = 0.35 \times f_{ub} \times A_s$ .

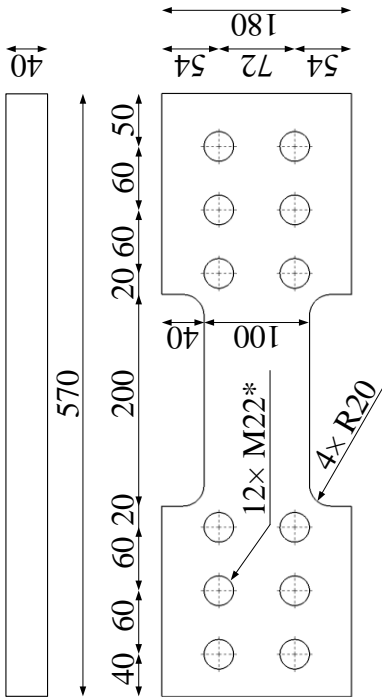
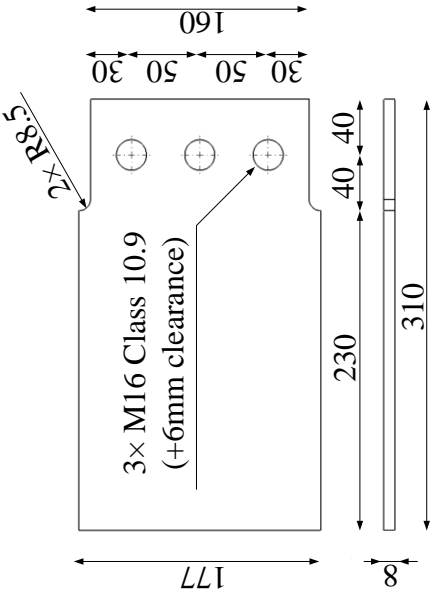
The use of different types of TCPs allowed for comparing tests results in pairs. Tests of each pair differed by changing one of the four parameters detailed above. For example the comparison between two tests in which both pairs of TCPs were stiffened, of the same steel grade, and connected with fully preloaded bolts allowed the investigation of the effect of bolt-holes size on the overall cyclic performance.

The labelling scheme for the joint specimens followed the format G-H-S-BP, where G represents the steel grade of the TCPs, either S235 or S355; H is the size of the TCPs bolt-holes, either NSH (Normal-Size Holes) or OSH (Oversized Holes); S reflects the use of TCPs stiffeners, either NS (No Stiffeners) or WS (With Stiffeners); and BP is the TCPs bolts preloading force, either FP (Full Preload) or HP (Half Preload). The types of TCPs used in the nice test specimens are detailed in Table 3.2.

**Table 3.1:** Geometry and properties of the joint components

Component	Number per specimen	Steel Grade	Geometry
I-section beam UKB 203×133×30	1	S355	
CHS column 244.5×10	1	S355	

**Table 3.1: Geometry and properties of the joint components**

Component	Number per specimen	Steel Grade	Geometry/ Cross section
Tapered Cover Plate (TCP) and its vertical stiffener (VS)	2	S235 or S355	<p>Stiffener; thickness=12mm</p>  <p>TCP; thickness=12mm          * Bolt-Holes size is either normal (24mm) or oversized (28mm)</p>
Web stub (WS)	1	S355	 <p>3x M16 Class 10.9 (+6mm clearance)</p>

**Table 3.1:** Geometry and properties of the joint components

Component	Number per specimen	Steel Grade	Geometry/ Cross section
Diaphragm plate (DP)	2	S355	<p>6 × M22 Class 10.9 (+2mm clearance)</p> <p>2 × R212</p> <p>Φ 247.5</p> <p>Φ 424</p> <p>Chamfer 13 × 45°</p> <p>180</p> <p>72</p> <p>564</p> <p>182</p> <p>212</p> <p>60</p> <p>60</p> <p>50</p>



**Table 3.2:** Tests label according to the type of TCPs used in the test specimens

Test number	Test label	Type of Tapered Cover Plates (TCPs)			
		Steel grade	Size of bolt-holes	Use of Stiffeners (Y/N)	Bolts preload force
1	S235-OSH-NS-FP	S235	Oversized	No	Full preload
2	S235-OSH-WS-FP	S235	Oversized	Yes	Full preload
3	S235-NSH-WS-FP	S235	Normal	Yes	Full preload
4	S355-OSH-NS-FP	S355	Oversized	No	Full preload
5	S355-OSH-WS-FP	S355	Oversized	Yes	Full preload
6	S235-NSH-NS-FP	S235	Normal	No	Full preload
7	S355-NSH-NS-FP	S355	Normal	No	Full preload
8	S235-OSH-NS-HP	S235	Oversized	No	Half preload
9	S355-OSH-WS-HP	S355	Oversized	Yes	Half preload

### 3.4. *Design calculations of the joint components*

This section lists the most important calculation checks carried out to verify that the chosen material distribution and the geometry of the joint components allow for achieving the desired joint performance. This is for having the formation of dissipative yield zones in the reduced section areas of the TCPs and sufficient overstrength in the rest of the components so that they deform within their elastic range.

In addition, the slip resistance of the TCPs connection at SLS is checked to ensure the activation of slip before the full plasticity of the dissipative zones. This is to create a second fuse for seismic energy dissipation. The calculations in this section neglected gravity loading and were categorised according to the component being checked.

The design calculations were initially carried out using nominal material properties. BS EN 1998-1: 2004 recommends multiplying the nominal yield strength of the dissipative zones by  $(1.1 \times \gamma_{ov})$  to ensure they yield before the other zones leave their elastic range during an earthquake; where  $\gamma_{ov}$  is the material overstrength factor with a value of 1.25.

As detailed in Chapter 4, tensile coupon tests were conducted in accordance with BS EN ISO 6892-1: 2009 to determine the actual steel properties in each component. The design calculations for this chapter were updated according to the actual material properties to achieve a more reliable and representative design. Subsequently, the material overstrength factor was taken equal to 1.0 and the yield strength of the dissipative zones was multiplied by a factor of 1.1.

### 3.4.1. Tapered cover plates (TCPs)

The reduced section area in a TCP was designed to be the main dissipative zone in the joint. Therefore, this area should yield before other zones in the joint leave their elastic range. Furthermore, for the TCPs to act as the sacrificial replaceable components of the joint, plastic regions should develop in their tapered sections under cyclic loading before yield onset in any other joint component.

Nine different types of the TCPs were used in the experimental program, as detailed in Section 3.3 of this chapter, and they were all considered in the design calculations of the joint. However, the calculations of only one type of the TCPs, which is the S235-NSH-WS-FP-TCP, is detailed in this section to avoid repetition.

#### 3.4.1.1. Geometric properties

The geometry of the nine types of the TCPs is identical except for the size of their bolt holes and the presence of the longitudinal stiffener. The main geometric properties of the S235-NSH-WS-FP-TCP and its stiffener are:

Width of the TCP	$W_{TCP} = 180 \text{ mm}$
Width of the reduced section area of the TCP	$W_{red} = 100 \text{ mm}$
Thickness of the TCP	$t_{TCP} = 12 \text{ mm}$
The bolt hole diameter	$d_0 = 24 \text{ mm}$
Height of the TCP stiffener	$h_s = 40 \text{ mm}$
Thickness of the TCP stiffener	$t_s = 12 \text{ mm}$

3.4.1.2. Material properties

The material properties of the S235–TCP and its stiffener were obtained from the tensile coupon tests detailed in Chapter 4.

Yield strength  $f_{y,TCP} = 304 \text{ N/mm}^2$

Ultimate strength  $f_{u,TCP} = 487 \text{ N/mm}^2$

$f_{y,TCP}$  was multiplied by 1.1 when calculating the design plastic resistance of the cross section of the tapered region because this is the intended plastic zone under seismic loads.

3.4.1.3. Design tension resistance

Under cyclic loading, the bending moment in the I-beam, in either direction, may be represented by axial forces in its top and bottom flanges. These forces are transmitted to the TCPs through the shear bolted connections. Consequently, the cross section of each TCP is subject to alternate tension–compression loading. The design tension resistance  $N_{TCP,t,Rd}$  of S235-NSH-WS-FP–TCP was taken as the smallest of:

- a) Design plastic resistance of the gross section  $N_{pl,Rd}$

$$N_{pl,Rd} = A_{gr} \times f_{y,TCP} / \gamma_{M0} = 803 \text{ kN.}$$

$$\text{with } A_{gr} = (W_{TCP} \times t_{TCP}) + (h_s \times t_s) = 2640 \text{ mm}^2.$$

$\gamma_{M0}$  is 1.0

- b) Design plastic resistance of the reduced section  $N_{red,pl,Rd}$

$$N_{red,pl,Rd} = A_{red} \times 1.1 \times f_{y,TCP} / \gamma_{M0} = 562 \text{ kN.}$$

$$\text{with } A_{\text{red}} = (W_{\text{red}} \times t_{\text{TCP}}) + (h_s \times t_s) = 1680 \text{ mm}^2.$$

c) Design ultimate resistance of the net cross-section at holes for bolts  $N_{u,Rd}$

$$N_{u,Rd} = 0.9 A_{\text{net}} \times f_{u,TCP} / \gamma_{M2} = 822 \text{ kN}.$$

$$\text{with } A_{\text{net}} = ((W_{\text{TCP}} - 2 \times d_0) \times t_{\text{TCP}}) + (h_s \times t_s) = 2064 \text{ mm}^2.$$

$\gamma_{M2}$  is 1.1

The design tension resistance of this TCP is  $N_{\text{TCP},t,Rd} = N_{\text{red},pl,Rd} = 562 \text{ kN}$ .

This finding agrees with the design concept of developing a plastic region in the TCP reduced section area before any failure in the other sections of the TCP. The size of bolt holes in the TCP did not affect its design tension resistance because the latter was governed by the resistance of the reduced section area. The steel grade and use of stiffeners were the two factors that varied the design tension resistance of the different TCPs. This can be further identified from the values of  $N_{\text{TCP},t,Rd}$  presented in the fifth column in Table 3.3 for the nine different TCP types. In the first two columns of Table 3.3, TCPs were classified into four groups according to their steel grade and use of stiffeners, which were presented in column 3 and 4 in the table.

**Table 3.3:** Design tension resistance of the TCPs

Group	TCP	Steel grade	Use of stiffener	$N_{\text{TCP},t,Rd} = N_{\text{red},pl,Rd}$ [kN]
1	S235-OSH-NS-FP S235-NSH-NS-FP S235-OSH-NS-HP	S235	No	401
2	S355-OSH-NS-FP S355-NSH-NS-FP	S355	No	508
3	S235-OSH-WS-FP S235-NSH-WS-FP	S235	Yes	562
4	S355-OSH-WS-FP S355-OSH-WS-HP	S355	Yes	711

### 3.4.2. I-section beam - UKB 203×133×30

The I-beam was assumed to be a non-dissipative member in seismic events and thus its maximum strength had to be limited to its design elastic bending resistance  $M_{b,el,y,Rd}$  in these calculations.

#### 3.4.2.1. Geometric properties

The geometric properties of the beam and its cross section are detailed here. The most critical section of the I-beam under bending moments is the one where the highest stress concentration and yield onset are expected. This critical section is located next to the connection zone for this joint arrangement, as indicated in the work of Sabbagh *et al.* (2013). Therefore, the beam critical length is identified here as the distance between the loading point and the most critical section of the I-beam.

Beam effective length	$L_{eff}$	= 2000 mm
Beam critical length	$L_{cr}$	= 1640 mm
Depth of cross section	$h$	= 206.8 mm
Depth of web	$h_w$	= 187.6 mm
Width of cross section	$b$	= 133.9 mm
Flange thickness	$t_f$	= 9.6 mm
Web thickness	$t_w$	= 6.4 mm
Root radius	$r$	= 7.2 mm
Area of cross section	$A_{beam}$	= 38.2 cm <sup>2</sup>
Second moment of area about the major axis	$I_y$	= 2896 cm <sup>4</sup>

Elastic section modulus about the major axis  $W_{el,y} = 280 \text{ cm}^3$

Plastic section modulus about the major axis  $W_{pl,y} = 314 \text{ cm}^3$

#### 3.4.2.2. Material properties

The material properties of the I-beam were obtained through tensile coupon tests as detailed in Chapter 4.

Yield strength  $f_{y,beam} = 420 \text{ N/mm}^2$

Ultimate strength  $f_{u,beam} = 560 \text{ N/mm}^2$

Modulus of elasticity  $E_{beam} = 202500 \text{ N/mm}^2$

#### 3.4.2.3. Cross section classification

The cross section is Class 1 under bending if both its flange under compression and web subject to bending are Class 1. The limiting value for Class 1 flange under pure compression is:

$$c / t_f \leq 9\varepsilon$$

where  $c$  is equal to  $(b - t_w - 2r) / 2 = 56.2 \text{ mm}$

$$\varepsilon = \sqrt{(235/f_y)} = 0.75$$

$$c / t_f = 5.8$$

$$9\varepsilon = 6.8$$

$$5.8 < 6.8$$

The I-beam flange is Class 1 under compression.

The limiting value for Class 1 web subject to bending is:

$$c / t_w \leq 72\varepsilon$$

where  $c$  is equal to  $h_w = 187.6$  mm

$$c / t_w = 29.3$$

$$72\varepsilon = 54$$

$$29.3 < 54$$

The I-beam web subject to bending is Class 1, and subsequently the I-beam cross section is Class 1 under bending.

#### 3.4.2.4. Design bending resistance

If the beam was to dissipate seismic energy then its resistance would have to be limited to its plastic strength amplified by a factor of (1.1) to ensure that the non-dissipative members of the joint would have sufficient overstrength. The design plastic bending resistance of the I-beam cross section about its major axis y-y is given by:

$$M_{b,pl,y,Rd} = W_{pl,y} \times 1.1 \times f_{y,beam} / \gamma_{M0} = 145 \text{ kN.m}$$

One of the main aims of the research is to provide a joint that limits the post-seismic damages to the replaceable links. Thus, the strength of the beam in this design is limited to its design elastic bending resistance that is given by:

$$M_{b,el,y,Rd} = W_{el,y} \times f_{y,beam} / \gamma_{M0} = 117.6 \text{ kN.m}$$

To allow the reduced sections of the TCPs, and their stiffeners when applicable, to reach full plasticity before the yield onset at the critical section of the I-beam, the following inequality should be satisfied:



$$M_{j,pl} < M_{j,b,el}$$

where  $M_{j,pl}$  is the joint moment when the reduced section areas of the TCPs and their stiffeners reach full plasticity, and is taken as:

$$M_{j,pl} = N_{TCP,t,Rd} \times z_1$$

where  $N_{TCP,t,Rd}$  is the design tension resistance of the TCPs, and its value for each type of the TCPs is given in Table 3.3.

$z_1$  is the lever arm between the coupling forces  $N_{TCP,t,Rd}$  when the reduced section areas of the TCPs are fully plastic and it is equal to the distance between the centroids of the top and bottom TCPs. The values of  $z_1$  and  $M_{j,pl}$  for the different types of TCPs are presented in the fifth and sixth columns in Table 3.4.

**Table 3.4:** The joint moment at full plasticity of the TCPs middle sections

Group	TCP	Steel grade	Use of stiffener	$z_1$ [mm]	$M_{j,pl} = N_{TCP,t,Rd} \times z_1$ [kN.m]
1	S235-OSH-NS-FP S235-NSH-NS-FP S235-OSH-NS-HP	S235	No	218.8	88
2	S355-OSH-NS-FP S355-NSH-NS-FP	S355	No	218.8	111
3	S235-OSH-WS-FP S235-NSH-WS-FP	S235	Yes	233.7	131
4	S355-OSH-WS-FP S355-OSH-WS-HP	S355	Yes	233.7	166

$M_{j,b,el}$  is the joint moment calculated at the beam end when the beam critical section reaches its design elastic bending resistance, as shown in Figure 3.3, and its value was taken, regardless of the TCP type, as:

$$M_{j,b,el} = M_{b,el,y,Rd} \times L_{eff} / L_{cr} = 143.4 \text{ kN.m}$$

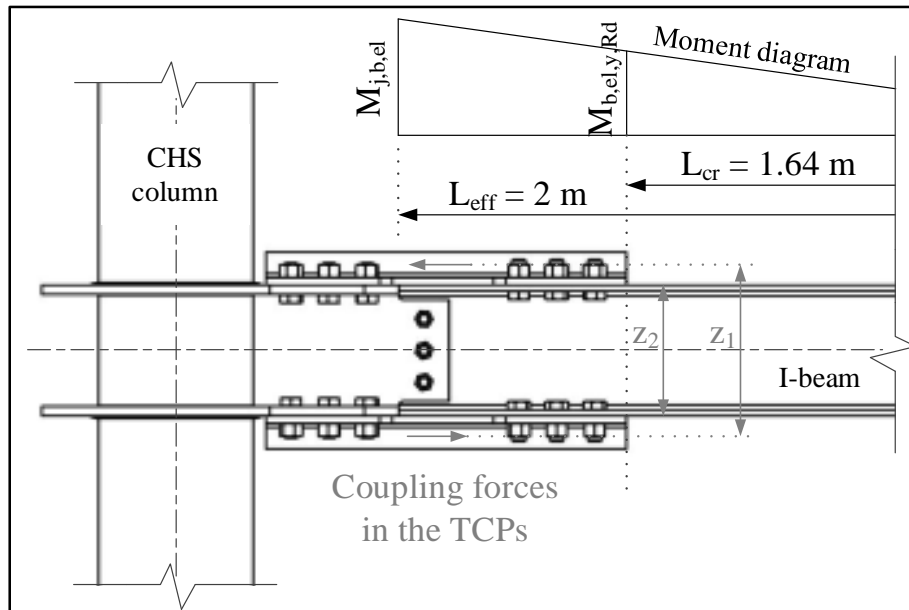


**Figure 3.3:** *Moment of the joint in relation to the beam moment*

It is clear from Table 3.4 that eight types of TCPs satisfy the inequality  $M_{j,pl} < M_{j,b,el}$ . The exception is for the stiffened S355–TCPs. This means that using stiffened or unstiffened S235–TCPs or unstiffened S355–TCPs will result in a partial strength joint, with respect to the beam elastic strength. In other words, these joints dissipate seismic energy by full plasticity in the reduced section areas of TCPs whilst the beams deform in the elastic range.

Using stiffened S355–TCPs will result in a partial strength joint with respect to the beam plastic strength because:

$$(M_{j,b,pl} = 177 \text{ kN.m}) > (M_{j,pl} = 166 \text{ kN.m}) > (M_{j,b,el} = 143.4 \text{ kN.m})$$

where  $M_{j,b,pl}$  is the joint moment calculated at the beam end when the beam critical section reaches its design plastic bending resistance; and its value is taken, regardless of the TCP type, as:

$$M_{j,b,pl} = M_{b,pl,y,Rd} \times L_{eff} / L_{cr} = 177 \text{ kN.m}$$

In other words, using stiffened S355–TCPs might create a seismic energy dissipation fuse that is full plasticity in the reduced section areas of the TCPs and another fuse that is inelastic deformation at the critical section in the I-beam. This joint behaviour is acceptable and could be beneficial in achieving a higher rotational capacity than that with one fuse in the TCPs. However, having plastic deformations in the beam is to be avoided in this research, if possible, to meet one of the design objectives, which is limiting the plastic deformations of the joint to the TCPs for effective post seismic repair.

#### 3.4.2.5. Design shear resistance

The design moment resistance of the beam does not need to be reduced if the design shear value  $V_{Ed}$  is less than 50% of the design plastic shear resistance of the beam  $V_{pl,Rd}$ .

$V_{pl,Rd}$  is calculated from  $A_v \times (1.1 \times f_{y,beam} / \sqrt{3}) / \gamma_{M0}$

where  $A_v$  is the shear area of the I-beam and it is taken as:

$$A_v = A_{beam} - 2bt_f + (t_w + 2r) t_f = 1457 \text{ mm}^2$$

$A_v$  should not be less than  $(\eta h_w \times t_w = 1201 \text{ mm}^2)$  where  $\eta = 1$  according to BS EN 1993-1-5: 2006 and its UK National Annex.

Therefore,  $A_v = 1457 \text{ mm}^2$  and  $V_{pl,Rd} = 389 \text{ kN}$

The design shear value is equal to the vertical load applied to the beam when its critical section becomes fully plastic, hence:

$$V_{pl,Ed} = M_{b,pl,y,Rd} / L_{cr} = 88.4 \text{ kN}$$

$$(V_{pl,Ed} = 88.4 \text{ kN}) < (0.5 V_{pl,Rd} = 194.5 \text{ kN})$$

Therefore, there was no need to reduce the design plastic moment resistance of the beam.

As the beam is to be designed to remain elastic, it is important to check that the design shear value at yield onset in the critical section of the beam  $V_{el,Ed}$  does not exceed the design elastic shear resistance of the beam  $V_{el,Rd}$ , as follows:

$$V_{el,Ed} < V_{el,Rd}$$

$$V_{el,Ed} = M_{b,el,y,Rd} / L_{cr} = 71.7 \text{ kN}$$

$$V_{el,Rd} = A_w \times (f_{y,beam} / \sqrt{3}) / \gamma_{M0} \quad \text{if } A_f / A_w \geq 0.6$$

where  $A_w$  is the area of the web:  $A_w = h_w \times t_w = 12 \text{ cm}^2$

$A_f$  is the area of the flange:  $A_f = b \times t_f = 12.9 \text{ cm}^2$

$$A_f / A_w = 1.1 > 0.6$$

$$V_{el,Rd} = 267 \text{ kN}$$

$$71.7 < 267 \text{ kN}$$

The I-beam shear resistance is adequate.

#### 3.4.2.6. Shear buckling check

There is no need to check the shear buckling resistance of the I-beam web if:

$$h_w / t_w \leq 72\varepsilon / \eta$$

$$29.3 < 54$$

The shear buckling resistance of the web did not need to be verified.

### 3.4.3. The connection between a TCP and an I-beam flange

In the proposed joint arrangement, each of the two TCPs was connected to a flange using a group of six M22 bolts of grade 10.9. The connection was loaded in shear during the cyclic bending and the bolts were pre-tensioned to have a Category-B connection that is slip resistant at SLS. This was to allow slip to be activated beyond the serviceability limit to act as an extra seismic energy dissipation fuse and delay the yield onset in the beam. The calculations of the design shear resistance, design slip resistance and some other design checks were carried out for the connection between an I-beam flange and a TCP taking into consideration all the different types of the TCPs used in this project, and it was found that the use of the proposed bolt group was adequate. To avoid repetition, this subsection details the most important design calculations and checks for one type of the TCPs that is S235-NSH-WS-FP.

#### 3.4.3.1. Geometric properties

The geometric properties of the I-beam and TCPs were presented in Subsections 3.4.1.1 and 3.4.2.1. The geometric properties of the M22 bolts and their holes in the S235-NSH-WS-FP-TCP are:

Bolt diameter	$d$	= 22 mm
Bolt hole diameter	$d_0$	= 24 mm
The gross cross section area of a bolt	$A_b$	= 380 mm <sup>2</sup>
The tensile stress area of a bolt	$A_s$	= 303 mm <sup>2</sup>
Number of bolts	$N$	= 6 bolts

The actual bolts spacing, end and edge distances fall within the range of minimum and maximum allowances specified in BS EN 1993-1-8: 2005, and are represented in Table 3.5.

**Table 3.5:** Spacing, end and edge distances for the TCP to the beam connection

	Spacing P <sub>1</sub> * (mm)	Spacing P <sub>2</sub> * (mm)	End distance e <sub>1</sub> * (mm)	Edge distance e <sub>2</sub> * (mm)
Minimum	52.8	57.6	28.8	28.8
Maximum	134.4	134.4	78.4	78.4
<i>Actual</i>	<i>60</i>	<i>72</i>	<i>50</i>	<i>Beam: 30.95</i> <i>TCP: 54</i>

\* where P<sub>1</sub> is the spacing between centres of bolt holes in a line in the direction of load transfer, P<sub>2</sub> is the spacing between centres of bolt holes in a line perpendicular to the load transfer direction, e<sub>1</sub> is the end distance from the bolt hole centre to the adjacent end of the connected part in a line in the direction of load transfer and e<sub>2</sub> is the edge distance from the bolt hole centre to the adjacent edge of the connected part measured in a line perpendicular to the load transfer direction.

#### 3.4.3.2. Material properties

The material properties of the I-beam and TCPs were presented in Subsections 3.4.1.2 and 3.4.2.2. The nominal material properties of the M22 bolts are:

Yield strength of the M22 bolts  $f_{yb} = 900 \text{ N/mm}^2$

Ultimate strength of the M22 bolts  $f_{ub} = 1000 \text{ N/mm}^2$

#### 3.4.3.3. Local buckling checks

According to BS EN 1993-1-8: 2005, the local buckling resistance of the TCP in compression between the bolts need not to be checked if:

$$P_1 / t < 9 \varepsilon$$

$$P_1 / t = 60 / 12 = 5$$

$$9 \varepsilon = 9 \times \sqrt{(235/f_{y,TCP})} = 7.5$$

$$5 < 7.5$$

Local buckling between the bolts of TCPs need not to be checked.

The edge distance of the bolts  $e_2$  should not exceed the local buckling requirements for an outstand element in compression members. This means that  $(e_2 / t_{TCP})$  should be smaller than  $9\varepsilon$ :

$$e_2 / t_{TCP} = 4.5$$

$$4.5 < 7.5$$

#### 3.4.3.4. Design shear resistance of the M22 bolt

The design shear resistance  $F_{v,Rd}$  of a single M22 bolt when the shear plane passes through its unthreaded portion is taken as follows:

$$F_{v,Rd} = \alpha_v \times f_{ub} \times A_b / \gamma_{M2} = 182 \text{ kN.}$$

where  $\alpha_v = 0.6$

$$\gamma_{M2} = 1.25$$

#### 3.4.3.5. Design bearing resistance of the M22 bolt in the TCP

$F_{TCP,b,Rd}$  is the design bearing resistance of a single M22 bolt in S235-NSH-WS-FP-TCP, and it is given by:

$$F_{TCP,b,Rd} = k_1 \times \alpha_b \times f_{u,TCP} \times d \times t_{TCP} / \gamma_{M2}$$

where  $\alpha_b$  is the smallest of  $\alpha_d$ ,  $(f_{ub} / f_{u,TCP} = 2.1)$  or 1

$\alpha_d$  is  $(e_1 / 3d_0 = 0.69)$  for end bolts and  $(p_1 / 3d_0 - 0.25 = 0.58)$  for inner bolts.

Therefore,  $\alpha_b = \alpha_d = 0.69$  for end bolts and  $\alpha_b = \alpha_d = 0.58$  for inner bolts.

$k_1$  is the smallest of  $(2.8 e_2 / d_0 - 1.7 = 4.6)$ ,  $(1.4 p_2 / d_0 - 1.7 = 2.5)$  and 2.5

Therefore,  $k_1 = 2.5$

The design bearing resistance of a single bolt in the TCP is:

For end bolts:  $F_{TCP,end,b,Rd} = 2.5 \times 0.69 \times 487 \times 22 \times 12 / (1.25 \times 1000) = 177 \text{ kN}$

For inner bolts:  $F_{TCP,inner,b,Rd} = 2.5 \times 0.58 \times 487 \times 22 \times 12 / (1.25 \times 1000) = 150 \text{ kN}$

#### 3.4.3.6. Design bearing resistance of the M22 bolt in the I-beam

The calculation of the design bearing resistance of a single M22 bolt in the beam flange  $F_{bf,b,Rd}$  is carried out, similarly to that in the TCP, using the geometrical and material properties of the I-beam flange:

For end bolts:  $F_{bf,end,b,Rd} = k_1 \times \alpha_{b,end} \times f_{u,beam} \times d \times t_f / \gamma_{M2} = 181 \text{ kN}$

For inner bolts:  $F_{bf,inner,b,Rd} = k_1 \times \alpha_{b,inner} \times f_{u,beam} \times d \times t_f / \gamma_{M2} = 105 \text{ kN}$

#### 3.4.3.7. Design resistance of the TCP-beam connection

The design shear resistance of the bolt group is taken as the number of bolts multiplied by the design shear resistance of a single bolt:

$V_{TCP-bf,v,Rd} = N \times F_{v,Rd} = 6 \times 182 = 1092 \text{ kN}$

However, because the design shear resistance of a single M22 bolt is calculated to be higher than its maximum bearing resistance for both TCP and beam, the design resistance of the connection is taken to be equal to the sum of the minimum bearing resistances of the individual bolts:

$V_{TCP-bf,Rd} = \sum(F_{b,Rd,min}) = 720 \text{ kN}$



BS EN 1998-1: 2004 specifies that, for bolted shear connections to dissipative zones, the shear resistance of the connection should be 20% higher than its bearing resistance. This detailing rule is satisfied for the TCP-beam connection as follows:

$$(V_{\text{TCP-bf,v,Rd}} = 1092 \text{ kN}) > (1.2 \times V_{\text{TCP-bf,Rd}} = 864 \text{ kN})$$

Another design check is to ensure that the design resistance of the connection is higher than the design shear value  $V_{\text{TCP-bf,v,Ed}}$ . The latter was calculated based on the joint moment when the critical section of the beam starts yielding:

$$V_{\text{TCP-bf,v,Ed}} = M_{j,b,el} / z_2 = 143.4 \times 1000 / 206.8 = 693 \text{ kN}$$

where  $z_2$  is the lever arm between the coupling forces  $V_{\text{TCP-bf,v,Ed}}$  that pass through the shear planes of the top and bottom TCP-flange connections.  $z_2$  is equal to the beam height as illustrated in Figure 3.3.

$$(V_{\text{TCP-bf,Rd}} = 720 \text{ kN}) > (V_{\text{TCP-bf,v,Ed}} = 693 \text{ kN})$$

The design resistance of the TCP-beam connection is adequate.

#### 3.4.3.8. Design slip resistance of the TCP-beam connection

The M22 bolt preloading force for the S235-NSH-WS-FP-TCP is taken as:

$$F_{p,Cd} = 0.7 \times f_{ub} \times A_s = 212 \text{ kN}$$

The design slip resistance of the bolt group  $F_{s,Rd}$  for a Category B connection is given by:

$$F_{s,Rd} = k_s \times n \times N \times \mu \times F_{p,Cd} / \gamma_{M3,ser} = 347 \text{ kN}$$

where  $k_s$  is a factor that depends on the hole size and it is equal to 1 for bolts in normal size holes.

$n$  is the number of friction planes:  $n = 1$

$\mu$  is the slip factor and was taken equal to 0.3

$\gamma_{M3,ser}$  is 1.1 for connections that are slip-resistant at SLS.

Connection slippage should occur before the yield onset in the critical section of the I-beam and before the full plasticity of the reduced section area of the TCP. This is to ensure that slip is activated to create a second seismic energy dissipation fuse. Both of these conditions are met with S235-NSH-WS-FP-TCP as follows:

$$F_{s,Rd} < V_{TCP-bf,v,Ed} \quad \text{and} \quad F_{s,Rd} < N_{TCP,t,Rd}$$

$$347 < 693 \text{ kN} \quad \text{and} \quad 347 < 562 \text{ kN}$$

The connection slip resistance was also checked against the serviceability limit shear load so that slip was activated beyond it.

#### 3.4.4. Diaphragm plates

The geometry of the diaphragm plates was chosen in line with the findings of Sabbagh *et al.* (2013) to provide uniform stress flow around the CHS column and avoid stress concentration in them that could lead to their failure or weld fracture. In this project, the DPs were designed to have sufficient overstrength for the full elastic strength of the beam so that they remain elastic during testing. The bending moment of the I-beam was assumed to be fully transmitted through the tapered cover plates into the diaphragm plates in the form of two coupling forces; tension in one of them and compression in the other one depending on the moment direction. In this subsection, the design tension resistance of the diaphragm plate is checked at three

cross sections; the rectangular section, the cross section at the column face and the ring cross section.

#### 3.4.4.1. Geometric properties

The geometry of the diaphragm plates is shown in Table 3.1 and Figure 3.4. The main dimensions are:

Ring width	$W_{DP,r} = 90 \text{ mm}$
Width at column face	$W_{DP,cf} = 340 \text{ mm}$
Flat-end width	$W_{DP,fe} = 180 \text{ mm}$
Thickness	$t_{DP} = 15 \text{ mm}$
Bolt hole diameter	$d_0 = 24 \text{ mm}$

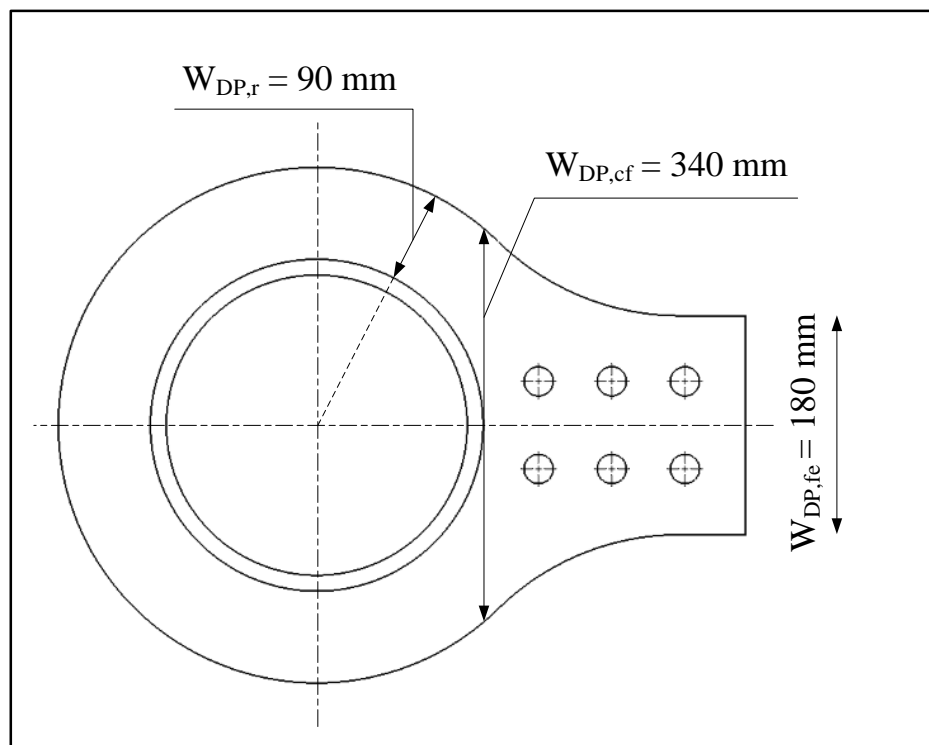


**Figure 3.4:** Widths of different sections in the DP

3.4.4.2. Material properties

The material properties of the DPs were obtained through tensile coupon tests as detailed in Chapter 4.

$$\text{Yield strength} \quad f_{y,DP} = 422 \text{ N/mm}^2$$

$$\text{Ultimate strength} \quad f_{u,DP} = 557 \text{ N/mm}^2$$

3.4.4.3. Design tension resistance of the rectangular part of the DP

The design tension resistance of the DP rectangular cross section  $N_{DP,rec,t,Rd}$  is taken as the smaller of:

- a) Design plastic resistance of the gross section  $N_{pl,Rd}$

$$N_{pl,Rd} = A_{DP,rec} \times f_{y,DP} / \gamma_{M0} = 2700 \times 422 / 1.0 / 1000 = 1139 \text{ kN}$$

$$\text{Where } A_{DP,rec} = (W_{DP,fe} \times t_{DP}) = 180 \times 15 = 2700 \text{ mm}^2$$

- b) Design ultimate resistance of the net cross-section at holes for bolts  $N_{u,Rd}$

$$N_{u,Rd} = 0.9 A_{net} \times f_{u,DP} / \gamma_{M2} = 902 \text{ kN}$$

$$\text{Where } A_{net} = ((W_{DP,fe} - 2 \times d_0) \times t_{DP}) = 132 \times 15 = 1980 \text{ mm}^2$$

Therefore,  $N_{DP,rec,t,Rd} = 902 \text{ kN}$

This value is checked against the design tension value in the diaphragm plate for the full elastic strength of the beam ( $N_{DP,rec,t,Ed}$ ) as follows:

$$N_{DP,rec,t,Rd} > N_{DP,rec,t,Ed}$$

$$N_{DP,rec,t,Ed} = (M_{b,el,y,Rd} \times L_{DP,rec} / L_{cr}) / z_3 = 785 \text{ kN}$$

where  $L_{DP,rec}$  is the distance between the loading point and the critical cross section of the rectangular part of the DP:

$$L_{DP,rec} = 2.1 \text{ m}$$

$z_3$  is the lever arm between the coupling forces  $N_{DP,rec,t,Ed}$  and is taken as:

$$z_3 = h - t_{DP} = 206.8 - 15 = 191.8 \text{ mm}$$

$$902 > 785 \text{ kN}$$

The design tension resistance of the DP rectangular cross section is adequate.

#### 3.4.4.4. Design tension resistance of the DP section at the column face

The design tension resistance of the DP cross section at the column face  $N_{DP,cf,t,Rd}$  should be higher than the design tension value in the same section  $N_{DP,cf,t,Ed}$  when the critical section of the beam starts yielding:

$$N_{DP,cf,t,Rd} > N_{DP,cf,t,Ed}$$

$$N_{DP,cf,t,Rd} = A_{DP,cf} \times f_{y,DP} / \gamma_{M0} = 2152 \text{ kN}$$

$$\text{where } A_{DP,cf} = (W_{DP,cf} \times t_{DP}) = 340 \times 15 = 5100 \text{ mm}^2$$

$$N_{DP,cf,t,Ed} = (M_{b,el,y,Rd} \times L_{cf} / L_{cr}) / z_3 = 834 \text{ kN}$$

where  $L_{cf}$  is the distance between the loading point and the column face:

$$L_{cf} = 2.23 \text{ m}$$

$$2152 > 834 \text{ kN}$$

The design tension resistance of the DP cross section at the column face is adequate.

#### 3.4.4.5. Design tension resistance of the DP ring section

Considering the ring cross sections at  $45^\circ$  and  $-45^\circ$  from the longitudinal axis of the diaphragm plate, as shown in Figure 3.5, Wang *et al.* (2011) suggested it may be assumed that the design tension force in the diaphragm plate,  $N_{DP,rec,t,Ed}$ , is resisted by the design tension plastic resistances of the two ring cross sections,  $N_{DP,r,t,Rd}$ , as illustrated in the same figure.

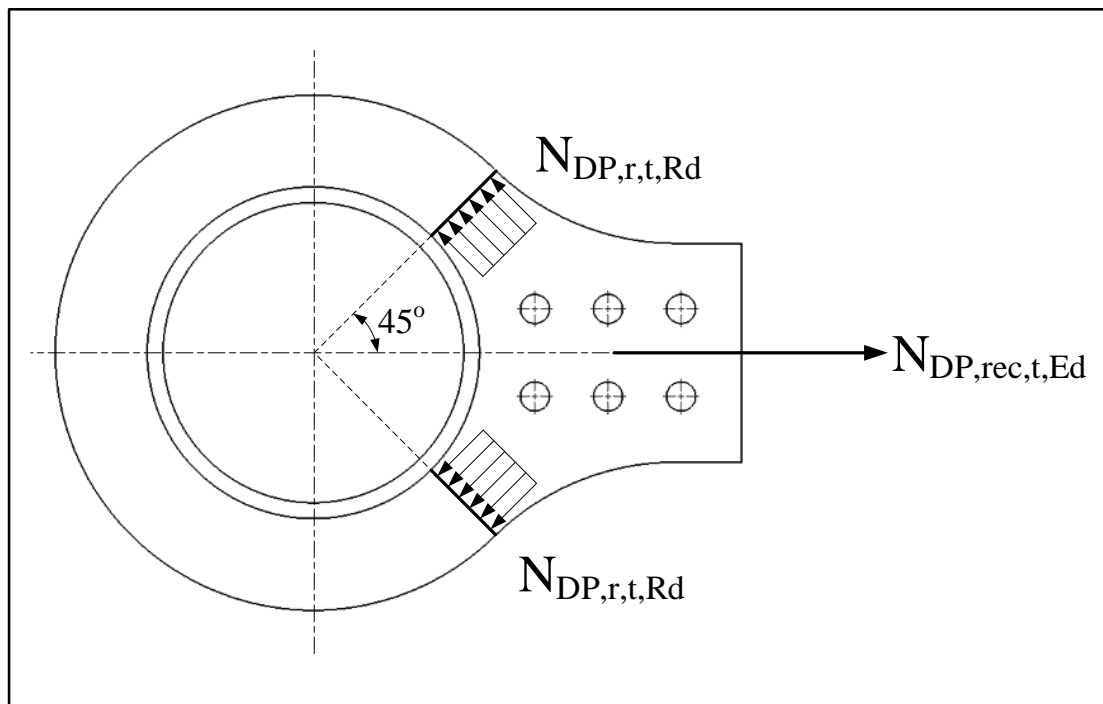


**Figure 3.5:** Design assumption for the DP ring according to Wang *et al.* (2011)

Therefore, the following inequality should be satisfied:

$$(2 \times N_{DP,r,t,Rd} \times \cos 45) > N_{DP,rec,t,Ed}$$

or: 
$$N_{DP,r,t,Rd} > N_{DP,rec,t,Ed} / \sqrt{2}$$

where  $N_{DP,rec,t,Ed} / \sqrt{2} = 555 \text{ kN}$

$$N_{DP,r,t,Rd} = A_{DP,r} \times f_{y,DP} / \gamma_{M0} = 570 \text{ kN}$$

where  $A_{DP,r} = (W_{DP,r} \times t_{DP}) = 90 \times 15 = 1350 \text{ mm}^2$

$570 > 555 \text{ kN}$

The design tension resistance of the ring is adequate.

#### 3.4.4.6. Local buckling check for the ring cross section

The width of the diaphragm plate ring when it is subject to compression should not exceed the local buckling requirements for an outstand element in compression members. This is expressed as follows:

$$W_{DP,r} / t_{DP} < 9 \varepsilon$$

$$W_{DP,r} / t_{DP} = 90 / 15 = 6$$

$$9 \varepsilon = 9 \times \sqrt{(235/f_{y,DP})} = 6.7$$

$$6 < 6.7$$

#### 3.4.5. *The connection between a TCP and a DP*

In the proposed joint arrangement, each of the two tapered cover plates was connected to a diaphragm plate using a group of six M22 bolts of grade 10.9.

##### 3.4.5.1. Geometric properties

The geometric properties of TCPs, M22 bolts and DPs were presented in Subsections 3.4.1.1, 3.4.3.1 and 3.4.4.1. The actual values of bolts spacing, end and edge distances for this connection fall within the range of minimum and maximum allowances specified in BS EN 1993-1-8: 2005 as shown in Table 3.6.

**Table 3.6:** Spacing, end and edge distances for the TCP to the DP connection

	Spacing P <sub>1</sub> (mm)	Spacing P <sub>2</sub> (mm)	End distance e <sub>1</sub> (mm)	Edge distance e <sub>2</sub> (mm)
Minimum	52.8	57.6	28.8	28.8
Maximum	168	168	88	88
<i>Actual</i>	<i>60</i>	<i>72</i>	<i>TCP: 40</i> <i>DP: 50</i>	<i>54</i>

#### 3.4.5.2. Material properties

The material properties of TCPs, M22 bolts and DPs were presented in Subsections 3.4.1.2, 3.4.3.2 and 3.4.4.2.

#### 3.4.5.3. Design shear resistance of the M22 bolt

$$F_{v,Rd} = 182 \text{ kN}$$

#### 3.4.5.4. Design bearing resistance of the M22 bolt in the TCP

$$\text{For end bolts: } F_{TCP,end,b,Rd} = 143 \text{ kN}$$

$$\text{For inner bolts: } F_{TCP,inner,b,Rd} = 150 \text{ kN}$$

#### 3.4.5.5. Design bearing resistance of the M22 bolt in the DP

$$\text{For end bolts: } F_{DP,end,b,Rd} = 255 \text{ kN}$$

$$\text{For inner bolts: } F_{DP,inner,b,Rd} = 214 \text{ kN}$$

#### 3.4.5.6. Design resistance of the TCP-DP connection

Because the design shear resistance of a single M22 bolt was found smaller than its maximum design bearing resistance in the diaphragm plate, the design resistance of the connection was taken as the number of bolts multiplied by the smallest design resistance of any of the individual bolts.



$$V_{\text{TCP-DP,Rd}} = N \times (F_{\text{Rd,min}}) = 6 \times 143 = 858 \text{ kN}$$

The design resistance of the connection  $V_{\text{TCP-DP,Rd}}$  is higher than the design shear value in the connection  $V_{\text{TCP-DP,v,Ed}}$ , and thus it is adequate.

#### 3.4.5.7. Design slip resistance of the TCP-DP connection

The design slip resistance of the bolt group in this connection is equal to that in the TCP-beam connection.

$$F_{\text{s,Rd}} = 347 \text{ kN}$$

#### 3.4.6. *Web stub*

The web stub is subject to the shear force transferred from the I-beam web through the web connection, and it was designed for the full elastic strength of the beam. The design shear resistance of the full-section of the web stub, which appears grey in Figure 3.6, is higher than that of the I-beam web. This is because the former has a bigger cross section and very similar steel strengths.

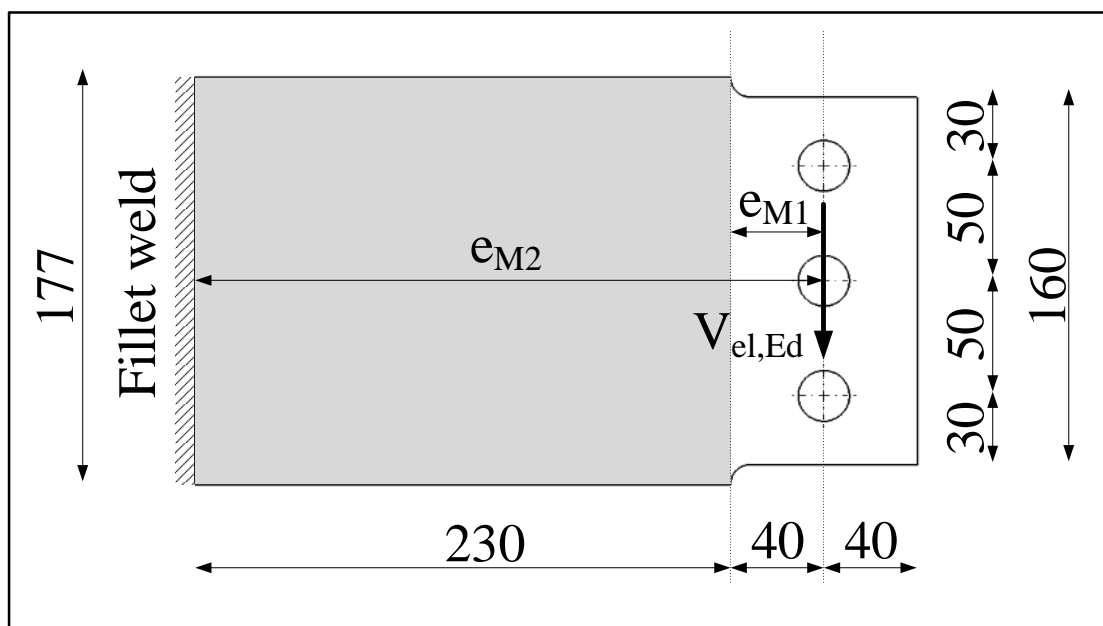


**Figure 3.6:** *Web stub subject to shear force*

The main design checks were carried out for the reduced section part of the web stub, which is referred to as the web plate in this subsection and appears white in Figure 3.6. The main checks carried out for the web plate were the design shear resistance, the design block tearing resistance and the design bending resistance.

#### 3.4.6.1. Geometric properties

The geometry of the web stub is shown in Table 3.1 and in Figure 3.6. The main dimensions of the web stub are:

Height of the gross section of the web stub	$h_{ws}$	= 177 mm
Height of the web plate	$h_{wpl}$	= 160 mm
Thickness of the web stub	$t_{ws}$	= 8 mm
Bolt hole diameter	$d_0$	= 22 mm

#### 3.4.6.2. Material properties

The material properties of the web stub were obtained through tensile coupon tests as detailed in Chapter 4.

Yield strength	$f_{y,ws}$	= 406 N/mm <sup>2</sup>
Ultimate strength	$f_{u,ws}$	= 570 N/mm <sup>2</sup>

#### 3.4.6.3. Design shear resistance of the web plate

The design plastic shear resistance of the web plate cross section  $V_{wpl,pl,Rd}$  was taken the smaller of:

- a) Design plastic resistance of the gross section  $V_{pl,Rd}$

$$V_{pl,Rd} = A_{wpl} \times (f_{y,ws} / \sqrt{3}) / \gamma_{M0} = 300 \text{ kN}$$

$$\text{Where } A_{\text{wpl}} = (h_{\text{wpl}} \times t_{\text{ws}}) = 160 \times 8 = 1280 \text{ mm}^2$$

b) Design ultimate resistance of the net cross-section at holes for bolts  $V_{\text{u,Rd}}$

$$V_{\text{u,Rd}} = A_{\text{net}} \times (f_{\text{u,ws}} / \sqrt{3}) / \gamma_{\text{M2}} = 225 \text{ kN}$$

$$\text{Where } A_{\text{net}} = ((h_{\text{wpl}} - 3 \times d_0) \times t_{\text{ws}}) = 94 \times 8 = 752 \text{ mm}^2$$

Therefore,  $V_{\text{wpl,pl,Rd}} = 225 \text{ kN}$

This value is checked against the design shear value in the web plate for the full elastic strength of the beam  $V_{\text{el,Ed}}$  as follows:

$$V_{\text{wpl,pl,Rd}} > V_{\text{el,Ed}}$$

$$225 > 71.7 \text{ kN}$$

The design plastic shear resistance of the web plate cross section is adequate.

As the web plate should be designed to remain elastic, the design elastic resistance of the web plate  $V_{\text{wpl,el,Rd}}$  should be verified by satisfying the following criterion:

$$\tau_{\text{Ed}} \leq (f_{\text{y,ws}} / \sqrt{3}) / \gamma_{\text{M0}}$$

where  $\tau_{\text{Ed}}$  is the design value of the local shear stress for the critical point of the cross section, and is given by:

$$\tau_{\text{Ed}} = V_{\text{el,Ed}} \times S_{\text{wpl}} / (I_{\text{wpl}} \times t_{\text{ws}})$$

where  $I_{\text{wpl}}$  is the second moment of area of the web plate cross section about its major axis:

$$I_{\text{wpl}} = t_{\text{ws}} \times (h_{\text{wpl}})^3 / 12 = 273 \text{ cm}^4$$

$S_{\text{wpl}}$  is the first moment of area for the web plate section above its major axis:

$$S_{wpl} = 25.6 \text{ cm}^3$$

$$\text{Therefore, } \tau_{Ed} = 84 \text{ N/mm}^2$$

$$84 < 234 \text{ N/mm}^2$$

The design elastic shear resistance of the web plate is adequate.

#### 3.4.6.4. Design block tearing resistance of the web plate

The block tearing failure is a combination of shear failure at the row of bolts along the shear face of the hole group and tensile rupture on the tension face of the bolt group, as illustrated in Figure 3.7. The design block tearing resistance of the web plate  $V_{eff,1,Rd}$  is taken as:

$$V_{eff,1,Rd} = 0.5 f_{t,ws} A_{nt} / \gamma_{M2} + (f_{y,ws} / \sqrt{3}) A_{nv} / \gamma_{M0}$$

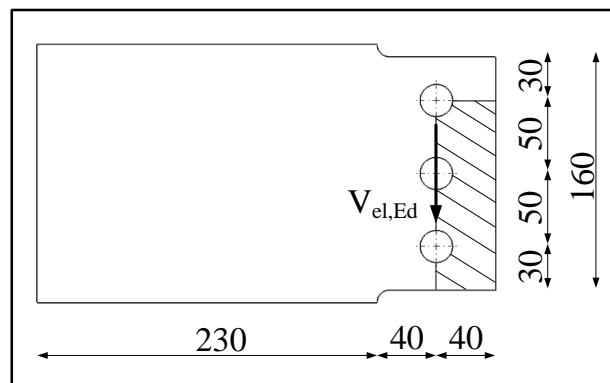


**Figure 3.7:** Block tearing of the web plate

Where  $A_{nt}$  is the net area subject to tension:

$$A_{nt} = t_{ws} \times (e_2 - 0.5d_0) = 8 \times (40 - 11) = 232 \text{ mm}^2$$

$A_{nv}$  is the net area subject to shear:

$$A_{nv} = t_{ws} \times (h_{wpl} - e_1 - 2.5d_0) = 8 \times (160 - 30 - 55) = 600 \text{ mm}^2$$

Therefore,  $V_{\text{eff},1,\text{Rd}} = 201 \text{ kN}$

$$V_{\text{eff},1,\text{Rd}} > V_{\text{el},\text{Ed}}$$

$$201 > 71.7 \text{ kN}$$

The design resistance to block tearing is adequate.

#### 3.4.6.5. Design bending resistance of the web plate

The shear force acting at the row of bolts of the web connection results in a bending moment in the web stub. The design bending value  $M_{\text{wpl},\text{ED}}$  in the plate may be calculated by multiplying the design shear force  $V_{\text{el},\text{Ed}}$  by the distance  $e_{\text{M1}}$  between the centre of the web connection and the edge of the web plate, see Figure 3.6:

$$e_{\text{M1}} = 40 \text{ mm}$$

$$M_{\text{wpl},\text{ED}} = V_{\text{el},\text{Ed}} \times e_{\text{M1}} = 71.7 \times 0.04 = 2.9 \text{ kN.m}$$

The design elastic bending resistance of the web plate cross section is taken as:

$$M_{\text{wpl},\text{el},\text{RD}} = W_{\text{wpl},\text{el},\text{y}} \times f_{\text{y},\text{ws}} / \gamma_{\text{M0}} = t_{\text{ws}} \times (h_{\text{wpl}})^2 \times f_{\text{y},\text{ws}} / 6 / \gamma_{\text{M0}} = 13.9 \text{ kN.m}$$

$$M_{\text{wpl},\text{el},\text{RD}} > M_{\text{wpl},\text{ED}}$$

$$13.9 < 2.9 \text{ kN.m}$$

The design elastic bending resistance of the web plate cross section is adequate.

#### 3.4.7. *The connection between the I-beam web and the web stub*

The I-beam web is connected to the web stub plate using a group of three M16 bolts of grade 10.9. The web connection is loaded in shear during the bending of the beam. The 3×M16 bolts were placed in oversized holes in the web stub plate with the

maximum practical clearance and they were appropriately preloaded to have a slip resistant connection for which slippage in the web connection would occur after the onset of the inelastic joint response. This was to avoid web distortion and to localise the plastic deformations in the TCPs following the findings in the work of Sabbagh *et al.* (2013).

#### 3.4.7.1. Geometric properties

The geometric properties of the I-beam and the web stub were presented in Subsections 3.4.2.1 and 3.4.6.1. The geometric properties of the M16 bolts and their holes in the I-beam web and the web stub plate are:

Bolt diameter	$d$	= 16 mm
Bolt hole diameter in the I-beam web	$d_{0,bw}$	= 18 mm
Bolt hole diameter in the web stub plate	$d_{0,wpl}$	= 22 mm
The gross cross section area of the bolt	$A_b$	= 201 mm <sup>2</sup>
The tensile stress area of the bolt	$A_s$	= 157 mm <sup>2</sup>
Number of bolts	$N$	= 3 bolts

**Table 3.7:** Spacing, end and edge distances for the web connection

	Spacing P <sub>1</sub> (mm)	Spacing P <sub>2</sub> (mm)	End distance e <sub>1</sub> (mm)	Edge distance e <sub>2</sub> (mm)
Minimum	Beam: 39.6 WS: 48.4	NA	Beam: 21.6 WS: 26.4	Beam: 21.6 WS: 26.4
Maximum	89.6	NA	65.6	65.6
<i>Actual</i>	<i>50</i>	<i>NA</i>	<i>Beam: 36.2</i> <i>WS: 30</i>	<i>40</i>

The actual bolts spacing, end and edge distances fall within the range of minimum and maximum allowances specified in BS EN 1993-1-8: 2005, and are presented in Table 3.7.

#### 3.4.7.2. Material properties

The material properties of the I-beam and web stub were presented Subsections 3.4.2.2 and 3.4.6.2. The material properties of the M16 bolts are:

Yield strength  $f_{yb} = 900 \text{ N/mm}^2$

Ultimate strength  $f_{ub} = 1000 \text{ N/mm}^2$

#### 3.4.7.3. Design shear resistance of the M16 bolt

$$F_{v,Rd} = \alpha_v \times f_{ub} \times A_b / \gamma_{M2} = 96 \text{ kN}$$

#### 3.4.7.4. Design bearing resistance of the M16 bolt in the I-beam web

For end bolts:  $F_{bw,end,b,Rd} = 77 \text{ kN}$

For inner bolts:  $F_{bw,inner,b,Rd} = 77.5 \text{ kN}$

#### 3.4.7.5. Design bearing resistance of the M16 bolt in the web stub

The bearing resistance of the M16 bolts in the web stub were multiplied by 0.8 because there holes were oversized.

For end bolts:  $F_{ws,end,b,Rd} = 53 \text{ kN}$

For inner bolts:  $F_{ws,inner,b,Rd} = 59.3 \text{ kN}$

#### 3.4.7.6. Design resistance of the web connection

Because the design shear resistance of a single M16 bolt was found larger than its maximum design bearing resistance in both components, the design resistance of the

connection was taken as the sum of the minimum design bearing resistances of the individual bolts:

$$V_{bw-ws,Rd} = \sum(F_{b,Rd,min}) = (1 \times 53) + (2 \times 59.3) = 172 \text{ kN}$$

$$172 > 71.7 \text{ kN}$$

The design resistance of the connection  $V_{bw-ws,Rd}$  is higher than the design shear value in the connection  $V_{el,Ed}$ , and thus it is adequate.

#### 3.4.7.7. Design slip resistance of the web connection

Connection slip was designed to occur after the onset of the inelastic joint response:

$$F_{s,Rd} > M_{j,pl} / L_{eff}$$

$$\text{For the S235-NSH-WS-FP-TCP: } M_{j,pl} / L_{eff} = 131 / 2 = 66 \text{ kN}$$

The M16 bolt full preloading force is taken as:

$$F_{p,Cd} = 0.7 \times f_{ub} \times A_s = 110 \text{ kN}$$

For this type of TCPs, the preloading force was taken equal to 100 kN. Therefore, the design slip resistance of the bolt group  $F_{s,Rd}$  is:

$$F_{s,Rd} = k_s \times n \times N \times \mu \times F_{p,Cd} / \gamma_{M3,ser} = 70 \text{ kN}$$

where  $k_s$  was taken 0.85 for the use of oversized holes, and  $\mu = 0.3$

$$70 > 66 \text{ kN}$$

The connection slip resistance is adequate for the S235-NSH-WS-FP-TCP.



### 3.4.8. CHS column

The column was designed to remain elastic for the full elastic strength of the beam. The design bending resistance of the column and the design plastic shear resistance of the column web panel are both checked in this subsection.

#### 3.4.8.1. Geometric properties

The geometric properties of the column cross section are detailed here:

External diameter	$D_0$	= 244.5 mm
Thickness	$t_c$	= 10 mm
Area of cross section	$A_c$	= 73.7 cm <sup>2</sup>
Elastic section modulus	$W_{c,el,y}$	= 415 cm <sup>3</sup>
Plastic section modulus	$W_{c,pl,y}$	= 550 cm <sup>3</sup>

#### 3.4.8.2. Material properties

The material properties of the CHS column were obtained through tensile coupon tests as detailed in Chapter 4.

Yield strength	$f_{y,c}$	= 372 N/mm <sup>2</sup>
Ultimate strength	$f_{u,c}$	= 510 N/mm <sup>2</sup>

#### 3.4.8.3. Cross section classification

The CHS column cross section is Class 1 under bending and/or compression if:

$$D_0 / t_c \leq 50\epsilon^2$$

$$D_0 / t_c = 24$$

$$50\epsilon^2 = 50 \times \sqrt{(235 / f_{y,c})} = 40$$

$$24 < 40$$

The CHS column is Class 1 under bending and/or compression.

#### 3.4.8.4. Design bending resistance

The column is designed to remain elastic for the full elastic strength of the I-beam.

Thus, the design elastic bending resistance of the column  $M_{c,el,y,Rd}$  should be higher than half the design bending value at the column centre  $M_{cc,ED}$ :

$$M_{c,el,y,Rd} > 0.5 \times M_{cc,ED}$$

$$M_{c,el,y,Rd} = W_{c,el,y} \times f_{y,c} / \gamma_{M0} = 154.4 \text{ kN.m}$$

$$M_{cc,ED} = M_{b,el,y,Rd} \times L_{cc} / L_{cr} = 117.6 \times 2.35 / 1.64 = 169 \text{ kN}$$

where  $L_{cc}$  is the distance between the loading point and the CHS column centre.

$$154.4 > 84.5 \text{ kN.m}$$

The design elastic bending resistance of the CHS column cross section is adequate.

#### 3.4.8.5. Design shear resistance

The stiffening effect of the diaphragm plates was neglected in the calculation of the design plastic shear resistance of the column web panel in this subsection. The design plastic shear resistance of an unstiffened column web panel is given in BS EN 1993-1-8: 2005 as:

$$V_{wp,Rd} = 0.9 f_{y,wp} A_{vc} / \sqrt{3} / \gamma_{M0} = 907 \text{ kN}$$

where  $f_{y,wp}$  is the yield strength of the column web panel which is similar to the yield strength of the CHS column for this joint and  $A_{vc}$  is the shear area of the column and it is given for CHS columns in BS EN 1993-1-1: 2005 as:

$$A_{vc} = 2 A_c / \pi = 46.9 \text{ mm}^2$$

The design shear resistance of the column web panel was verified against the design shear value  $V_{wp,Ed}$  that was assumed to be equal to the axial force in the diaphragm plate at the column face for the full elastic strength of the beam:

$$V_{wp,Ed} = N_{DP,cf,t,Ed} = 834 \text{ kN}$$

$$907 > 834 \text{ kN}$$

The design shear resistance of the column web panel is adequate.

### 3.4.9. *Design of weld*

Details of the different weld work carried out in the test specimens are presented in Chapter 5. As an example of the weld design calculations done in this project, the design checks for the fillet weld between the web stub and the column face are given in this subsection.

#### 3.4.9.1. Geometric properties

The web stub was welded to the column face using double-sided fillet weld along its full height. The geometry of the web stub and column were presented in Subsections 3.4.6.1 and 3.4.8.1. The geometrical details of the fillet weld between these two components are:

$$\text{Number of fillet weld lines} \quad N_w = 2$$

Leg size	S	= 10 mm
Effective throat thickness	a	= 7.1 mm
Total length of fillet weld in each line	$L_w$	= 177 mm
Effective length of fillet weld in each line	$L_{w,eff}$	= 163 mm
Elastic modulus of the fillet weld cross section	$W_{w,el,y}$	= 74 cm <sup>3</sup>

#### 3.4.9.2. Material properties

The ultimate strength of the fillet weld ( $f_{u,w}$ ) was taken equal to the ultimate strength of the weakest part connected, which is the column.

Ultimate strength	$f_{u,w} = f_{u,c} = 510 \text{ N/mm}^2$
-------------------	--

#### 3.4.9.3. Design resistance of the weld subject to shear

Using the simplified method recommended by BS EN 1993-1-8: 2005, the design resistance of the fillet weld is adequate if:

$$F_{w,Rd} > F_{w,Ed}$$

Where  $F_{w,Ed}$  is the design value of the weld force per unit length:

$$F_{w,Ed} = V_{el,Ed} / (N_w \times L_{w,eff}) = 71.7 \times 1000 / (2 \times 163) = 220 \text{ N/mm}$$

$F_{w,Rd}$  is the design weld resistance per unit length:

$$F_{w,Rd} = f_{vw,d} \times a = 1852 \text{ N/mm}$$

Where  $f_{vw,d}$  is the design shear strength of the weld:

$$f_{vw,d} = f_{u,w} / (\sqrt{3} \times \beta_w \times \gamma_{M2}) = 262 \text{ N/mm}^2$$

where  $\beta_w$  is a correlation factor of 0.9 for S355 steel.

$\gamma_{M2}$  is 1.25

1852 > 220 N/mm

The design shear resistance of the weld is adequate.

#### 3.4.9.4. Design resistance of the weld to combined shear and bending

Assuming that the bending moment in the web stub, which is a result of the shear force in the web connection, is all resisted by the fillet weld that connects the web stub to the column face, the extreme fibres of the fillet weld should be checked for the normal and shear stresses combination.

The design bending value at the fillet weld cross section was calculated by multiplying the design shear force  $V_{el,Ed}$  by the distance  $e_{M2}$  between the centre of the web connection and the fillet weld section, see Figure 3.6:

$$M_{w,ED} = V_{el,Ed} \times e_{M2} = 71.7 \times 0.27 = 19.4 \text{ kN.m}$$

Using the directional method in BS EN 1993-1-8: 2005, the design resistance of the weld is adequate if:

$$[\sigma_{\perp}^2 + 3(\tau_{\perp}^2 + \tau_{\parallel}^2)]^{0.5} \leq f_{u,w} / (\beta_w \times \gamma_{M2}) \quad \text{and} \quad \sigma_{\perp} < 0.9 f_{u,w} / \gamma_{M2}$$

where  $\sigma_{\perp}$  is the normal stress perpendicular to the throat and  $\tau_{\perp}$  is the shear stress (in the plane of the throat) perpendicular to the axis of the weld.  $\sigma_{\perp}$  and  $\tau_{\perp}$  may be taken as the components of the stress generated by the bending moment  $M_{w,ED}$  in the extreme fibres of the weld:

$$\sigma_{\perp} = \tau_{\perp} = (M_{w,ED} / W_{w,el,y}) \times (\cos 45^{\circ}) = 185 \text{ N/mm}^2$$

$\tau_{\parallel}$  is the shear stress (in the plane of the throat) parallel to the axis of the weld, and it may be taken as the shear stress resisting the design shear force in the web stub:

$$\tau_{\parallel} = F_{w,Ed} / a = 220 / 7.1 = 31 \text{ N/mm}^2$$

$$[\sigma_{\perp}^2 + 3 (\tau_{\perp}^2 + \tau_{\parallel}^2)]^{0.5} = 374 \text{ N/mm}^2$$

$$f_{u,w} / (\beta_w \times \gamma_{M2}) = 453 \text{ N/mm}^2$$

$$0.9 f_{u,w} / \gamma_{M2} = 367 \text{ N/mm}^2$$

$$374 < 453 \text{ N/mm}^2 \quad \text{and} \quad 185 < 367 \text{ N/mm}^2$$

Both conditions are satisfied and thus the design resistance of the fillet weld is adequate.

### 3.5. *Concluding remarks*

This chapter presents the arrangement of the proposed single-sided beam to column joint and details the main calculations carried out at the design stage to verify the adopted design philosophy. The adequacy of the design calculations showed the potential for the joint to achieve the desired performance of limiting the plastic deformations under cyclic loading to the replaceable links (TCPs) of the joint whilst the other components deform within their elastic range. Next chapter focuses on the tensile coupon tests that were conducted to obtain the actual material properties of steel in the different joint components.

# *Chapter 4*

## *Tensile Coupon Tests*

### *4.1. Introduction*

Tensile coupon (TC) tests were crucial to determine the actual material properties of the steels for the different components in the test specimens. 25 coupons were extracted from the joint components, and material tensile tests were carried out on these coupons in accordance with BS EN ISO 6892-1: 2009. This chapter focuses on the preparation of the tensile coupons, the instrumentation, the test procedure and the tests results.

## 4.2. *Tensile coupons preparation*

Geometry of test pieces was governed by the geometry of the metallic products they were cut from, and the location of cut was selected to be in accordance with BS EN 10025-1: 2004. For example, the coupon extracted from the I-beam web was cut at a quarter of the total height of the I-beam, while the coupon obtained from the I-beam flange was cut two-thirds of the way from the flange centreline to the flange edge. Table 4.1 presents the number and cut location of the tensile-testing coupons for the different joint components.

The dimensions of all tensile-testing coupons were chosen in accordance with BS EN ISO 6892-1: 2009. The thickness ( $a_0$ ) of each test coupon was kept similar to the full thickness of the component it was cut from; while its width ( $b_0$ ) was chosen so that the width to thickness ratio did not exceed 8:1, and that the cross-section area of the coupon allowed for fracture to be obtained within the load range of the testing machine, which is 0 to 250 kN. The curved surfaces of the CHS column coupons were not flattened.

Each test piece was machined to have a reduced-section area in the middle, connected to the two ends of the test piece with four 12mm transition radiuses as illustrated in Figure 4.1. The length of the reduced-section area in the coupon is known as the parallel length ( $L_c$ ); while the length of the parallel portion of the test piece on which elongation can be measured at any time during the test is known as the gauge length. The original gauge length value ( $L_0$ ) was set to be proportional to the original cross section ( $S_0$ ) of the test piece as given by Equation (4.1). The obtained value for  $L_0$  was rounded up to the nearest multiple of 5mm.

$$L_0 = 5.65\sqrt{S_0} \quad (4.1)$$



**Table 4.1:** Number and cut location of the tensile coupons

Joint component	Number of coupons	Cut location
<p>I-section beam UKB: 203×133×30</p>	<p>6 coupons (4 flange coupons + 2 web coupons) cut longitudinally</p>	
<p>CHS column 244.5×10</p>	<p>4 coupons cut longitudinally (avoiding the seam weld region)</p>	
<p>Diaphragm plate</p>	<p>6 coupons</p>	

**Table 4.1:** Number and cut location of the tensile coupons

Joint component	Number of coupons	Cut location
Web stub	3 coupons	
Tapered cover plate S355	3 coupons	
Tapered cover plate S235	3 coupons	

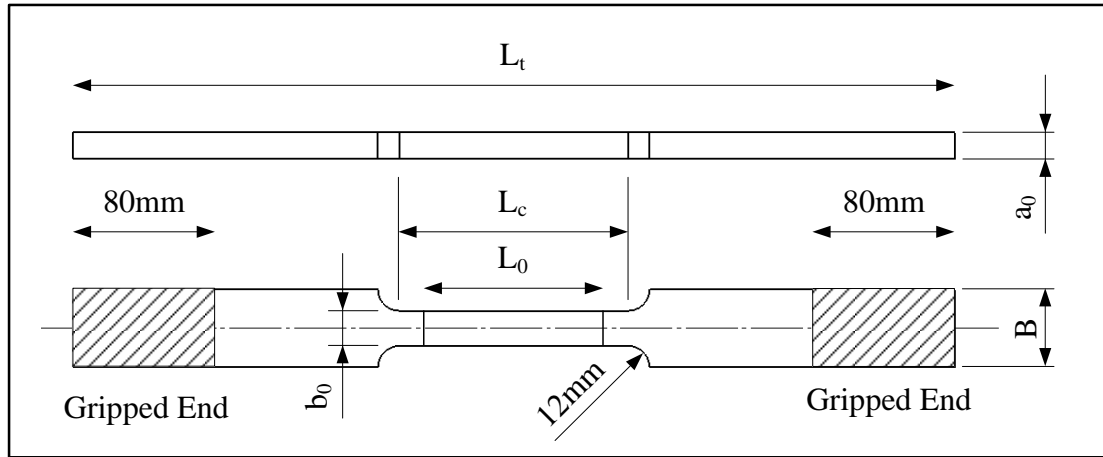


**Figure 4.1:** General shape and geometry of the tensile coupons

The cross-section dimensions of the coupon reduced-section area were measured at five different locations and then averaged to get the mean values for  $a_0$  and  $b_0$ . The original cross-section area of the specimen ( $S_0$ ) was calculated by Equation (4.2) for all coupons, including the slightly curved ones cut from the CHS column because the width of the column coupon ( $b_0$ ) to the external diameter of the column ( $D_0$ ) ratio was less than 10%. The minimum parallel length of each coupon was calculated by Equation (4.3) and rounded up to a multiple of 5mm.

$$S_0 = a_0 \times b_0 \quad (4.2)$$

$$L_c \geq L_0 + 1.5\sqrt{S_0} \quad (4.3)$$

The overall length of the test piece ( $L_t$ ) was governed by the parallel length, length of the instrumentation fixed to the coupon and size of the testing machine grips. The detailed nominal dimensions of all the tensile coupons are presented in Table 4.2. The gauge length was marked onto the surface of the coupons with fine lines to determine the elongation parameters after the end of tests.

Table 4.2: Detailed dimensions of the tensile coupons

Coupon source	Dimensions of the tensile-testing Coupons							
	$a_0$ , nominal (mm)	$b_0$ , nominal (mm)	$B$ nominal (mm)	$S_{0, \text{nominal}}$ (mm <sup>2</sup> )	$S_{0, \text{measured}}$ (mm <sup>2</sup> )	$L_0$ (mm)	$L_c$ (mm)	$L_t$ (mm)
I-section beam flange	9.6	20	44	192	196.9	80	105	500
I-section beam web	6.4	20	44	128	125.9	65	90	500
CHS column	10	20	44	200	194.5	80	105	500
DP	15	20	44	300	294.8	100	130	500
WS	8	20	44	160	161.7	75	95	500
S355 TCP	12	20	44	240	257.1	90	115	500
S235 TCP	12	20	44	240	239.8	90	115	500

### 4.3. *Instrumentation of the tensile coupon tests*

Electrical post-yield strain gauges of type YFLA–10mm, from TML (2012), were fixed at the centre of each face of the tensile coupons to monitor and record axial strains during the tests. The central area of the front and back faces of the coupons was grinded to remove all dust and rust traces from these surfaces and make them ready to stick strain gauges onto. This allowed strain gauges to be in full contact with the metal surfaces in order to achieve reliable strain readings. The central axes of the front and back faces of the coupons were marked with fine lines. These marks were useful guides for sticking a strain gauge onto a coupon face while keeping the axes of both in alignment. It should be noted that all the coupon surface marks were scribed gently to avoid making notches that could result in a premature fracture of the specimen.

Although strain gauges are effective in measuring strain during the elastic range, they cover a small area of the coupons surfaces and they may fail before fracture of the test piece or even before coupon reaches the maximum stress. Hence, test coupons were instrumented with two strain gauges and a displacement transducer to ensure good agreement between their results and to measure failure strains {O'Brien and Salpekar (1993)}. Subsequently, this helped to obtain the full stress-strain model of the tested steel.

The initial length over which extension is measured by means of a displacement transducer is called the initial displacement transducer gauge length ( $L_e$ ). Following the recommendations of BS EN ISO 6892-1: 2009, the value of  $L_e$  was taken equal to  $L_0$  in all TC tests to enable the measurement of the stress-strain curve parameters up to the maximum test force and beyond. A 50mm displacement transducer was

calibrated and then clamped to one side of the tensile coupon using two attachments as illustrated in Figure 4.2. The attachments were fixed to the coupon, before testing, in two reference points between which was the initial displacement transducer gauge length. Figure 4.3 shows all the instrumentation fixed to a tensile coupon. Load, displacement and strain were all recorded during tension loading and logged to a computer using the National Instruments (NI) data-logging system and its software package LabVIEW (2010).

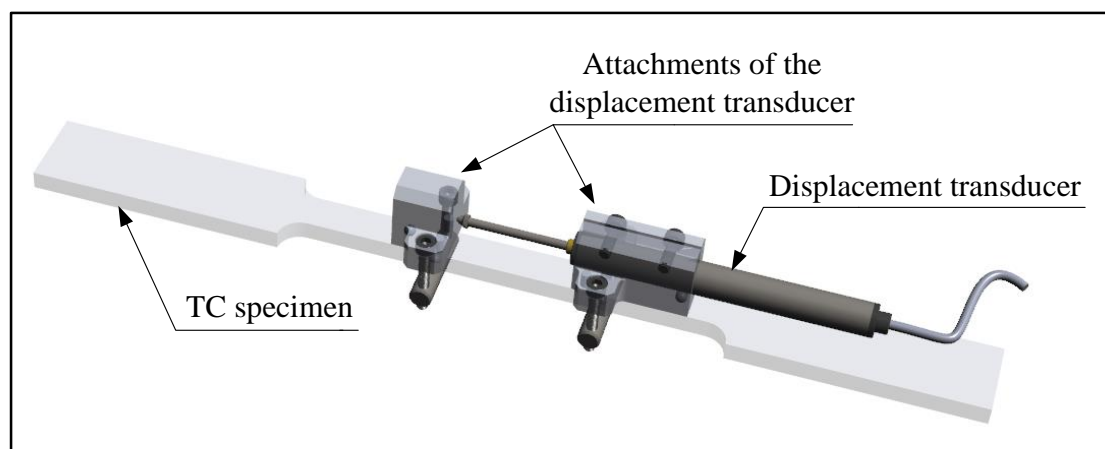


**Figure 4.2:** *Attachments of the displacement transducer to a tensile coupon*

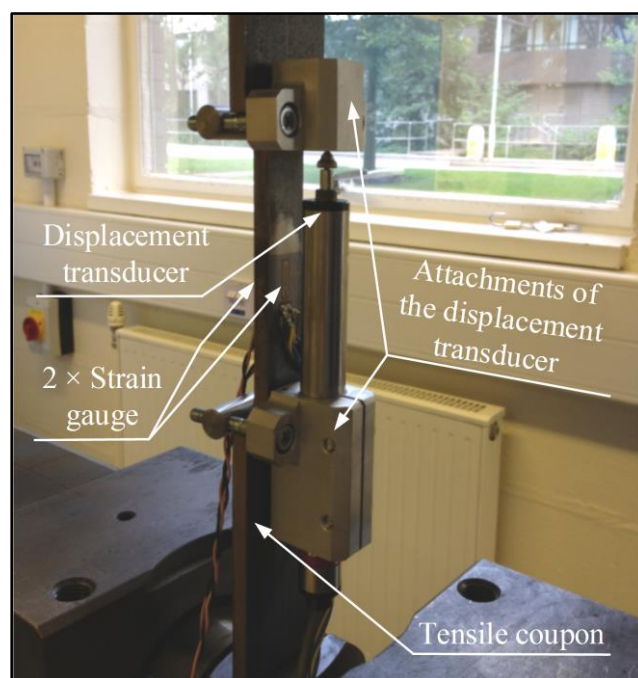


**Figure 4.3:** *Instrumentation of tensile coupon tests*

#### 4.4. *TC test procedure*

Tensile Coupon tests were carried out using the hydraulic DARTEC 9500 testing facility, seen in Figure 4.4, in the Materials Laboratory at the School of Engineering, University of Warwick. The strain rates of the tests were estimated in accordance with BS EN ISO 6892-1: 2009. A strain rate of  $0.00007 \text{ s}^{-1}$  was used for the elastic part of the tests, whereas a strain rate of  $0.00025 \text{ s}^{-1}$  was used for both the yielding plateau and work hardening parts. The strain rate over a coupon parallel length was controlled by the speed of the DARTEC crossheads separation. The crossheads separation velocities, presented in the third and fifth columns in Table 4.3, were calculated for a coupon by multiplying the test estimated strain rates, presented in the second and fourth columns in the same table, by the coupon parallel length.

TC tests were conducted after all the preparations of the coupons, instrumentation, data-logging system and computer programme were completed. The tests were initiated using the chosen strain rate for the elastic range until a drop in stress occurred indicating the end of the elastic range and the onset of yielding. At this point, the crossheads movement was stopped to allow the load to stabilise to get a static rather than a dynamic yield stress.

Ziemian (2010) advises that for cases when the yield plateau was not reached and the total strain is the 0.2% offset value ( $0.002 + (f_y \times E)$ , where  $f_y$  is the nominal yield stress of the tested material and  $E$  is its modulus of elasticity), the crosshead movement should be stopped for either five minutes or until the load stabilises. Ziemian (2010) explained that the purpose of stopping the crossheads movement was to get the static yield stress. Testing was resumed at the chosen strain rate in Table 4.3 for the yield plateau, during which movement of the crossheads was stopped

three times before the commencement of strain hardening. Straining was then resumed during the work-hardening range of strain up until coupon fracture.

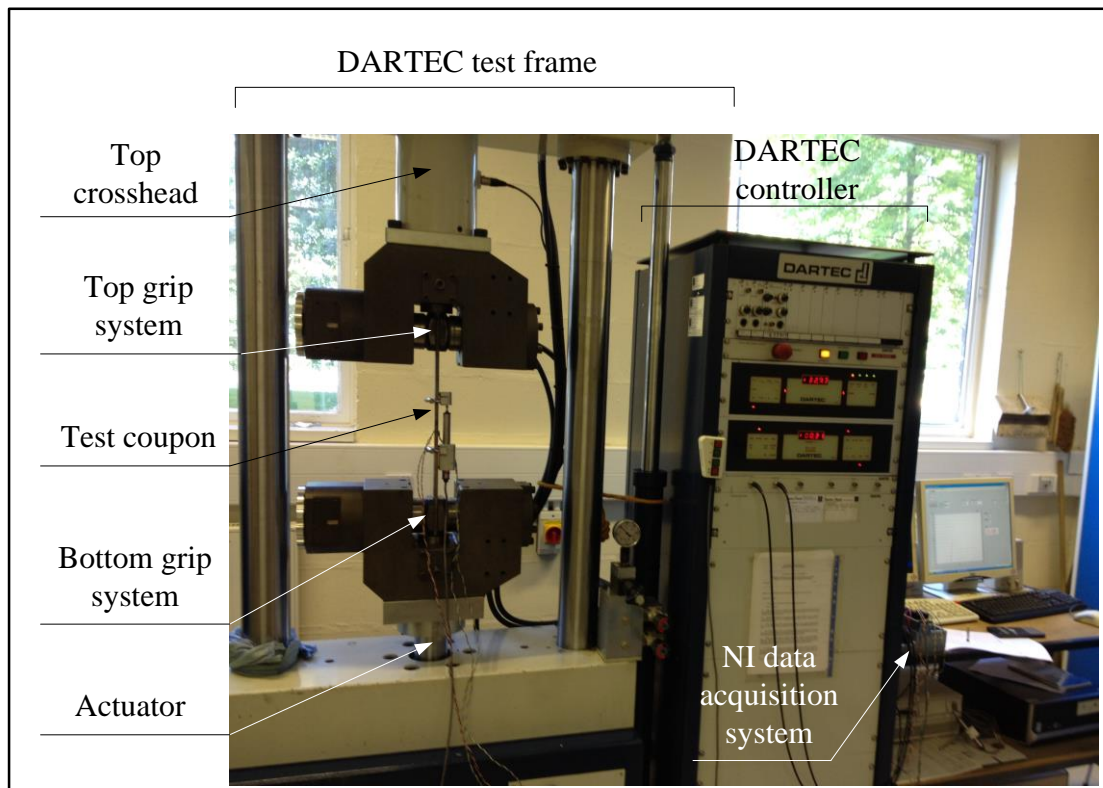


**Figure 4.4:** A tensile coupon test using the DARTEC 9500 testing facility

**Table 4.3:** Strain rates and crossheads separation velocities for the TC tests

TC	Elastic range		Yielding plateau and work-hardening range	
	Strain rate (s <sup>-1</sup> )	Crossheads separation speed (mm/s)	Strain rate (s <sup>-1</sup> )	Crossheads separation speed (mm/s)
I-beam flange	0.00007	0.007	0.00025	0.026
I-beam web		0.006		0.023
CHS column		0.007		0.026
DP		0.009		0.033
WS		0.007		0.024
S355 TCP		0.008		0.029
S235 TCP		0.008		0.029



#### 4.5. *TC test results*

Figure 4.5 shows a coupon before and after testing. After the end of each test, the final gauge length after fracture ( $L_u$ ) was determined manually by fitting the two broken pieces back together, so that their longitudinal axes are in a straight line. A millimetre tape measure is used to measure the distance between the gauge length marks. The percentage elongation after fracture ( $A$ ) was calculated by:

$$A = (L_u - L_0) \times 100 / L_0 \quad (4.4)$$

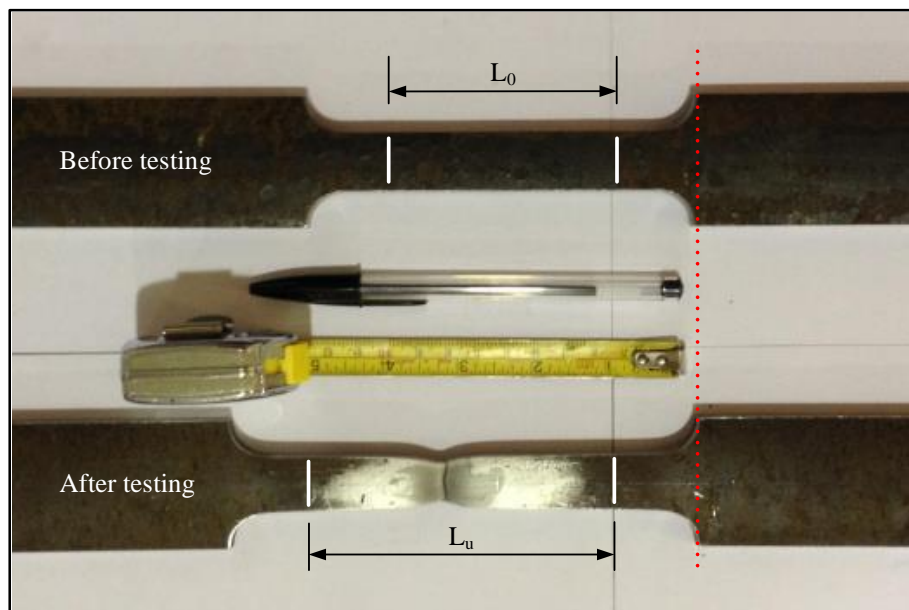


**Figure 4.5:** *A tensile coupon before and after testing*

Results from the TC tests were reported in the form of engineering stress-strain curves. For each test, stress values were obtained by dividing force by the original cross-section area ( $S_0$ ). Strain obtained from averaging the measurements of the two strain gauges showed good agreement with strain from the extension measured by means of the attached displacement transducer. Strain for the engineering stress-strain curve was given by the strain gauges averaged measurements up to their failure, and from the displacement transducer measurements for the rest of the test.

The engineering stress-strain curves were then analysed in accordance with BS EN ISO 6892-1: 2009 to obtain the main properties of the tested steel such as the modulus of elasticity ( $E$ ), yield strength ( $f_y$ ), yield strain ( $\epsilon_y$ ), work-hardening strain ( $\epsilon_{sh}$ ), ultimate strength ( $f_u$ ) and ultimate strain ( $\epsilon_u$ ). Table 4.4 presents the key results from the TC tests and their means and coefficients of variation (COV). The obtained average engineering stress-strain curves of the joint components are presented in Figure 4.6.

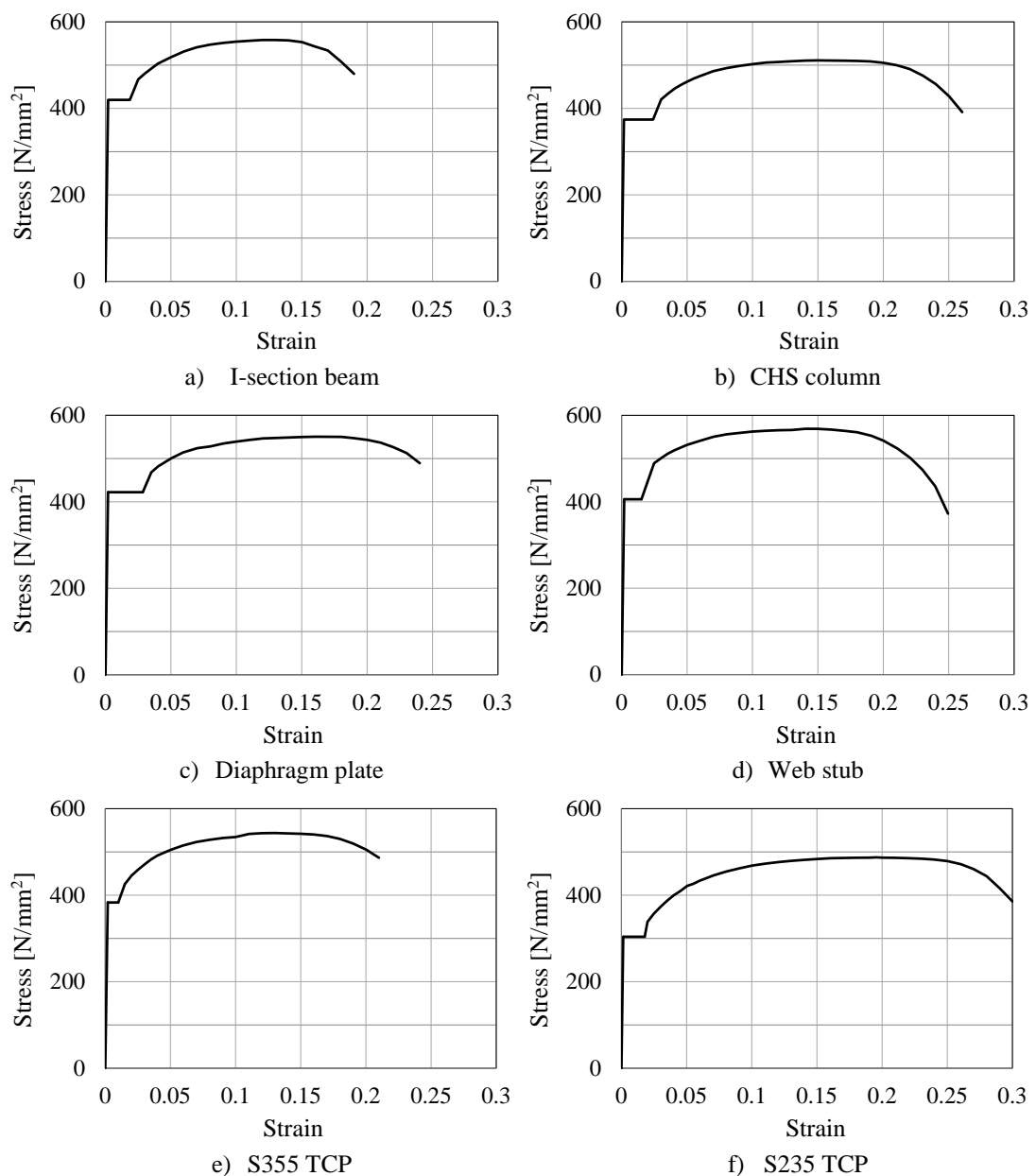


**Figure 4.6:** Average engineering stress-strain curves of the joint components

**Table 4.4:** Key results from the tensile coupon tests

Coupon		E (N/mm <sup>2</sup> )	f <sub>y</sub> (N/mm <sup>2</sup> )	ε <sub>y</sub>	ε <sub>sh</sub>	f <sub>u</sub> (N/mm <sup>2</sup> )	ε <sub>u</sub>
I-section beam	TC-1	203000	406	0.00200	0.01842	546	0.12029
	TC-2	205000	411	0.00201	0.01240	558	0.16943
	TC-3	193000	416	0.00216	0.02117	555	0.13503
	TC-4	205000	436	0.00213	0.02246	571	0.11510
	TC-5	203000	414	0.00204	0.01888	551	0.11636
	TC-6	207000	435	0.00210	0.01861	579	0.13428
	<i>Mean</i>	<i>203000</i>	<i>420</i>	<i>0.00207</i>	<i>0.01866</i>	<i>560</i>	<i>0.13175</i>
	<i>COV</i>	<i>0.024</i>	<i>0.030</i>	<i>0.032</i>	<i>0.186</i>	<i>0.022</i>	<i>0.155</i>
CHS column	TC-7	213000	376	0.00176	0.02395	513	0.16533
	TC-8	213000	372	0.00177	0.02398	508	0.15540
	TC-9	214000	364	0.00170	0.02395	504	0.14960
	TC-10	211000	376	0.00179	0.02400	514	0.15162
	<i>Mean</i>	<i>213000</i>	<i>372</i>	<i>0.00176</i>	<i>0.02397</i>	<i>510</i>	<i>0.15549</i>
	<i>COV</i>	<i>0.006</i>	<i>0.015</i>	<i>0.022</i>	<i>0.001</i>	<i>0.009</i>	<i>0.045</i>
Diaphragm plate	TC-11	215000	426	0.00198	0.02584	565	-
	TC-12	213000	432	0.00203	0.02931	565	-
	TC-13	219000	411	0.00188	0.02953	551	0.17765
	TC-14	214000	419	0.00196	0.02918	552	0.16641
	TC-15	216000	422	0.00196	0.03031	554	0.17164
	TC-16	212000	422	0.00198	0.02479	554	0.15438
	<i>Mean</i>	<i>215000</i>	<i>422</i>	<i>0.00196</i>	<i>0.02816</i>	<i>557</i>	<i>0.16752</i>
	<i>COV</i>	<i>0.012</i>	<i>0.017</i>	<i>0.025</i>	<i>0.080</i>	<i>0.012</i>	<i>0.059</i>
Web stub	TC-17	<i>Technical error led to unreliable results and TC-17 was neglected.</i>					
	TC-18	202000	449	0.00222	0.01853	610	0.14117
	TC-19	211000	363	0.00172	0.01176	529	0.13472
	<i>Mean</i>	<i>207000</i>	<i>406</i>	<i>0.00197</i>	<i>0.01515</i>	<i>570</i>	<i>0.13795</i>
	<i>COV</i>	<i>0.031</i>	<i>0.150</i>	<i>0.179</i>	<i>0.316</i>	<i>0.100</i>	<i>0.033</i>
S355 TCP	TC-20	189000	373	0.00197	0.01000	536	0.12042
	TC-21	201000	400	0.00199	0.01026	552	0.13642
	TC-22	201000	381	0.00190	0.00992	537	-
	<i>Mean</i>	<i>197000</i>	<i>385</i>	<i>0.00195</i>	<i>0.01006</i>	<i>542</i>	<i>0.12842</i>
	<i>COV</i>	<i>0.035</i>	<i>0.036</i>	<i>0.024</i>	<i>0.018</i>	<i>0.017</i>	<i>0.088</i>
S235 TCP	TC-23	213000	310	0.00145	0.01870	489	0.19390
	TC-24	215000	299	0.00139	0.01737	486	0.18606
	TC-25	208000	303	0.00146	0.01760	487	0.20681
	<i>Mean</i>	<i>212000</i>	<i>304</i>	<i>0.00143</i>	<i>0.01789</i>	<i>488</i>	<i>0.19559</i>
	<i>COV</i>	<i>0.019</i>	<i>0.018</i>	<i>0.026</i>	<i>0.040</i>	<i>0.003</i>	<i>0.054</i>

#### *4.6. Concluding remarks*

This chapter presents the tensile coupon testing carried out to obtain the steel properties in the different joint components. Details on the preparation of the coupons, their instrumentation, the test procedure and the main findings are presented. The average values of the components steel properties were used to update the design calculations in Chapter 3 and monitor strain levels in the areas of interest in the joint during the test programme reported in Chapters 5 and 6. Next chapter details all the preparation work that was carried out in the Structures Laboratory at the School of Engineering prior to the nine joint tests.

# *Chapter 5*

## *Experimental Set-up*

### *5.1. Introduction*

This chapter focuses on all the work that was undertaken to prepare for and conduct the laboratory experiments of the proposed joint between a steel I-section beam and a circular hollow section (CHS) column. The experimental set-up included preparing the test specimens, designing the test rig and its attachments, conducting geometry and geometry imperfection measurements of the test specimens and their components, adopting an appropriate loading protocol and preparing the required instrumentation for the experiments. Nine full-scale laboratory experiments of the external diaphragm joint were then conducted. The results of the experiments are provided in the next chapter. All dimensions in this chapter are in millimetres unless otherwise stated.

## 5.2. *Preparation of test specimens*

Firstly, the column assembly shown in Figure 5.1 was prepared by Full-Penetration Butt (FPB) welding the diaphragm plates to the full outer circumference of the CHS column, FPB-welding the column ends to the column end plates and fillet welding the web stub plate to the column face and the diaphragm plates. Figure 5.2 shows two photographs of all the weld work carried out in the column assembly. Figures 5.3 and 5.4 details the fillet welds and FPB welds in the column assembly.

The weld work was inspected visually and then subjected to ultrasonic magnetic examination by a specialist from the industrial inspection company ULTRASPEC N.D.T to assure that it complied with the weld inspection standard BS EN ISO 17640: 2010.

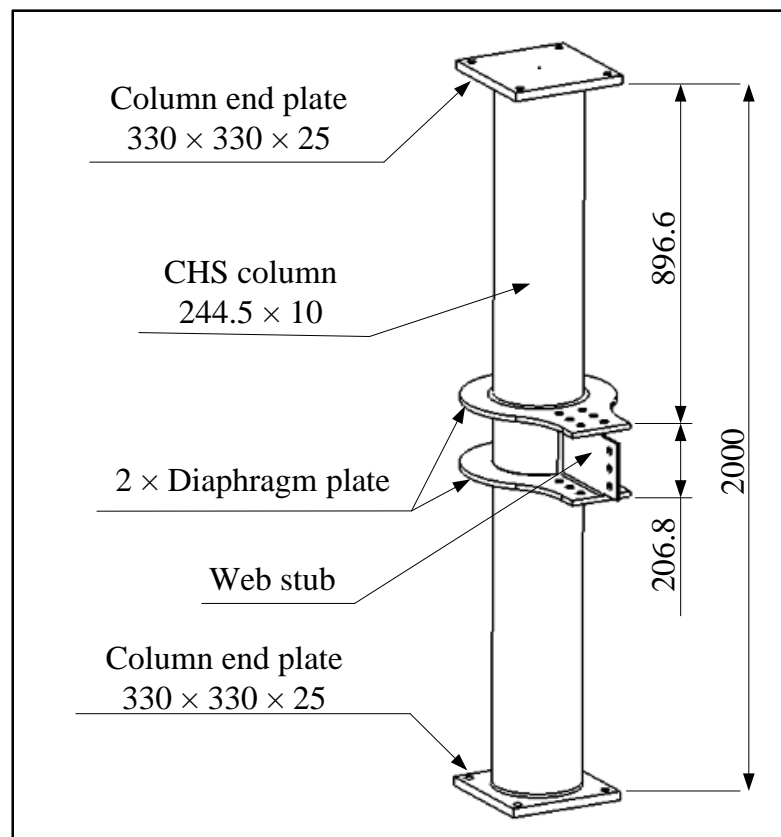


**Figure 5.1:** *The column assembly - dimensions in [mm]*

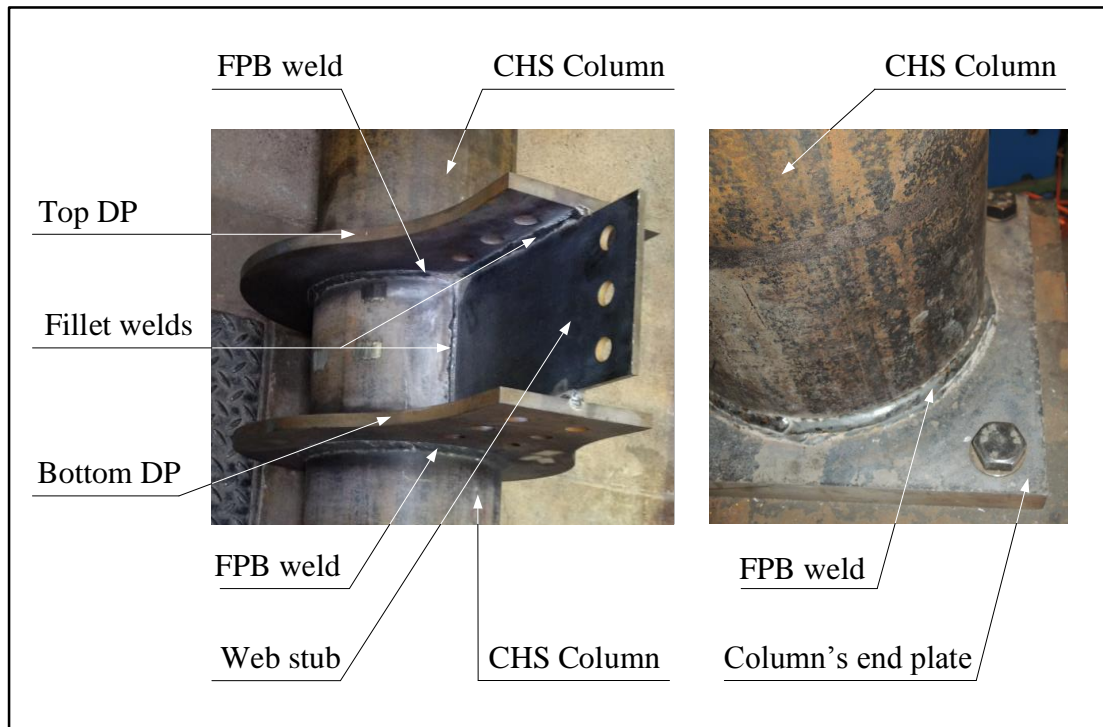


**Figure 5.2:** *Photographs of the weld work in the column assembly, taken in the Structures Laboratory at the School of Engineering*

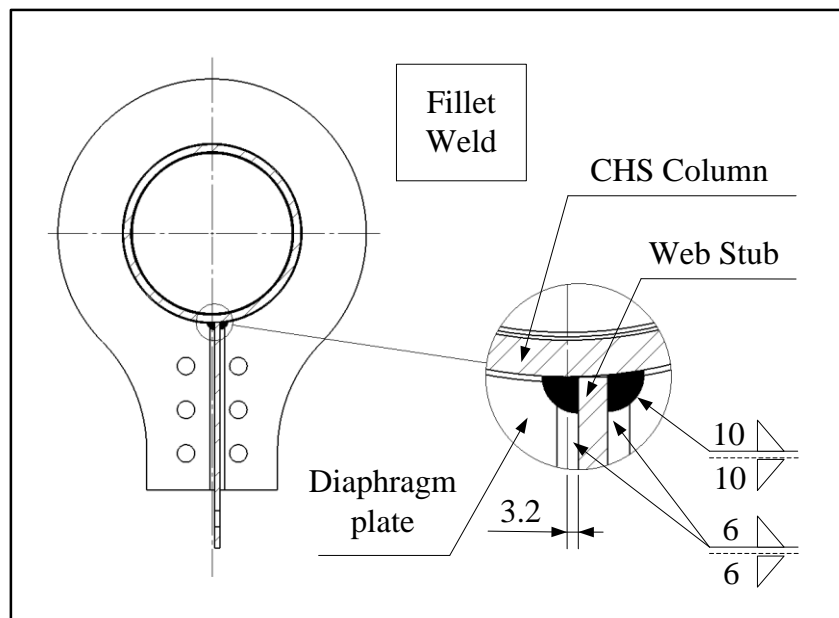


**Figure 5.3:** *Details of the fillet welds in the column assembly - dimensions in [mm]*

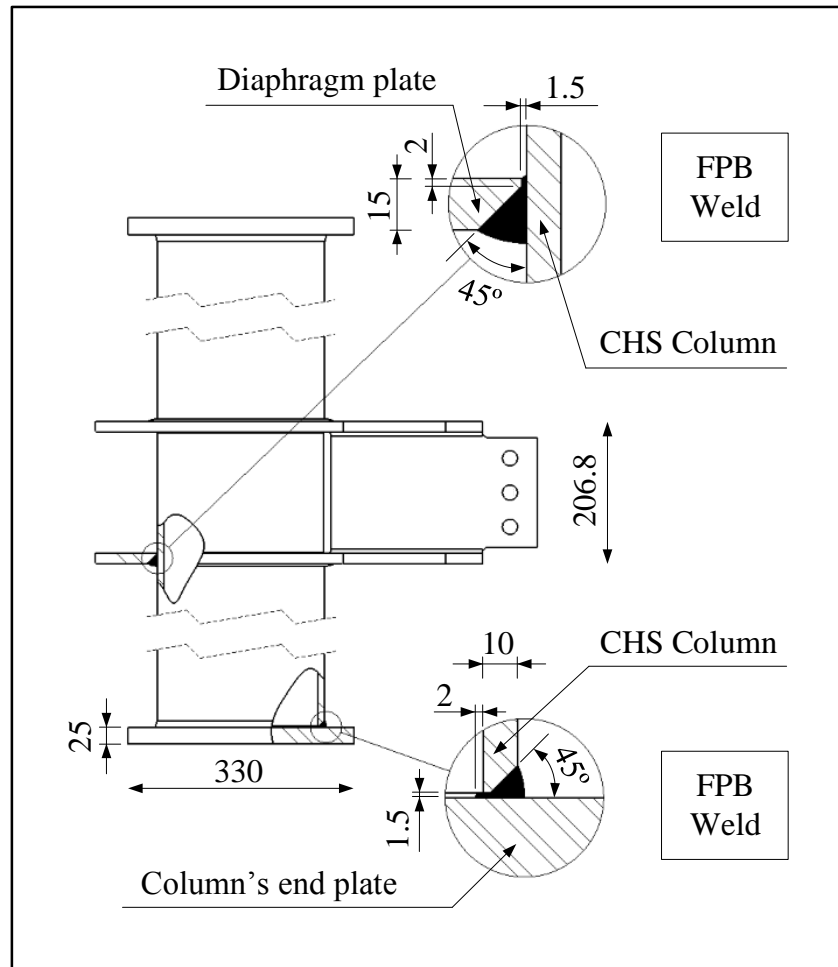


**Figure 5.4:** Details of the FPB welds in the column assembly - dimensions in [mm]

Secondly, the beam assembly was prepared by welding six stiffeners of grade S355 to the I-section beam: UKB 203×133×30, three stiffeners to each side of the beam web, at the load application region (under the actuator). Each beam stiffener was fillet-welded along its short edges to the inner surfaces of the beam flanges, and one of its long edges was fillet-welded to the beam web. Figure 5.5 shows the location of the beam stiffeners and their weld size. Figure 5.6 shows the geometry of a stiffener with two chamfer cuts ( $15\text{mm} \times 45^\circ$ ) to fit the component where the beam fillet radii are. Figure 5.7 shows a photograph of the weld work carried out on one side of the beam web.



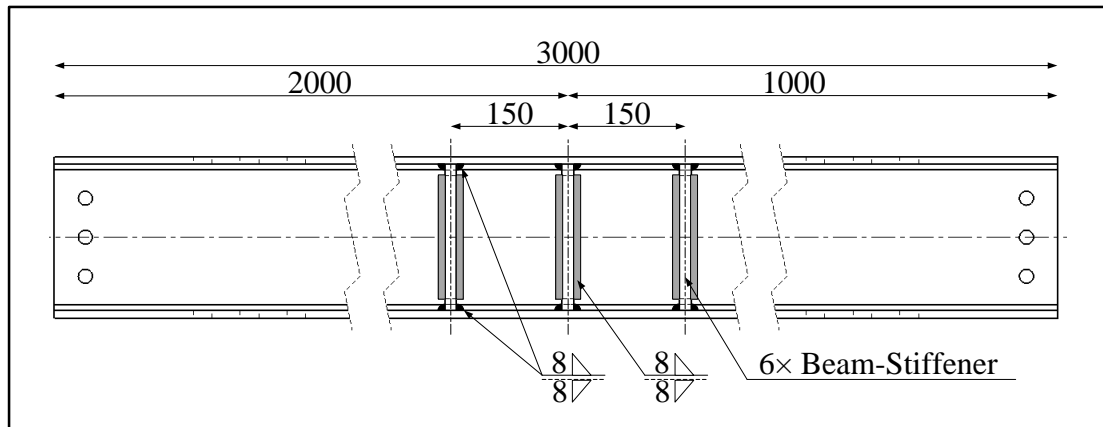


**Figure 5.5:** *Details of the fillet welds in the beam assembly - dimensions in [mm]*

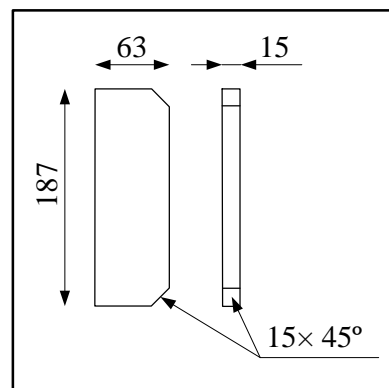


**Figure 5.6:** *Geometry of the beam stiffener - dimensions in [mm]*

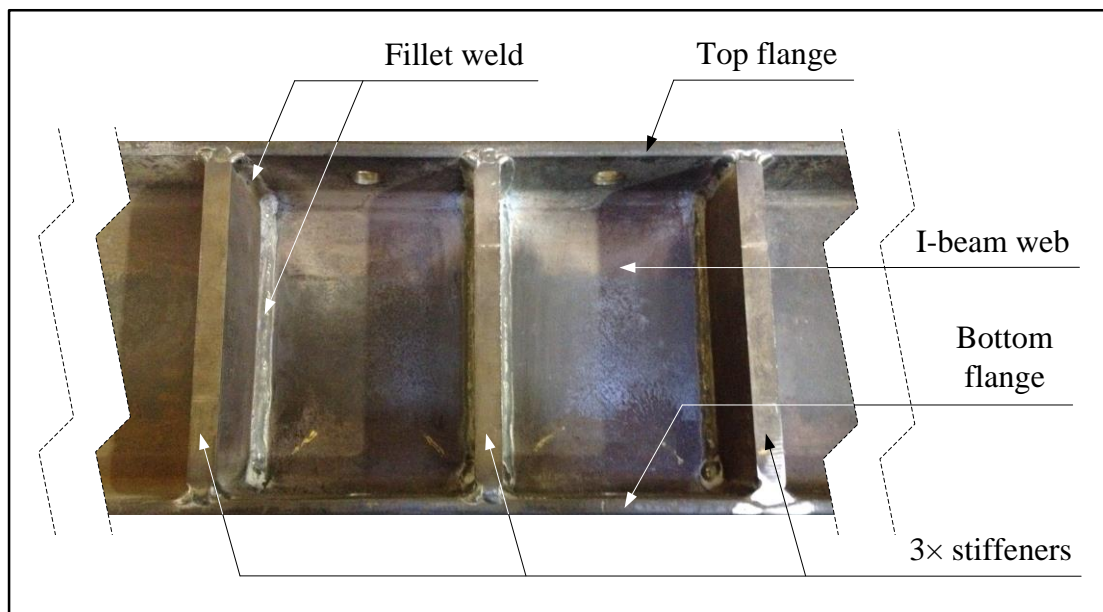


**Figure 5.7:** *A photograph of the weld work in the beam assembly*

Thirdly, for test specimens with stiffened TCPs, two cover plate assemblies were prepared by fillet-welding a rectangular stiffener to the longitudinal axis of each tapered cover plate. The tapered cover plates and their stiffeners were cut from the same steel plate to have identical steel grade. The completed TCP assembly and its weld details are shown in Figure 5.8.

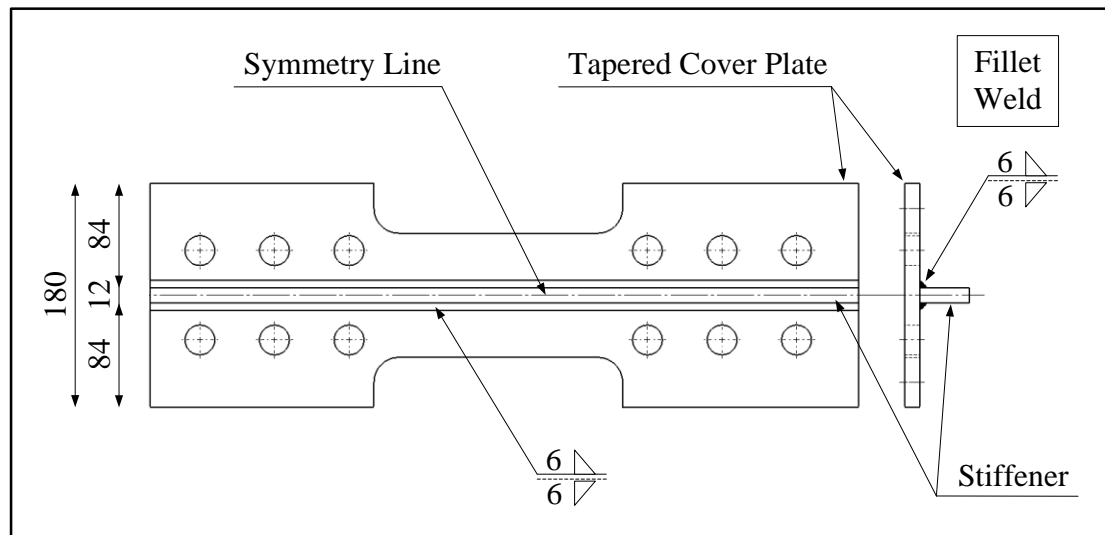


**Figure 5.8:** *A tapered cover plate assembly and its weld details - dimensions in [mm]*

Finally, the column assembly was placed in the test rig and joined together with the beam assembly by the cover plates/ cover plate assemblies and the web connection. Bolts for the TCPs and the web connection were placed approximately in the centres of their holes and tightened to their designated preloading force values prior to each test. Tightening of bolts was carried out using a torque wrench, which has a torque range of 80 to 400 N.m, and a 5:1 torque multiplier. Figure 5.9 shows the method of tightening one of the TCPs bolts. Figure 5.10 shows a test specimen inside the test rig after assembling all of its components and tightening all bolts.

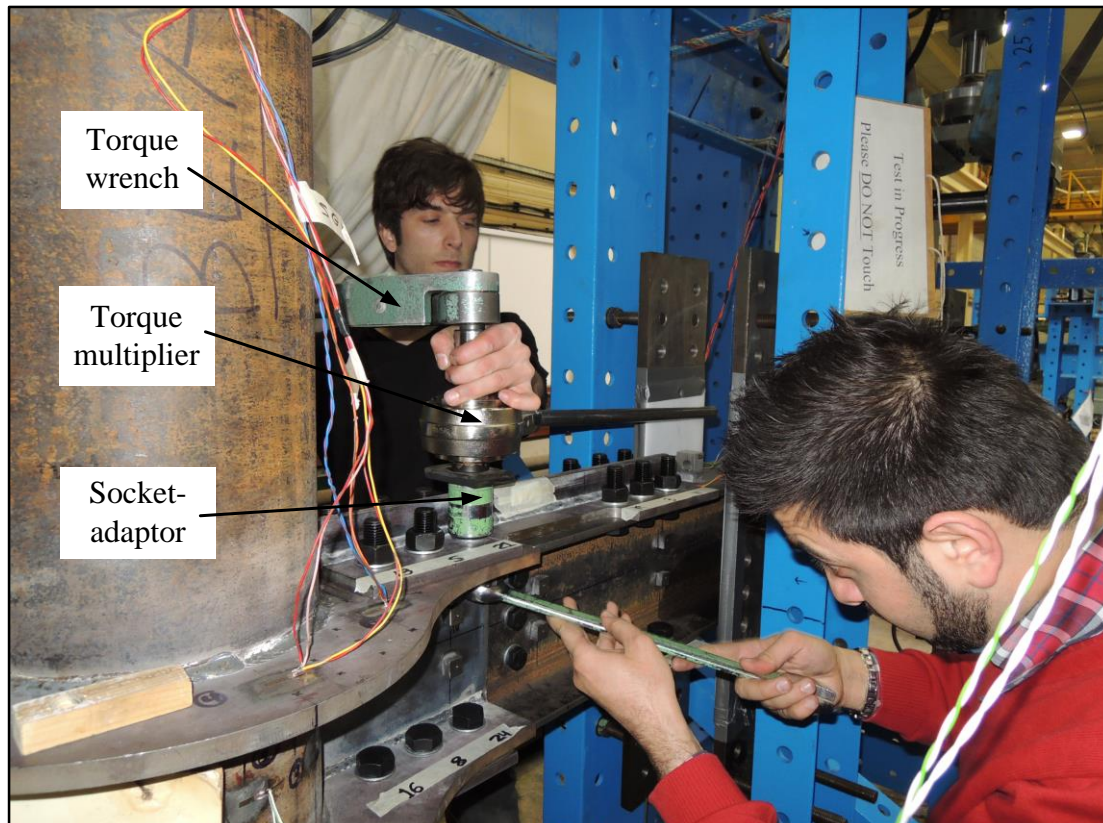


**Figure 5.9:** Bolt tightening process using a torque wrench and a torque multiplier

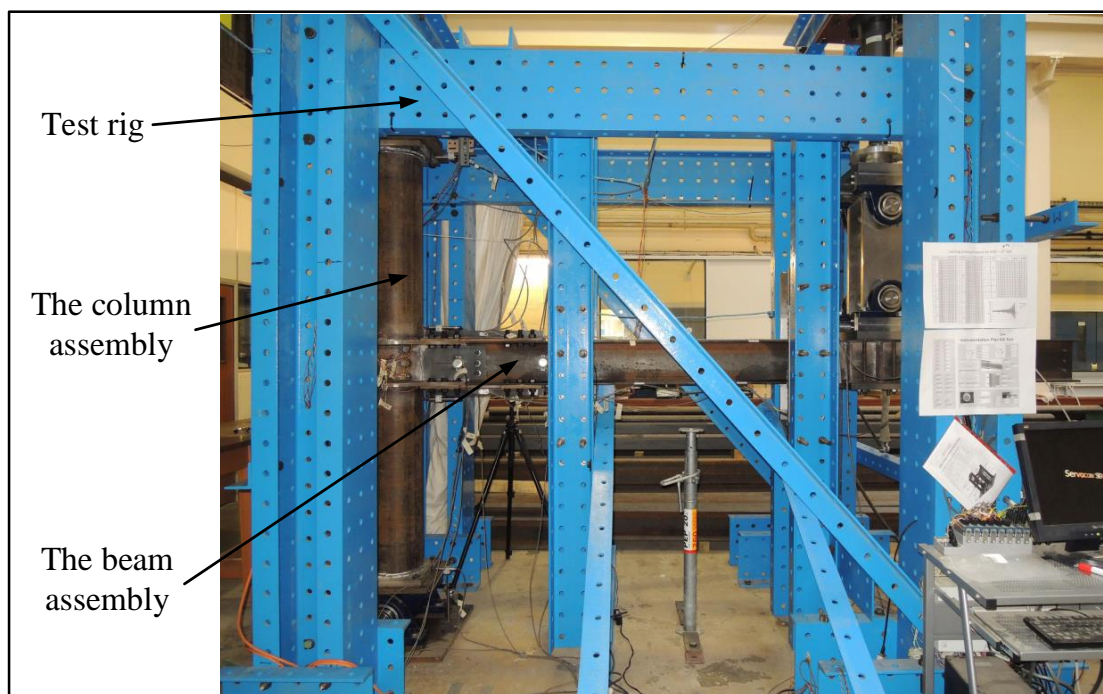


**Figure 5.10:** Test specimen assembled inside the test rig in the Structures Laboratory

### 5.3. *Test rig*

A test rig was built on the Structures Laboratory in the School of Engineering at the University of Warwick to transfer safely the loads applied to test specimens to the strong floor. A 100 kN hydraulic actuator, connected to a reaction frame, was used to apply vertical displacement-controlled loading into the specimen I-beam. A loading mechanism including swivel hinges, similar to that used in the work of Elghazouli *et al.* (2009) at Imperial College London, was designed to accommodate the large joint rotations expected whilst maintaining the verticality of the actuator. Design calculations for the swivel hinges were conducted in accordance with BS EN 1993-1-1: 2005 and BS EN 1993-1-8: 2005. A detailed drawing of the swivel hinges and their components is shown in Figure 5.11. The photograph in Figure 5.12, taken during one of the tests, shows how the bottom part of the swivel hinges rotated along the rotation of the beam whilst maintaining the verticality of the actuator.

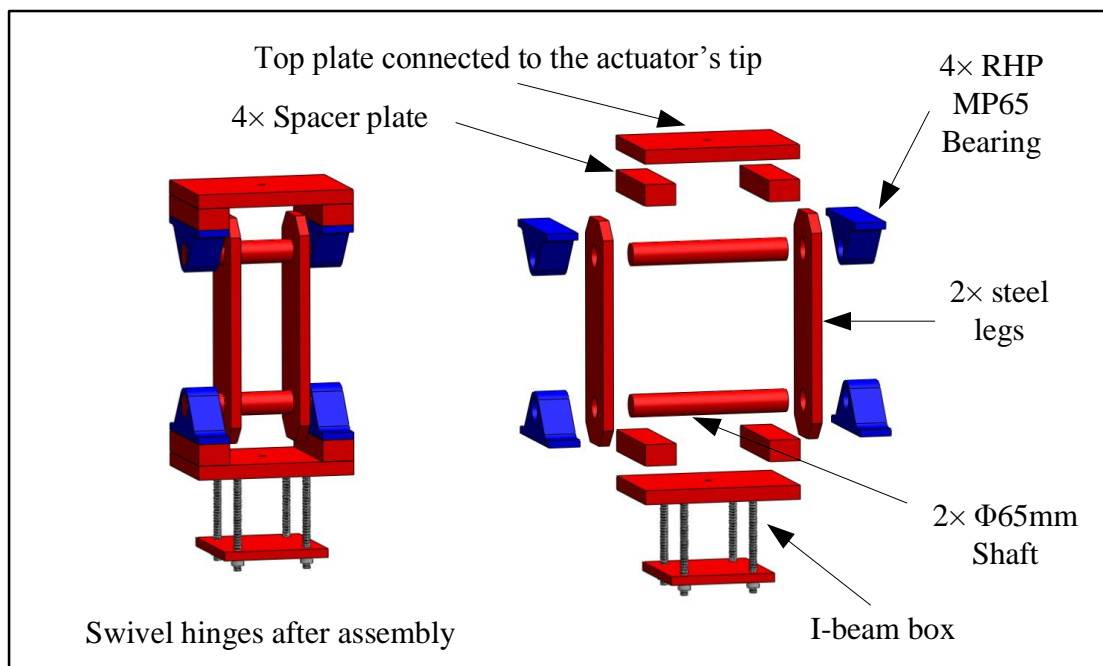


**Figure 5.11:** 3D illustration of the swivel hinges (left) and their components (right)

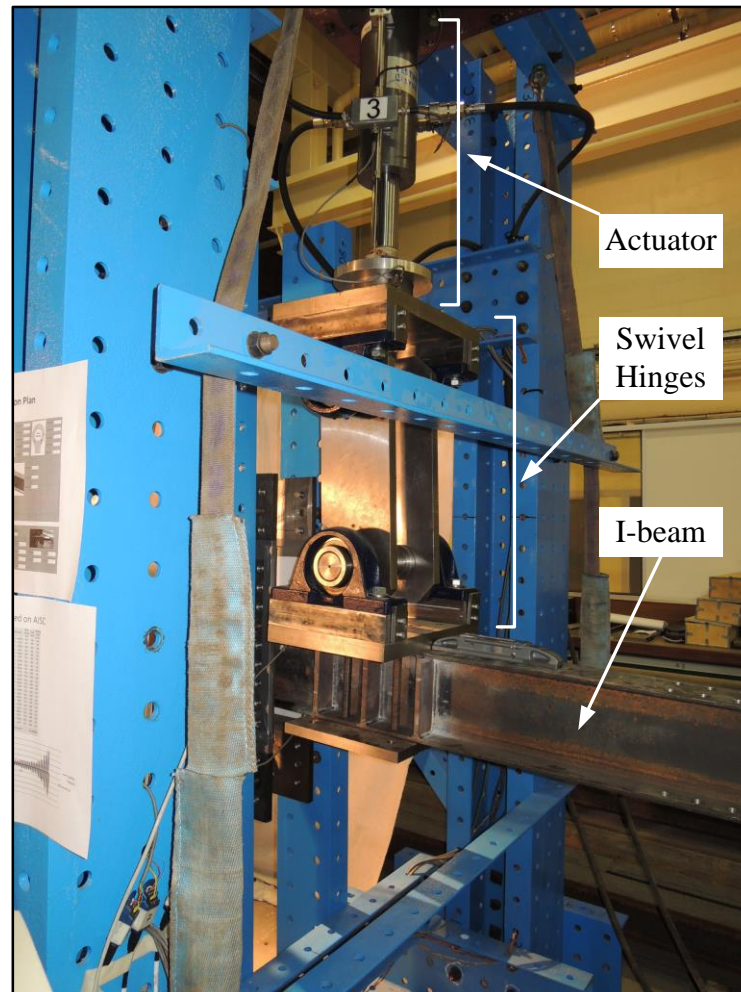


**Figure 5.12:** *Function of the swivel hinges*

Another reaction frame was built to restrain the column at both ends and transfer test-generated forces to the strong floor. The two reaction frames were connected together with horizontal and diagonal bracing to provide out-of-plane stability. High strength friction bolts (HSFB) were used to connect the meccano pieces together to form the test rig. This method of connection was to eliminate any possible relative slip between the connected meccano pieces under large cyclic loads. The schematic arrangement of the test rig used for the laboratory experiments is shown in Figure 5.13.

To avoid any lateral torsional buckling of the I-beam under deformation, lateral supports were designed and built on both sides of the beam. Lateral supports were

provided in two locations where high levels of stress concentration in the beam are expected. The first location was next to the beam-to-column connection zone and the second was right before the swivel hinges.

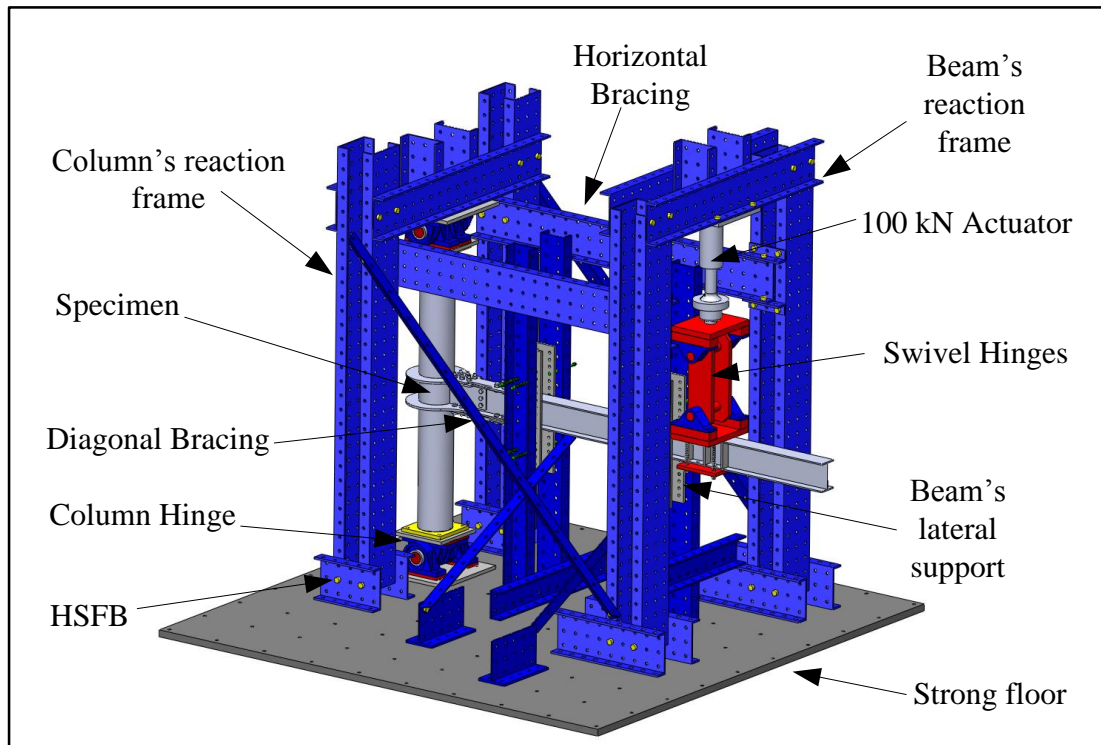


**Figure 5.13:** *Schematic arrangement of the test rig*

Lateral supports comprised two steel plates, fixed to the meccano by long threaded bars, and wrapped with sheets of Polytetrafluoroethylene (PTFE), which is a material known for having one of the lowest friction coefficients against any other solid material. This was to reduce friction between the lateral support plates and the beam during its cyclic movement. The width of the lateral support plates was chosen to be 180mm each, and their height was designed to accommodate the beam height plus its maximum expected vertical displacement in both directions during testing. A schematic arrangement of the lateral supports is shown in Figure 5.14 without showing the rest of the test rig for clarity, and two photographs of this arrangement are shown in Figure 5.15.

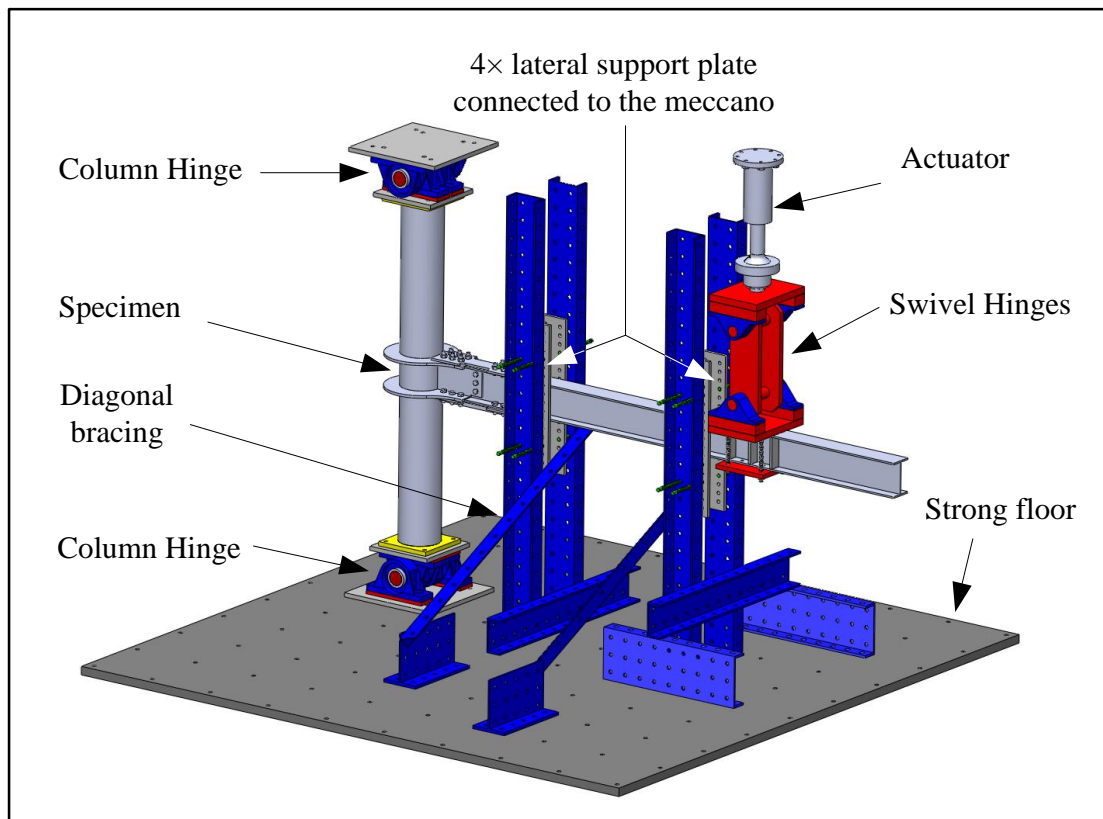


**Figure 5.14:** *Schematic arrangement of the lateral supports for the I-section beam*

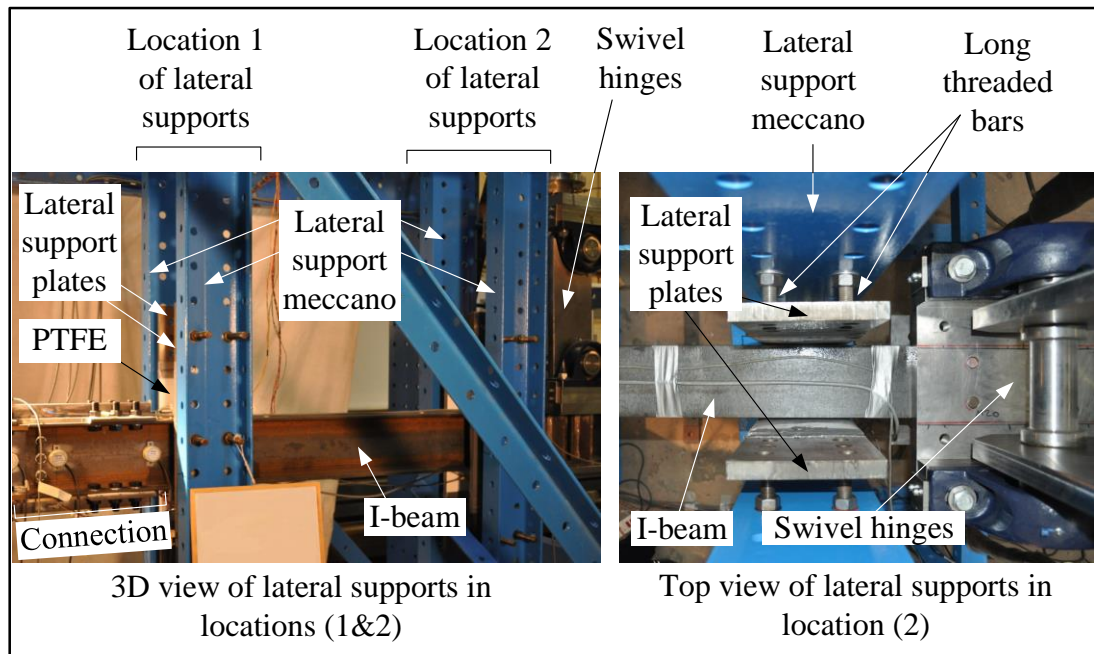


**Figure 5.15:** *Photographs of the lateral support arrangement for the I-section beam, taken in the Structures Laboratory*

The displacement boundary conditions at the ends of the CHS column were hinged in the design to allow specimen end rotation during the tests. Figure 5.16 illustrates the schematic arrangement of the column bottom hinge before and after assembling its components. Two hinges were designed and connected to the ends of the specimen column. The main components of each hinge were four RHP-MP85 bearings, with capacity of 71.5 kN each, joined together with an 85mm cylindrical shaft. The outer bearings in the column bottom hinge were connected to a plate that was bolted to the strong floor, while the inside bearings were pointed up and connected to a plate bolted to the column end plate. The four bearings were separated by three steel rings fixed to the shaft to keep the bearings horizontally in place. Figure 5.17 shows a photograph of the column bottom hinge.

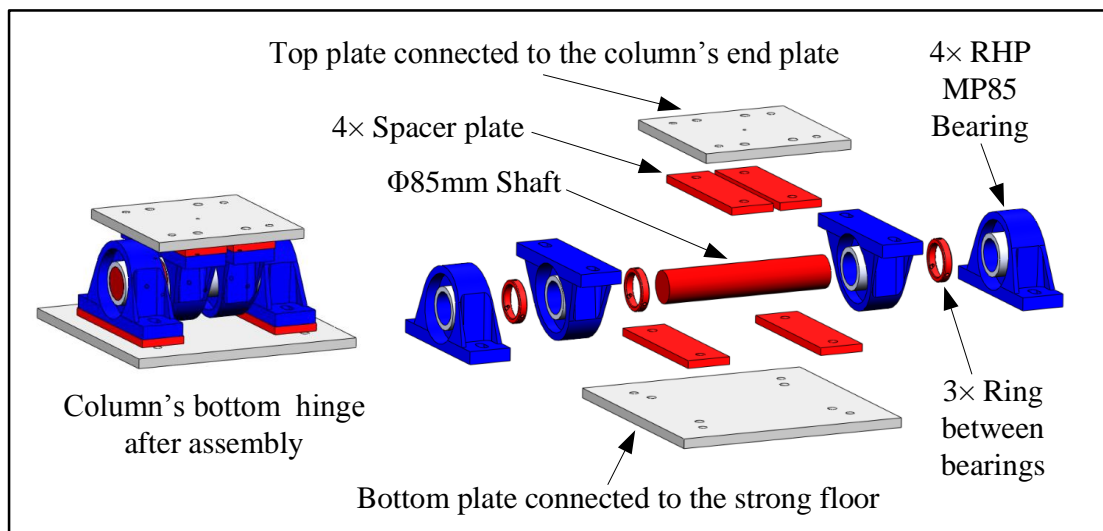


**Figure 5.16:** *The column bottom hinge assembly (left) and its components (right)*

The column top hinge had the same details as the bottom one. It was located upside down and connected to the column reaction frame from its top side, and to the top column end plate from its bottom side. Design calculations for the column hinges were conducted in accordance with BS EN 1993-1-1: 2005 and BS EN 1993-1-8: 2005.



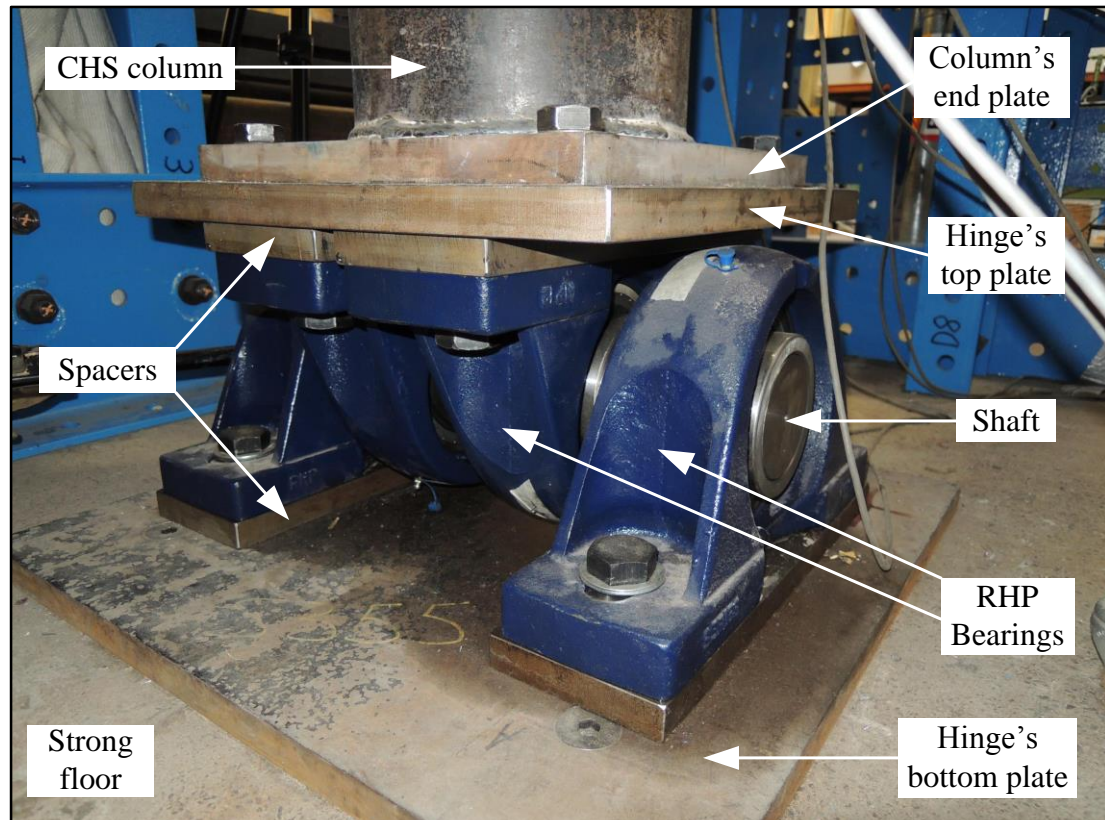


**Figure 5.17:** *Photograph of the column bottom hinge*

A safe system of work (SSoW) form was prepared for the construction of the test rig and the operation of the 100 kN actuator in line with the health and safety measures related to working in the Structures Laboratory. The form included instructions about the order of the construction operations and identified potential hazards associated with them. Mitigation measures were recommended in this form as well.

#### 5.4. *Geometry measurements*

Geometry measurements of all components were conducted before assembling the specimen. The measurements were taken using the electronic digital calliper, which has a 0.01mm resolution and 0.01 repeatability, shown in Figure 5.18. However, because of the curved surface of the CHS column, the measurements of its thickness were taken using the Ball-Micrometer, which has a resolution of 0.004mm. It is shown in Figure 5.19.



**Figure 5.18:** *The digital calliper*



**Figure 5.19:** *The Ball-Micrometer*

The geometry measurements taken on the beam section are illustrated in Figure 5.20. The obtained thickness measurements of the flanges and web, and the diameter measurements of the bolt-holes are all presented in Table 5.1. The mean values and coefficients of variation of the flange and web thicknesses were calculated and reported in the same table. The average width and height of the beam were determined to be 133.9mm and 210mm respectively; these two measurements are not in Table 5.1. The deviation from nominal on all the measured dimensions of the beam section are found to be within the tolerance values given by BS EN 10034: 1993; these are reported in Table 5.2.

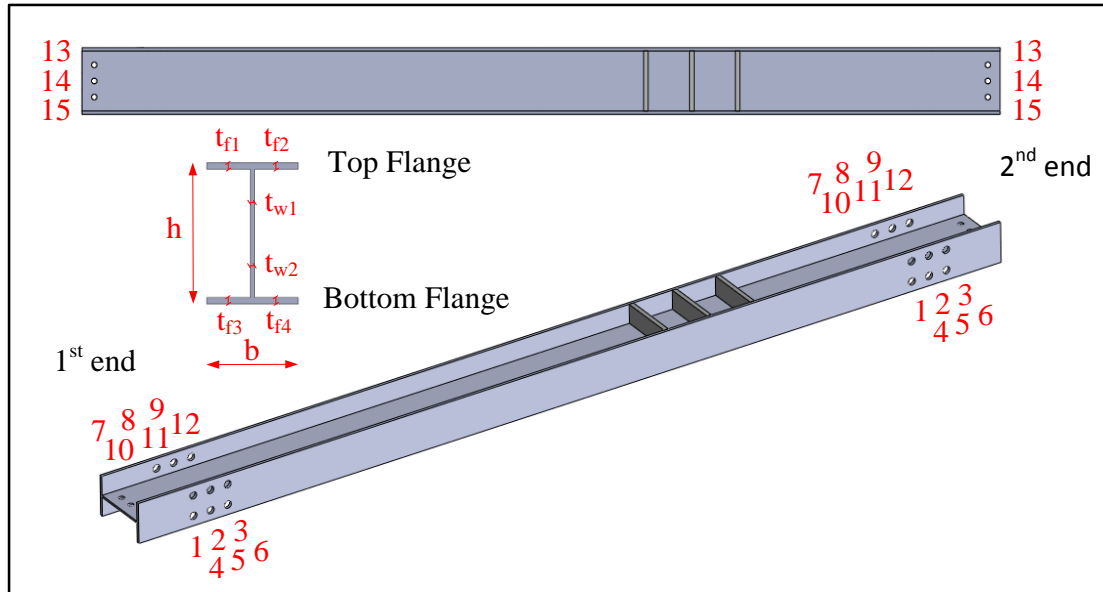


**Figure 5.20:** Geometry measurements of the I-section beam

**Table 5.1:** Geometry measurements of UKB 203×133×30

	Section	Bolt-hole diameter [mm] ( $d_{0,nominal} = 24\text{mm}$ in the flanges and 18mm in the web)		Thickness [mm]						
		1 <sup>st</sup> end	2 <sup>nd</sup> end		1 <sup>st</sup> end	2 <sup>nd</sup> end				
I-section Beam	Top Flange	$d_{0,1}$	23.97	24.10	$t_{f1}$	9.98	9.83			
		$d_{0,2}$	24.00	24.14						
		$d_{0,3}$	23.89	24.12						
		$d_{0,4}$	23.93	24.16						
		$d_{0,5}$	24.11	24.28				$t_{f2}$	9.87	10.03
		$d_{0,6}$	24.11	24.02						
	Bottom Flange	$d_{0,7}$	23.94	24.02	$t_{f3}$	10.00	9.75			
		$d_{0,8}$	24.06	24.06						
		$d_{0,9}$	24.03	24.06						
		$d_{0,10}$	24.03	24.02				$t_{f4}$	9.70	10.00
		$d_{0,11}$	24.15	24.03						
		$d_{0,12}$	23.97	24.06				<i>Mean</i>	<i>9.90</i>	
Web	$d_{0,13}$	17.72	17.65	$t_{w1}$	6.39	6.41				
	$d_{0,14}$	17.75	17.58				$t_{w2}$	6.40	6.41	
	$d_{0,15}$	17.55	17.90							
							<i>Mean</i>	<i>6.40</i>		
				<i>COV</i>	<i>0.001</i>					

**Table 5.2:** *Tolerance on the measured dimensions of UKB 203×133×30*

I-section Beam	Dimensions of the I-section beam [mm]			Measured (average)
	Nominal	Tolerance range: BS EN 10034: 1993		
		Minimum	Maximum	
Section height	206.8	204.8	210.8	210
Flange width	133.9	131.9	137.9	133.9
Flange thickness	9.6	8.6	11.6	9.9
Web thickness	6.4	5.7	7.1	6.4

The actual height of the beam at 210mm is 3.4mm greater than the distance between the outer surfaces of the diaphragm plates in the column assembly. This difference resulted from designing the column assembly using the beam section nominal dimensions. A packing plate was manufactured to fill the difference-gap so that the beam flanges and the diaphragm plates were at the same horizontal level.

Geometry measurements were taken for the CHS column thickness and diameter. Four thickness and two diameter measurements were taken at each end. The obtained measurements are presented in Table 5.3. The deviation from nominal dimensions for the 244.5 × 10mm CHS column are seen to fall within the tolerance values specified by BS EN 10210-2: 2006.

The geometry measurements taken for the diaphragm plates are illustrated in Figure 5.21, and Table 5.4 presents the DPs thicknesses and their bolt-holes diameters. The average values for the rest of the DPs measurements were identical to the nominal ones. The measurements of the bolt-holes diameters in the web stub plate are presented in table 5.5. The other geometry measurements for the web stub plate gave, when averaged, similar results to the nominal ones, and hence they are not reported herein. Geometry measurements of the different tapered cover plates were also not presented because they gave similar results to the nominal values.

**Table 5.3:** Geometry measurements of the CHS column

CHS column	Section	Thickness [mm]		Diameter [mm]	
	1 <sup>st</sup> end	t <sub>c1</sub>	9.60	D <sub>0,1</sub>	244.50
t <sub>c2</sub>		9.70			
t <sub>c3</sub>		9.75			
t <sub>c4</sub>		9.71			
2 <sup>nd</sup> end	t <sub>c5</sub>	9.79	D <sub>0,2</sub>	244.50	
	t <sub>c6</sub>	9.68			
	t <sub>c7</sub>	9.61			
	t <sub>c8</sub>	9.70			
	<i>Mean</i>	9.69	<i>Mean</i>	244.38	
	<i>COV</i>	0.007	<i>COV</i>	0.001	

**Table 5.4:** Geometry measurements of the diaphragm plates

	Thickness [mm]		hole diameter [mm] (d <sub>0,nominal</sub> = 24mm)	
	Top Diaphragm	t <sub>DP1</sub>	15.01	d <sub>0,1</sub>
t <sub>DP2</sub>		14.91	d <sub>0,2</sub>	23.98
t <sub>DP3</sub>		15.07	d <sub>0,3</sub>	23.48
t <sub>DP4</sub>		14.81	d <sub>0,4</sub>	23.97
<i>Mean</i>		14.95	d <sub>0,5</sub>	23.96
<i>COV</i>		0.008	d <sub>0,6</sub>	23.79
Bottom Diaphragm	t <sub>DP1</sub>	15.09	d <sub>0,1</sub>	23.62
	t <sub>DP2</sub>	15.00	d <sub>0,2</sub>	23.45
	t <sub>DP3</sub>	15.08	d <sub>0,3</sub>	23.48
	t <sub>DP4</sub>	14.88	d <sub>0,4</sub>	23.50
	<i>Mean</i>	15.01	d <sub>0,5</sub>	23.36
	<i>COV</i>	0.006	d <sub>0,6</sub>	23.42

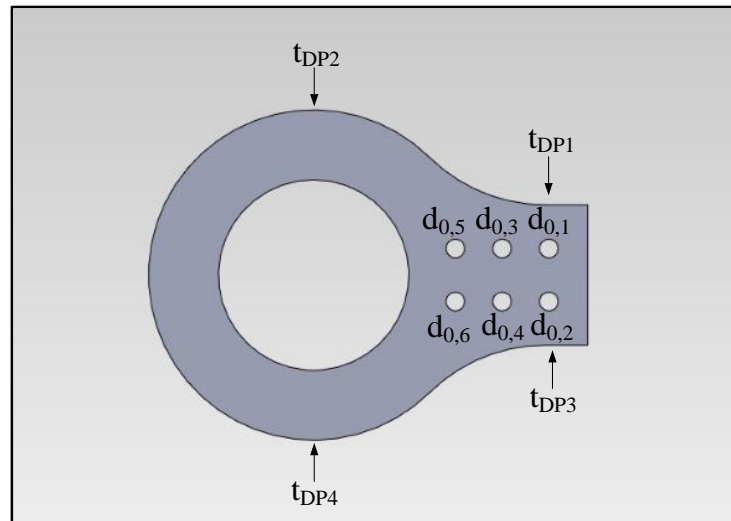


**Figure 5.21:** *Geometry measurements of a diaphragm plate*

**Table 5.5:** *Geometry measurements of the web stub*

	Bolt-hole diameter [mm] ( $d_{0,nominal} = 22\text{mm}$ )	
Web stub	$d_{0,1}$	21.5
	$d_{0,2}$	21.6
	$d_{0,3}$	21.5

Finally, general geometry measurements of the test specimen, after assembling its components, were taken. All were found to be equal to the designated dimensions except for the distance between the centre of the swivel hinges plate, which is also the centre of the loading application area, and the beam connected end. This distance was found to be 1990mm and not 2000mm. The 10mm difference was due to the slight inaccuracy in the location of the hand-drilled bolt-holes in the meccano pieces that form the test rig, and this subsequently resulted in 10mm shorter distance than the designated one between the two reaction frames of the rig. This was taken into consideration when calculating moments at the connected end of the beam by multiplying load by 1990mm.

### 5.5. *Geometry imperfection measurements*

The geometry imperfection measurements determined for the I-section were out-of-squareness and major-axis out-of-straightness. The definitions of these two imperfection measurements were in accordance with BS EN 10034: 1993, and are illustrated in Figure 5.22. No out-of-plane imperfection measurement was needed because the lateral supports prevented the possibility of elastic lateral torsional buckling during testing.

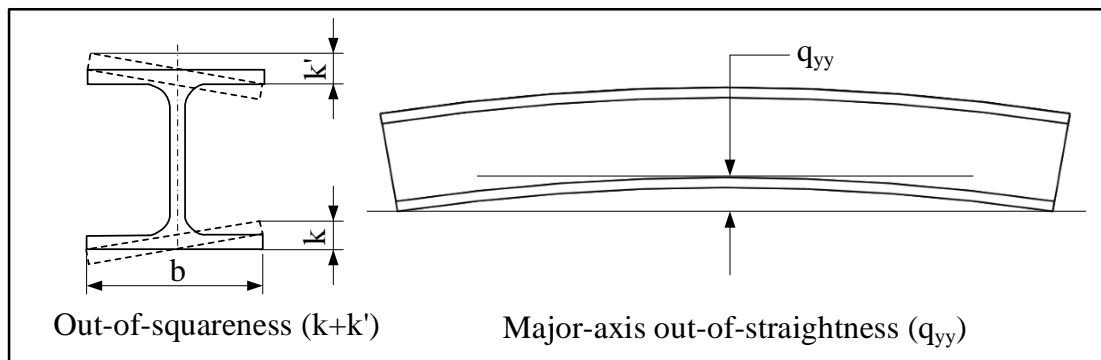


**Figure 5.22:** *Geometry imperfection measurements of the I-beam in accordance with BS EN 10034: 1993*

To measure these two geometry imperfections, the beam length was placed on a levelled flat surface so that its web was parallel to it. A strain gauge displacement transducer was mounted on a track that was parallel to the beam top flange. The transducer was positioned in a horizontal plane, perpendicular to the top flange and pointing at its central line. An attachment to the track allowed for a free movement of the transducer in both the horizontal and vertical planes. Over the length of 3000mm, measurements were made at sixteen sections with 200mm intervals. Figure 5.23 shows the points at which geometry imperfection measurements for the top flange were taken.

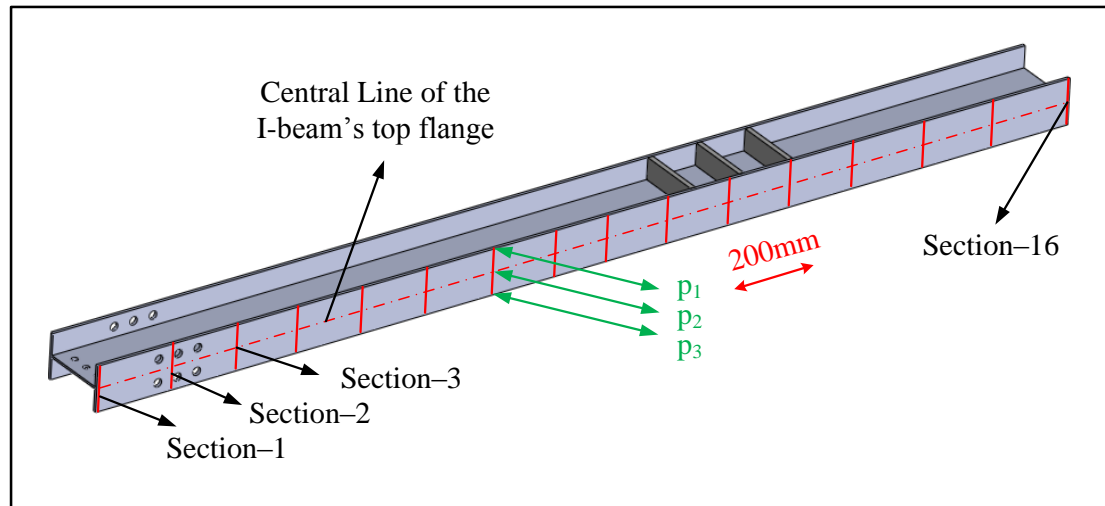


**Figure 5.23:** *Geometry imperfection measurements of the I-beam top flange*

To measure the major-axis out-of straightness of the I-beam top flange, the displacement transducer was set to zero displacement at the centre of the first section, and then it was run horizontally along the track recording the displacement values at the centres of the other predefined fifteen sections. The measurements were then used to calculate the departure of section centres from a straight line connecting the two ends of the top beam flange, as shown in Figure 5.22.

For the out-of-squareness measurements, the displacement transducer was set back to zero at the centre of section-1, and then it was run vertically along this section to get the displacement readings at the top and bottom outstand edges with reference to the midpoint. This process was repeated at the other fifteen sections by setting the transducer to zero displacement at the midpoint of each section ( $p_2$  in Figure 5.23) and then running it vertically to obtain the displacement readings at the top and bottom points ( $p_1$  and  $p_3$  respectively). The absolute sum of the two recorded displacements at a given section gave the out-of-squareness measurement for the top flange.



After completing the geometry imperfection measurements for the top flange, the beam was flipped over and the same imperfection measurements described above were taken and recorded for its bottom flange. Table 5.6 reports the out-of-squareness measurements of the top and bottom flanges in its second and third columns. The sums of the out-of-squareness measurements for both flanges, reported in the fourth column, are in the range of 1.2 to 2.55mm. This range is within the tolerance value (2.7mm) given in BS EN 10034: 1993 and reported in the fifth column of Table 5.6.

**Table 5.6:** *The I-beam out-of-squareness measurements*

Section	Measured out-of-squareness			Tolerance on out-of-squareness [mm]
	Top flange k' [mm]	Bottom flange k [mm]	k+k' [mm]	
1	0.15	1.05	1.2	2.7
2	0.25	1	1.25	
3	0.3	1.05	1.35	
4	0.35	1	1.35	
5	0.15	1	1.15	
6	0.3	1.1	1.4	
7	0.45	0.85	1.3	
8	0.5	0.8	1.3	
9	0.6	0.85	1.45	
10	0.85	0.9	1.75	
11	0.75	1.35	2.1	
12	0.95	1.5	2.45	
13	0.8	1.6	2.4	
14	0.7	1.65	2.35	
15	0.55	1.75	2.3	
16	0.65	1.9	2.55	

Table 5.7 reports the major-axis out-of-straightness measurements for the top and bottom flanges in its second and third columns. The maximum measurement is found

to be 0.3mm, which is below the tolerance value (4.5mm) given in BS EN 10034: 1993 and reported in the fourth column of Table 5.7.

**Table 5.7:** *The major-axis out-of-straightness measurements of the I-beam*

Section	Measured out-of-straightness [mm]		Tolerance on out-of-straightness [mm]
	Top flange	Bottom flange	
1	0	0	4.5
2	0.09	0.05	
3	0.13	0.1	
4	0.17	0.2	
5	0.21	0.2	
6	0.15	0.25	
7	0.19	0.25	
8	0.23	0.15	
9	0.17	0.15	
10	0.06	0.25	
11	0.05	0.3	
12	0.04	0.25	
13	0.08	0.15	
14	0.02	0.05	
15	0.04	0.05	
16	0	0	

### 5.6. *Loading protocol*

The loading protocol adopted for this experimental study was based on the ANSI/AISC 341-10 (2010) provisions for qualifying cyclic tests of beam-to-column moment connections in special and intermediate moment frames. The American method was used instead of the recommended testing procedure of ECCS (1986) for assessing the behaviour of structural steel elements under cyclic loads, because the AISC protocol will cover a bigger range of elastic cycles.

The deformation parameter in the American loading protocol is the interstorey drift angle ( $\theta_{dr}$ ) imposed on the test specimen. The cyclic loading was conducted by controlling the vertical deflection of the beam section located under the actuator. Vertical displacements of the actuator ( $d_a$ ) were calculated by multiplying the recommended drift angle values “ $\theta_{dr}$ ” from the loading protocol by the beam effective length ( $L_{eff} \approx 2$  m), as illustrated in Figure 5.24.

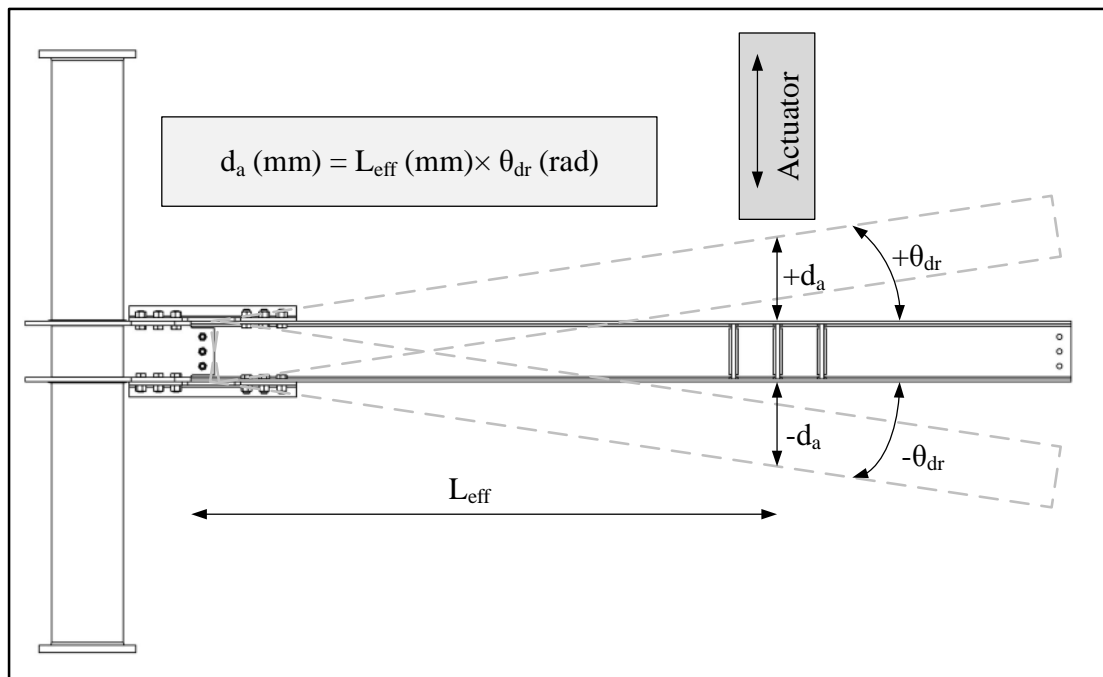


**Figure 5.24:** *Calculation of the actuator displacements for the loading protocol*

Table 5.8 presents the proposed drift angles in the protocol and the equivalent actuator displacements. The loading programme was limited to a maximum of 30 cycles because of the imposed stroke-capacity limitation of the actuator. Figure 5.25 shows the displacement-controlled loading for the completed 30 cycle test. Each cycle started and ended with a zero vertical deflection of the beam, and included one positive and one negative peak. The loading protocol was conducted at the stroke rate of 0.5mm/sec via the actuator control computer.

**Table 5.8:** *The loading protocol used for the joint tests*

Cycle number	Drift angle $\theta_{dr}$ (rad)	Vertical displacement $d_a$ [mm]
[1 – 6]	$\pm 0.00375$	$\pm 7.5$
[7 – 12]	$\pm 0.005$	$\pm 10$
[13 – 18]	$\pm 0.0075$	$\pm 15$
[19 – 22]	$\pm 0.01$	$\pm 20$
[23 – 24]	$\pm 0.015$	$\pm 30$
[25 – 26]	$\pm 0.02$	$\pm 40$
[27 – 28]	$\pm 0.03$	$\pm 60$
[29 – 30]	$\pm 0.04$ <td $\pm 80$	

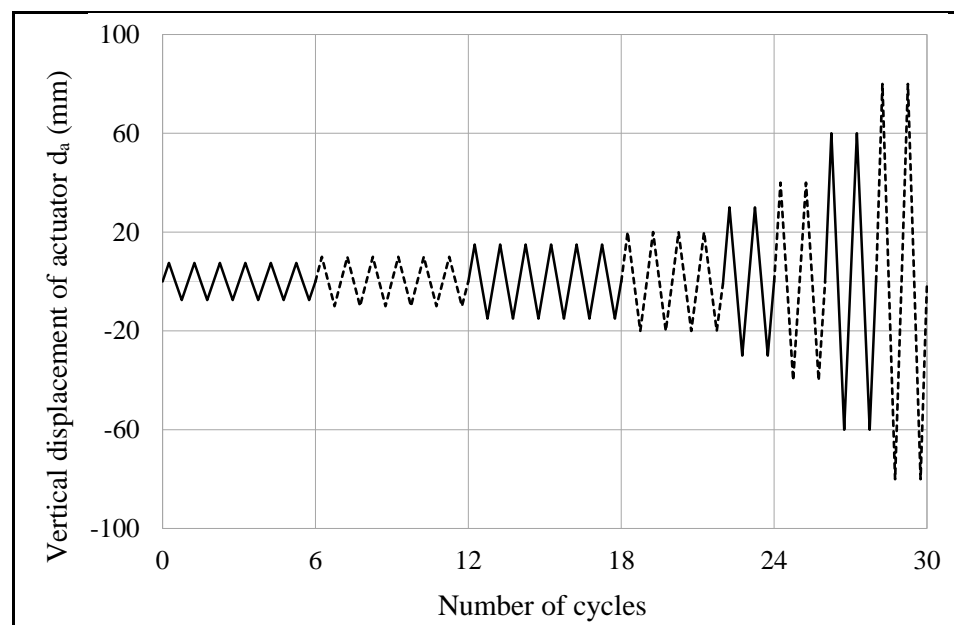


**Figure 5.25:** *Displacement-controlled loading cycles - ANSI/AISC 341-10 (2010)*

## 5.7. *Test instrumentation*

The use of instrumentation was essential to monitor and record different types of measurements from the areas of interest in the test specimens. Together with the actuator built-in displacement transducer and load cell, instrumentation involved a number of strain gauges, displacement transducers and inclinometers to capture measurements that were essential to understand a joint structural performance. Descriptions of the different types of instruments used, their location, purpose, calibration and set-up are detailed in Sections 5.7.1 to 5.7.4. For the ease of describing the locations of instruments on test specimens, it is assumed in this thesis that the front face of the specimen is the face that can be seen from a front view where the column is located to the left side of the specimen and the actuator is located to its right side, and vice versa.

### 5.7.1. *Actuator*

Vertical displacements at the tip of the I-beam effective length and the corresponding forces were measured using the actuator built-in displacement transducer, of  $\pm 80$ mm capacity, and load cell, of 100 kN capacity, respectively. The actuator measurements were logged to a computer and recorded during each of the nine tests through the National Instruments (NI) data-logging system and its software package LabVIEW (2010).

Before conducting the first test, the load cell was calibrated by an engineer from “Servocon Systems Limited” in tension and compression to BS EN ISO 7500-1: 2004 and its displacement transducer was calibrated to National Standards. Figure 5.26 shows the calibration process of the actuator load cell in tension in the Structures Laboratory.



**Figure 5.26:** *Calibration of the actuator load cell in tension*

The actuator measurements of load and displacement were then calibrated through the NI data-logging system to determine the linearly proportional relationship between the actual load and displacement measurements and the corresponding voltage outputs. The calibration process was repeated three times to minimise calibration errors and uncertainty by averaging the results of the three iterations.

### 5.7.2. *Strain gauges*

Strain gauges (SGs) were used at the expected location for plastic hinges and stress concentrations. Some joint components designed not to have any significant stress concentration, such as the column web panel, were also equipped with strain gauges to monitor strain levels throughout the tests.

Measurements of all strain gauges were logged to a computer and recorded during tests through the National Instruments (NI) data-logging system and its software package LabVIEW (2010). The strain gauges were calibrated through the NI system before the beginning of each test to set their initial strain value to zero.

All strain gauges were electrical post-yield strain gauges of type YFLA–10mm, supplied by TML (2012). These gauges measure large strains up to 15% to 20%. Because it was slightly difficult to bond the 10mm strain gauges uniformly to the curved surface of the CHS column, it was decided to have the smaller strain gauge of YEFLA–5mm, supplied by TML (2012), on the column web panel. The 5mm sized gauges had a lower maximum strain capacity of 10% and 15%.

A sketch of the column web panel with the location of its three strain gauges is shown in Figure 5.27. Figure 5.28 shows a photo of the column web panel taken in the Structures Laboratory after attaching the three strain gauges to its surface.

SG–1 and SG–2 were fastened to the surface of the column web panel zone to check that the material remained elastic during the test. SG–1 was fixed at the mid-height of the web panel at 90 degree from the plane of the web stub plate, while SG–2 was fixed to the front face of the column web panel, near the weld of the top diaphragm plate, at 45 degree from the plane of the web stub plate. This arrangement of two strain gauges on the column web panel was used in Tests 1 to 4.

SG–3 was added to this arrangement from Test 5 onwards, and was fixed to the front face of the column web panel, near the weld of the bottom diaphragm plate, directly below SG–2. The purpose of adding SG–3 was to have a comparison with SG–2 since their positions were symmetric with respect to the web panel mid-height.

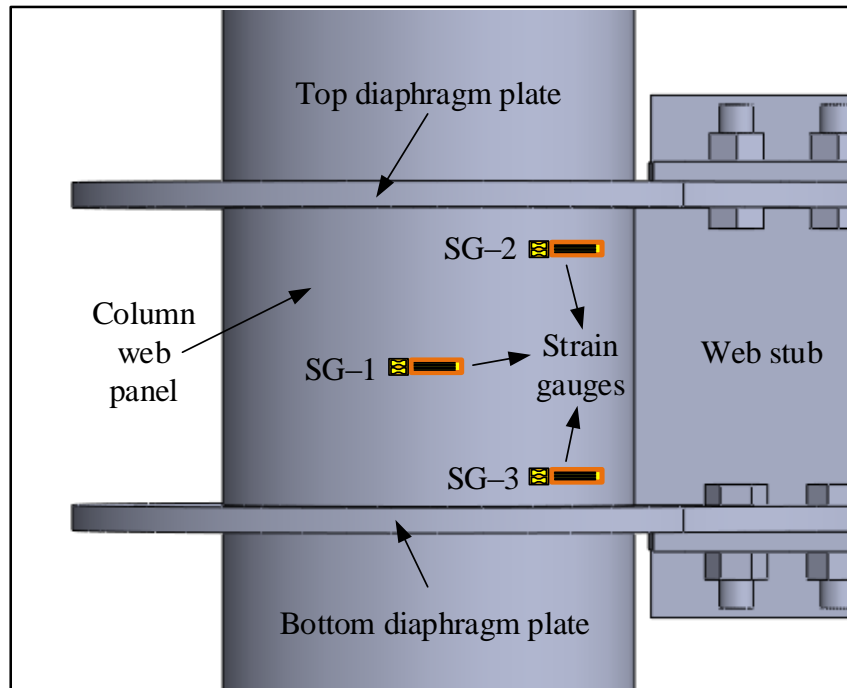


**Figure 5.27:** *Sketch of the column web panel zone and its strain gauges*

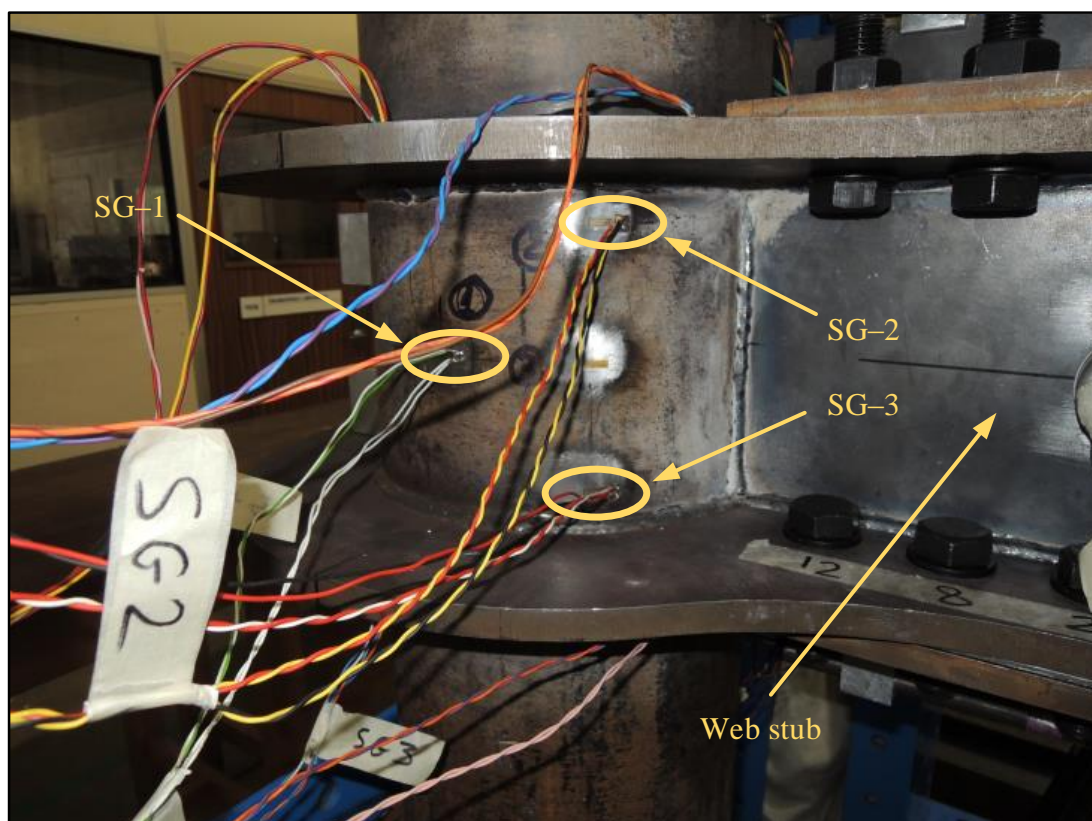


**Figure 5.28:** *Location of strain gauges on the column web panel zone*



Ten gauges SG-4 to SG-13 were placed on the two diaphragm plates (DPs), with five on each plate as illustrated in Figure 5.29, to monitor the force flow from the DPs into the column, observe strain levels in the DPs and assure steel does not reach  $\epsilon_y$  during the loading protocol.

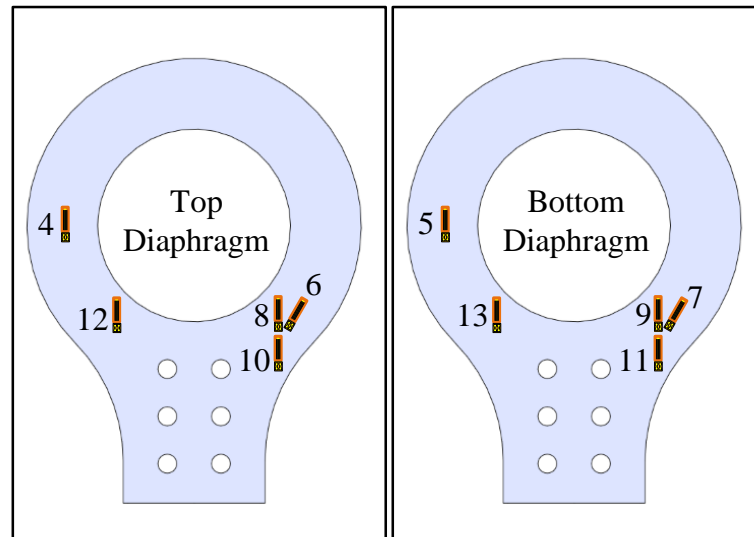


**Figure 5.29:** Sketch of the two diaphragm plates and their strain gauges

The gauges for the top DP are SG-4, SG-6, SG-8, SG-10 and SG-12. SG-4 was fixed along the tangential line of the central portion of the top diaphragm plate ring at 90 degree from the longitudinal axis. SG-6 was fixed along the tangential line of the central portion of the top DP ring at 45 degree from its longitudinal axis. SG-8 was fixed right next to SG-6, parallel to the longitudinal axis. SG-10 was fixed 40mm away from the column face, with its axis aligned with SG-8. SG-12 was fixed in a location that is symmetric to the location of SG-8.

As seen in Figure 5.29, SG-5, SG-7, SG-9, SG-11 and SG-13 were fixed to the bottom diaphragm plate in locations similar to those of SG-4, SG-6, SG-8, SG-10 and SG-12 respectively. Fixing strain gauges to both diaphragm plates in an identical arrangement allowed for the comparison between their measurements to

check their agreement. Figures 5.30 and Figure 5.31 show photos of the top and bottom diaphragm plates respectively after attaching the groups of strain gauges.

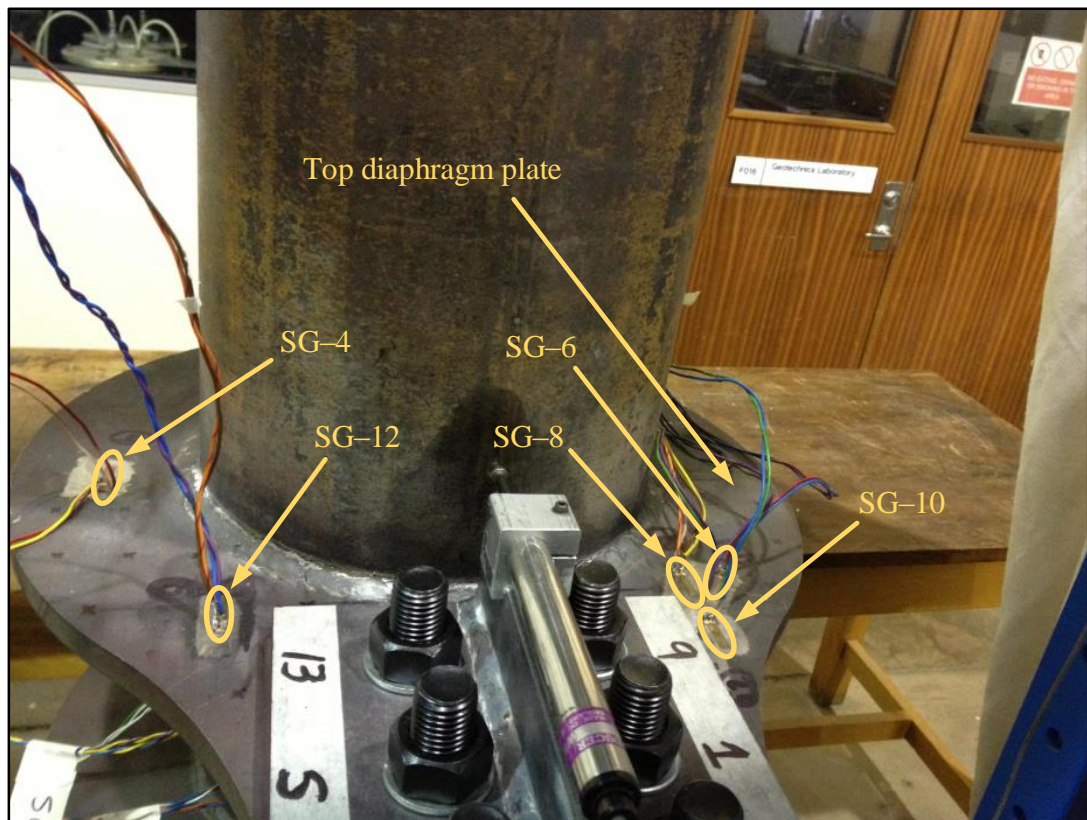


**Figure 5.30:** *Location of strain gauges on the top diaphragm plate*

Each TCP was strain gauged on the reduced section region, because the latter was the expected location of a plastic hinge in the joint. In tests where the TCPs were not stiffened (numbered 1, 4, 6–8 in Table 3.2), three gauges SG–14, SG–16 and SG–18 were fixed to the top surface of the top cover plate along its longitudinal axis on the left side, centre and right side of its reduced-section region. Similarly, three gauges SG–15, SG–17 and SG–19 were fixed to the bottom surface of the bottom cover plate. A sketch for a pair of unstiffened TCPs with their strain gauges is given in Figure 5.32.

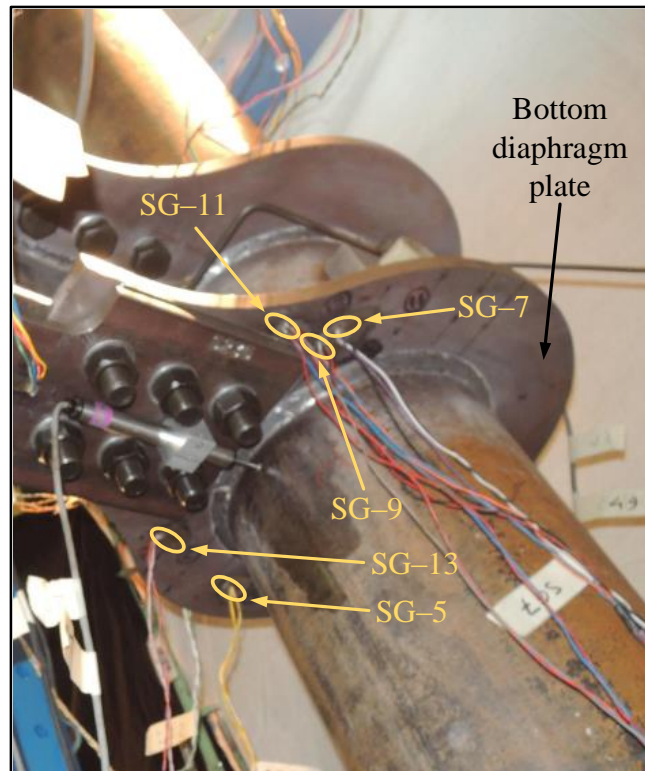


**Figure 5.31:** *Location of strain gauges on the bottom diaphragm plate*

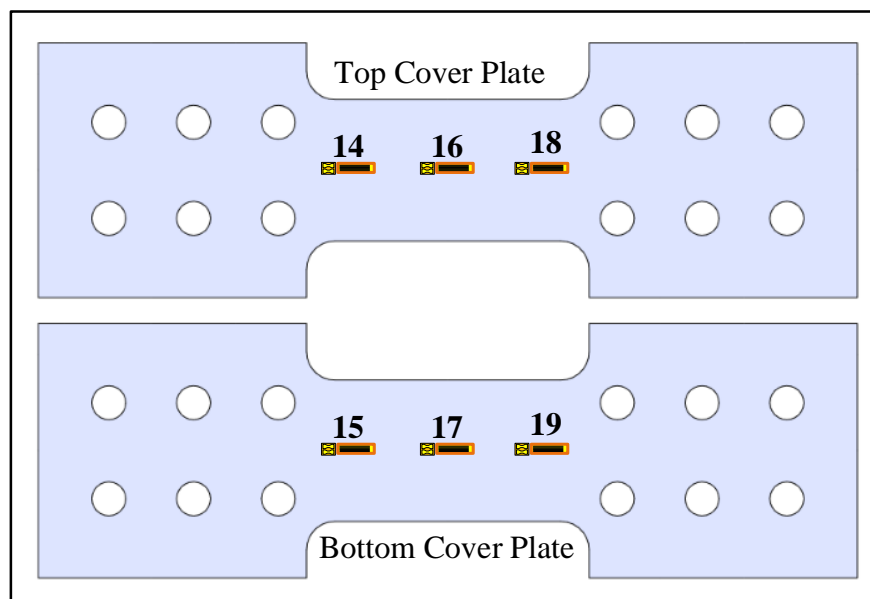


**Figure 5.32:** *Sketch of two unstiffened TCPs and their strain gauges*

Figures 5.33 and 5.34 are for photos of a top and a bottom unstiffened TCP respectively after strain gauging them.

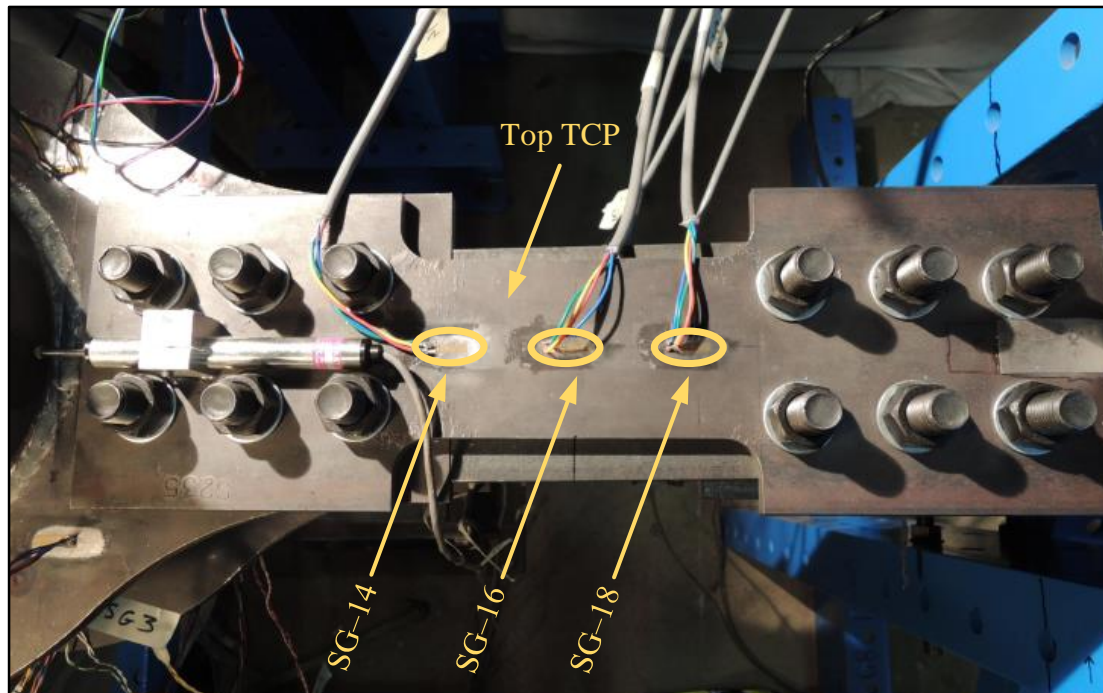


**Figure 5.33:** *Location of strain gauges on a top unstiffened TCP*

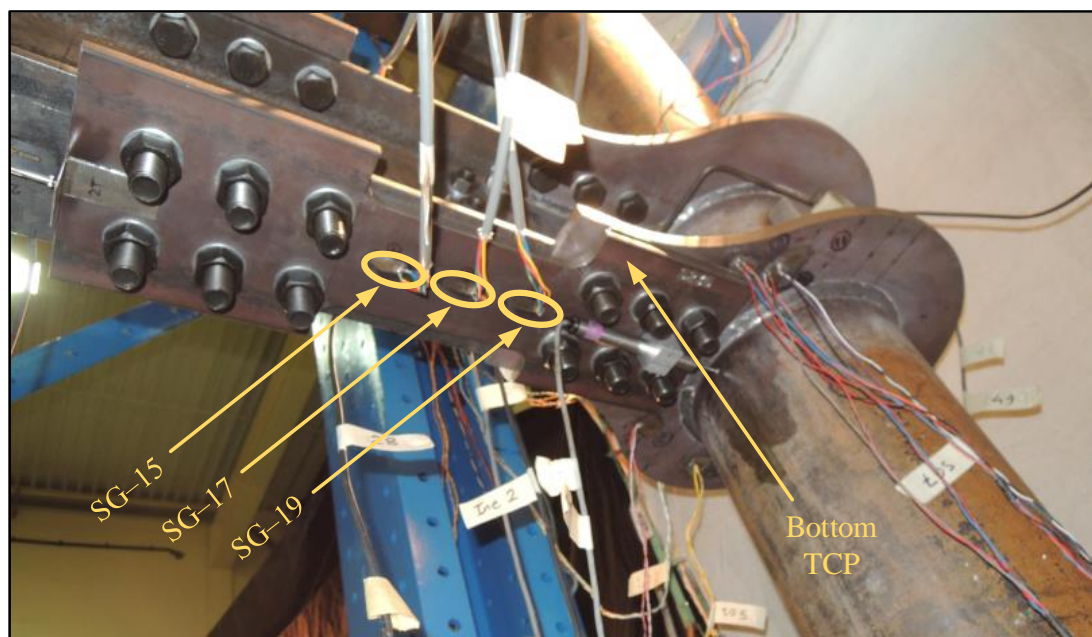


**Figure 5.34:** *Location of strain gauges on a bottom unstiffened TCP*

In tests where the TCPs were stiffened (numbered 2–3, 5, and 9 in Table 3.2), the three SGs were fixed to the TCP reduced-section region along the midline of the portion between its longitudinal edge and the stiffener. A single strain gauge was applied to the stiffener at its centre; SG–20 for the top stiffener and SG–21 for the

bottom one. Drawings of two stiffened TCPs with their strain gauges are shown in Figure 5.35. Figure 5.36 is for a front view photo for the two gauged stiffeners. Figures 5.37 and 5.38 are for photos for a gauged top and a gauged bottom stiffened TCP.

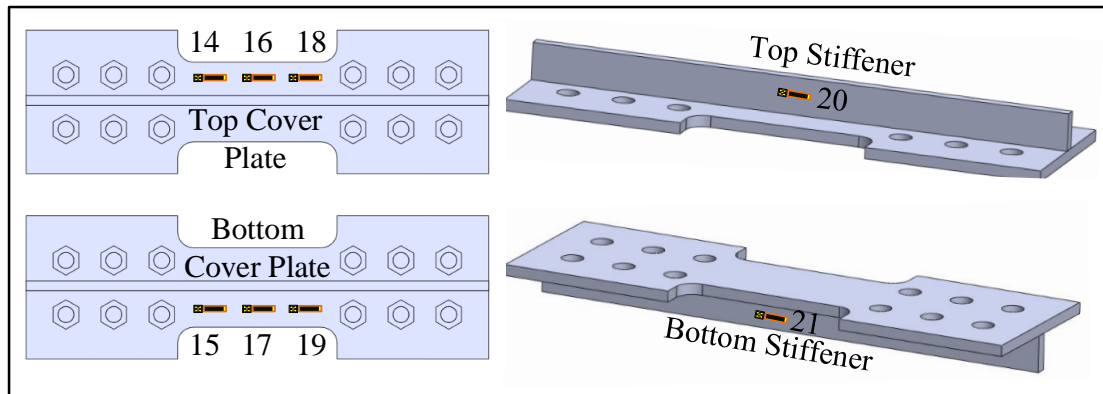


**Figure 5.35:** *Top view (left) and 3D view (right) of two stiffened TCPs and their SGs*

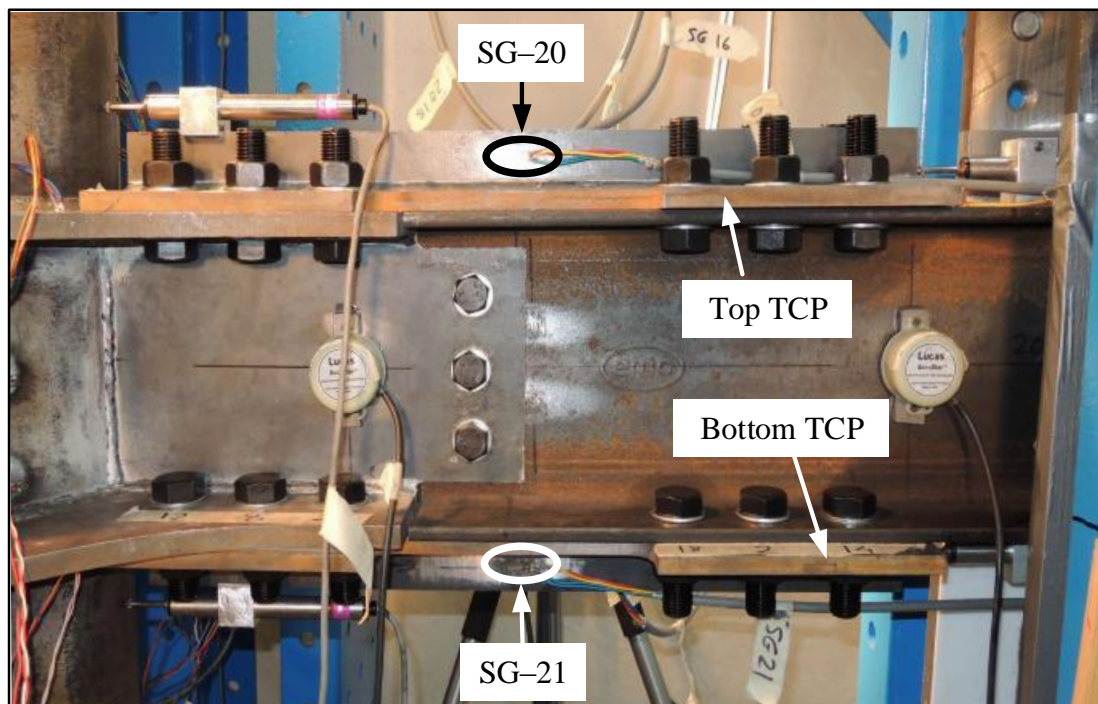


**Figure 5.36:** *Location of strain gauges on top and bottom TCP stiffeners*

Finally, the three gauges SG-22, SG-23 and SG-24 were affixed to the I-beam most critical section, which, as shown in Figure 5.39, was next to the connection zone. These gauges were to monitor strains in the region where the highest stresses were –

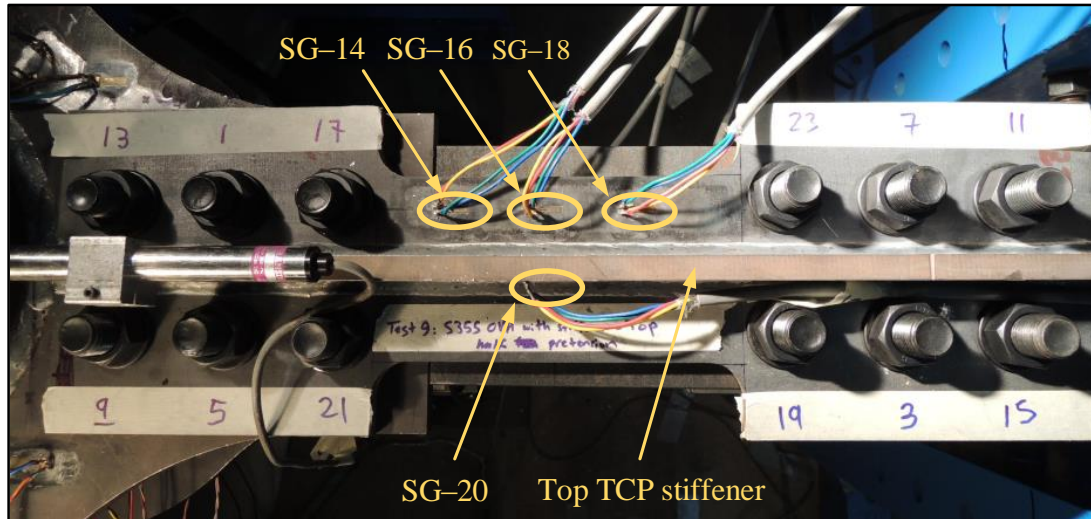


**Figure 5.37:** *Location of strain gauges on a top stiffened TCP*

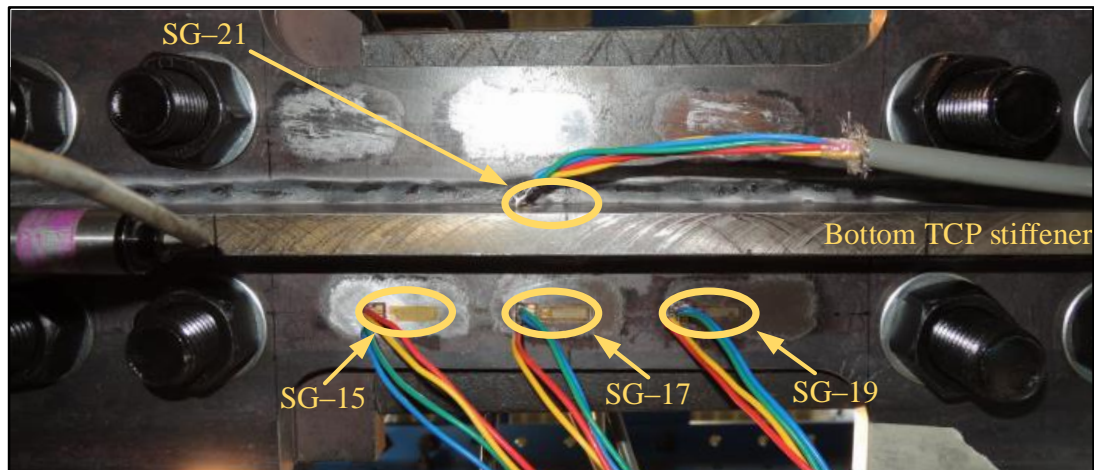


**Figure 5.38:** *Location of strain gauges on a bottom stiffened TCP*

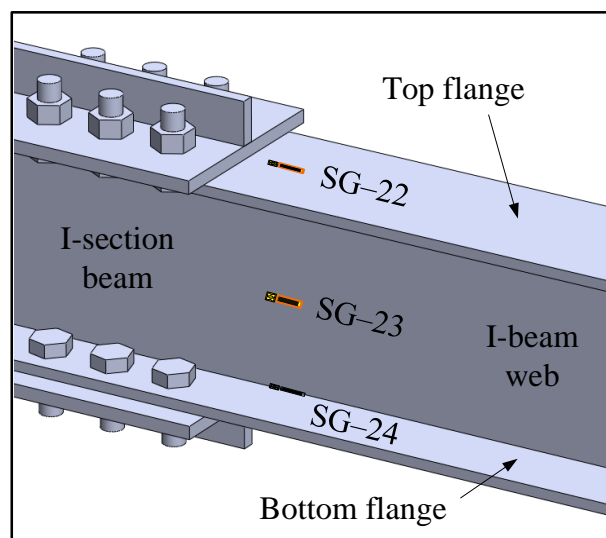


**Figure 5.39:** *Location of strain gauges on the I-section beam*

–expected. SG–22 and SG–24 are located centrally on the top and bottom flange, and SG–23 is positioned at the web mid-height. SG–24 is drawn with dashed lines in Figure 5.39 to indicate that it is located on the lower flange surface and cannot be seen in this sketch.

### 5.7.3. *Inclinometers*

Electronic inclinometers (INCs), having a linear range of  $\pm 45$  degree, a resolution of 0.001 degree and a repeatability of 0.05 degree, were used to measure angles of rotation in five different locations to establish joint rotation and examine the components deformation. A sketch of a specimen with the label and location for the five inclinometers is given in Figure 5.40. INC–2, INC–4 and INC–5 in this figure are darker than INC–1 and INC–3 to indicate that the former three were mounted on the front face of the specimen while the latter two were mounted on the back.

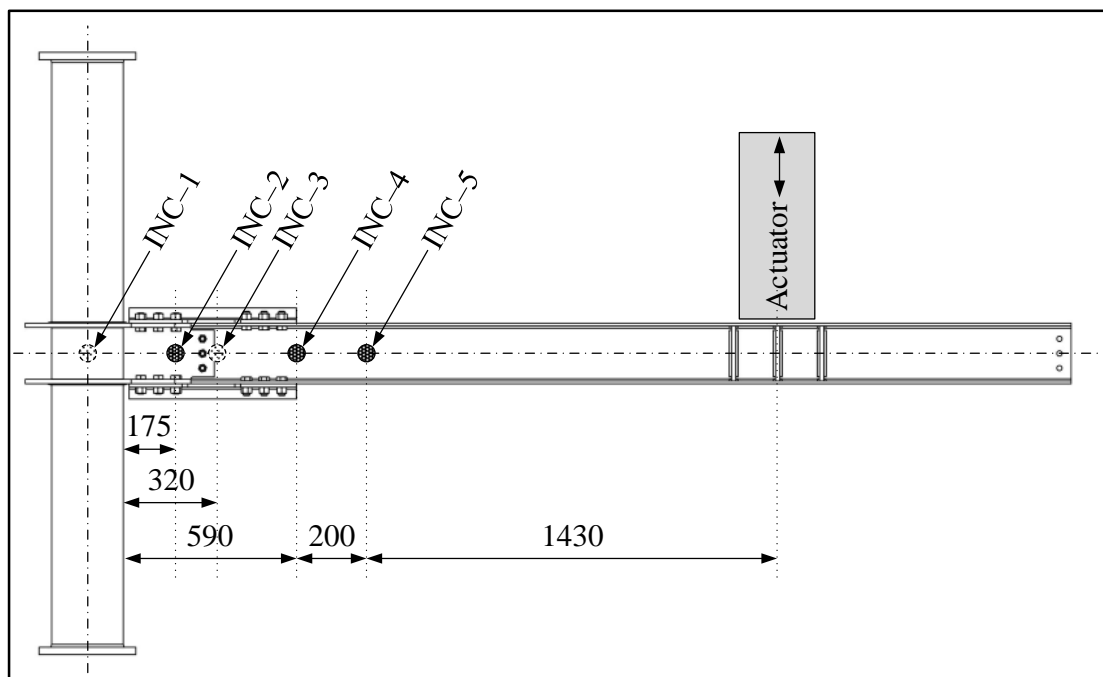


**Figure 5.40:** Sketch of the test specimen detailing the location of INCs – dimensions in [mm]

INC-1 was fixed at mid-height of the column web panel central section. Rotation measurements  $\theta_1$  obtained via INC-1 comprise the rotation components from the column hinges  $\theta_{c,h}$  and the web panel  $\theta_{wp}$ . Thus, it was important to deduct the rotations for hinges from  $\theta_1$  to get a reliable estimation of the actual web panel rotation ( $\theta_{wp} = \theta_1 - \theta_{c,h}$ ).  $\theta_{c,h}$  was measured through the use of displacement transducers as described in Section 5.7.4. It was decided to fix INC-1 to the back face of the column so that it did not interfere with the strain gauges (SG-1 to SG-3). Figure 5.41 shows the fixing arrangement of INC-1 to the column web panel. A metal attachment was manufactured to provide a suitable fixture for attaching INC-1 to the curved surface of the CHS. The inner face of this fixation was glued to the surface of the column and had a similar curvature to assure effective contact between the two surfaces. The opposite face was flat to fix the inclinometer in the vertical plane.

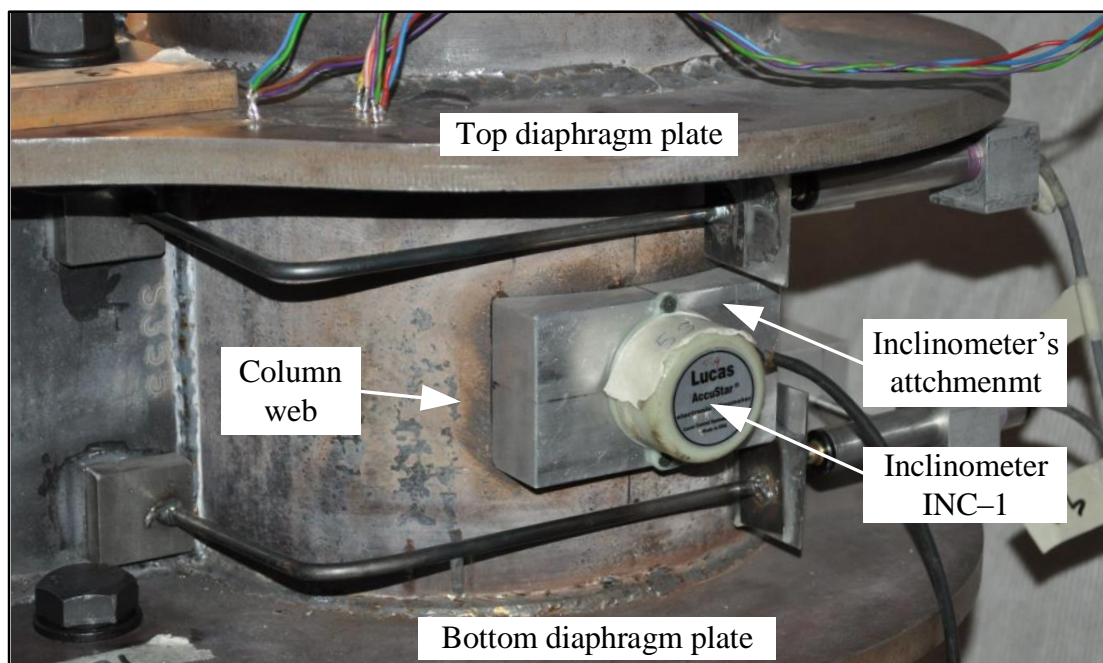


**Figure 5.41:** *Fixing arrangement of INC-1 to the column web panel*



As seen in Figure 5.42, INC-2 was fixed at mid-height of the web stub and below the third line of the top TCP-DP bolts, counted from the column face. The purpose of INC-2 was to capture the maximum rotation of the web stub during testing.  $\theta_2$  from INC-2 represented the rotation of the column hinges  $\theta_{c,h}$ , web panel  $\theta_{wp}$  and web stub  $\theta_{ws}$ . Hence,  $\theta_1$  was later deducted from  $\theta_2$  to get a reliable estimation of the actual web stub rotation ( $\theta_{ws} = \theta_2 - \theta_1$ ).

Two metal square plates were manufactured to be used as fixtures for the attachment of INC-2. The back face of each plate was glued to the web stub surface, and the inclinometer was fixed to the front faces of the plates by two screws. This fixing arrangement was also used for INC-3, INC-4 and INC-5.

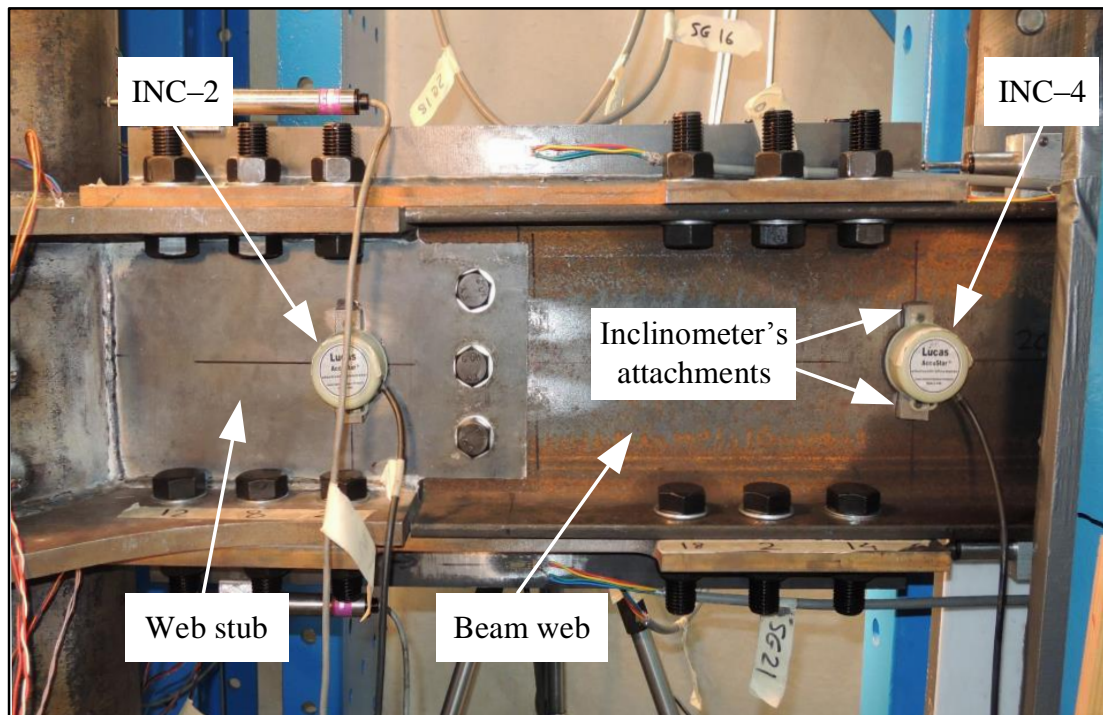


**Figure 5.42:** Fixing arrangements of INC-2 and INC-4 to the specimen front face

To capture the angle of rotation of the beam-to-column joint  $\phi$ , there is INC-3 positioned at mid-height of the beam web and between the centres of the two TCPs (305mm from the column face). As shown in Figure 5.43, this inclinometer is on the

back face of the specimen. Because INC-3 would coincide with the nuts for the web connection bolts, it was not practical to position the inclinometer exactly between the short axes of the TCPs. The best location of INC-3 was therefore 15mm away from the designated one, making it 320mm from the column face. To obtain reliable estimation of the joint rotation during a test, rotations of the column hinges were deducted from INC-3 measurements when analysing tests results ( $\phi = \theta_3 - \theta_{c,h}$ ).

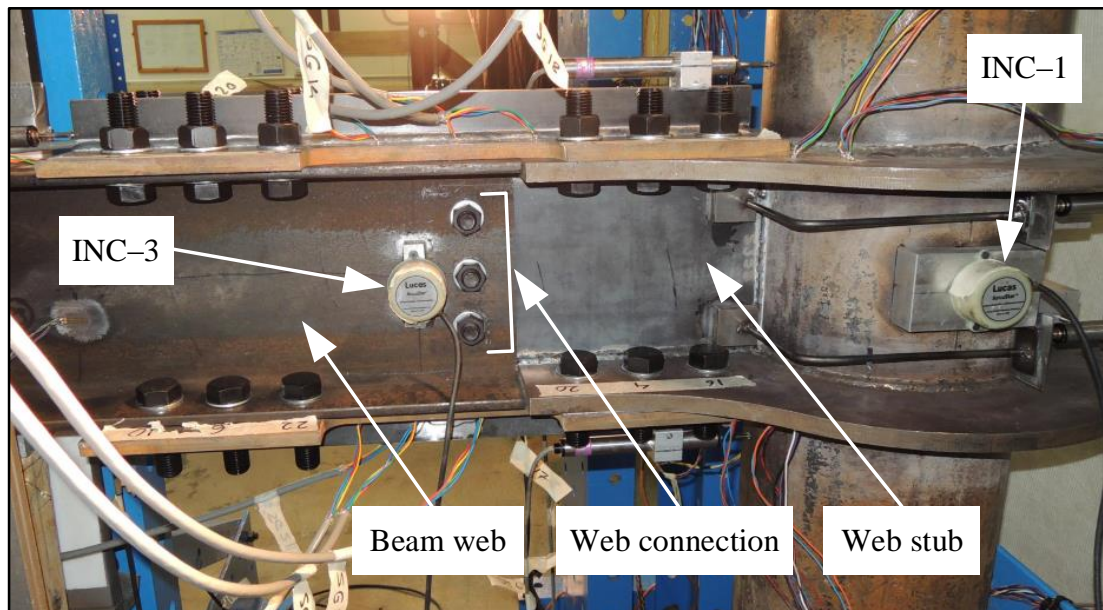


**Figure 5.43:** Fixing arrangement of INC-3 to the back face of the beam web

Figure 5.42 shows that INC-4 was fixed at mid-height of the beam web at the end of the connection, between the short edges of the top and bottom cover plates. This is to assess the rotation of the beam critical section  $\theta_{b,crit}$  by subtracting measurements of INC-3 from INC-4 when analysing tests results ( $\theta_{b,crit} = \theta_4 - \theta_3$ ).

The last inclinometer (INC-5) was mounted at mid-height of the beam web and 200mm horizontal from the connection end to capture the beam rotation  $\theta_b$  to check whether the section experienced any inelastic deformations ( $\theta_b = \theta_5 - \theta_4$ ).

External power source was essential for the five inclinometers to function. All inclinometers were connected to a nominal voltage supply of  $\pm 12$  volts. The inclinometers were calibrated prior to the tests through the National Instruments (NI) data-logging system and its software package LabVIEW (2010) to determine the relationship between their voltage outputs and changes in rotation angle. The obtained calibration results allowed for a computational interpretation of the inclinometers outputs into accurate rotation measurements during testing.

The calibration process was carried out by fixing the five inclinometers to one leg of a 90 degree angle-plate, while resting its other leg on a flat surface. Five voltage readings from the five inclinometers were recorded while the angle plate was in the flat position having  $0^\circ$  rotation. An anticlockwise angle rotation was applied to the angle-plate by placing a slip gauge of known size under the right edge of its bottom leg, and the voltage reading changes for a known rotation were recorded for the five inclinometers.

The sign convention used in this calibration process assumed rotations were positive when they were anticlockwise and negative when they were clockwise. Seven different heights of slip gauges (10, 20, 30, 40, 50, 60 and 70mm) were used to obtain voltage readings from the inclinometers for the seven anticlockwise angle rotations of  $+1^\circ$ ,  $+2^\circ$ ,  $+3^\circ$ ,  $+4^\circ$ ,  $+5^\circ$ ,  $+6^\circ$  and  $+7^\circ$ . Similarly, seven clockwise angle rotations of  $-1^\circ$ ,  $-2^\circ$ ,  $-3^\circ$ ,  $-4^\circ$ ,  $-5^\circ$ ,  $-6^\circ$  and  $-7^\circ$  were applied by placing each of the seven slip gauges under the left edge of the angle-plate bottom leg. An illustration of the inclinometers calibration process is shown in Figure 5.44.

Calibration factors for each inclinometer were obtained by analysing the linearly proportional relationship between the applied rotation angles and the corresponding

voltage outputs. The whole calibration process described above was repeated three times to minimise calibration errors and uncertainty by averaging the results of the three iterations. The calibration process was repeated for the five INCs after the end of tests to check the accuracy of the calibration factors used throughout testing. It was found that the calibration factors did not change. It was concluded by the author that the measurements of rotation obtained from the INCs were reliable and needed no modification.

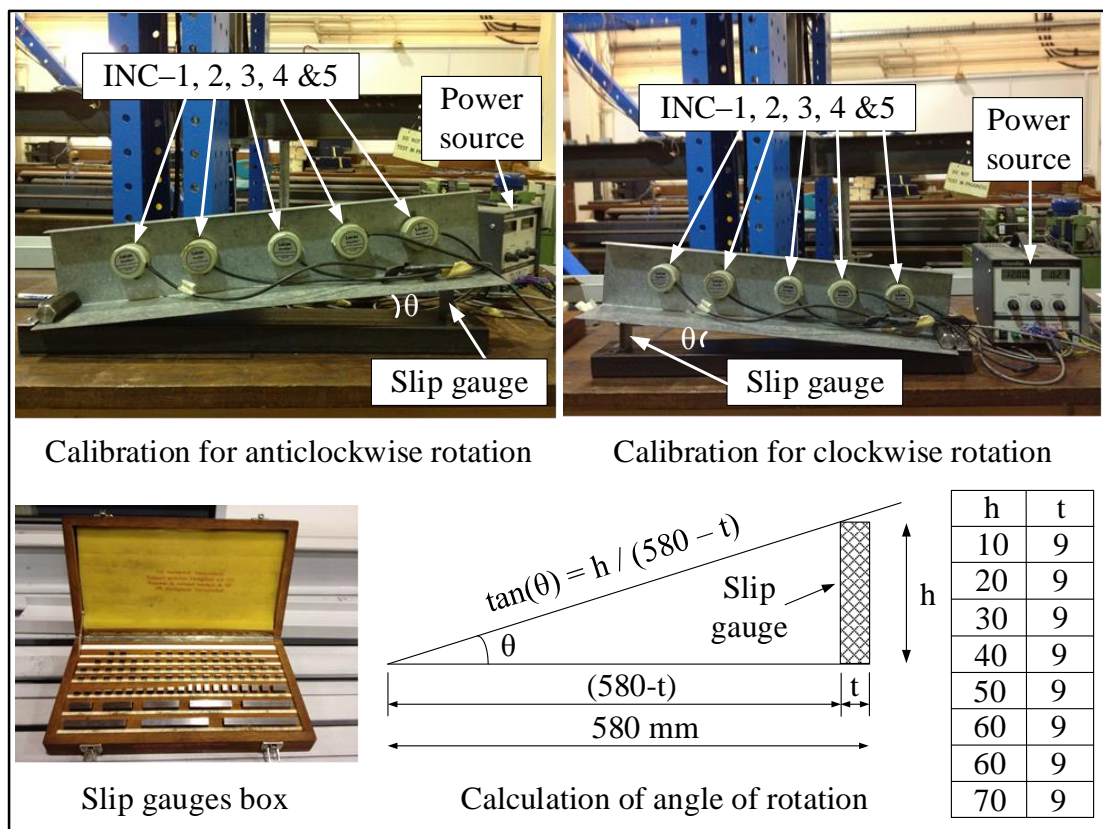


**Figure 5.44:** Calibration of inclinometers - dimensions in [mm]

During testing, the sign convention for rotations was kept identical to the one used in the calibration of inclinometers. Thus, it was assumed that the upward movement of the actuator resulted in positive anticlockwise rotations of the specimen and vice versa. This assumption allowed for the use of the calibration factors for INC-2, INC-4 and INC-5 in the actual tests because these inclinometers were fixed to the

front face of the specimen; while the calibration factors for INC-1 and INC-3, which were mounted to the back face of the specimen, were multiplied by (-1) to unify the sign convention for all five inclinometers. The rotation measurements of all inclinometers were logged to a computer and recorded during the tests through the NI data-logging system and its software package LabVIEW (2010).

#### 5.7.4. *Displacement transducers*

Eight strain gauge Displacement Transducers (DTs), with improved linearity, were installed horizontally at different locations on a specimen to measure primary slips and displacements. A sketch of the specimen with the DTs labels and locations is given in Figure 5.45. DT-2 and DT-3 are drawn with dashed lines to indicate that they were attached to the back face of the specimen.

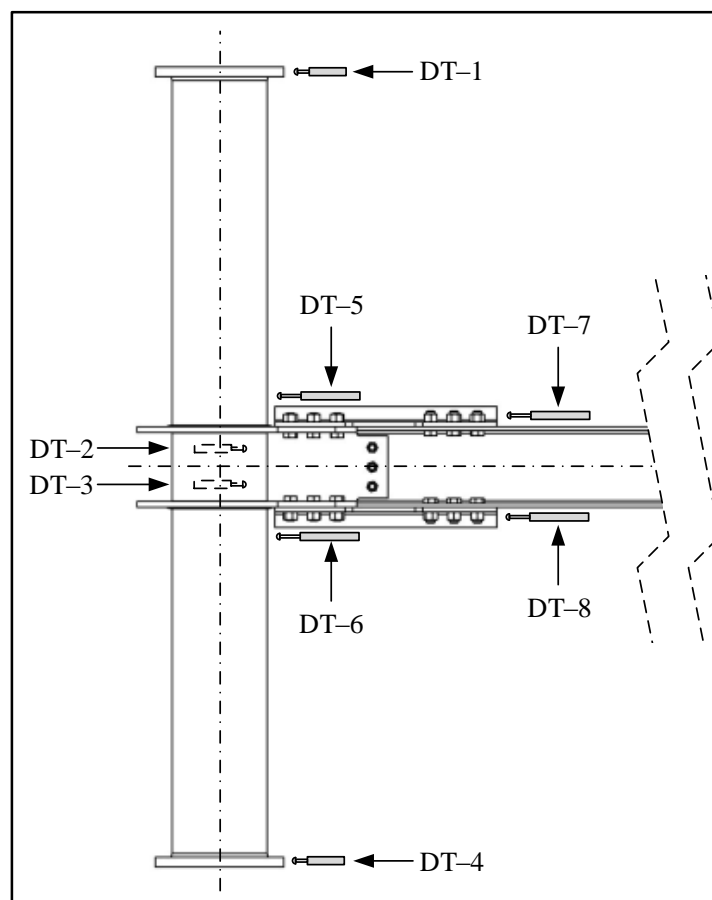


**Figure 5.45:** *Location of displacement transducers (DTs) on a test specimen*

DT-1 to DT-4 had a measurement range of 0 to 25mm and a strain sensitivity of  $510 \times 10^{-6}/\text{mm}$ . They were set at their mid-range to be capable of measuring 12.5mm displacement in either direction. DT-5 to DT-8 had a measurement range of 0 to 50mm and a strain sensitivity of  $150 \times 10^{-6}/\text{mm}$ . They were set at their mid-range to be capable of measuring 25mm displacement in each direction. These four transducers were chosen to have the longer range to accommodate the relatively larger displacements anticipated at their locations as a result of possible connection-slips.

As seen in Figure 5.45, DT-1 and DT-4 were held horizontally, with the use of suitable attachments, against the column top and bottom end plates to monitor their movements and subsequently to be used to calculate the hinge rotations. The overall  $\theta_{c,h}$  was determined by summing displacement measurements from DT-1 and DT-4, and dividing the result by the height difference between the two transducers. Since the rotations from the column end hinges were captured by all five inclinometers, it was important to deduct  $\theta_{c,h}$  from the measured rotations  $\theta_1$  to  $\theta_5$  when analysing tests results.

The fixing arrangements of DT-1 and DT-4 are illustrated in Figure 5.46. The body of DT-1 was held tightly in a holder, while its tip was positioned against a small thin plate (support plate) glued to the top column end plate. The transducer holder was fixed to metal attachments, which in turn were connected to the test rig, to keep the transducer in place and horizontal at all times. Similarly, DT-4 was held tightly in a holder while its tip was positioned against a thin plate glued to the column bottom end plate. The DT-4 holder was kept in place by connecting it to a stand whose magnetic base was attached to the bottom plate of the column bottom hinge. The magnetic base provided stability for DT-4 and its fixing arrangement during testing.

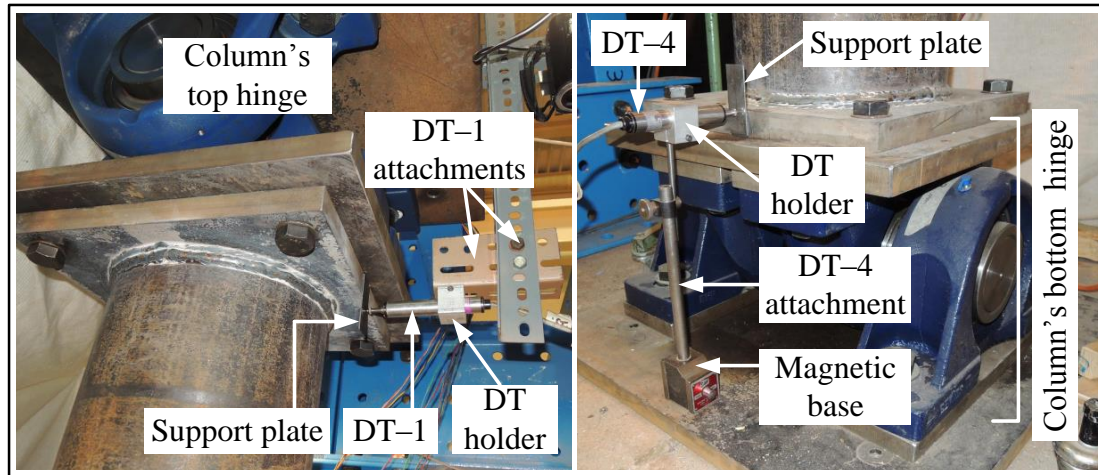


**Figure 5.46:** Fixing arrangements of DT-1 (left) and DT-4 (right)

DT-2 and DT-3 were used in all tests to measure local deformations of the column web panel. To obtain their measurements, they were held horizontally, using the fixing arrangement shown in Figure 5.47 that is between two points at the column web panel face furthest from the connection and two reference points located at the web stub next to its vertical weld.

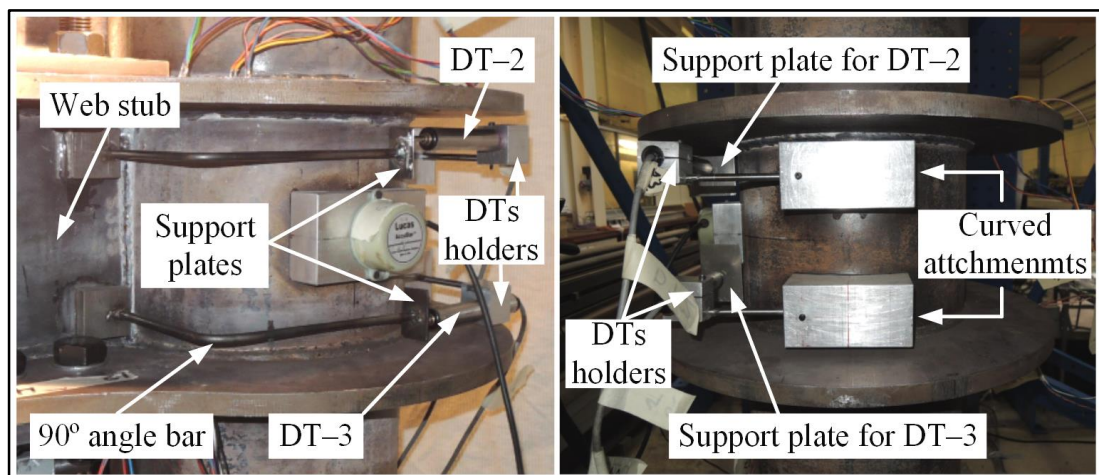


**Figure 5.47:** Fixing arrangement of DT-2 and DT-3 viewed from different angles

DT-2 was positioned right below the top diaphragm plate, while DT-3 was positioned right above the bottom diaphragm plate. This arrangement allowed the two transducers to measure two deformations on the rear face of the web panel in reference to region that was not expected to experience any significant deformations.

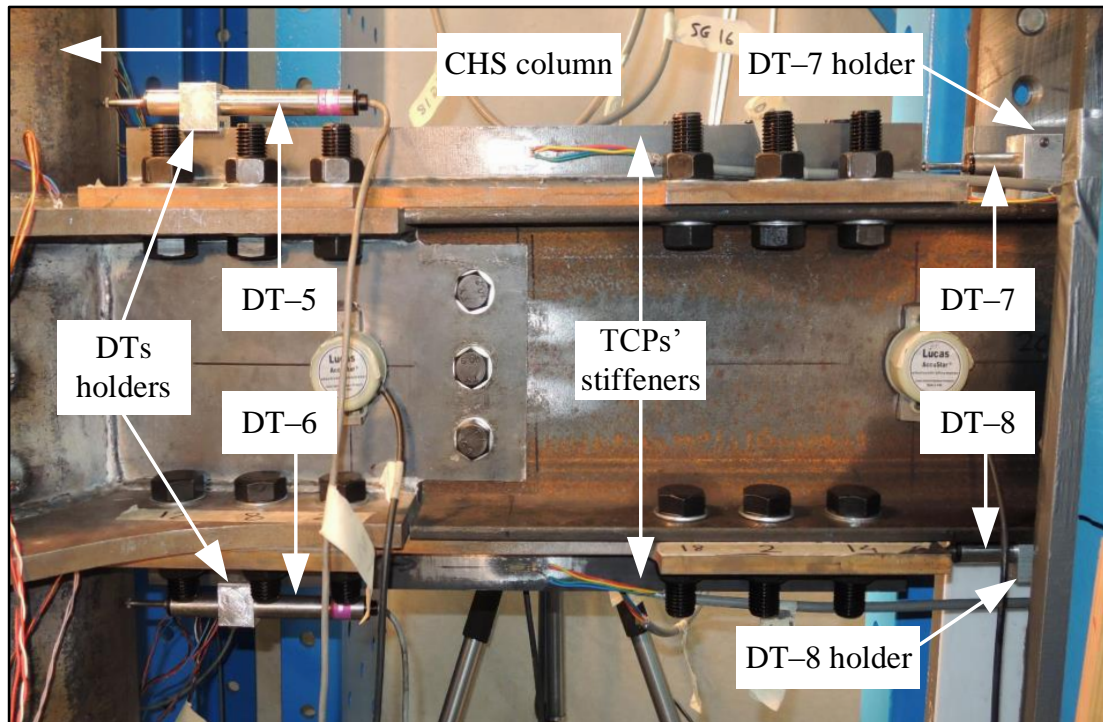
The angular deformation of the column web panel was calculated by dividing the difference between the measurements from DT-2 and DT-3 by the vertical distance of 110mm separating them.

Figure 5.47 shows that the two transducers were held tightly in metal holders to keep them horizontal during testing. The holders were kept in place by connecting them to metal attachments glued to the column web panel face furthest from the connection. To fix these metal attachments firmly to the column curved surface, they were manufactured to have a similar geometry to the attachment of INC-1 described in section 5.7.3. The tips of DT-2 and DT-3 were positioned against two thin plates welded to the ends of two 90 degree angle bars. The other ends of the two bars were welded to square plates glued to the web stub at the reference points. This arrangement was constructed on the back face of the specimen to avoid congestion with other transducers and the wires of SG-1 to SG-3 that are on the front face.

DT-5 and DT-6 were used to measure the relative deformation and connection slippage between the tapered cover plates and the diaphragm plates. Figure 5.48 shows that DT-5 was held tightly in a holder glued to the upper surface of the top TCP stiffener. With no stiffener, DT-5 was attached to the upper surface of the cover plate itself. Both transducers were kept horizontal and centrally aligned with their TCPs during testing.

DT-5 was set initially at its mid-stroke and its tip was positioned against the column surface. This fixing arrangement of DT-5 allowed its measurements to represent the relative connection slippage between the top TCP and top DP. The fixing arrangement and set-up of DT-6 on the bottom TCP were identical to that of DT-5 on the top one.





**Figure 5.48:** *Locations of DT-5, DT-6, DT-7 and DT-8 on a test specimen*

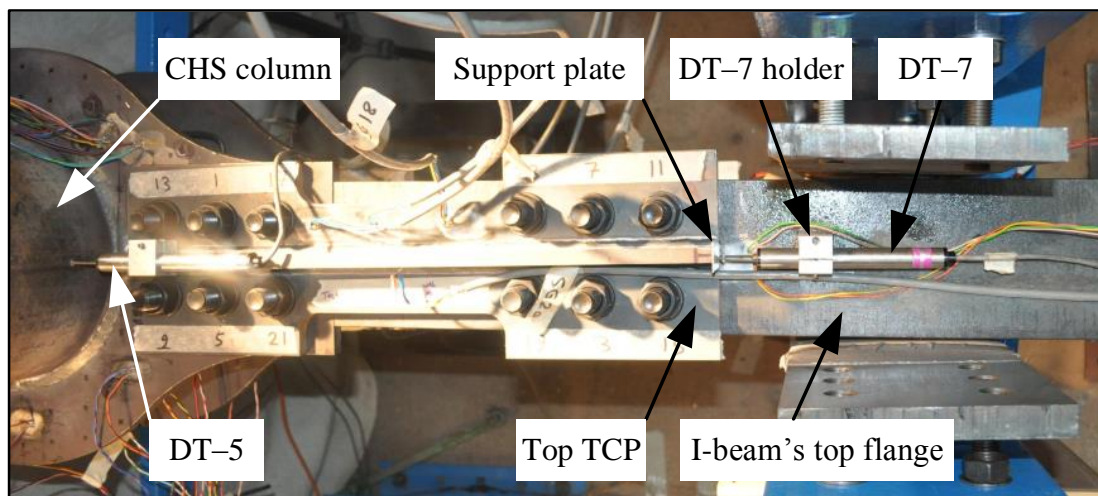


**Figure 5.49:** *Top view of the fixing arrangement of DT-7*

DT-7 and DT-8 were used to measure the relative deformation and connection slippage between the tapered cover plates and the I-beam flanges. Figure 5.49 shows that DT-7 was held tightly in a holder that was glued to the upper surface of the I-beam top flange to always keep the transducer horizontal and centrally aligned. DT-7 was set initially at its mid-stroke and its tip was positioned against a thin support

plate glued to the side face of the top TCP stiffener. For specimens with unstiffened TCPs, the support plate was glued to the central portion of the top TCP side face. This fixing arrangement allowed measurements of DT-7 to indicate the presence or absence of relative connection slips between the top TCP and the I-beam top flange. The fixing arrangement and set-up of DT-8 on the I-beam bottom flange were identical to that of DT-7.

The DTs used required only low voltage and current to function, which were provided by connecting them to the computer-based measurement hardware from National Instruments (NI). The eight displacement transducers were calibrated prior to the first test. Via the NI data-logging system and its software LabVIEW (2010), the author determined the relationship between their electrical outputs and changes in displacement (extensions of the DTs cores). The calibration results obtained allowed for a computational conversion of the DTs outputs to reliable displacements during cyclic testing.

The eight DTs were calibrated individually following the same steps; a DT was placed into the transducer mounting block and adjusted to the appropriate position as shown in Figure 5.50. The fitting bolts to the mounting block were tightened to securely hold the DT in position.

The position of the DT rod was adjusted five different times using slip gauges of known size, and the corresponding electrical outputs were recorded. Assuming the zero reference for displacements to be at the mid-stroke, the sign convention used in this calibration assumed displacements were positive when the DT rod was pushed inside the DT body and negative when it extended beyond the zero reference point. The 25mm-size DTs were calibrated for displacements in the range of [-5mm,

+5mm] at equal intervals of 2.5mm displacement; while the 50mm-size DTs were calibrated for displacements in the range of [-10mm, +10mm] at equal intervals of 5mm displacement.

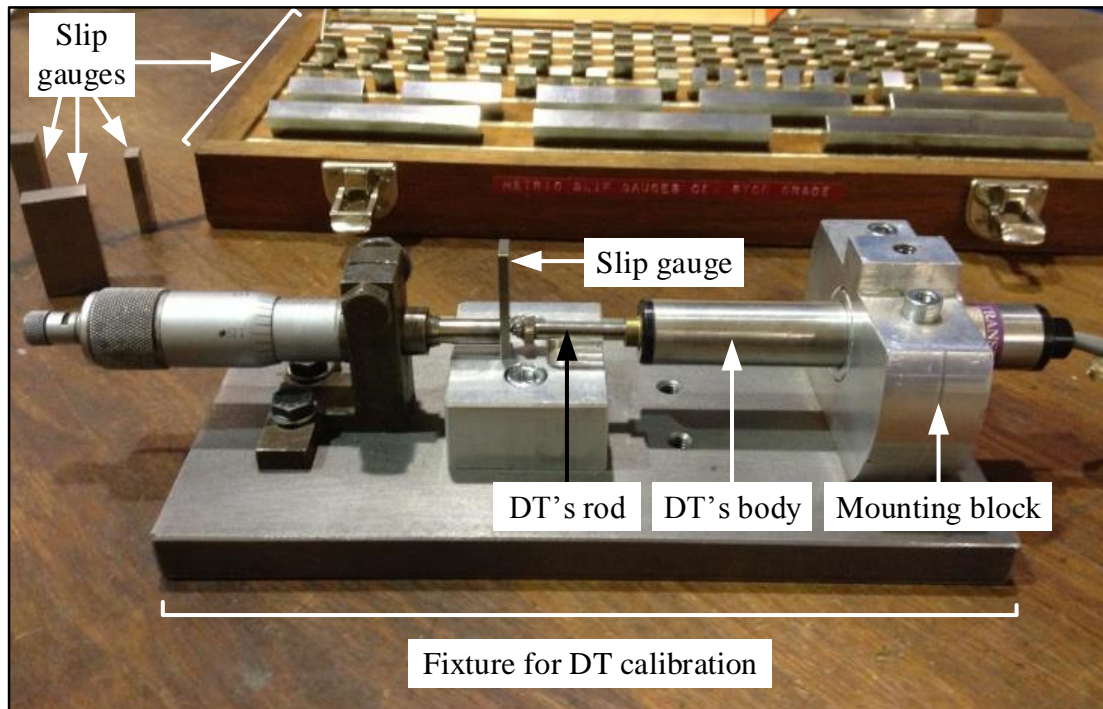


**Figure 5.50:** *Calibration of displacement transducers*

Calibration factors for each displacement transducer were obtained by analysing the linearly proportional relationship between the applied extensions to the DT core and the corresponding electrical outputs. The whole calibration process described above was repeated three times for each DT to minimise calibration errors and uncertainty by averaging the results of the three iterations. The calibration process was repeated for the eight DTs after the end of the experimental programme to check the reliability of their calibration factors that were used throughout the nine tests. It was found that the calibration factors did not change. Hence, the measurements obtained from the DTs were reliable and needed no modification.

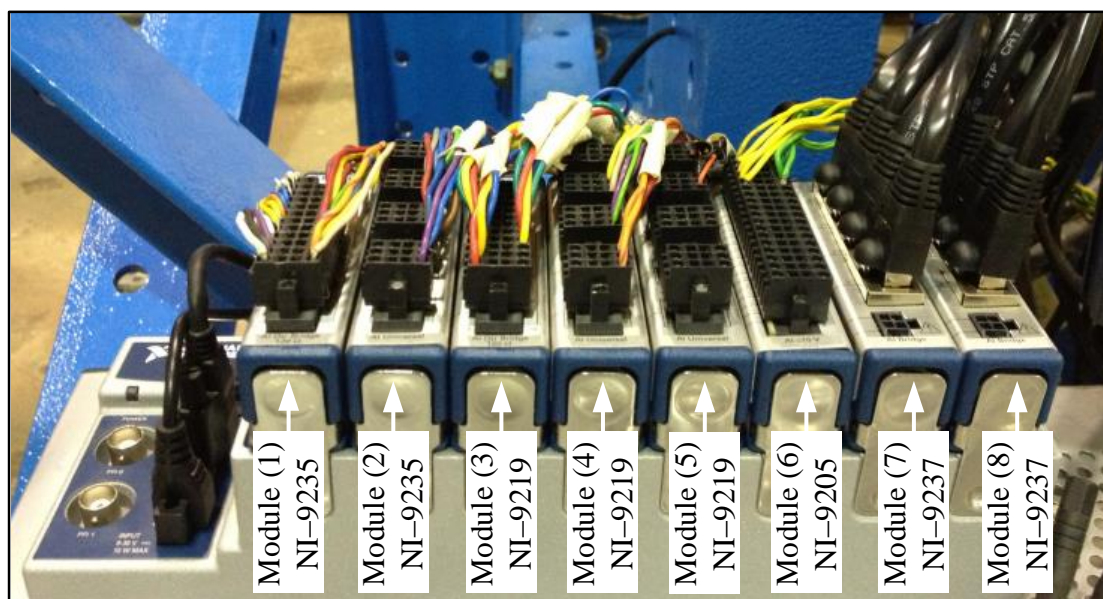
The sign convention for horizontal displacements in the actual tests was kept similar to the one used in the calibration of DTs. It was also assumed that horizontal displacements of the specimen towards its right end ( $\rightarrow$ ), when facing its front face, were positive; while displacements towards the left end of the specimen ( $\leftarrow$ ) were negative. This assumption, combined with the sign convention used for DTs, allowed the use of the calibration factors for DT-1, DT-4, DT-5, DT-6, DT-7 and DT-8 in the actual tests because these transducers were fixed to the test specimen pointing towards its left side; while the calibration factors for DT-2 and DT-3, which were mounted in the column web panel zone pointing towards the right end of the specimen, were multiplied by (-1) to unify the sign convention for all the DTs. Measurements of the eight DTs were logged to a computer and recorded during the tests through the NI data-logging system and its software LabVIEW (2010).

#### *5.7.5. Test-data logging*

Each of the instruments described in Subsections 5.7.1 to 5.7.4 was connected to its appropriate physical channel, either strain or voltage, in one of the eight measurement-hardware modules from National Instruments (NI), shown in Figure 5.51. Table 5.9 presents the type of the NI modules used in the tests, and the instruments connected to each of them. A computational programme was written using LabVIEW (2010), which is a graphical NI platform, to synchronise outputs from the instruments, apply the appropriate calibration factors, monitor the calibrated measurements on the front panel of LabVIEW during testing, produce plotted results to view during testing and to record all the results to a file saved on the test-computer. Figure 5.52 shows photographs of the test-computers and the front panel of the testing programme built in LabVIEW. The LabVIEW block diagram (graphical code) of the test programme is presented and explained in Appendix A.

**Table 5.9:** *Instruments connections to the National Instruments hardware modules*

Number of NI module	Type of NI module	Instruments connected	Type of measurement
1	NI-9235	8× Strain gauges (SG-1, 2, 3, 4, 5, 6, 7 and 8)	Strain
2	NI-9235	8× Strain gauges (SG-9, 10, 11, 12, 13, 14, 15 and 16)	Strain
3	NI-9219	4× Strain gauges (SG-17, 18, 19 and 20)	Strain
4	NI-9219	4× Strain gauges (SG-21, 22, 23 and 24)	Strain
5	NI-9219	Actuator built-in load cell and displacement transducer	Voltage
6	NI-9205	5× Inclinometers (INC-1, 2, 3, 4 and 5)	Voltage
7	NI-9237	4× 25mm displacement transducers (DT-1, 2, 3 and 4)	Strain
8	NI-9237	4× 50mm displacement transducers (DT-5, 6, 7 and 8)	Strain

**Figure 5.51:** *The measurement hardware modules from National Instruments*

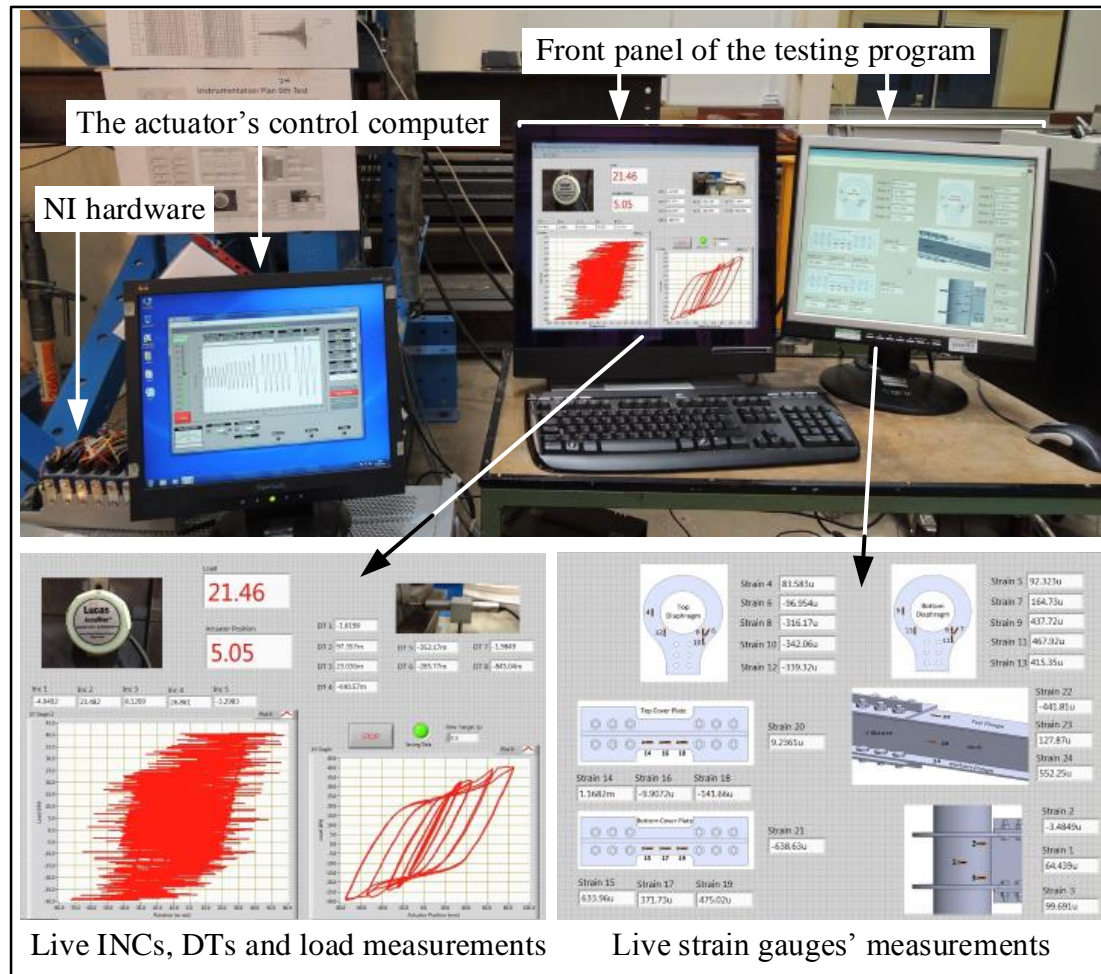


**Figure 5.52:** *The front panel of the testing program*

## 5.8. Concluding remarks

This chapter presents the laboratory preparations carried out prior to the full-scale testing of the nine joints. The assembling process of a test specimen and the arrangement of the test rig are detailed. The geometry and geometry imperfection measurements of the specimens components are found to fall within the tolerance ranges specified in the relevant standards. The planning and application of the cyclic loading protocol, instrumentation and data-logging are covered too. The nine beam-to-column joint tests were conducted after finishing all the preparation work. The tests results and their analysis are presented in the next chapter.

# *Chapter 6*

## *Experimental Results and Discussion*

### *6.1. Introduction*

This chapter covers a comprehensive analysis of the results from the nine joint experiments. Section 6.2 presents the tests results, including stress levels in the different joint components, failure modes, hysteretic responses, energy dissipation and initial rotational stiffness of the joints. Section 6.3 reports the observations of comparing different results in pairs to understand the influence of the different parameters investigated in this experimental programme on the overall joint hysteretic response and energy dissipation.

During some of the tests, loud noise was heard hence these tests were stopped, for health and safety reasons, before completing the loading protocol introduced in Section 5.6. It was realised later that the noise was caused by the damages to the PTFE sheets as a result of high friction between them and the I-beam. The number of completed cycles for each test is presented in Table 6.1.

In each comparison, the results were considered up to the maximum loading cycle that was reached in both tests. For example, when comparing the results of Test–1 and Test–2, those from Test–1 were considered up to the end of cycle 28 to match the same number of cycles achieved in Test–2. To avoid confusion in any results representation, tests were referred to with their labels followed by the number of cycles considered in that representation. For example when Test–1 is compared to Test–2, the former is referred to as “Test–1: S235-OSH-NS-FP: 28 cycles” whereas the same test is referred to as “Test–1: S235-OSH-NS-FP: 30 cycles” when its results were presented independently.

**Table 6.1:** *The number of completed loading cycles for the nine joint tests*

Test number	Test label	Number of completed loading cycles
1	S235-OSH-NS-FP	30
2	S235-OSH-WS-FP	28
3	S235-NSH-WS-FP	30
4	S355-OSH-NS-FP	30
5	S355-OSH-WS-FP	26
6	S235-NSH-NS-FP	28
7	S355-NSH-NS-FP	26
8	S235-OSH-NS-HP	29
9	S355-OSH-WS-HP	30

## 6.2. *Tests results*

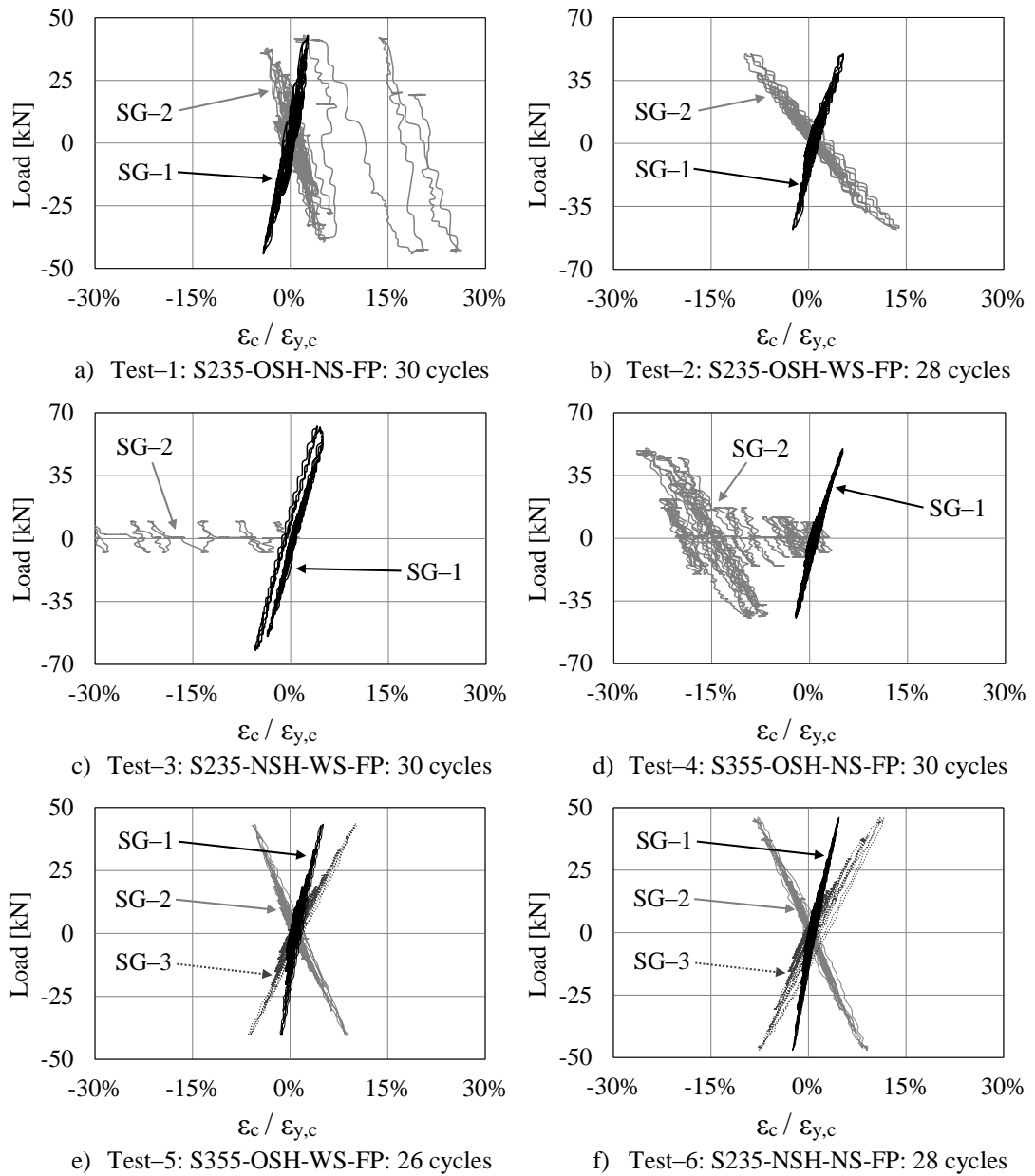
### 6.2.1. *Strain levels in the joint components*

This subsection presents the strain distribution in the joint components by means of strain and local deformations measurements captured by strain gauges, displacement transducers and inclinometers.



6.2.1.1. Column web panel

Strain measurements obtained from the strain gauges fixed on the column web panel zone during the nine tests are presented in the plots of Figure 6.1. The column web panel strain  $\epsilon_c$  was normalised by the yield strain of the CHS column steel ( $\epsilon_{y,c}$ ), which was determined to be 0.00176 from the tensile coupon tests. The loads from the actuator built-in load cell are plotted against the strain percentages ( $\epsilon_c / \epsilon_{y,c}$ ).



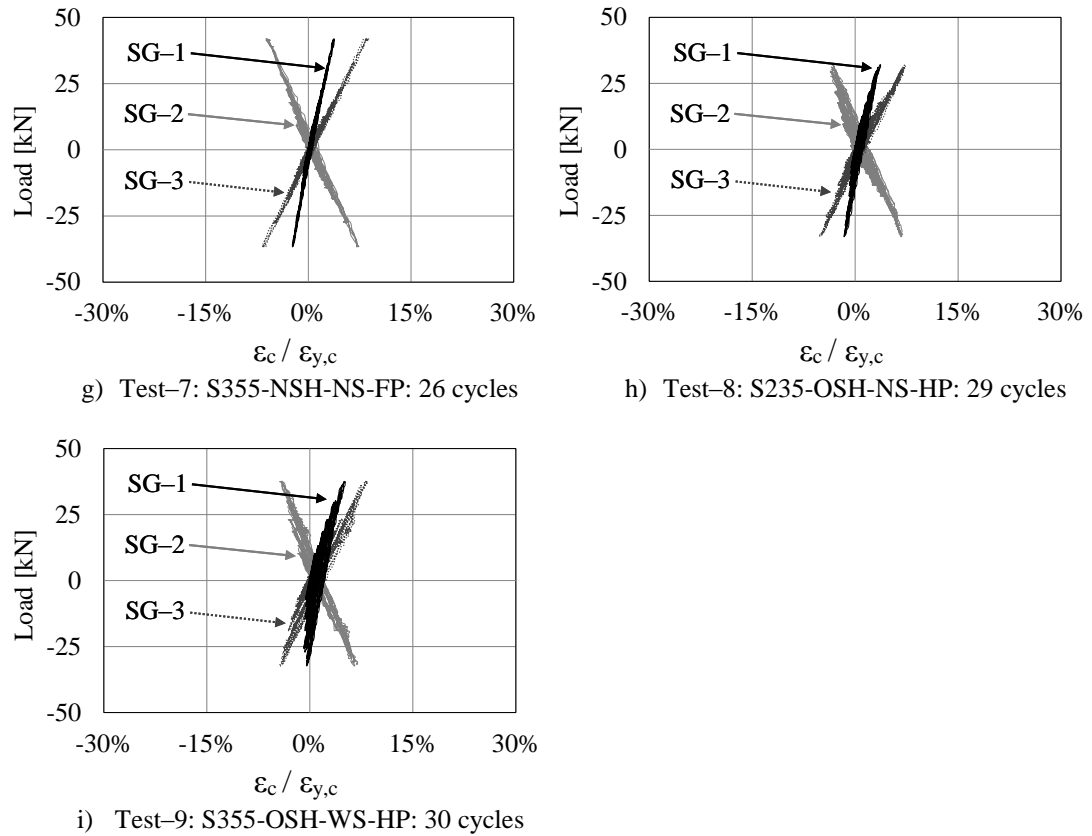


**Figure 6.1:** Load–strain curves of the column web panel in Tests 1–9

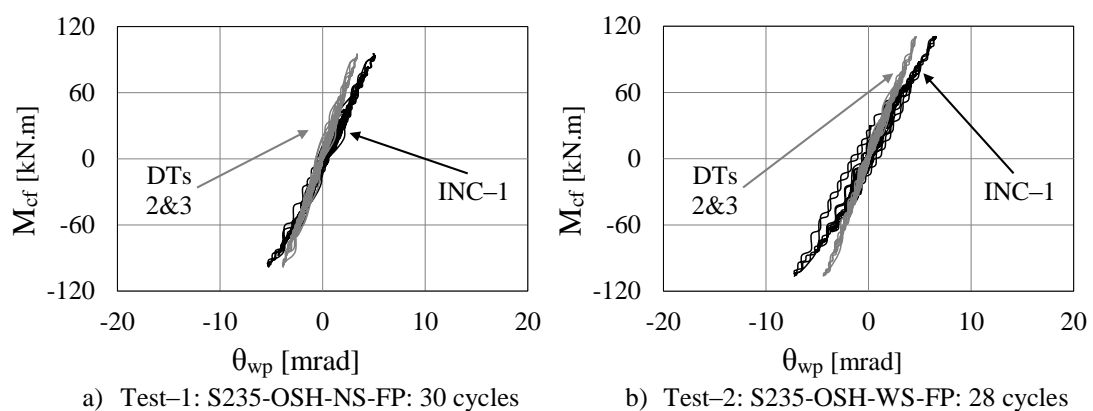
The locations of strain gauges SG-1 to SG-3 are detailed in Subsection 5.7.2. SG-1 and SG-2 were used in the first four tests (numbered 1 to 4) and SG-3 was added in tests numbered 5 to 9. As it can be seen from the SG-2 results in Figures 6.1(a, c and d), there are abnormal readings in tests 1, 3 and 4 causing its measurements to be unreliable. The plots also revealed that the maximum strain levels reached in the web panel zone were generally less than 10% of  $\varepsilon_{y,c}$ , which satisfied the design criterion of keeping the column web elastic throughout the cyclic loading protocol.

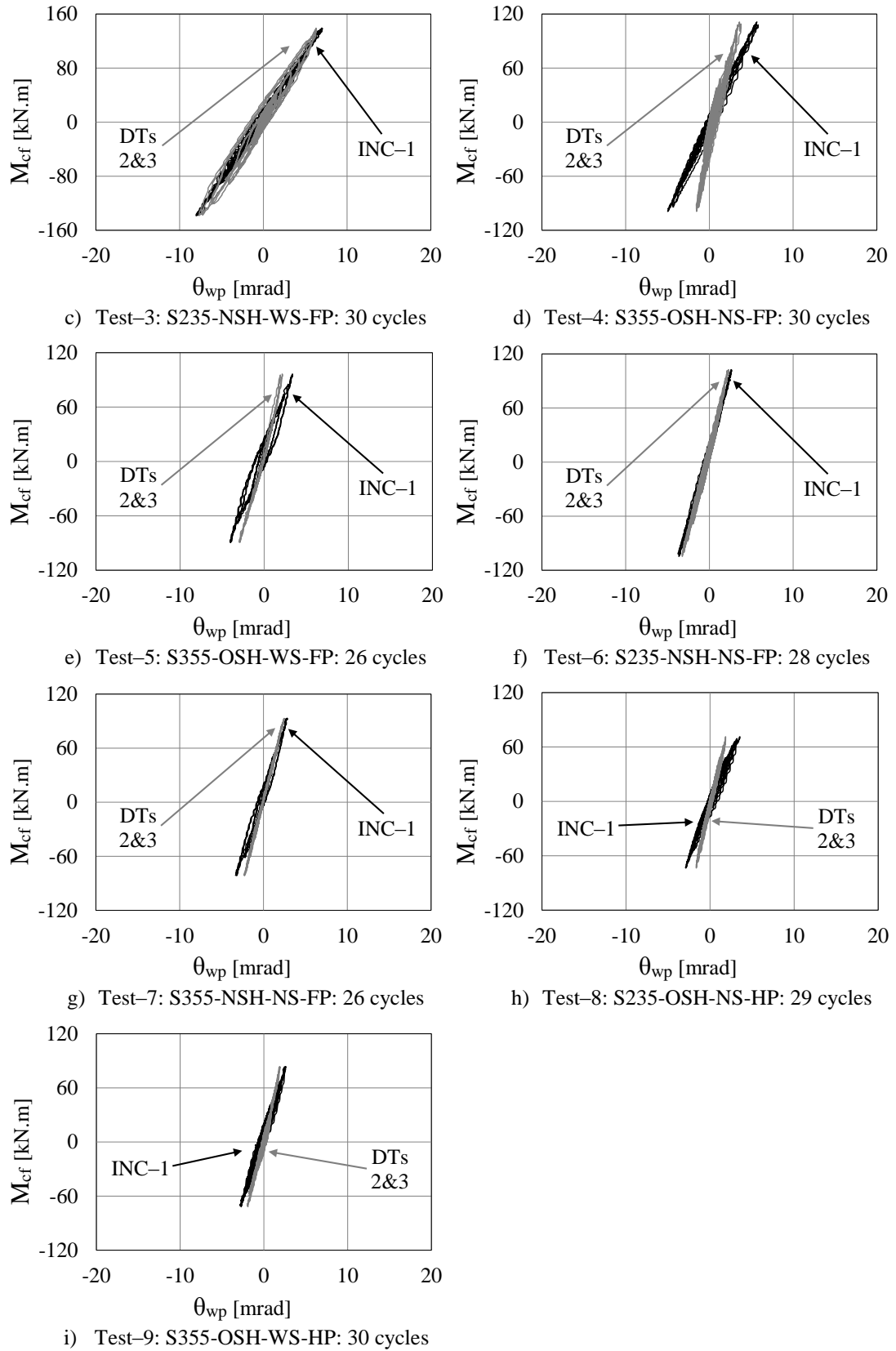
The performance of the web panel was further checked by examining its rotational response. Rotation of the web panel  $\theta_{wp}$  was calculated by subtracting from  $\theta_1$  the column hinges rotations, which are presented for the nine tests in Appendix B.

The displacement measurements obtained from the horizontal displacement transducers DT-2 and DT-3 were used to obtain rotation values of the web panel by dividing the difference between their measurements over the vertical distance between them.

Moments calculated at the column face  $M_{cf}$  were plotted against both  $\theta_{wp}$  calculated from  $\theta_1 - \theta_{c,h}$  and  $\theta_{wp}$  obtained using DT 2&3. The resulted plots for the nine tests are given in Figure 6.2 and they show that the moment-rotation relationship is linear. This confirms that the web panel only experienced elastic deformations for the loading protocol applied.

It can be also noted from these plots that  $\theta_{wp}$  obtained using DT-2 and DT-3 are slightly smaller than those obtained via INC-1 in most of the tests. This difference is believed to be mostly due to the inaccuracy of predicting the arm distance between the two transducers because the vertical distance between the DTs bodies was different to that between their holders or between their attachments. It is recommended to keep the vertical distance between the DTs equal to that between their attachments in any future work to improve the accuracy of the results.

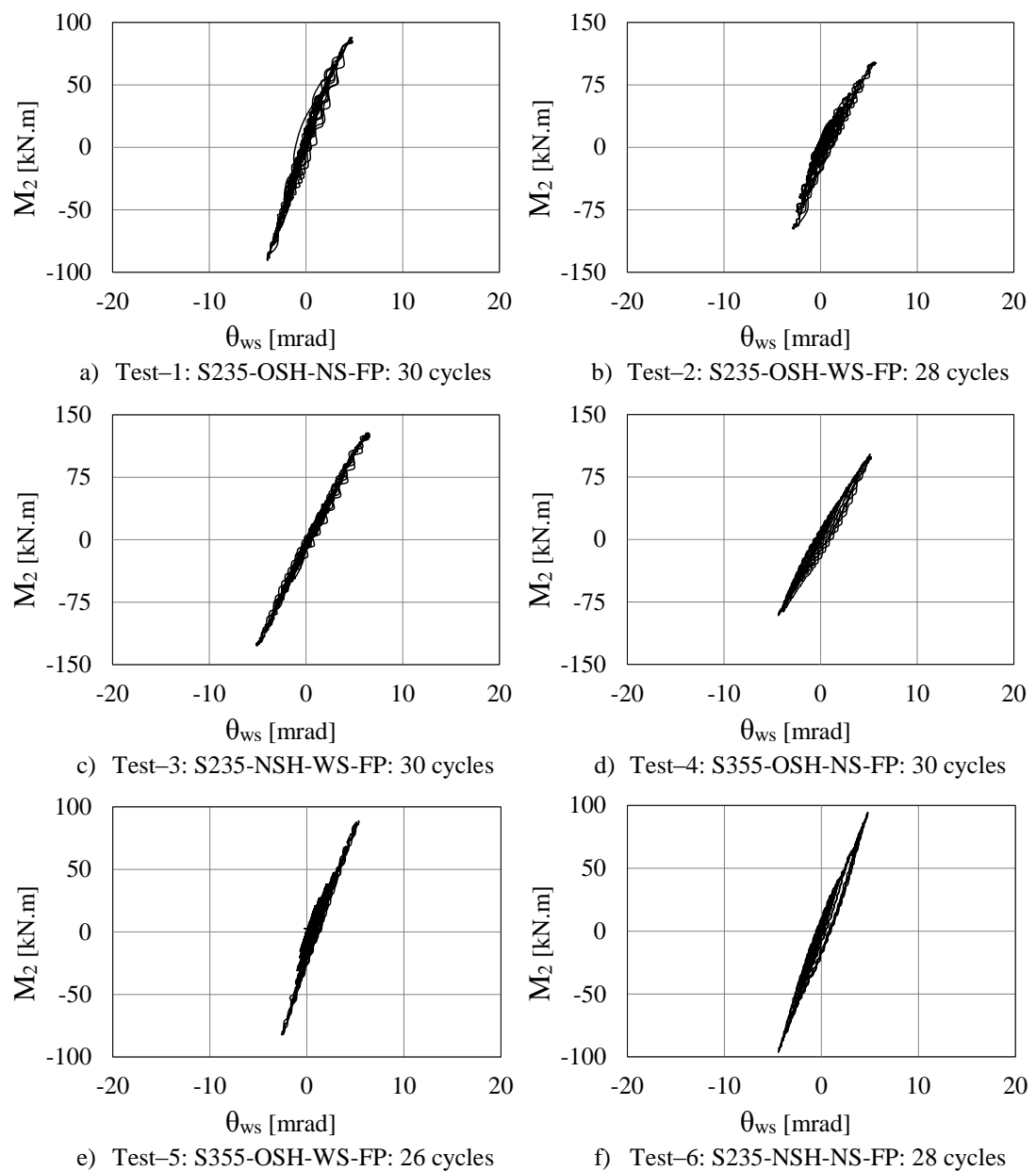




**Figure 6.2:** Local deformation of the column web panel in Tests 1–9

## 6.2.1.2. Web stub

The performance of the web stub was checked through examining its rotational behaviour. The rotation of the web stub  $\theta_{ws}$  was calculated from  $\theta_2 - \theta_1$ . The moment  $M_2$  calculated at the location of INC-2 is plotted against  $\theta_{ws}$  for the nice tests, as shown in the plots of Figure 6.3. The linear plots and the small maximum rotation of 6.6 mrad confirms that the web stub sustained elastic deformations only.



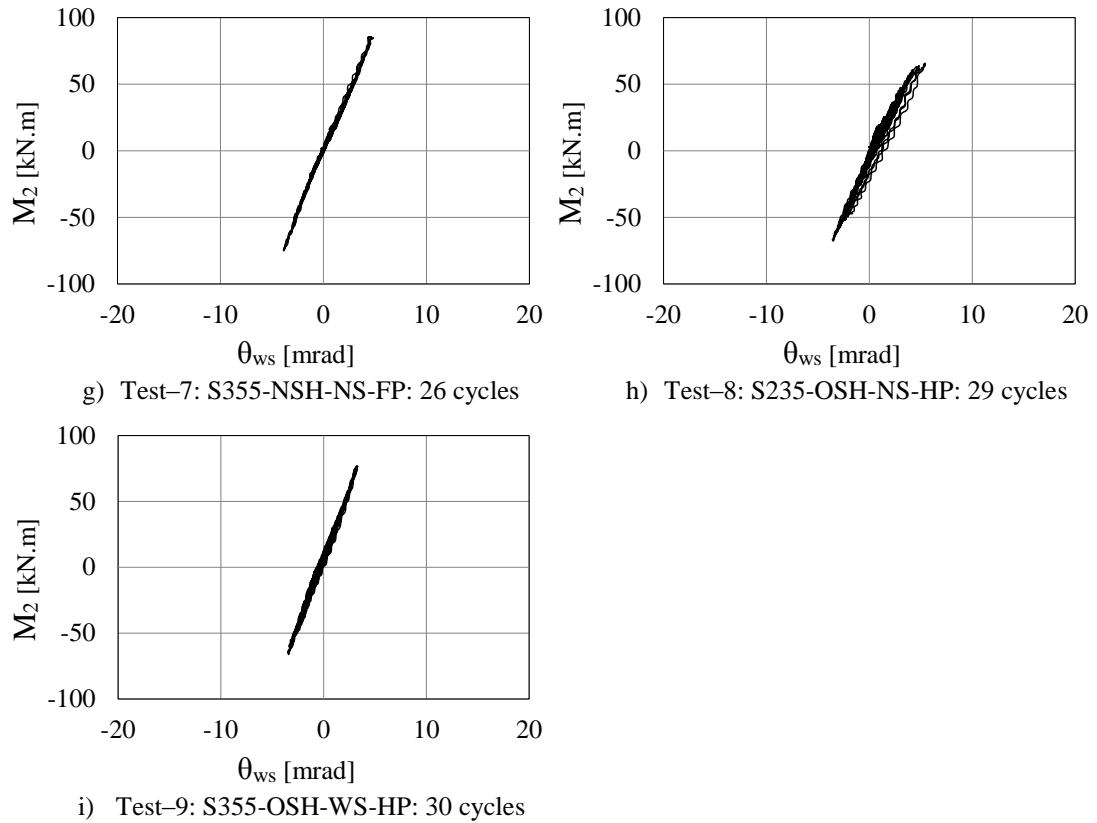
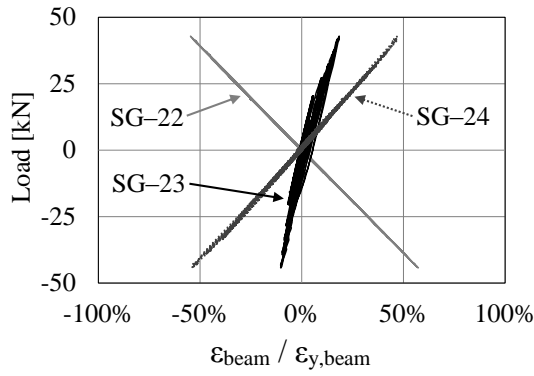


**Figure 6.3:** *Local deformation of the web stub in Tests 1–9*

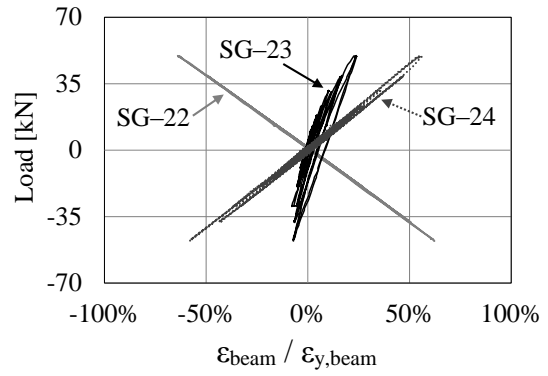
### 6.2.1.3. I-section beam: UKB 203×133×30

Strains  $\varepsilon_{\text{beam}}$  were obtained in the web and flanges in the I-beam critical section located next to the connection end by means of SG-22 to SG-24, see Figure 5.39. The locations of these axial strain gauges are detailed in Subsection 5.7.2. Strain measurements were normalised with respect to the beam yield strain ( $\varepsilon_{y,\text{beam}} = 0.00207$ ) obtained from the TC tests. Loads from the load cell are plotted in Figures 6.4 (a) to (i) against the strain percentages ( $\varepsilon_{\text{beam}} / \varepsilon_{y,\text{beam}}$ ) for the nine tests.

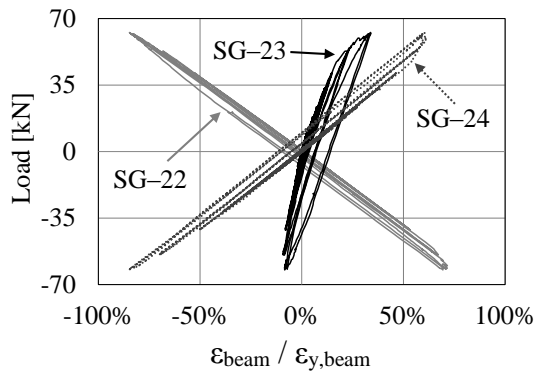
The plots reveal that  $\varepsilon_{y,\text{beam}}$  was not reached in the I-beam in the nine tests and so the beam was subjected to elastic deformations only. It can be seen from the strain results in Figure 6.4 that stress levels were not similar due to the use of different types of cover plates. The effect of using different types of TCPs on the strain level in the I-beam is detailed in Section 6.3.



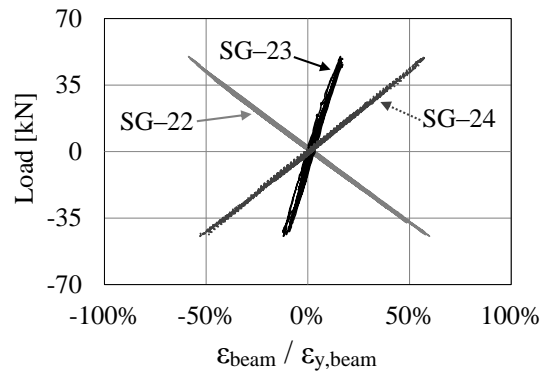
a) Test-1: S235-OSH-NS-FP: 30 cycles



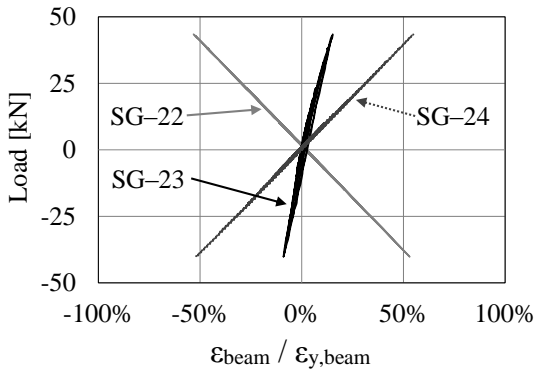
b) Test-2: S235-OSH-WS-FP: 28 cycles



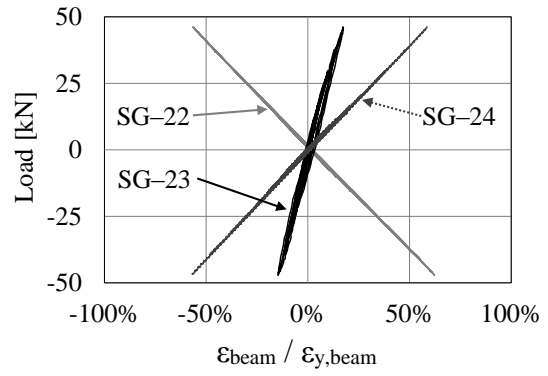
c) Test-3: S235-NSH-WS-FP: 30 cycles



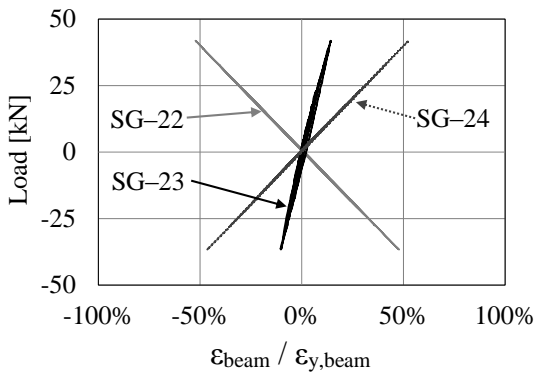
d) Test-4: S355-OSH-NS-FP: 30 cycles



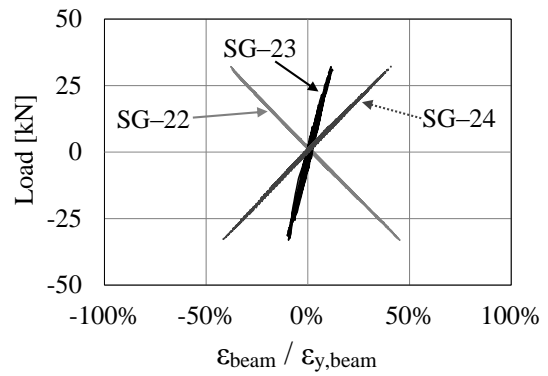
e) Test-5: S355-OSH-WS-FP: 26 cycles



f) Test-6: S235-NSH-NS-FP: 28 cycles



g) Test-7: S355-NSH-NS-FP: 26 cycles



h) Test-8: S235-OSH-NS-HP: 29 cycles

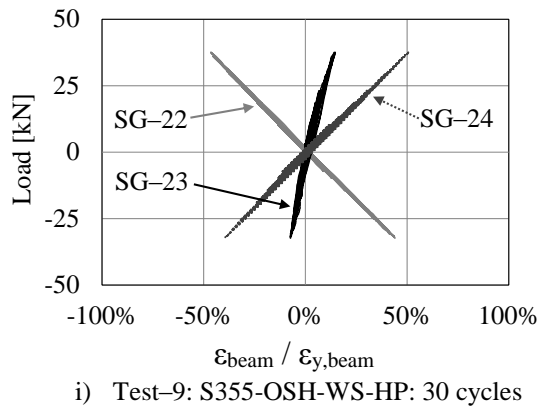


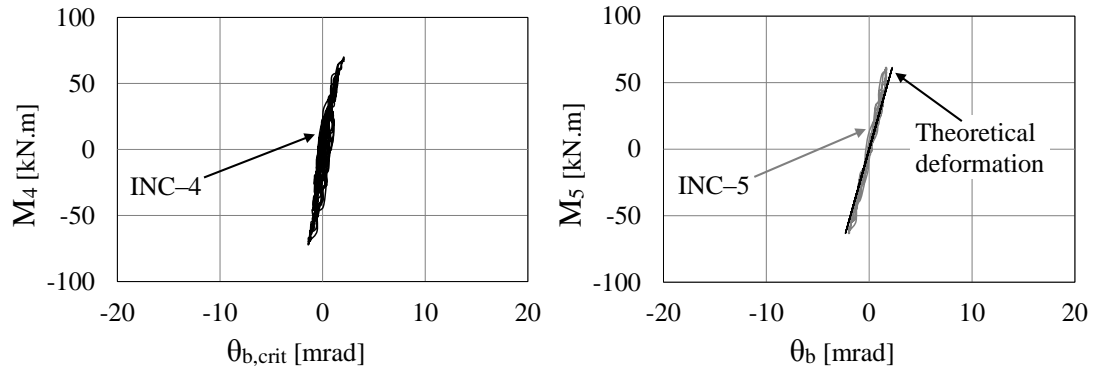
**Figure 6.4:** *Load–strain curves of the I-beam critical section in Tests 1–9*

Rotation measurements at the beam critical section  $\theta_{b,crit}$  were calculated from  $\theta_4 - \theta_3$ . Moments  $M_4$  calculated at the location of INC-4 (at the end of the connection) are plotted against  $\theta_{b,crit}$  for the nine tests, and referred to as “INC-4” in Figure 6.5. The curves are seen to be linear and cover a range of small rotation values (less than 3 mrad). This confirms that all the deformations at the critical section were elastic.

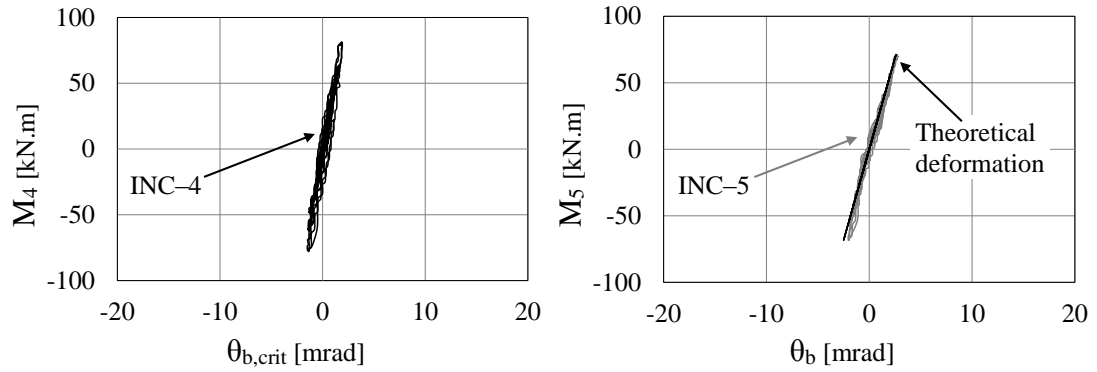
Similarly, the relative rotation of the I-beam  $\theta_b$ , between the section located at the end of the connection (location of INC-4) and the section located 200mm further (location of INC-5), was calculated from  $\theta_5 - \theta_4$ . Moments  $M_5$  calculated at the location of INC-5 are plotted against  $\theta_b$  for the nine tests, and referred to as “INC-5” in Figure 6.5. The curves are seen to be linear and the maximum rotation achieved is 2.6 mrad. This indicates the occurrence of elastic deformations only.

To check the reliability of this finding, the theoretical elastic deformation of the I-beam between the locations of INC-4 and INC-5 was calculated assuming a cantilever beam fixed at one end. The analysis is detailed in Appendix C.  $M_5$  are also plotted against the theoretical elastic deformations in Figure 6.5. The resulted plots showed a very good agreement with the plots derived from tests results.

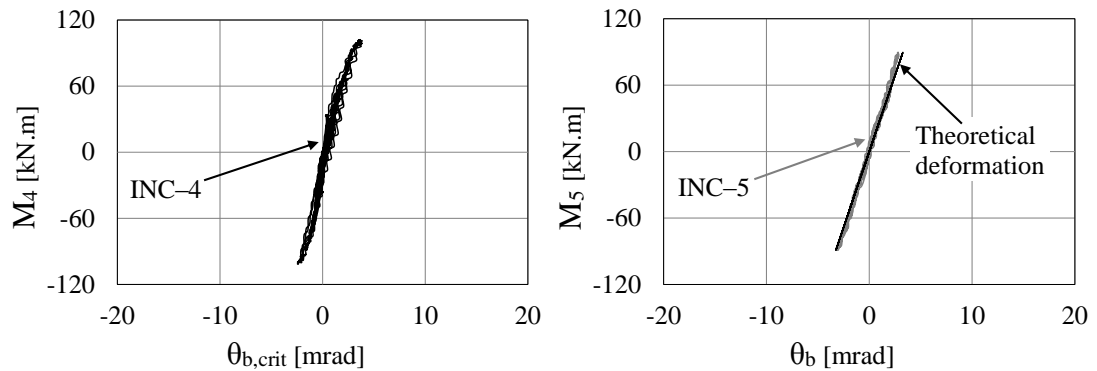




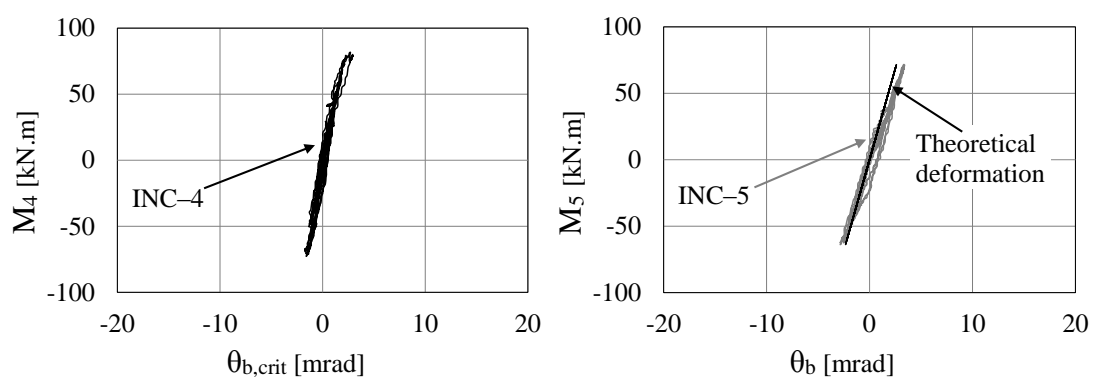
a) Test-1: S235-OSH-NS-FP: 30 cycles



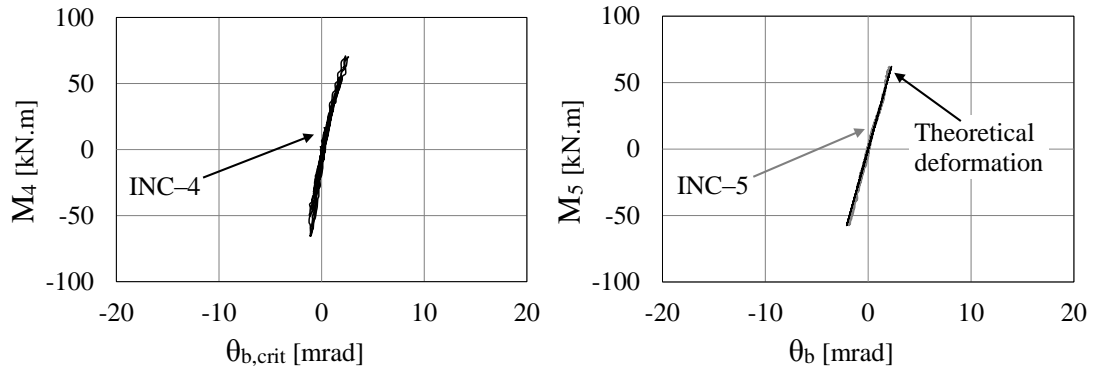
b) Test-2: S235-OSH-WS-FP: 28 cycles



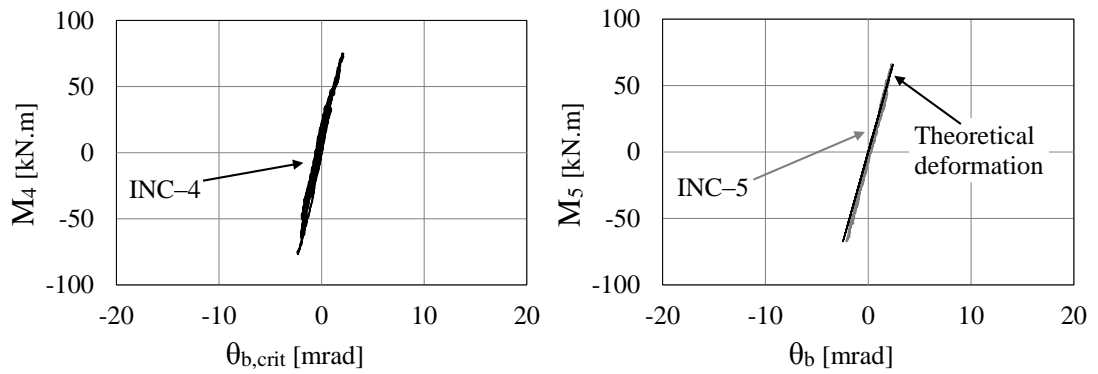
c) Test-3: S235-NSH-WS-FP: 30 cycles



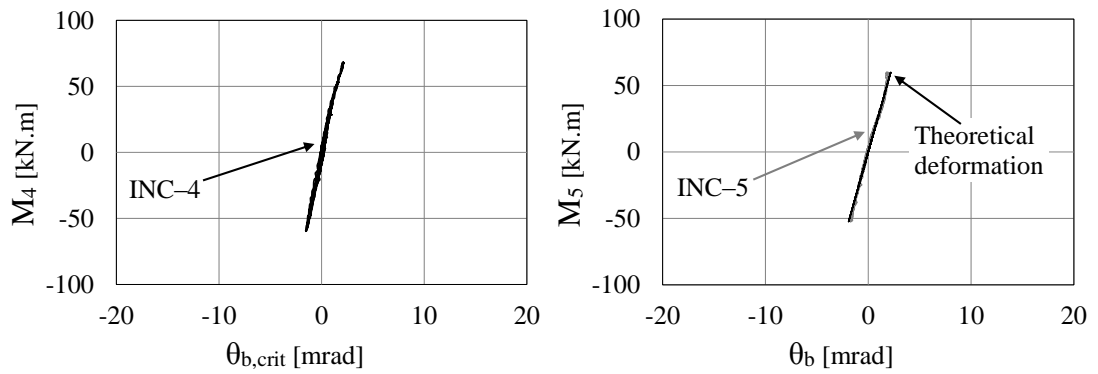
d) Test-4: S355-OSH-NS-FP: 30 cycles



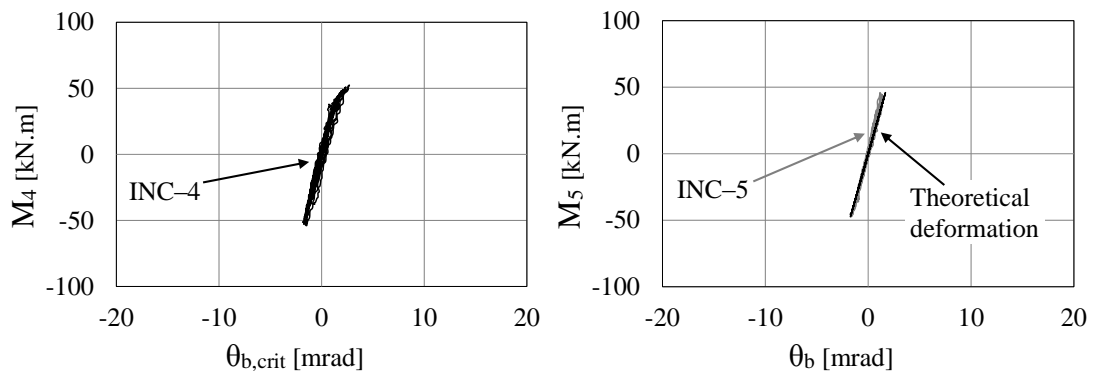
e) Test-5: S355-OSH-WS-FP: 26 cycles



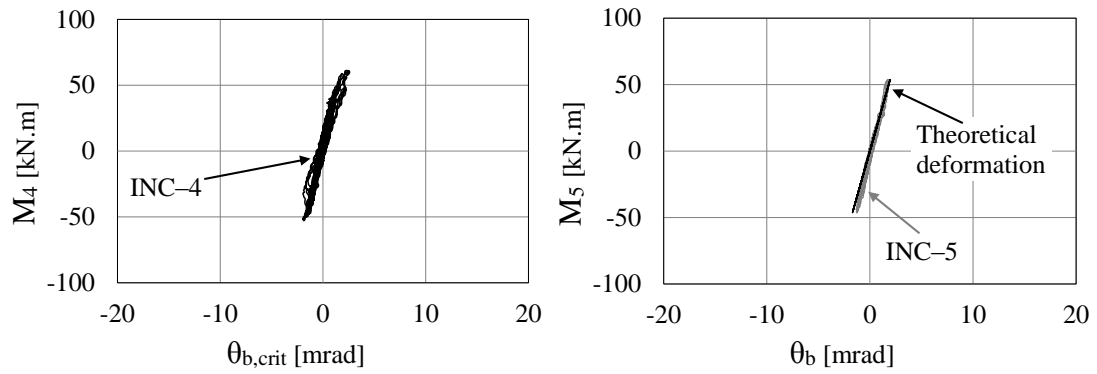
f) Test-6: S235-NSH-NS-FP: 28 cycles



g) Test-7: S355-NSH-NS-FP: 26 cycles



h) Test-8: S235-OSH-NS-HP: 29 cycles



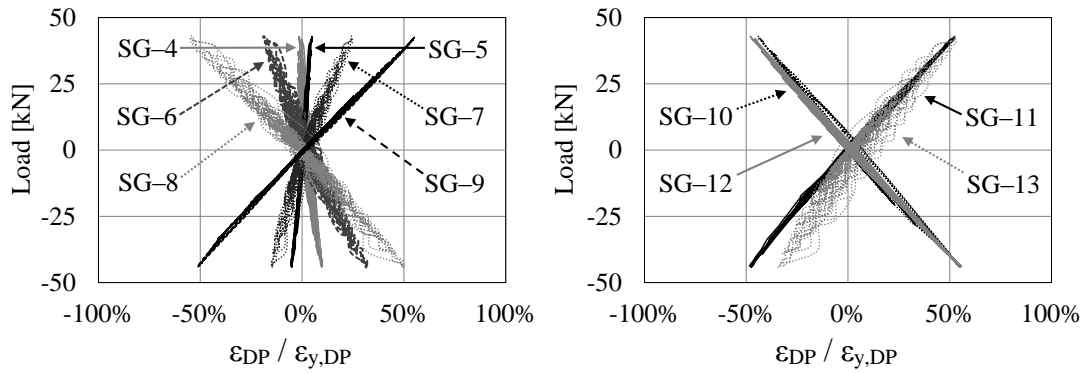
i) Test-9: S355-OSH-WS-HP: 30 cycles

**Figure 6.5:** *Moment-rotation curves of the I-beam in Tests 1–9*

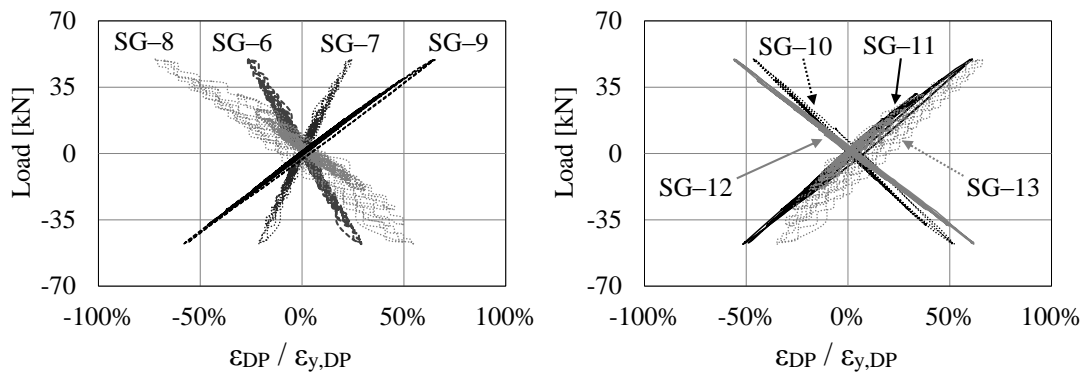
#### 6.2.1.4. Diaphragm plates

Strain measurements  $\varepsilon_{DP}$  from the ten strain gauges SG-4 to SG-13 on the two diaphragm plates are presented in the plots of Figure 6.6.  $\varepsilon_{DP}$  has been normalised by the yield strain of the DPs steel ( $\varepsilon_{y,DP}$ ), which was determined to be 0.00198 from the tensile coupon tests. Loads are plotted against the strain percentages ( $\varepsilon_{DP} / \varepsilon_{y,DP}$ ) for the nine tests. The locations of the strain gauges are detailed in Subsection 5.7.2.

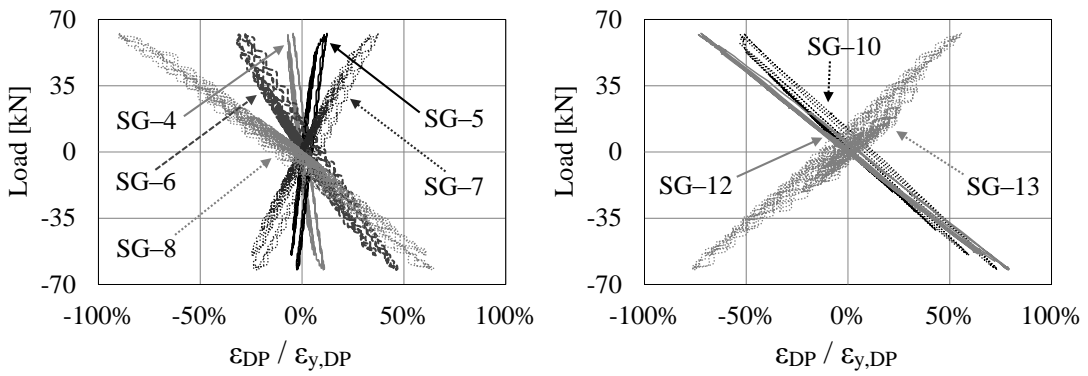
Some of the strain gauges showed abnormal readings in Tests 2, 3 and 4 and their measurements were not included in the plots of Figure 6.6 because they were considered unreliable. The strain results plotted in Figure 6.6 reveal that  $\varepsilon_{y,DP}$  was never reached in the diaphragm plates and so the DPs endured elastic deformations only. This finding is evidence that the author has satisfied the design criterion for the DPs. Stress levels in the DPs were not similar in all tests due to the use of different types of cover plates. The effect of using different types of TCPs on the strain level in the DPs is detailed in Section 6.3.



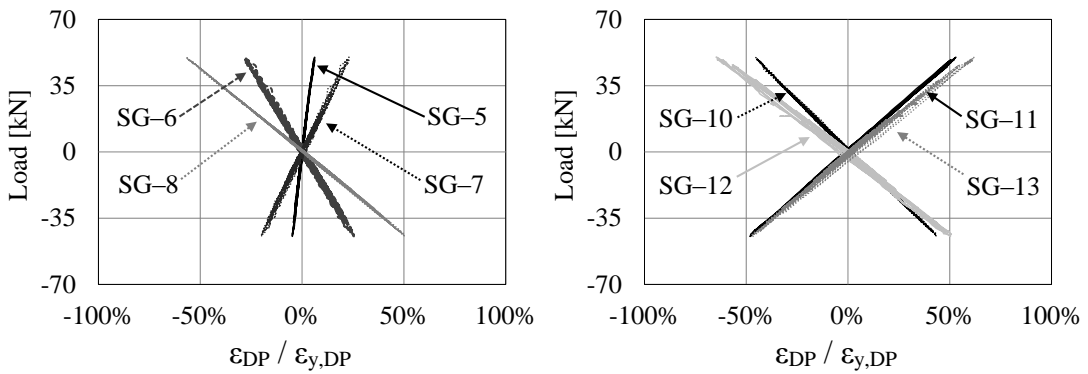
a) Test-1: S235-OSH-NS-FP: 30 cycles



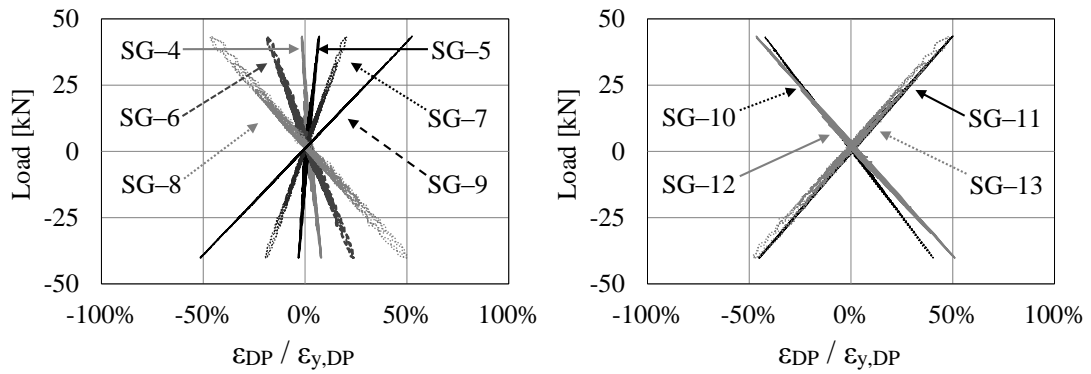
b) Test-2: S235-OSH-WS-FP: 28 cycles



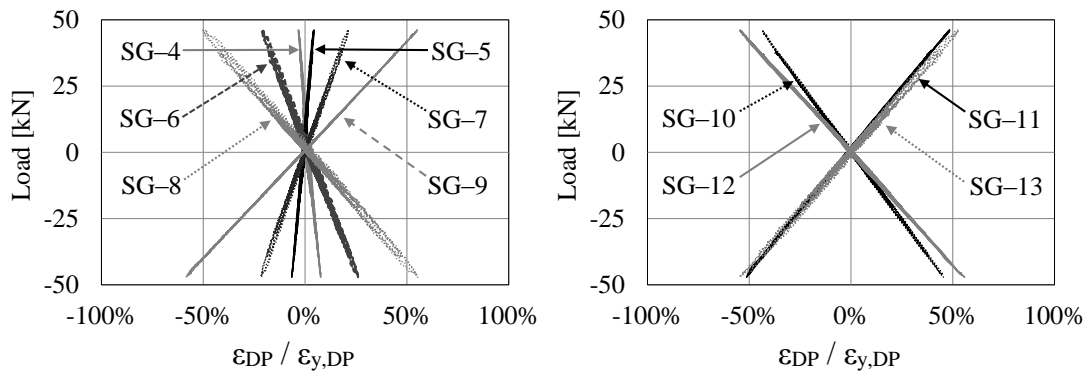
c) Test-3: S235-NSH-WS-FP: 30 cycles



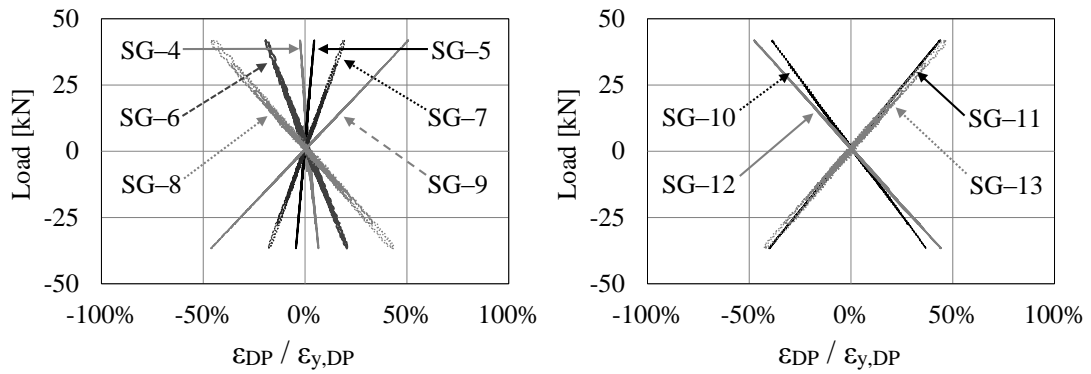
d) Test-4: S355-OSH-NS-FP: 30 cycles



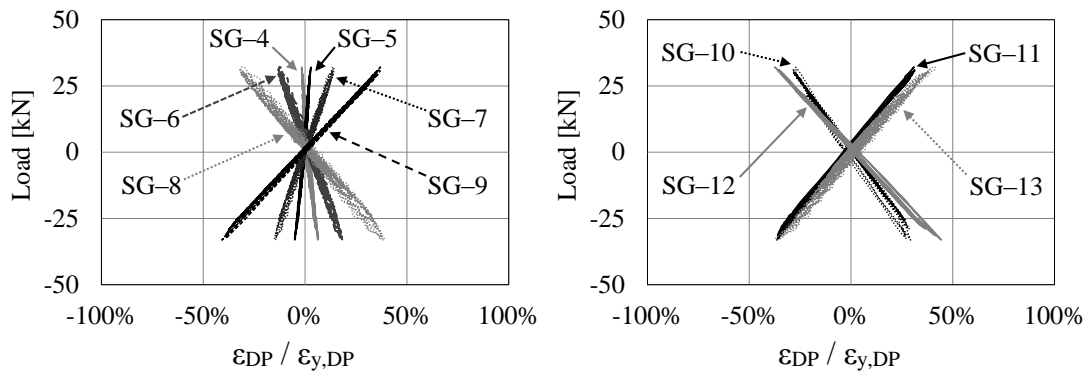
e) Test-5: S355-OSH-WS-FP: 26 cycles



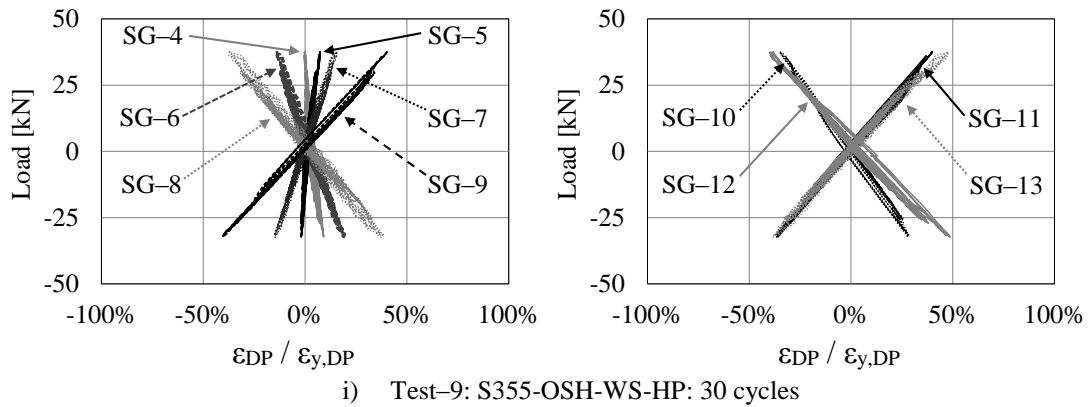
f) Test-6: S235-NSH-NS-FP: 28 cycles



g) Test-7: S355-NSH-NS-FP: 26 cycles



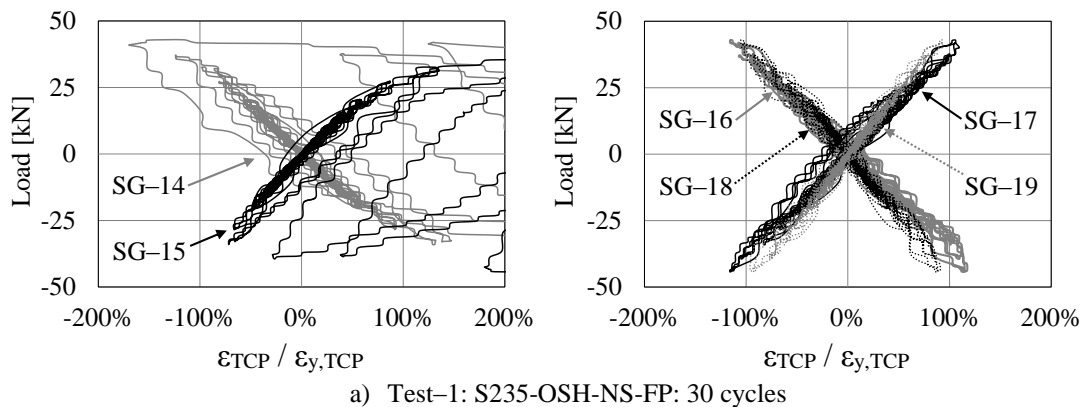
h) Test-8: S235-OSH-NS-HP: 29 cycles

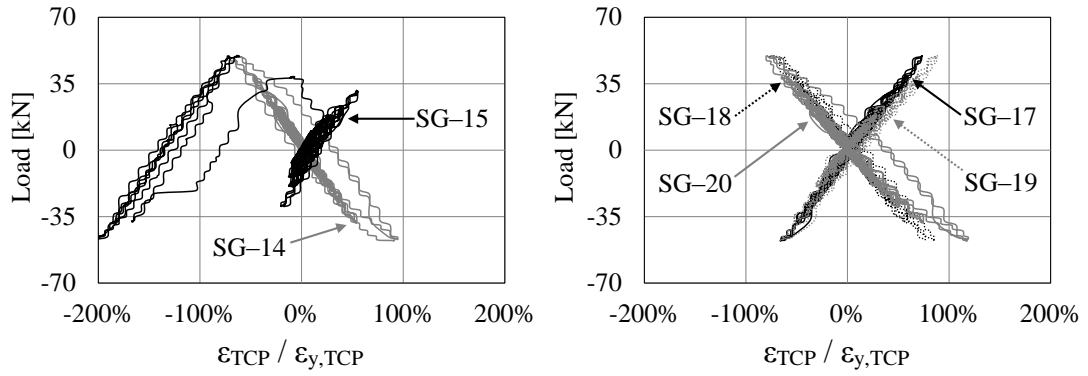


**Figure 6.6:** Load–strain curves of the diaphragm plates in Tests 1–9

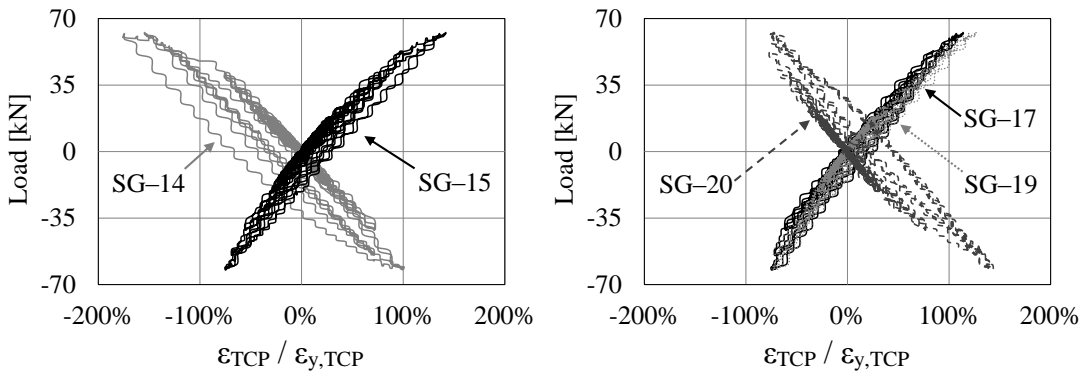
#### 6.2.1.5. Tapered cover plates

Strain measurements  $\varepsilon_{TCP}$  were obtained for the TCPs with and without stiffeners by means of eight strain gauges SG-14 to SG-21. Locations of the gauges are given in Subsection 5.7.2.  $\varepsilon_{TCP}$  were normalised with respect to the TCPs yield strain ( $\varepsilon_{y,TCP}$ ) obtained from the TC tests (0.00143 for steel grade S235 and 0.00195 for steel grade S355). Loads are plotted against the strain percentages ( $\varepsilon/\varepsilon_{y,TCP}$ ) in Figure 6.7. Abnormal readings were detected in Figure 6.7(b) from the plot of SG-15 in Test-2, and so its measurements were considered unreliable. This was also noted in the results of SG-16, SG-18 and SG-21 in Test 3 and SG-16 in Test 4, and so the curves of these gauges measurements were not included in the Figures 6.7(c) and (d).

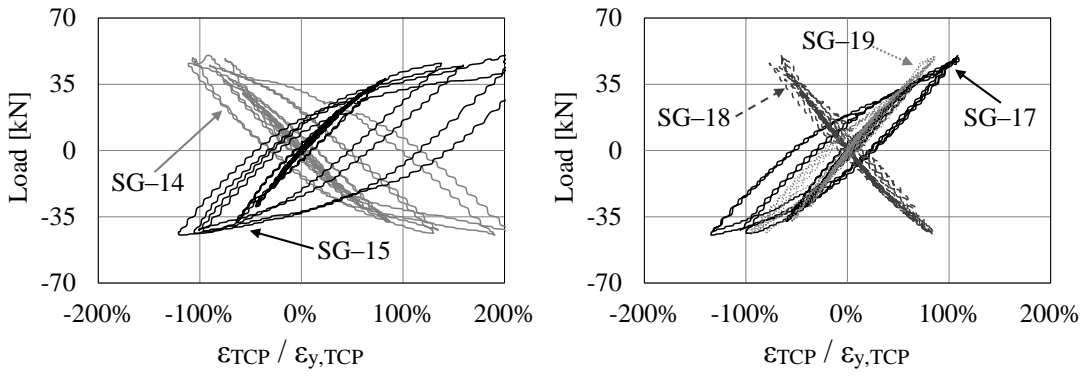




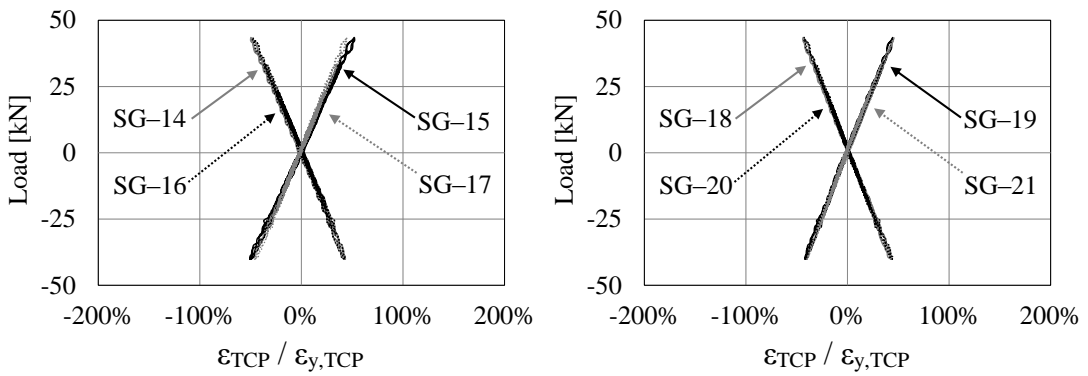
b) Test-2: S235-OSH-WS-FP: 28 cycles



c) Test-3: S235-NSH-WS-FP: 30 cycles



d) Test-4: S355-OSH-NS-FP: 30 cycles



e) Test-5: S355-OSH-WS-FP: 26 cycles

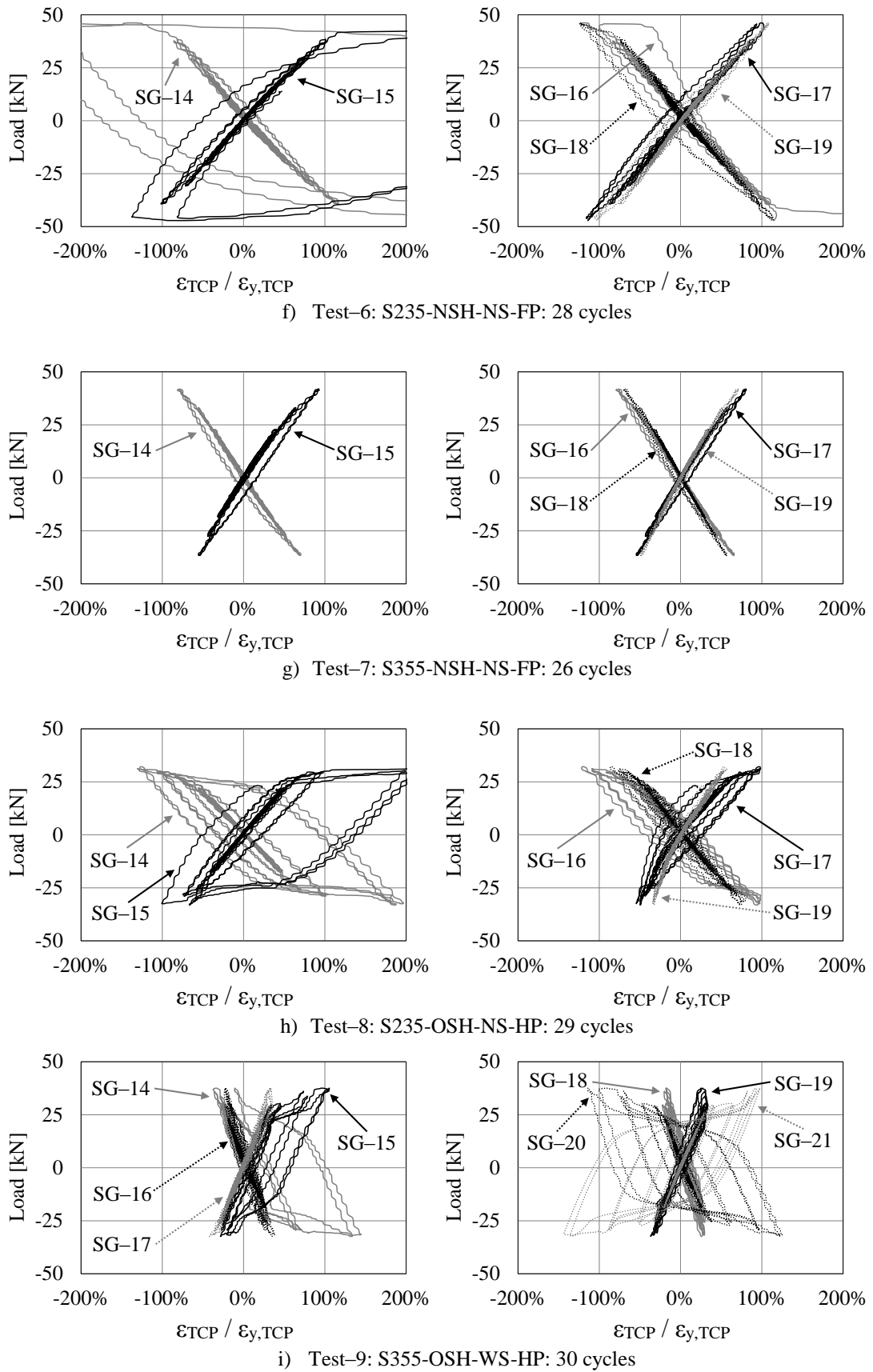


**Figure 6.7:** Load–strain curves of the tapered cover plates in Tests 1–9



The plots shown in Figure 6.7 reveal that strain levels in the reduced section areas of the TCPs reached  $\varepsilon_{y,TCP}$  in seven of the nine tests (Tests 1-4, 6 and 8-9), and that they were relatively significant compared to strain levels in the other joint components in Tests 5 and 7. This satisfied the design criterion of limiting yield in the joint to the TCPs whilst the rest of the joint components deformed within their elastic range. The normalised strain values in Figure 6.7 were limited to a range of -200% to +200% to keep the plots clear. This was justified because strain hardening was never reached.

### 6.2.2. *Failure mode*

As mentioned in Section 6.2.1, stress levels in the reduced sections of the TCPs are significantly higher than those in the other joint components in the nine tests. Yield onset in the TCPs has been detected in seven tests whilst the rest of the components remained elastic during testing. The maximum resistance of the joint was never reached in the nine tests. As Figure 6.8 shows, the onset of buckling failure in the reduced section area of the top TCP was observed at the beginning of the 29<sup>th</sup> loading cycle in Test-6: S235-NSH-NS-FP. Only twenty eight loading cycles were considered in the results presentation of Test-6 because this test was stopped before the end of its 29th loading cycle. No failure onset was observed in the other tests.

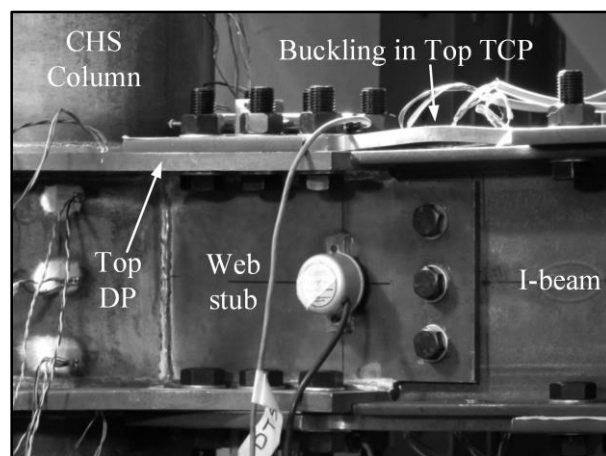


**Figure 6.8:** *Buckling in the top TCP in Test-6: S235-NSH-NS-FP*

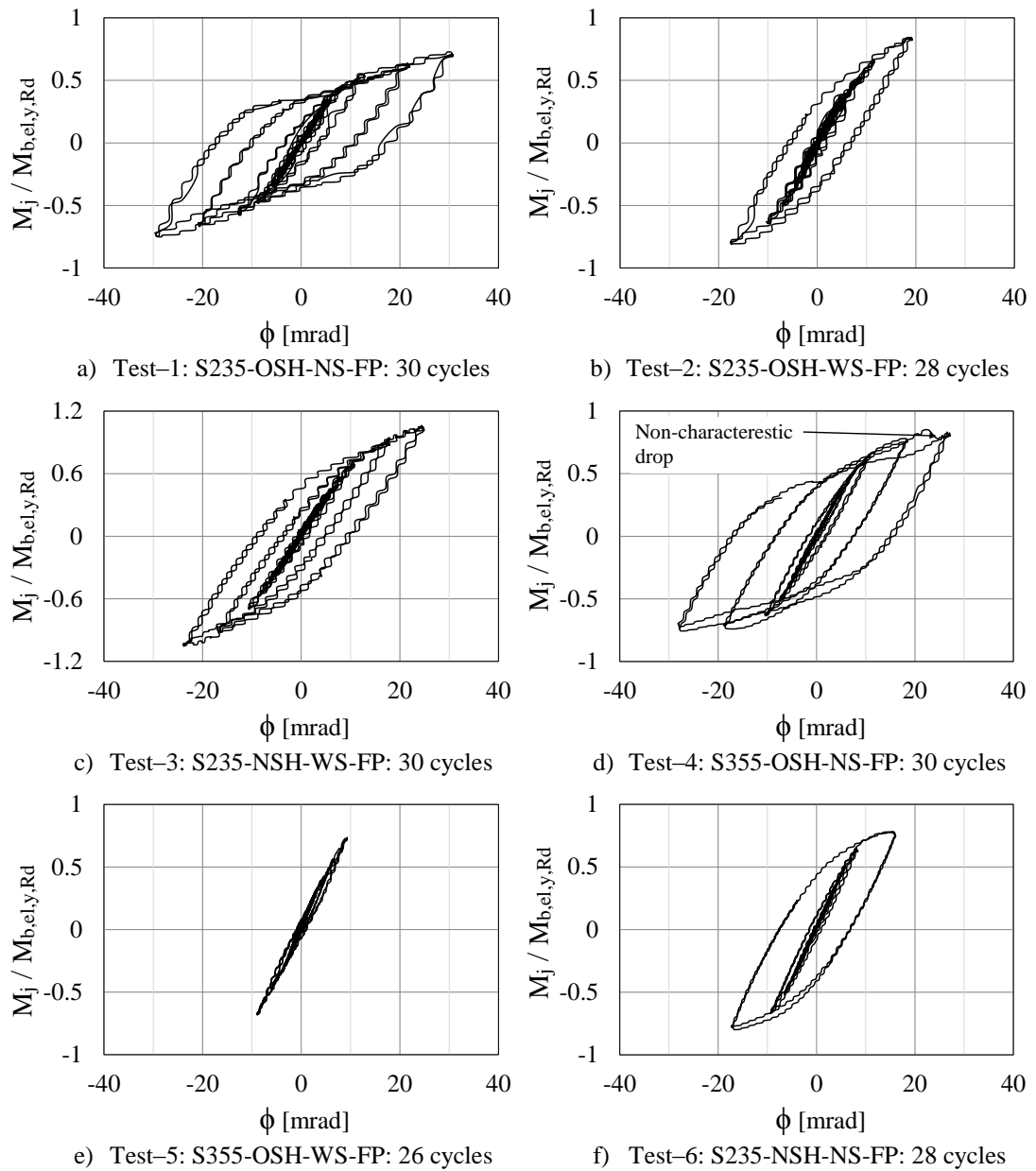
### 6.2.3. *Hysteretic response*

The main response parameters obtained from the nine tests are presented in Table 6.2. The joint moment  $M_j$  is calculated at the beam connected end and has been normalised by the design elastic bending resistance of the beam ( $M_{b,el,y,Rd} = 118 \text{ kN.m}$ ). Maximum joint moments  $M_{j,max}$  and their normalised values are reported in the third and fourth columns in Table 6.2. The joint rotation  $\phi$  is calculated from  $\theta_3 - \theta_{c,h}$ . The maximum joint rotations  $\phi_{max}$  are reported in the fifth column in Table 6.2. The sixth column in the table presents the joint moments at yield onset in the TCPs after being normalised by  $M_{b,el,y,Rd}$ . The normalised joint moments  $M_j / M_{b,el,y,Rd}$  were plotted against  $\phi$  to produce the joint hysteresis plots in Figures 6.9 (a) to (i).

**Table 6.2:** *The main response parameters obtained from the nine joint tests*

Test number	Test label	Maximum joint moment $M_{j,max}$ [kN.m]	Normalised maximum joint moment $M_{j,max} / M_{b,el,y,Rd}$	Maximum joint rotation $\phi_{max}$ [mrad]	Normalised joint Moment at the yield onset in TCPs
1	S235-OSH-NS-FP: 30 cycles	88.1	75%	30.8	50%
2	S235-OSH-WS-FP: 28 cycles	99.2	84%	19.3	72%
3	S235-NSH-WS-FP: 30 cycles	124.7	106%	24.9	81%
4	S355-OSH-NS-FP: 30 cycles	99.6	85%	28.1	71%
5	S355-OSH-WS-FP: 26 cycles	86.5	74%	9.3	–
6	S235-NSH-NS-FP: 28 cycles	93.8	80%	17.3	63%
7	S355-NSH-NS-FP: 26 cycles	83.4	71%	9.6	74%*
8	S235-OSH-NS-HP: 29 cycles	65.9	56%	32.6	50%
9	S355-OSH-WS-HP: 30 cycles	74.8	64%	31.2	63%

It can be noted from Test-7 results in Table 6.2 that the normalised joint moment at yield onset at 74% is higher than the normalised maximum joint moment at 71%. This is because Test-7 was stopped before the completion of its 27th loading cycle, which was the cycle for yield onset. All the other results for Test-7, including the  $M_{j,max}$ , are presented up to the end of the 26<sup>th</sup> cycle, which is the last completed loading cycle.



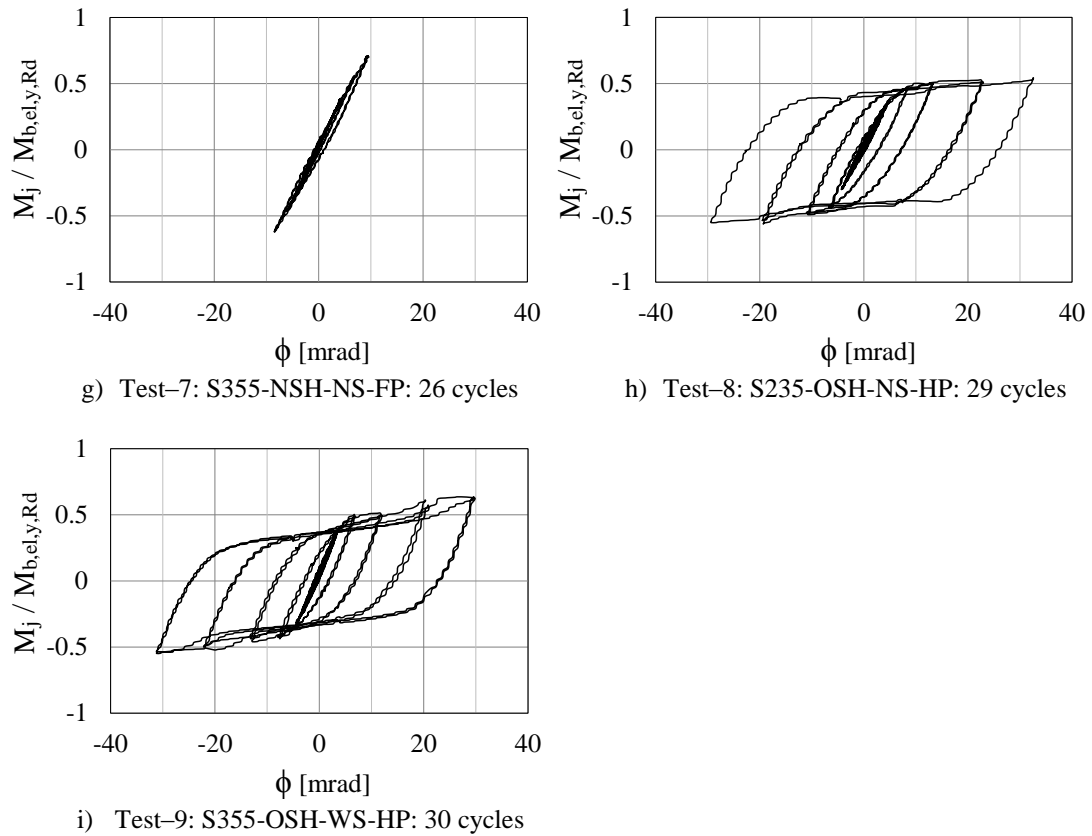
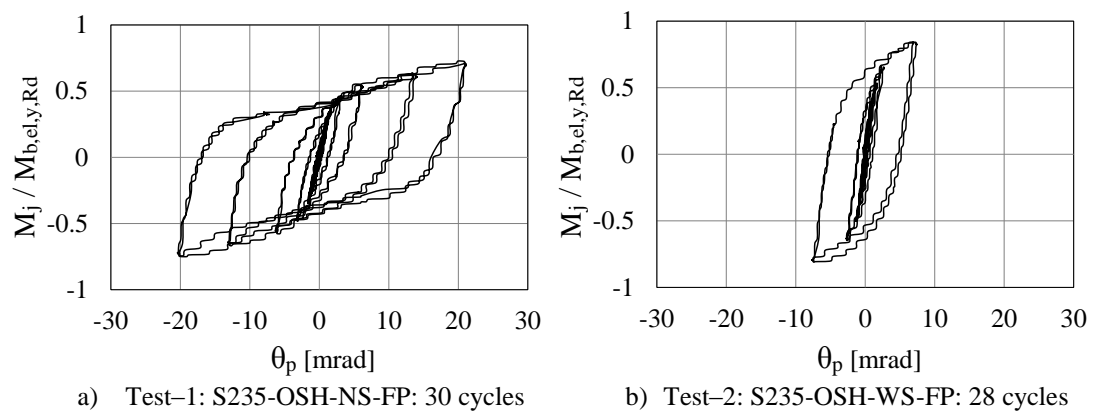


**Figure 6.9:** *Normalised moment-rotation curves of the joint in Tests 1–9*

It was noted during the tests that large inelastic cycles generated frictional forces between the beam and its lateral support plates (LSPs) on one side. This test feature could be a result of asymmetry issues in the test rig. In cycle 29 of Test-4, friction between the beam and the LSPs built-up a resistance to the beam cyclic movement, which was temporary, and which was released when PTFE sheets that cover the support plates were damaged. This undesirable stage in testing can be seen in the normalised  $M_j$ - $\phi$  curve, shown in Figure 6.9(d), where a sudden drop in  $M_j$  occurs. Thus, this moment drop was not considered a characteristic of the joint, such as strength degradation. To avoid similar scenarios in later Tests 5 to 9, extra care was taken by monitoring the distance between the beam and the LSPs during testing and adjusting the gap between them whenever needed.

It can be noted from the normalised  $M_j$ - $\phi$  results in Figure 6.9 that the joint exhibited stable hysteretic behaviour generally. Further analysis of the test results is presented in Section 6.3 to highlight the influence of using different types of TCPs on the overall joint performance to the cyclic loading protocol. The design moment resistance of the joint could not be determined from the experimental results because it is clear from the hysteresis loops in Figure 6.9 that no test joint reached its maximum strength.

For joints in dissipative moment resisting frames, BS EN 1998-1: 2004 specifies in Clause 6.6.4 (3) that the joint design should be that the rotation capacity of the plastic hinge region exceeds 35mrad for high ductility class (DCH) structures and 25mrad for medium ductility class (DCM) structures. This should be satisfied under cyclic loading without degradation of strength and stiffness greater than 20%. Furthermore, Clause 6.6.4 (5) states that the column web panel elastic deformation should not be included in the evaluation of the rotation capacity of the plastic hinge region. Since the web panel and the web stub deformed elastically in the nine tests, rotation of the plastic hinge region  $\theta_p$  is established from  $\theta_3 - \theta_2$ . Figures 6.10 (a) to (i) show normalised hysteresis plots for the plastic hinge region, which is in the reduced sections of TCPs.



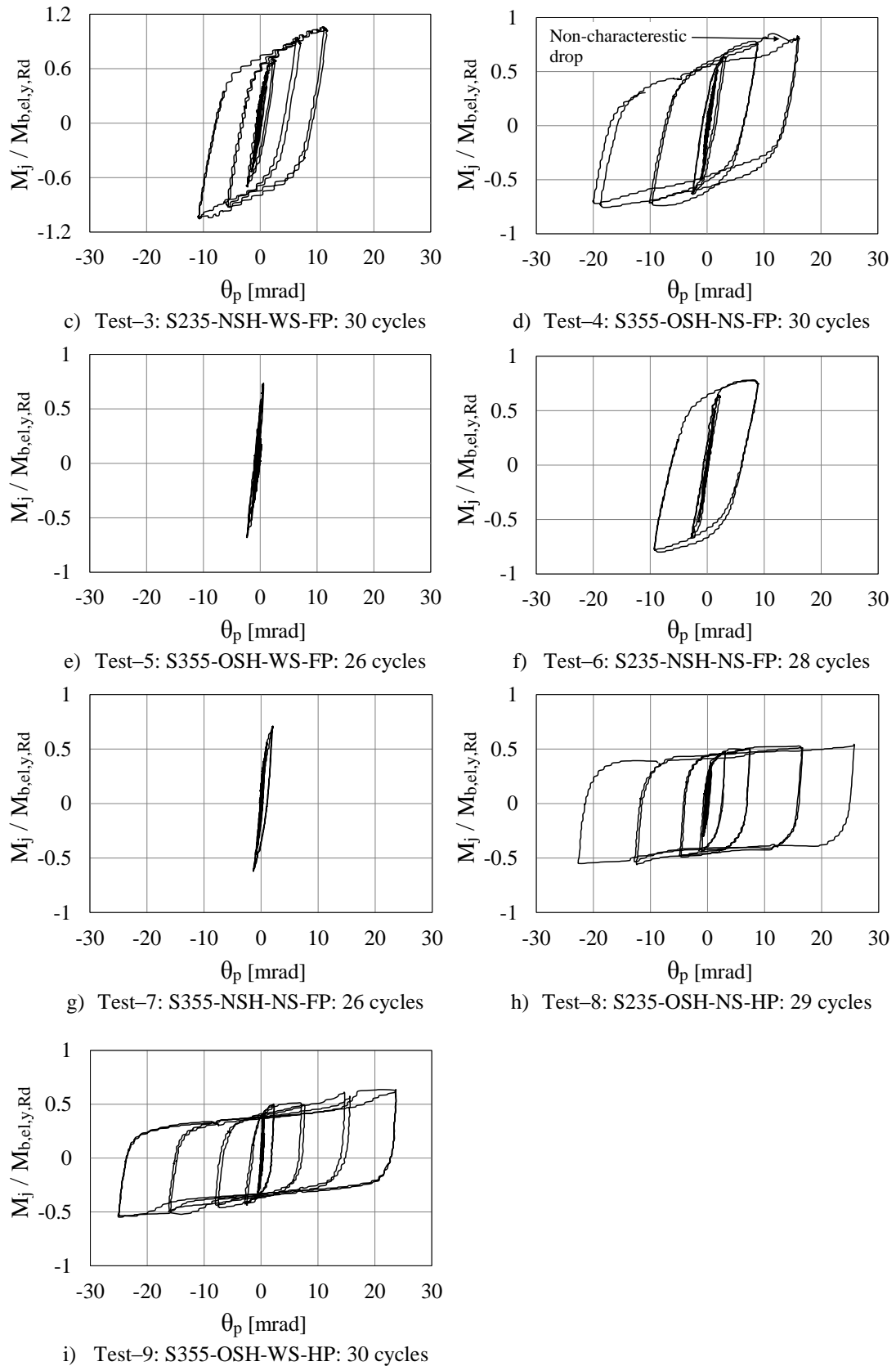


**Figure 6.10:** *Normalised moment-rotation curves of the plastic hinge region in Tests 1–9*

The plots in Figure 6.10 show that no degradation of strength or stiffness greater than 20% occurred in the nine tests, and thus the actual rotation capacity of either the plastic hinge region or the joint could not be obtained. Finite element analyses of the specimens can be used to determine these important joint parameters and overcome the limitation of the actuator stroke capacity in the laboratory experiments.

Table 6.3 reports the maximum rotation of the plastic hinge region  $\theta_{p,max}$  in the third column.  $\theta_{p,max}$  has been normalised by the minimum rotation capacity in the plastic hinge region for DCM structures ( $\theta_{p,DCM} = 25\text{mrad}$ ).  $\theta_{p,max} / \theta_{p,DCM}$  percentages are reported in the fourth column in Table 6.3. The joint design in Test 8 and 9 achieved sufficient rotation for the plastic hinge region (at  $> 25\text{mrad}$ ) as shown in the table, and so they qualify to be used in DCM structures.

**Table 6.3:** *Maximum rotation of the plastic hinge region in the nine joint tests*

Test number	Test label	Maximum rotation of the plastic hinge region $\theta_{p,max}$ [mrad]	Normalised Maximum rotation of the plastic hinge region $\theta_{p,max} / \theta_{p,DCM}$
1	S235-OSH-NS-FP: 30 cycles	21.1	85%
2	S235-OSH-WS-FP: 28 cycles	7.7	31%
3	S235-NSH-WS-FP: 30 cycles	11.9	48%
4	S355-OSH-NS-FP: 30 cycles	20.1	80%
5	S355-OSH-WS-FP: 26 cycles	2.4	10%
6	S235-NSH-NS-FP: 28 cycles	9.3	37%
7	S355-NSH-NS-FP: 26 cycles	2.1	8%
8	S235-OSH-NS-HP: 29 cycles	25.8	103%
9	S355-OSH-WS-HP: 30 cycles	25.1	100%

#### 6.2.4. *Initial rotational stiffness of the joint*

Joint rotational stiffness is defined in BS EN 1993-1-8: 2005 as the moment required to produce unit rotation in that joint. The initial rotational stiffness,  $S_{j,ini}$ , for the nine joints was obtained by calculating the slope of the linear part to the joint moment-rotation curve. Joint moments are not normalised in these curves. The linear portion of the  $M_j-\phi$  curve was taken from the corresponding test results considering the first twenty two loading cycles during which the joint response was elastic. The third column in Table 6.4 presents  $S_{j,ini}$  for the nine joints.

**Table 6.4:** *Initial rotational stiffness of the joint in Tests 1-9*

Test number	Test label	Initial rotational stiffness of the joint $S_{j,ini}$ [kN.m/mrad]
1	S235-OSH-NS-FP: 22 cycles	7.27
2	S235-OSH-WS-FP: 22 cycles	7.97
3	S235-NSH-WS-FP: 22 cycles	8.47
4	S355-OSH-NS-FP: 22 cycles	8.06
5	S355-OSH-WS-FP: 22 cycles	8.67
6	S235-NSH-NS-FP: 22 cycles	7.96
7	S355-NSH-NS-FP: 22 cycles	7.78
8	S235-OSH-NS-HP: 22 cycles	7.56
9	S355-OSH-WS-HP: 22 cycles	8.38

Clause 5.2 in BS EN 1993-1-8: 2005 classifies joints according to  $S_{j,ini}$  as rigid, semi-rigid or pinned. The classification boundaries for rigid and pinned joints in unbraced frames were calculated and found to be 36700 kN.m/rad and 700 kN.m/rad respectively. Because  $S_{j,ini}$  values given in Table 6.4 are found to fall between these two classification boundaries, the nine joints are classified as semi-rigid. Figure 6.11 shows that the linear parts of the nine  $M_j-\phi$  curves fall within the semi-rigid range.



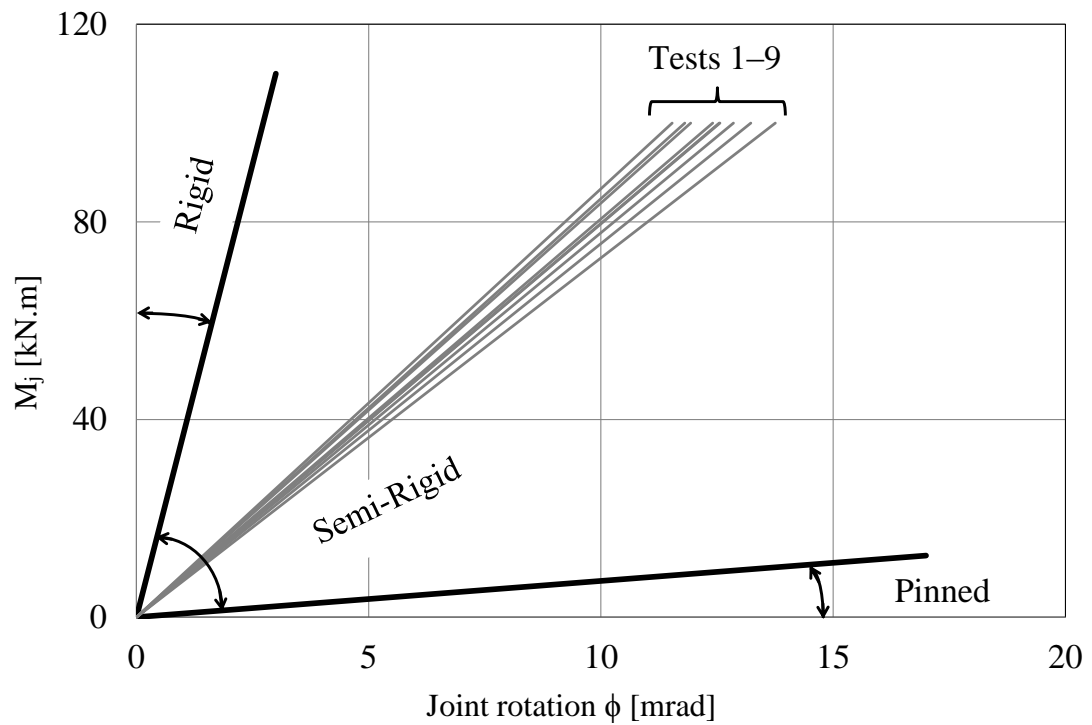


**Figure 6.11:** *Stiffness classification of the joint in Tests 1-9*

#### 6.2.5. *Energy dissipation*

Accumulated energy dissipation values at the end of each loading cycle were obtained by calculating the areas enclosed by the moment–rotation hysteresis loops of the plastic hinge region. Joint moments were not normalised for this calculation. The actual accumulated energy dissipations per load cycle are plotted in Figure 6.12. It can be seen from the results in Figure 6.12 that the energy dissipations were very small (at  $< 1$  kN.m.rad), and the difference between them was negligible, up to cycle 24. For higher cycle numbers, there is a dramatic increase in dissipations due to the onset of yield in the TCPs, slip in the bolted connection or both. In order to examine the energy dissipation in the nine tests more closely, the accumulated values from the 25<sup>th</sup> cycle onwards are presented in Table 6.4 and plotted in Figure 6.13. The influence of using different types of TCPs on the accumulated energy dissipation per joint is compared in Section 6.3.

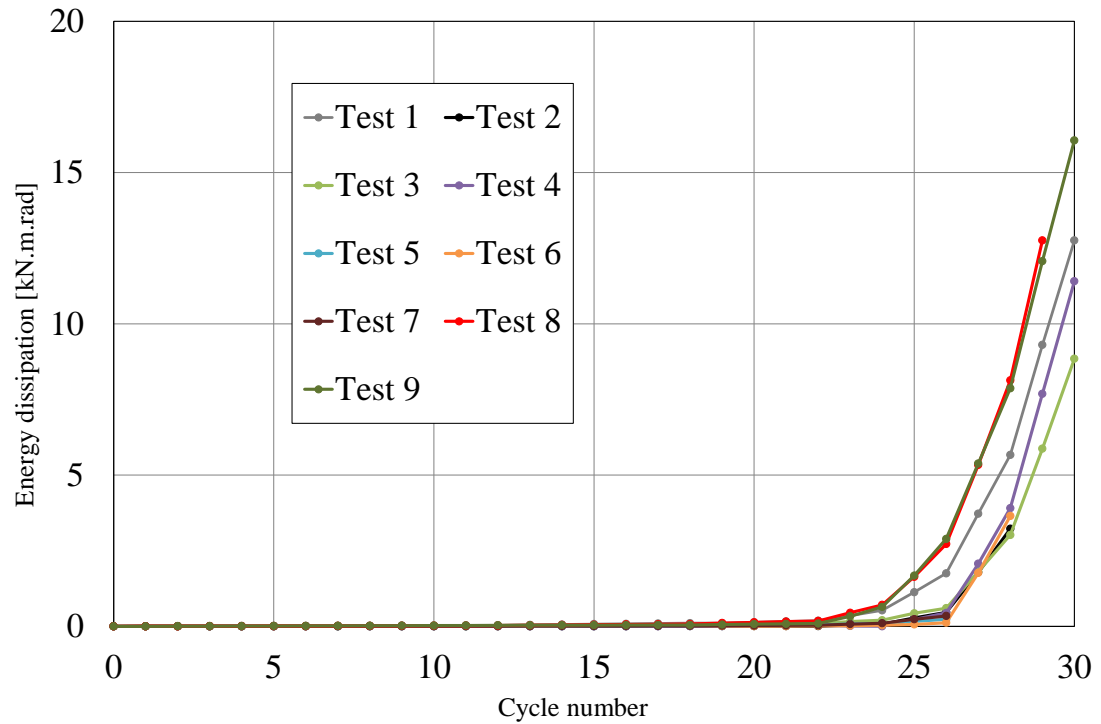


**Figure 6.12:** *Accumulated energy dissipation in Tests 1–9*

**Table 6.5:** *Accumulated energy dissipation in Tests 1-9*

Test number	Test label	Accumulated energy dissipation at the end of cycle: [kN.m.rad]					
		25	26	27	28	29	30
1	S235-OSH-NS-FP	1.13	1.75	3.73	5.67	9.30	12.76
2	S235-OSH-WS-FP	0.28	0.46	1.78	3.23	-	-
3	S235-NSH-WS-FP	0.43	0.6	1.81	3.02	5.87	8.85
4	S355-OSH-NS-FP	0.23	0.44	2.07	3.91	7.69	11.41
5	S355-OSH-WS-FP	0.17	0.23	-	-	-	-
6	S235-NSH-NS-FP	0.06	0.12	1.77	3.65	-	-
7	S355-NSH-NS-FP	0.23	0.34	-	-	-	-
8	S235-OSH-NS-HP	1.64	2.72	5.34	8.13	12.76	-
9	S355-OSH-WS-HP	1.68	2.89	5.38	7.87	12.07	16.06

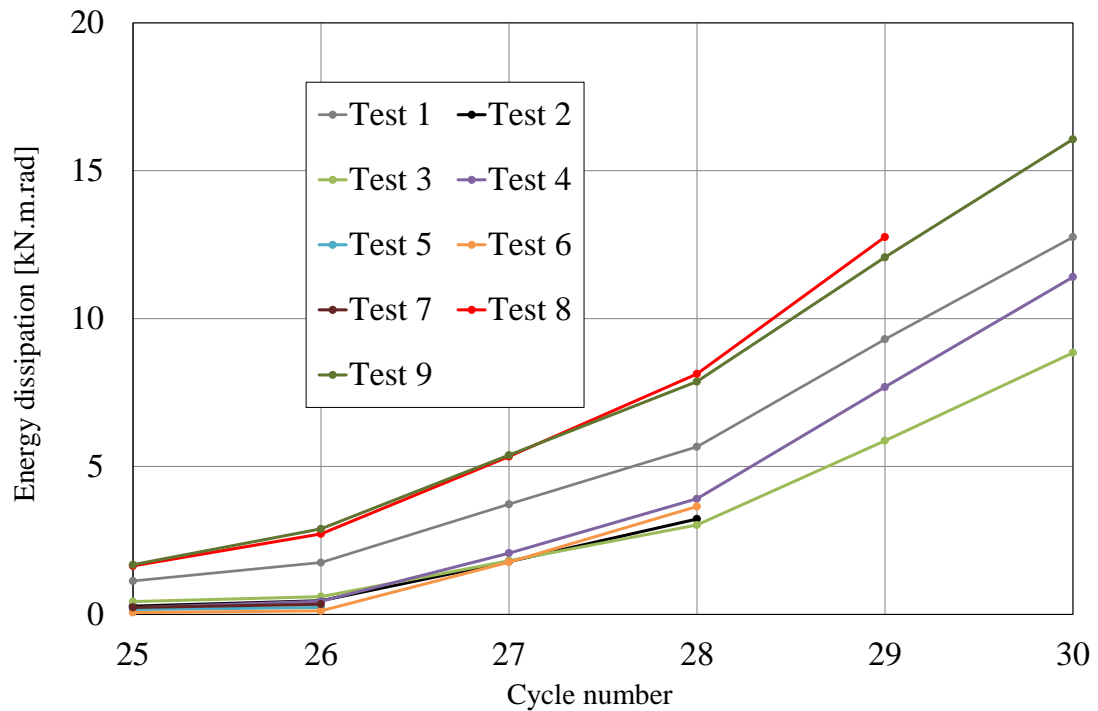


**Figure 6.13:** Accumulated Energy dissipation beyond the 25<sup>th</sup> cycle in Tests 1–9

### 6.3. Analysis and comparison of the tests results

As introduced in Table 3.2, the tests differed in the type of the TCPs employed. This section compares the tests results in pairs. Tests of each pair differed from each other by one parameter out of four. The parameters are: the steel grade of the TCPs; use or absence of vertical stiffeners; bolt preloading force; or size of bolt holes. The comparisons were divided according to the differing parameter into four subsections. This is to understand the influence of each parameter, individually, on the overall hysteretic behaviour of the joint to the cyclic loading protocol.

To ensure the validity of the comparisons, a pair of results were considered up to the common maximum loading cycle. Comparisons included an assessment of the: maximum joint moments; maximum plastic hinge rotations; and energy dissipations. Furthermore, the maximum measured strain levels reached in the main joint components, such as the I-beam and the diaphragm plates, were compared.

In the comparisons,  $M_{j,max}$  and  $\theta_{p,max}$  were normalised by  $M_{b,el,y,Rd}$  and  $\theta_{p,max}$  respectively. The maximum strains reached in the I-beam ( $\epsilon_{max,beam}$ ) and the DPs ( $\epsilon_{max,DP}$ ) were normalised by their corresponding yield strain, namely  $\epsilon_{y,beam}$  and  $\epsilon_{y,DP}$ , obtained from the tensile coupon tests presented in Chapter 4. The normalisation procedure helped to present comparisons in the form of bar-charts for simplicity and clarity.

### 6.3.1. *Steel grade comparison*

This subsection compares three different pairs of tests in which the TCPs were identical in all parameters except their grade of steel. The first comparison, shown in Figure 6.14, is between Test–1 and Test–4; in which both pairs of TCPs were Not Stiffened (NS), had Oversized Bolt Holes (OSH) and Fully Preloaded (FP) bolts. The steel grades in Tests 1 and 4 were S235 and S355. The comparison in Figure 6.14 includes results for Test–1 and Test–4 up to the end of the 30<sup>th</sup> loading cycle.

Figure 6.14(c) shows that the maximum normalised joint moments in Test–1 and Test–4 are 75% and 85%, which means that the joint with S355–TCPs is 10% stronger. However, comparing strain measurements reveals that there are higher strain demand in the I-beam and the DPs when the steel grade is S355. Furthermore,  $\theta_{p,max}$  with S355–TCPs is 5% less than its S235 counterpart. The last observation was given support in Figure 6.14(b) by the higher accumulated energy dissipations with S235–TCPs in all the inelastic loading cycles.

The second comparison, presented in Figure 6.15, is between Test–2 and Test–5; in which both pairs of TCPs were With Stiffeners (WS), had OSH and FP bolts. The steel grades of the TCPs in Tests 2 and 5 were S235 and S355. Test–5 was

conducted up to the end of cycle 26, and so the results from Test–2 were for the same number of cycles, thereby ignoring the results from the 27<sup>th</sup> and 28<sup>th</sup> cycles.

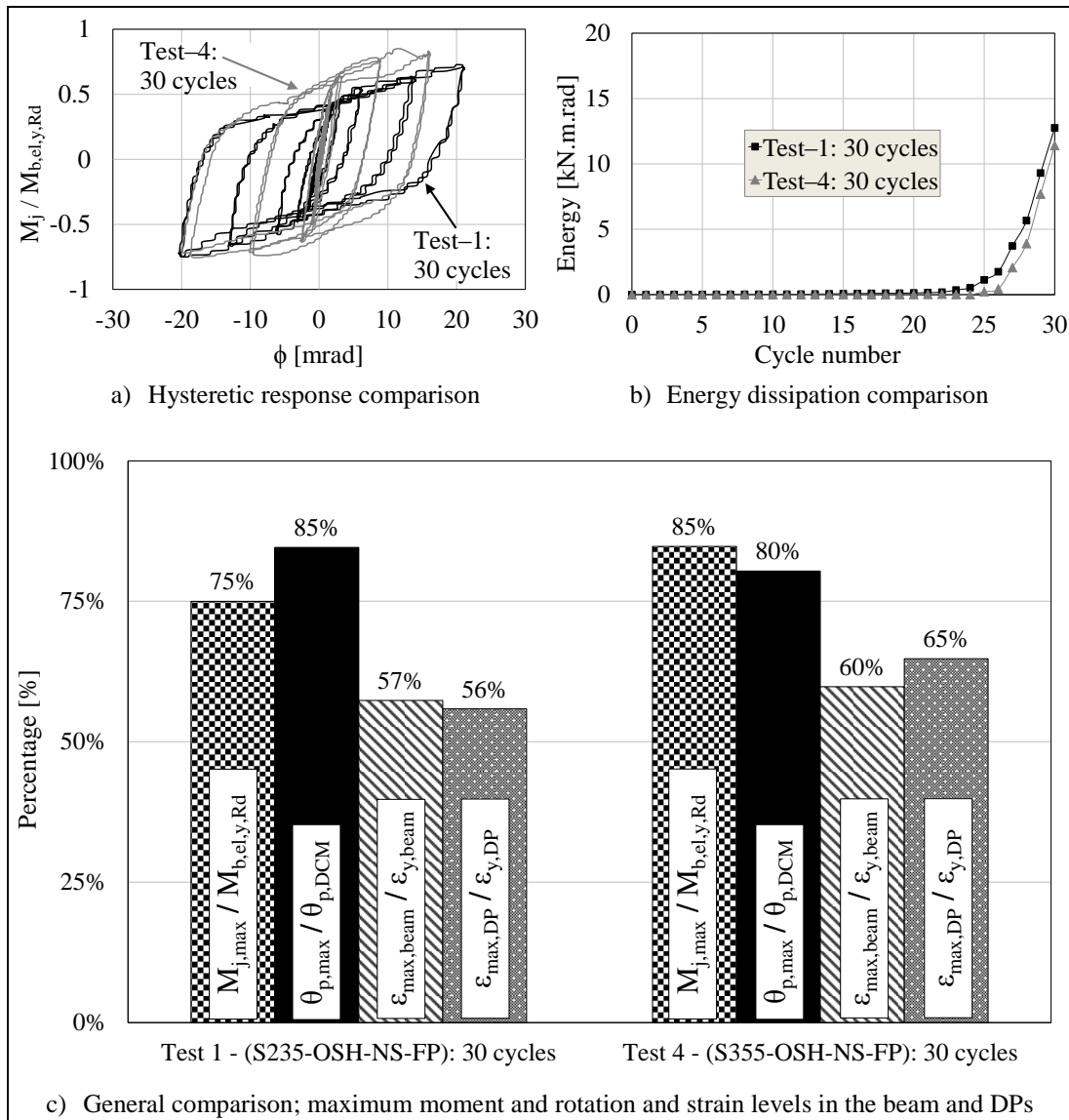


**Figure 6.14:** Steel grade comparison between the results of Test–1 and Test–4

Figure 6.15(c) shows that  $M_{j,max}$  in Test–2 and Test–5 are 67% and 74%. This confirms the observation from the previous comparison of getting a stronger joint when using S355–TCPs. Comparing strain measurements and  $\theta_{p,max}$  show relatively insignificant differences between the two tests. This is due to the limitation in this comparison of terminating at 26 loading cycles before there was any significant

inelastic deformation. The same limitation led to negligible energy dissipation in both tests, as illustrated in Figure 6.15(b).

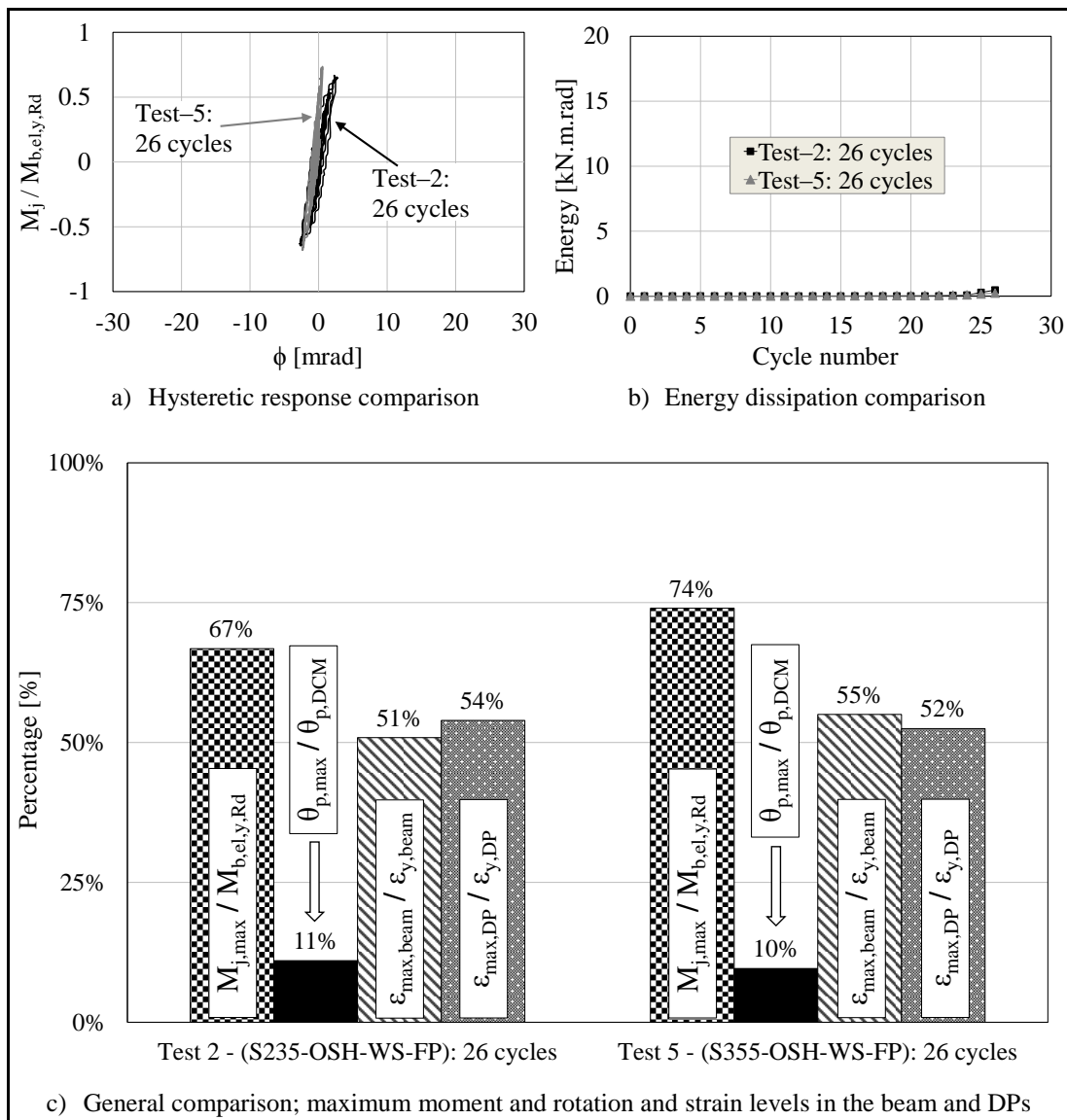


**Figure 6.15:** Steel grade comparison between the results of Test-2 and Test-5

The third comparison, shown in Figure 6.16, is between Test-6 and Test-7; in which both pairs of TCPs were NS, had Normal-Sized Holes (NSH) and FP bolts. The steel grades of the TCPs in Tests 6 and 7 were S235 and S355. Because Test-7 was stopped at the end of the 26<sup>th</sup> loading cycle, the results from Test-6 were to the 26<sup>th</sup> cycle too.

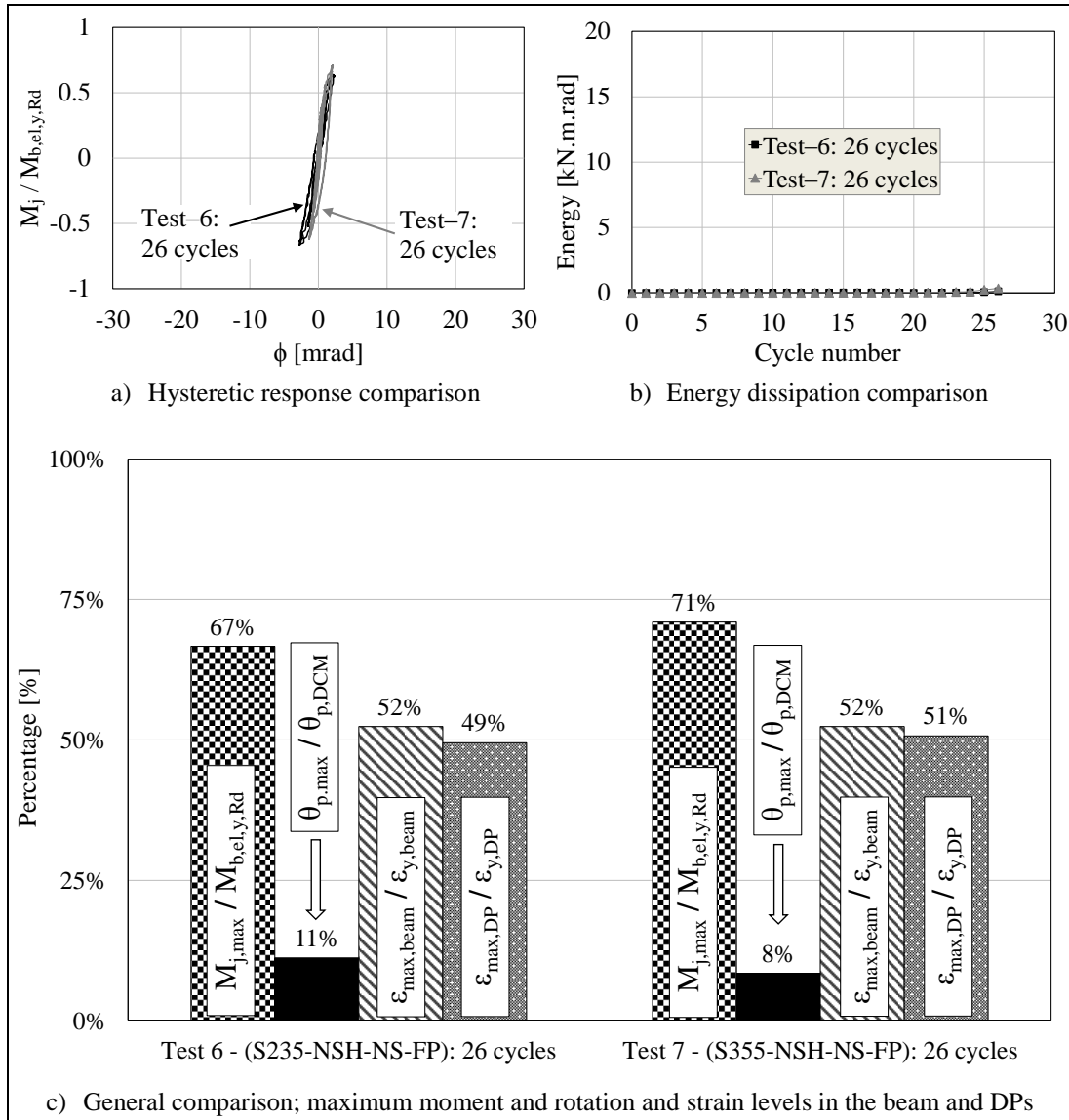


**Figure 6.16:** Steel grade comparison between the results of Test-6 and Test-7

The comparison reveals very similar observations to those from the comparison with Test-2 and Test-5. Figure 6.16(c) shows that  $M_{j,max}$  in Test-6 and Test-7 are 67% and 71%, respectively, confirming that the use of S355-TCPs gives a stronger joint than the one with S235-TCPs. The absence of the inelastic loading cycles (27<sup>th</sup>, 28<sup>th</sup>, 29<sup>th</sup> and 30<sup>th</sup>) leads to relatively insignificant differences (at < 5%) between  $\theta_{p,max}$   $\epsilon_{max,beam}$  and  $\epsilon_{max,DP}$  in the two tests, as shown in Figure 6.16(c), as well as negligible energy dissipation values (at < 1 kN.m.rad), as illustrated in Figure 6.16(b).

The three comparisons, based on the steel grade of the TCPs, show that the use of S235–TCPs enhances the joint performance due to the earlier onset of yield. This is confirmed by the higher rotation of the plastic hinge region and consequently the higher accumulated energy dissipation. Another important design criterion that is satisfied is achieving a lower strain demand in the beam and the DPs to keep all joint components elastic, while at the same time the TCPs are to perform as the joint replaceable links after seismic events. The previous observations were not very clear in the comparisons of test results that were limited to 26 loading cycles due to the absence of the inelastic loading cycles (at > 26<sup>th</sup> cycle).

The findings of this subsection conform to the recommendation in BS EN 1998-1: 2004 on choosing the steel grade for different components in a moment frame, so that the nominal yield strength in non-dissipative members shall exceed the upper value of the yield strength in the dissipative zones. Using grade S355 for the non-dissipative components (the I-beam, column, diaphragm plates and web stub) when having grade S235 for the dissipative components (the TCPs) satisfies this recommendation.

### *6.3.2. Use of stiffeners comparison*

This subsection compares three different pairs of tests in which the TCPs were identical in all parameters except the use or absence of vertical stiffeners welded along their longitudinal axis. The first comparison, shown in Figure 6.17, is between Test–1 and Test–2; in which both pairs of TCPs were of S235 and had OSH and FP bolts. The TCPs in Test–1 were NS, and in Test–2 they were WS. The comparison in Figure 6.17 includes results up to the end of the 28<sup>th</sup> loading cycle, because this was the maximum common cycle in both tests.



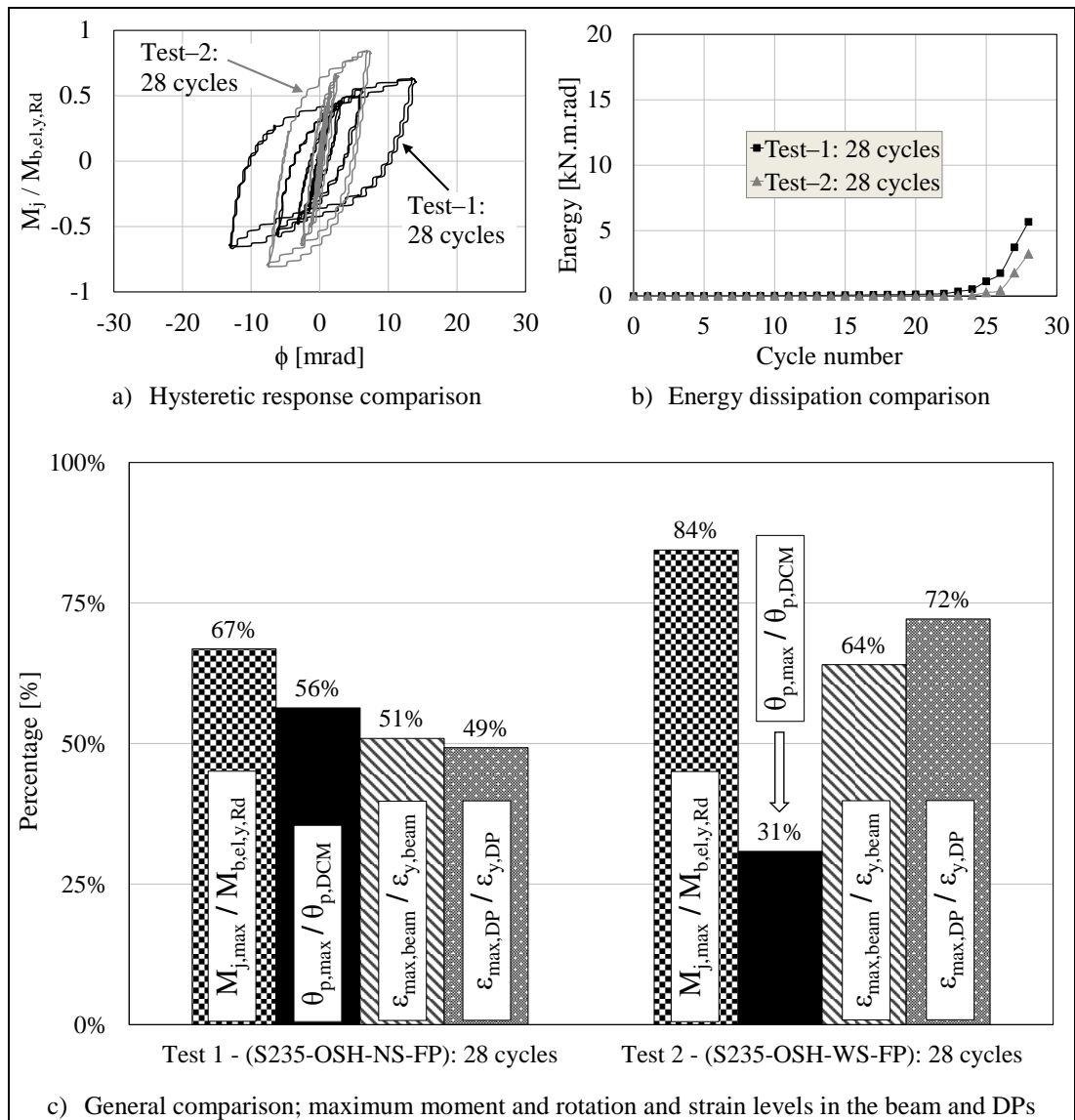


**Figure 6.17:** Use of stiffeners comparison between the results of Test-1 and Test-2

Figure 6.17(c) shows that the maximum normalised joint moments in Test-1 and Test-2 are 67% and 84%, respectively. This reveals that the use of stiffeners in TCPs resulted, as expected, in a stronger joint. The same figure shows that stiffening the TCPs increased the maximum normalised strain in the I-beam and the DPs from 51% to 64% and from 49% and 72%. The absence of stiffeners allowed for a 25% increase in the normalised rotation of the plastic hinge region, and as can be seen from the darker curve in Figure 6.17(b) resulted in higher accumulated energy dissipation when entering the inelastic loading cycles.

The second comparison, presented in Figure 6.18, is between Test–6 and Test–3; in which both pairs of TCPs were of S235 and had NSH and FP bolts. The TCPs in Test–6 and Test–3 were NS and WS respectively. Test–6 was conducted up to the end of cycle 28, and thus the results from Test–3 were for the same number of cycles, ignoring the results during the 29<sup>th</sup> and 30<sup>th</sup> cycles.

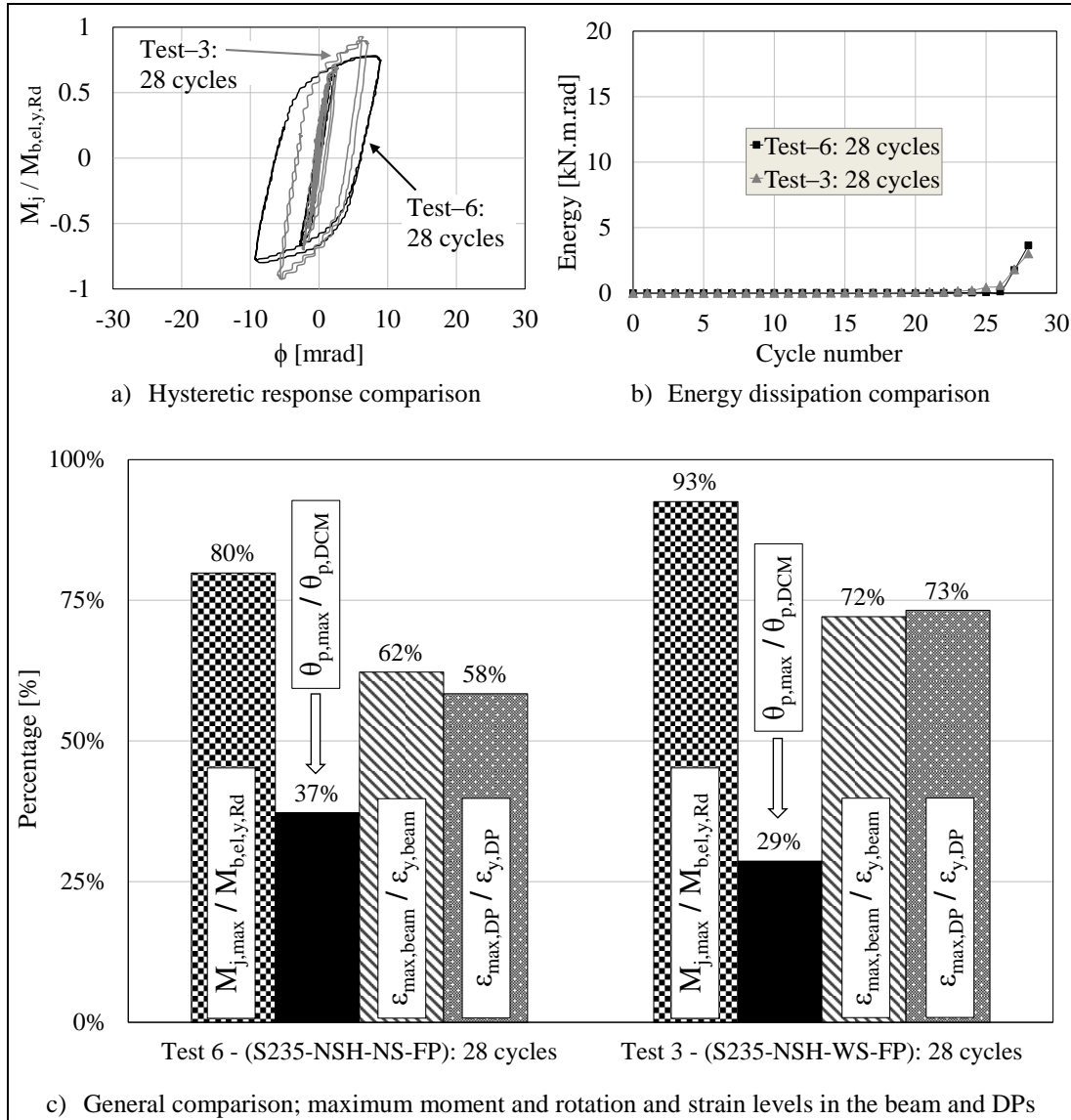


**Figure 6.18:** Use of stiffeners comparison between the results of Test–6 and Test–3

Figure 6.18(c) shows that  $M_{j,max} / M_{b,el,y,Rd}$  in Test–6 and Test–3 are 80% and 93%. This confirmed the observation from the comparison of Tests 1 and 2 of getting a stronger joint with stiffened TCPs. Comparing strains from both tests showed that

welding vertical stiffeners to the TCPs increased the maximum normalised strain in the I-beam and the DPs by 10% and 15%, respectively. Moreover, the presence of stiffeners is seen to reduce  $\theta_{p,max} / \theta_{p,DCM}$  from 37% to 29%. Figure 6.18(b) compares the accumulated energies and shows that they are very similar up to the 25<sup>th</sup> loading cycle and slightly higher with the unstiffened TCPs in Test-6 at the end of the 28<sup>th</sup> loading cycle.

The third comparison, illustrated in Figure 6.19, is between Test-4 and Test-5; in which both pairs of TCPs were of S355 and had OSH and FP bolts. The TCPs in Test-5 were stiffened whereas those in Test-4 were not. Because Test-5 was stopped at the end of the 26<sup>th</sup> loading cycles, Test-4 results were for the same number of cycles.

The comparison demonstrates similar observations to those from the comparison of Tests 6 and 3, but on a smaller scale due to the lower number of inelastic cycles. Figure 6.19(c) shows that  $M_{j,max} / M_{b,el,y,Rd}$  in Test-4 and Test-5 are 65% and 74%, confirming that the use of stiffeners results in a stronger joint. The maximum strain levels reached in the I-beam and the DPs are slightly higher in the joint with stiffened TCPs. The maximum normalised rotation of the plastic hinge region is slightly higher at 3% when the TCPs were unstiffened. It can be noted from Figure 6.19(b) that there are no significant differences in the energy dissipation between the two tests during the 26 loading cycles.

The three comparisons, which were based on the use of vertical stiffeners to TCPs, show that the absence of these stiffeners reduces the strain demand in the I-beam and the DPs and increases the maximum rotation of the plastic hinge region and subsequently the energy dissipation. Although the performance of the joint detailing

appears to be enhanced in the absence of stiffeners, stiffening TCPs is recommended to avoid early buckling failure in their reduced section areas, such as the buckling failure onset that was observed in the top unstiffened TCP in Test-6 at the beginning of the 29<sup>th</sup> loading cycle.

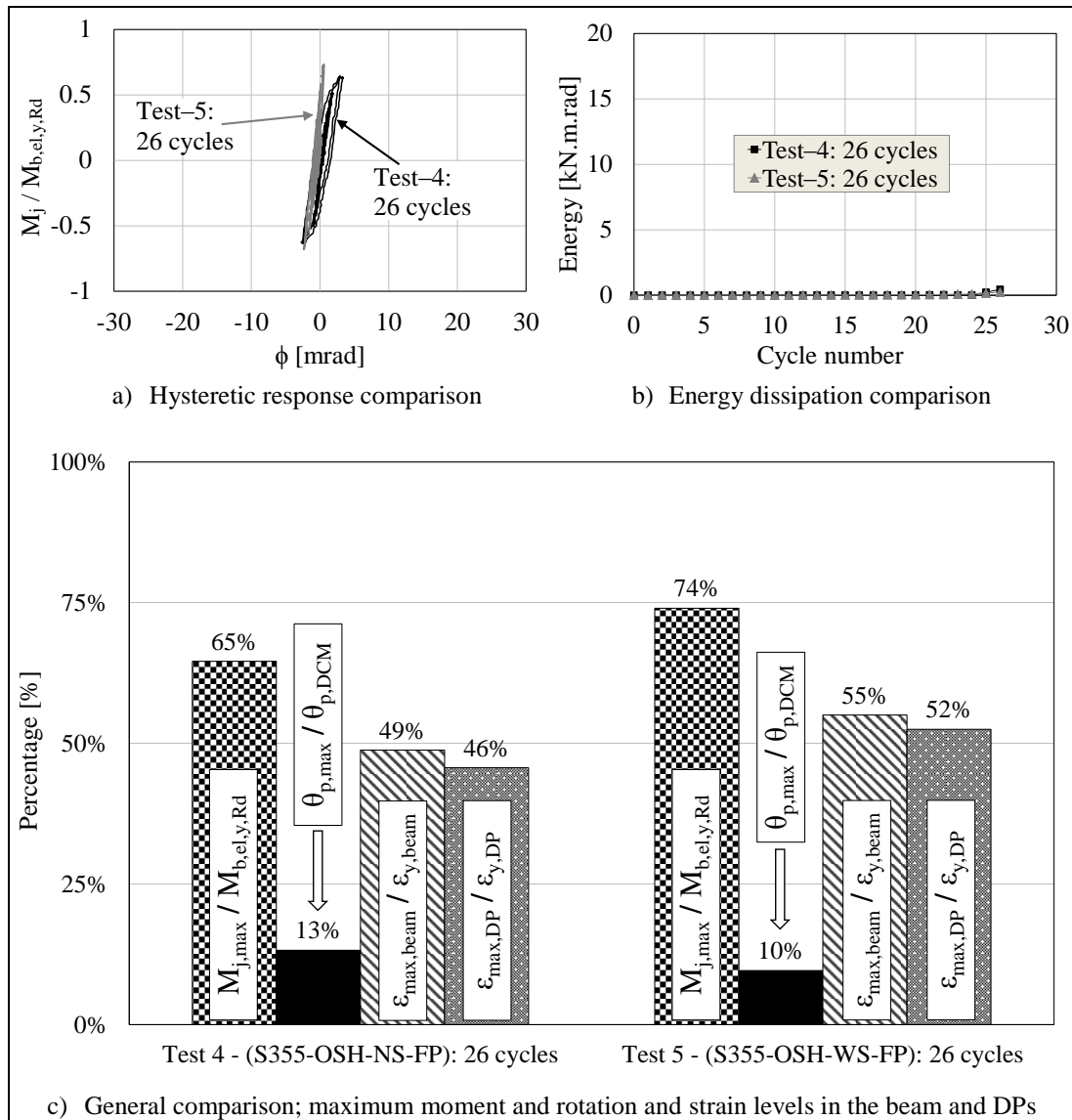


**Figure 6.19:** Use of stiffeners comparison between the results of Test-4 and Test-5

### 6.3.3. Size of bolt holes comparison

This subsection compares three different pairs of tests in which the TCPs were identical in all parameters but the size of their bolt holes. The first comparison,

shown in Figure 6.20, is between Test–1 and Test–6; in which both pairs of TCPs were of S235, NS and had FP bolts. The TCPs in Test–1 had OSH ( $d_0 = d + 6\text{mm} = 28\text{mm}$ ), and those in Test–6 had NSH ( $d_0 = d + 2\text{mm} = 24\text{mm}$ ). The results comparison in Figure 6.20 was limited to 28 loading cycles. The results from the 29<sup>th</sup> and 30<sup>th</sup> cycles in Test–1 were ignored because cycle–28 was the last completed cycle in Test–6.

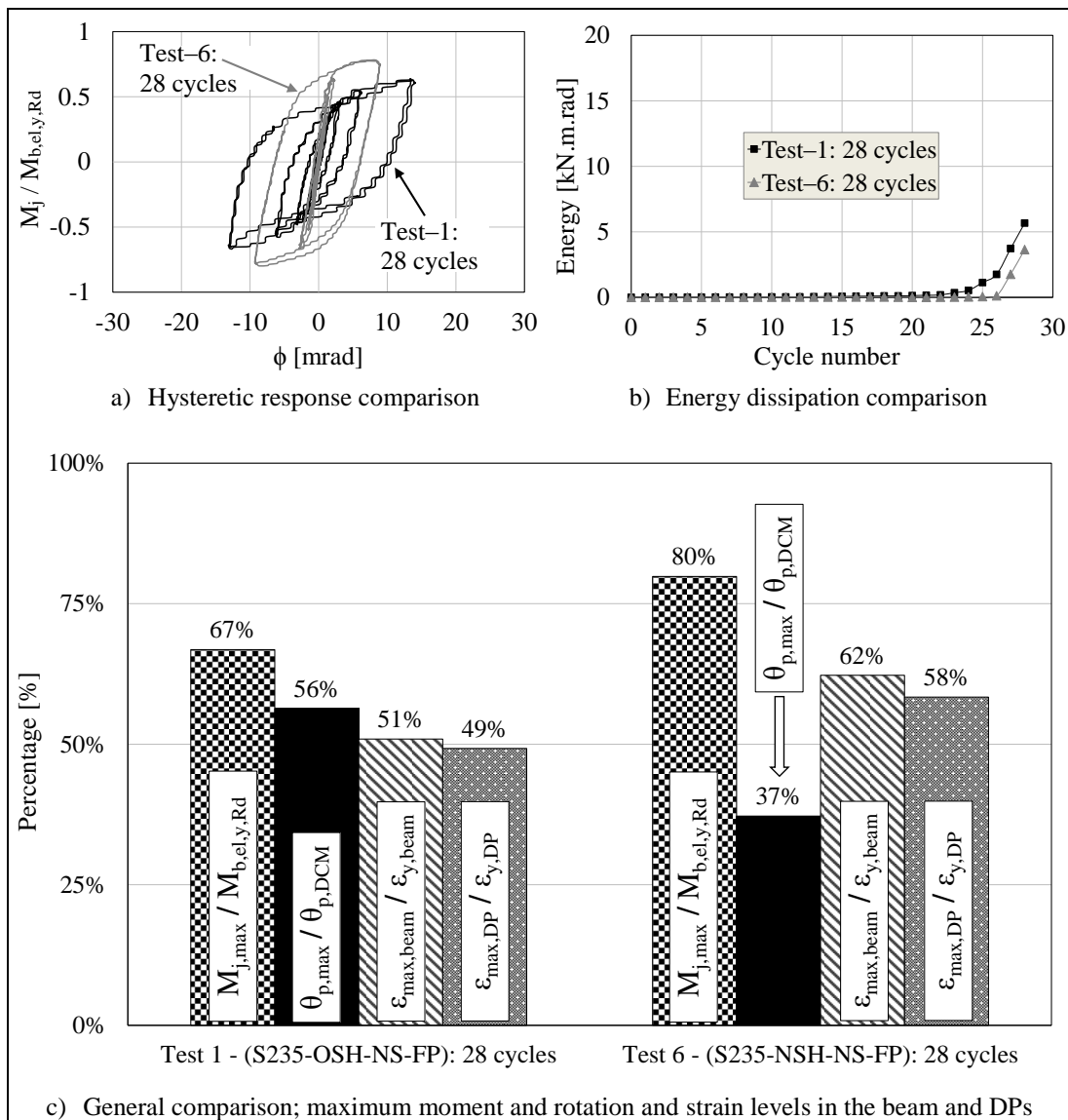


**Figure 6.20:** *Size of holes comparison between the results of Test–1 and Test–6*

Figure 6.20(c) shows that  $M_{j,max} / M_{b,el,y,Rd}$  in Test–1 and Test–6 are 67% and 80%, which reveals that NSH-TCPs results in a stronger joint. The same figure shows that

the use of normal-sized holes in the TCPs increases the maximum normalised strain in the I-beam and the DPs by 11% and 9%. It can be noted that oversizing the holes in the TCPs resulted in higher  $\theta_{p,max} / \theta_{p,DCM}$  at approximately 20% and as can be seen from Figure 6.20(b) in higher accumulated energy dissipation during the inelastic loading cycles.

The second comparison, presented in Figure 6.21, is between Test-2 and Test-3; in which both pairs of TCPs were of S235, WS and had FP bolts. The TCPs had OSH in Test-2 and NSH in Test-3. The results were for 28 loading cycles.

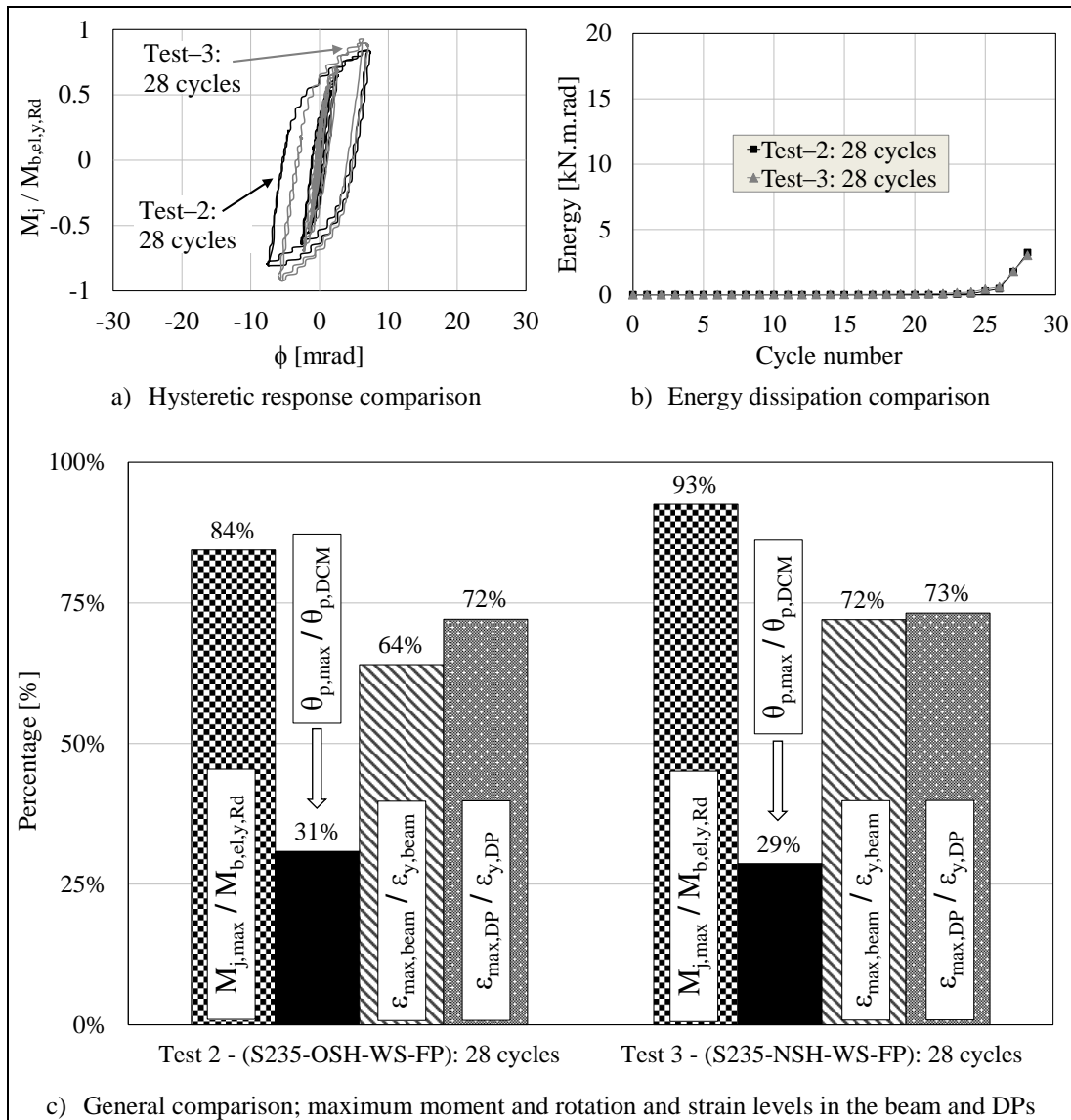


**Figure 6.21:** Size of holes comparison between the results of Test-2 and Test-3

Figure 6.21(c) shows that  $M_{j,max} / M_{b,el,y,Rd}$  in Test-2 and Test-3 are 84% and 93%. This confirmed the observation from the comparison of Tests 1 and 6 of getting a stronger joint when using NSH-TCPs. Comparing strain measurements from both tests showed that oversizing the holes in the TCPs reduces the maximum normalised strain on the I-beam by 8%, whereas there were no significant differences (at < 3%) in the strain demand in the DPs, the plastic hinge rotation or the energy dissipation.

Although this comparison covered as many loading cycles as the previous one, and although connection slippage was not detected in any of the tests compared, it was clear that oversizing the holes in the unstiffened S235-TCPs had a higher impact on the maximum plastic hinge rotation and the energy dissipation than those with stiffened S235-TCPs. This led to the conclusion that the impact of OSH on the energy dissipation of the joint is not, in this case, due to the occurrence of larger bolt slippage in the larger hole clearance; but was a result of reducing the size of the net section in TCPs by 8mm in comparison to the net section size when the holes are normal-sized. This subsequently resulted in an earlier yield onset in the net sections of the OSH-TCPs, and the yield contributed to the overall energy dissipation. Adding the stiffeners to the S235-TCPs delayed the yield onset in both their reduced section areas and net sections, and thus the energy dissipation in the tests of the second comparison were similar and not largely affected by the size of the bolts holes.

The third comparison, illustrated in Figure 6.22, is between Test-4 and Test-7; in which both pairs of TCPs were of S355, NS and had FP bolts. The TCPs in Test-4 and Test-7 had OSH and NSH respectively. The comparison in Figure 6.22 is for the results from Test-4 and Test-7 up to the end of the 26<sup>th</sup> loading cycle, because this was the maximum common cycle.

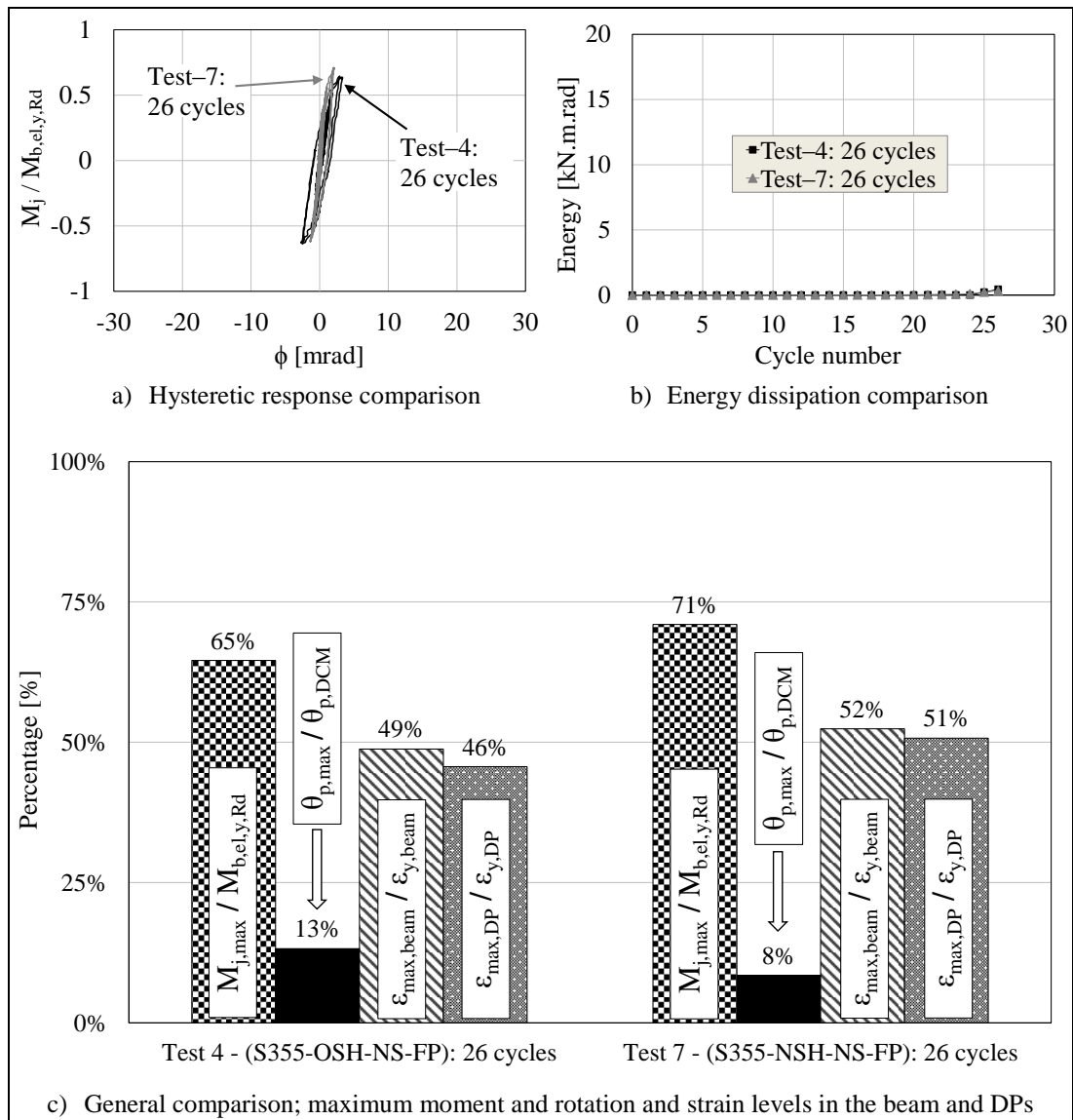


**Figure 6.22:** Size of holes comparison between the results of Test-4 and Test-7

Figure 6.22(c) shows that  $M_{j,max} / M_{b,el,y,Rd}$  in Test-4 and Test-7 are 65% and 71%. The strain levels in the I-beam and DPs are slightly higher (at 3 to 5%) in the joint with NSH. The use of OSH in Test-4 increased the maximum normalised rotation of the plastic hinge slightly (at 5%) in comparison with NSH. Figure 6.22(b) shows that the energy dissipations are negligible in both tests. The impact of OSH on the joint response to the loading protocol was not very significant in this case due to the low number of inelastic cycles and the relatively high grade of steel (S355).



The three comparisons of this subsection, which were based on the size of holes in the TCPs, showed that using OSH reduces the strain demand in the beam and DPs, increases the maximum rotation of the plastic hinge region and improves the energy dissipation performance, particularly after the yield onset in the net sections of the TCPs. The delay in yield onset when using either S355–TCPs or stiffened S235–TCPs limits the influence of hole size on the joint performance, whereas this influence is clearer in the joints with unstiffened S235–TCPs due to the early yield in their net sections.

The influence of having OSH rather than NSH on the energy dissipation through bolt slippage was not observed in any of the three comparisons because there were no significant slips in any of the tests discussed, as shown in Appendix D. This was due to the high slip resistance in the bolted connections. The use of a smaller, yet controlled, preloading force can increase significantly the positive impact of using OSH on the energy dissipation of the joint. This joint response will be shown in Subsection 6.3.4.

#### *6.3.4. Bolt preloading force comparison*

This subsection compares two different pairs of tests in which the TCPs were identical in all parameters except the preloading force acting on their bolts. The first comparison, shown in Figure 6.23, is between Test–1 and Test–8. In this comparison, both pairs of TCPs were of S235, NS and had OSH. The Bolts for TCPs in Test–1 were FP, and the value of the preloading force ( $F_{p,Cd}$ ) was specified in accordance with Clause 3.9.1 in BS EN 1993-1-8: 2005 for slip-resistant connections, where ( $F_{p,Cd} = 0.7 \times f_{ub} \times A_s$ ). The TCP bolting in Test–8 were preloaded

to half the specified design bolt torque (HP). The results comparison in Figure 6.23 was limited to 29 loading cycles.

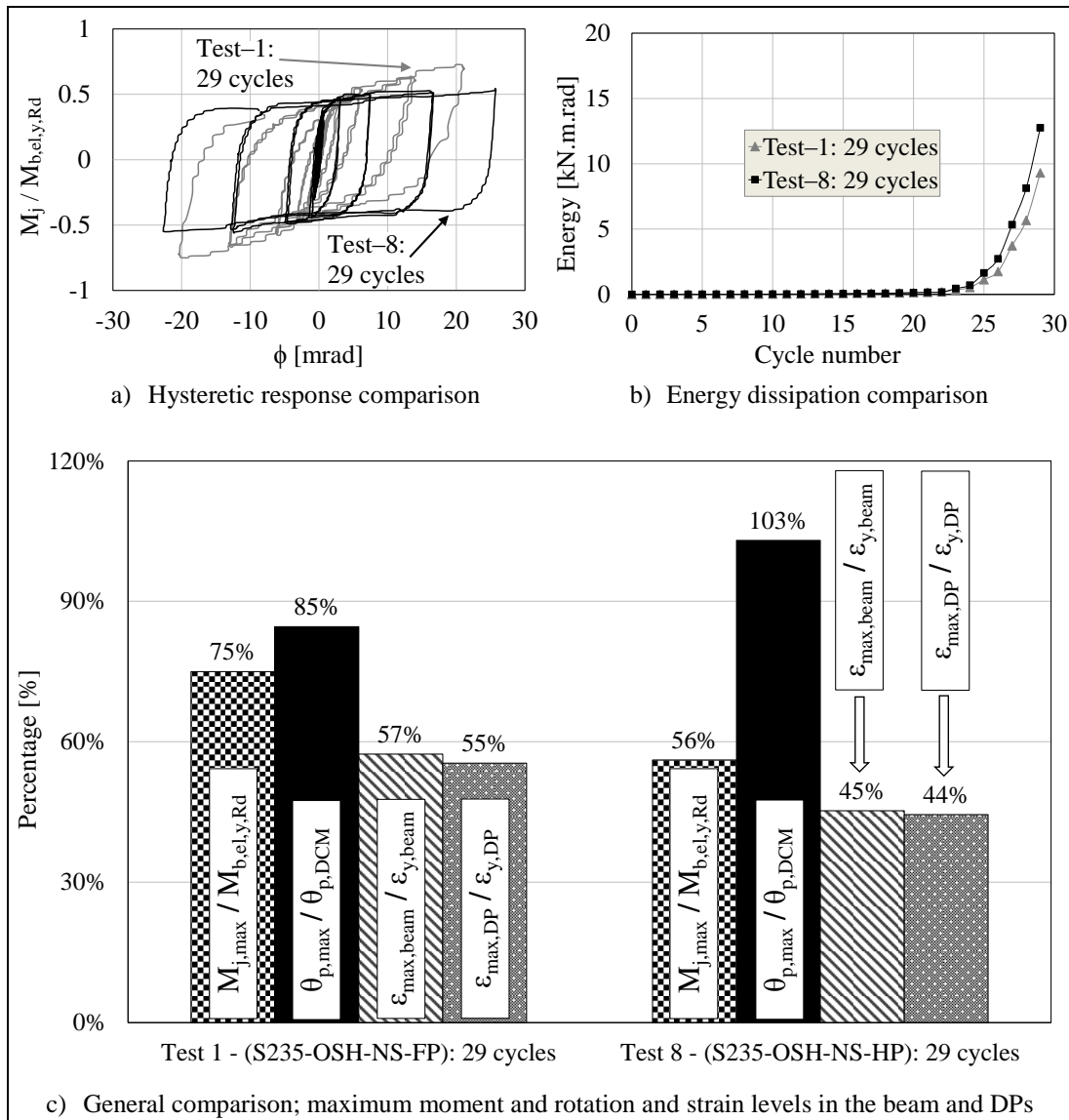


**Figure 6.23:** Preloading force comparison between the results of Test-1 and Test-8

Figure 6.23(c) shows that the maximum normalised joint moments in Test-1 and Test-8 are 75% and 56%. This revealed that FP bolting resulted in approximately 20% stronger joint, for the number of cycles considered, than the one with HP bolts. The same figure shows that FP bolts in Test-1 increased the maximum normalised strains in the I-beam and DPs by 12% and 11%. Moreover, reducing the bolt preloading force by 50% improved the normalised maximum rotation of the plastic

hinge region by 18% due to the activation of connection slippage, as shown in Appendix D. This further resulted in the joint dissipating higher energy in Test–8 than in Test–1, as can be seen from the energy curves in Figure 6.23(b). The change in joint properties also allowed the rotation of the plastic hinge to exceed (at 103%) the minimum rotation capacity required in plastic hinge regions for DCM structures which is 25 mrad. Comparing the energy dissipations between Test–1 and Test–8, which are shown in Table 6.5, shows that the slip activation in Test–8 increased the energy dissipation significantly by an average of 45% between the 25<sup>th</sup> and the 29<sup>th</sup> loading cycles. In other words, slip activation contributed to an average of 30% of the total energy dissipation during these cycles. The other 70% was mainly dissipated via yield in TCPs.

The second comparison, presented in Figure 6.24, is between Test–5 and Test–9; in which both pairs of TCPs were of S355, WS and had OSH. The TCPs bolts were FP in Test–5 and HP in Test–9. The results were for 26 cycles only. Figure 6.24(c) shows that  $M_{j,max} / M_{b,el,y,Rd}$  in Test–5 and Test–9 are 74% and 51%. Comparing strain measurements showed that using FP bolts imposed 14% higher  $\epsilon_{max,beam} / \epsilon_{y,beam}$  and  $\epsilon_{max,DP} / \epsilon_{y,DP}$  than HP bolts. Furthermore, the maximum normalised rotation of the plastic hinge region at the end of the 26<sup>th</sup> cycle was three times higher in the joint with HP bolts due to the activation of bolt slippage. This further led to higher accumulated energy dissipation for the joint with HP bolts, as can be seen from the energy curves in Figure 6.24(b).

The two comparisons of this subsection, which were based on the value of the preloading force acting on the TCPs bolts, showed that reducing the preloading force to half the value specified in BS EN 1993-1-8: 2005 for slip-resistant connections

enhanced the joint response and allowed the rotation of the plastic hinge region to exceed the minimum rotation capacity threshold of 25mrad in DCM structures.

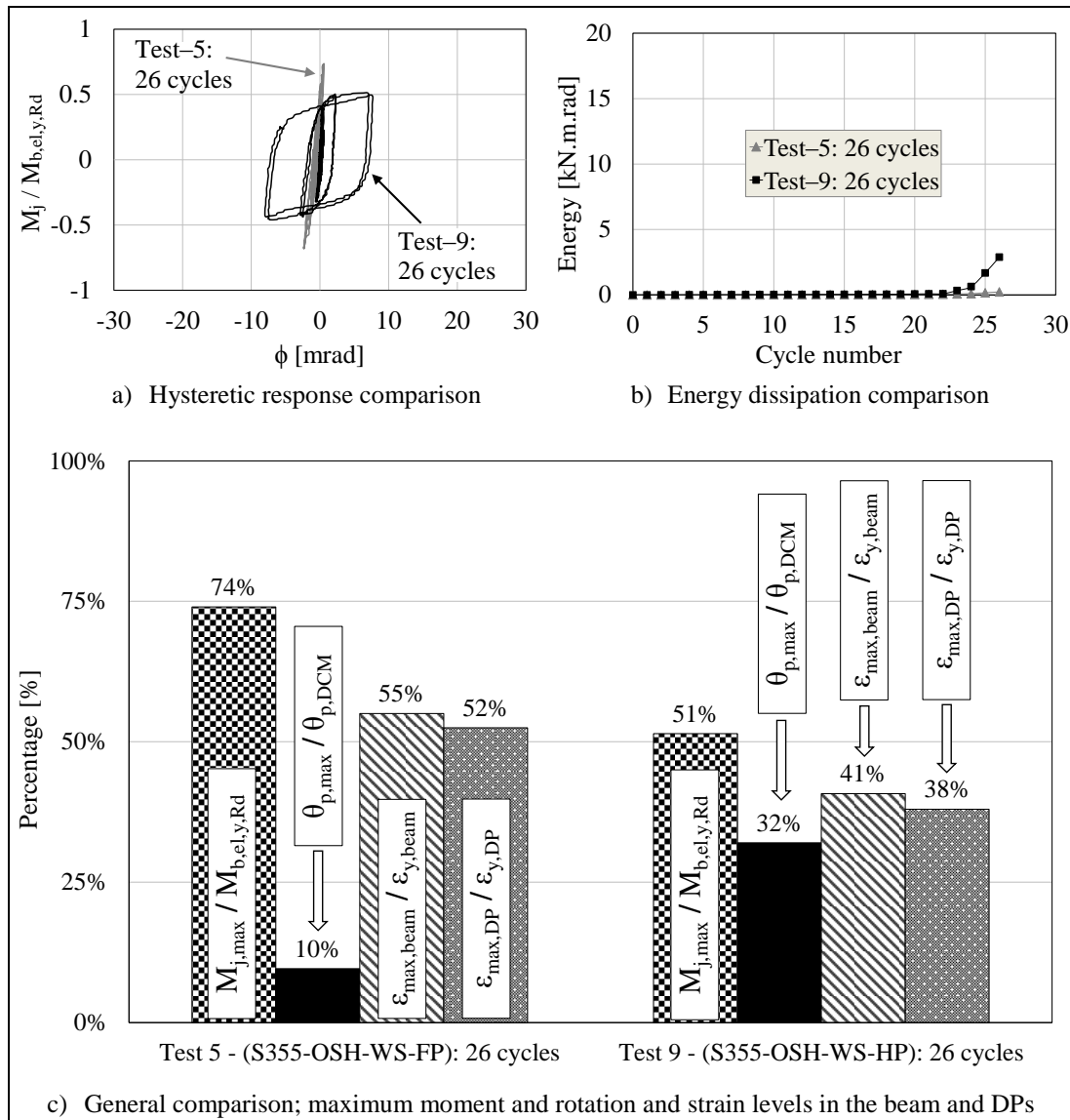


**Figure 6.24:** Preloading force comparison between the results of Test-5 and Test-9

Furthermore, the reduction in bolts preloading force reduced the force demand imposed on the beam and DPs. This satisfied the design criterion of allowing the development of plastic hinge region in the TCPs whilst the main joint components remain elastic. Accumulated energy dissipations for the joint with HP bolts showed the highest values amongst all nine tests. This is due to the activation of slip, which created a second fuse for energy dissipation in addition to the already existing fuse

that is yielding of the reduced section areas of the TCPs. It is important to combine the reduction of the bolts preloading force with the use of oversized holes to allow for greater bolt slippage, obtain higher rotations of the plastic hinge region and enlarge the contribution of connection slip to the energy dissipation.

#### *6.4. Concluding remarks*

This chapter presents and analyses the results of the nine joint experiments. Comparisons between test results were done in pairs to understand the influence of using different types of TCPs on the joint response to the loading protocol. It was found that the use of S355–TCPs and longitudinal stiffeners increased the joint strength in comparison with the use of S235 and unstiffened TCPs respectively. However, strengthening the joint was accompanied by a reduction in both the rotation of the plastic hinge region and the energy dissipation, and an increase in the force demand imposed on the beam and DPs. The use of stiffeners is considered important to avoid early buckling failure in the reduced section areas of the TCPs. A compromise should be made between the strength of the joint and its rotational ductility when designing it. The combination of reduced, yet controlled, bolt preloading force with the use of oversized holes was found to create a second fuse for energy dissipation and enhance the rotational ductility of the joint.

In spite of the limitation of the actuator stroke capacity, the proposed joint met the criteria for DCM structures. In addition to that, the aim of using TCPs as replaceable links after seismic events was proved to be achievable by keeping all the joint components, except the TCPs, in the elastic range of strain. None of the joints reached the maximum moment of resistance and no strength or stiffness degradation greater than 20% was observed from their moment-rotation curves. Thus, future

work on the tested joints is important to get their full performance profiles and extend their suitability to meet the criteria for high ductility class (DCH) structures by achieving a rotation capacity greater than 35mrad for the plastic hinge region. Next chapter includes an overview of the main findings of this project, its limitations and suggestions for future work.

# *Chapter 7*

## *Conclusions*

This chapter presents a summary of the research, its key findings and limitations, suggestions for future work and the scientific outcomes.

### *7.1. Research summary*

Tubular columns possess many structural and architectural features that, in certain cases, make them more favourable than open-section columns in steel moment-resisting frames. These advantages are sometimes underexploited due to the relative lack of seismic design guidance on joints to tubular columns in moment-resisting frames, especially for semi-rigid joints. The structural performance of a single sided external diaphragm joint between a steel I-section beam (UKB 203×133×30) and a CHS column (244.5×10mm) has been investigated experimentally under cyclic loading. The proposed joint included two diaphragm plates welded to the outer circumference of the CHS and bolted to the beam flanges with two tapered cover plates. A web stub was welded to the column face and bolted to the beam web.

The main objectives of this project were to identify the joint detailing that achieves the required structural response and ductility in dissipative moment-resisting frames under seismic loading, and to avoid permanent deformations in the primary members of the moment frame to reduce the time required for repair after seismic events. The latter objective was tackled by designing the TCPs to be the main seismic energy dissipation fuse that are sacrificial components to be replaced after a seismic event for the purpose of fast reoccupation of the structure.

The bolted connections between the TCPs and the beam flanges and between the TCPs and the DPs were all designed to be slip resistant at the serviceability limit state, and their slip resistance was set to allow connection slippage to be activated before the tapered sections of the cover plates reached full plasticity. This is to create a second fuse for seismic energy dissipation and increase the overall rotational ductility of the joint.

A review of published literature, which is relevant to the subject, is presented in Chapter 2, with a particular focus on joints made with external diaphragm plates. Design calculations of the proposed joint and its components are carried out in Chapter 3 to verify the chosen geometry and material properties of the joint components against the adopted design philosophy. The calculations showed the potential for the joint to achieve the desired performance that limits the plastic deformations to TCPs and provides the rest of the joint components with sufficient overstrength to remain elastic that allow for the development of cyclic yielding only in the required dissipative zones. As reported in Chapter 4, Material properties of the steel components are determined from tensile coupon tests for more reliable design calculations.



The preparations for the full-scale laboratory experiments are covered in Chapter 5. The test specimens were prepared by shop-welding the column assembly and field-bolting the beam to the external diaphragm plates using two TCPs per specimen. Details of the test rig arrangement and its attachments, such as the column hinges and the loading hinge, were presented. Geometry and geometry imperfection measurements were carried out for the joint components, and were found to fall within the tolerance ranges specified in the relevant standards.

The AISC loading protocol used in the experiments was presented taking into consideration the load and displacement capacities of the actuator available in the Structures Laboratory at the School of Engineering, University of Warwick. The tests instrumentation plan, set-up and calibration and the data-logging programme and hardware are presented too in Chapter 5.

The nine beam-to-column joint tests were conducted after finishing all the preparation work. The tests results and analysis are presented in Chapter 6. Strain levels in the joint components were measured and compared. The hysteretic response in the nine joints and the accumulated energy dissipation are presented. The initial rotational stiffness is also calculated.

Comparisons between test results are done in pairs to understand the influence of using different types of TCPs on the overall seismic performance of the proposed joints. In each pair, test results were considered up to the maximum common loading cycle. The comparisons included the assessment of the maximum joint moment, maximum rotation of the plastic hinge region and the energy dissipation in the tests being compared. Furthermore, the maximum strains in the main joint components, such as the beam and the diaphragm plates, were also compared.

## 7.2. *Key findings of the research*

The test results showed that the joints are, according to the classification boundaries specified in BS EN 1993-1-8: 2005, partial-strength semi-rigid joints. The strain and local deformation measurements of the different joint components showed that they all deformed within their elastic range, except for the TCPs where plastic deformations developed in their tapered sections as intended in the design. The tested joints showed generally stable hysteretic response, and sufficient ductility (rotation of the plastic hinge region at  $> 25\text{mrad}$ ) when the bolts were properly preloaded. Although some tests were stopped before the full 30 cycles in the loading protocol, their results are still significant for the purpose of performance comparisons.

Three pairs of tests, in which the TCPs were identical in all parameters except for their grade of steel, are compared and it is found that TCPs of S355 increased the joint moment of resistance when compared to S235. However, this was accompanied by an increase in the force demand in the beam and diaphragm plates and a reduction in the maximum rotation of the plastic hinge region. The last two observations of TCPs indicate the use of the weaker steel grade (S235) as a more favourable option than S355 when the comparison is based solely on the grade of steel. Similarly, three pairs of tests in which the TCPs were identical in all parameters, except for the presence or absence of their longitudinal stiffeners, are compared. The use of stiffened TCPs is found to have a similar impact on the joint response to that obtained with the higher steel grade TCPs. This suggests that the absence of stiffeners might be the better option for TCPs to enhance the maximum joint rotation and reduce strain levels in the beam and the DPs. However, the use of stiffeners is

found to be important in the joint detailing to avoid premature buckling failure in the reduced section of the TCPs.

Compared are three different pairs of tests, in which the TCPs were identical in all parameters but the size of their bolt holes. Although connection slippage is not found to have occurred due to the high preloading force acting on the bolts ( $F_{p,Cd} = 212\text{kN}$ ) giving high slip resistance in the bolted connections, it was found that having oversized holes (OSH) enhanced the maximum rotation of the plastic hinge region, imposed less strain demand in the beam and the DPs and reduced the maximum joint moment in comparison with having normal-sized holes (NSH). This difference is due to the earlier onset of yielding in the net sections of the TCPs when the holes were oversized. The extent of this observation was less significant when both compared tests had stiffened TCPs due to the delay in yield onset at the net sections.

The main aim for having OSH was to get larger connection slips than those with NSH to enlarge the contribution of connection slippage to the seismic energy dissipation. To achieve this goal, the last two tests in the applied programme were conducted with half the connection slip resistance applied in the previous seven tests. The combination of reduced slip resistance of the bolted connections and the use of oversized holes in TCPs activated connection slippage and created a second fuse for seismic energy dissipation (in addition to the first fuse that was cyclic yielding of the reduced section areas of the TCPs). Subsequently, these two joint details achieved the highest rotations and accumulated energy dissipations. For example, Slip activation was found to contribute significantly (at  $> 30\%$ ) to the total energy dissipation for the S235-OSH-NS-HP joint. Moreover, it was found that this combination of details reduced the maximum strains imposed in the beam and DPs. The maximum rotation of the plastic hinge region in both tests exceeded the

minimum rotation capacity threshold of 25mrad that is specified in Clause 6.6.4(3) in BS EN 1998-1: 2004 for structures of medium ductility class, known as DCM.

### *7.3. Limitations of this project*

A few limitations related to the laboratory facilities were imposed on this research and consequently the extent of its results. The limited displacement capacity of the available actuator at the Structures Laboratory restricted the range of the displacement-controlled loading cycles adopted in the loading protocol of the experiments. None of the joints reached its maximum moment of resistance or rotational ductility and thus the full performance profiles of these joints were not obtained.

The uncertainty about the actual friction class of the connection surfaces, and consequently the actual slip factors, resulted in uncertainty about the theoretically-calculated slip resistance of the connection. Furthermore, no bolt-pretension measuring machine was available at the Structures Laboratory to measure the bolt preload introduced by the torque wrench that was used for tightening the bolts. This added to the uncertainty of the actual value of slip resistance that resulted from the application of the theoretically-calculated torque values.

The results of the first seven tests showed that the actual connection slip resistance, which corresponded to the bolt preloading value recommended in BS EN 1993-1-8: 2005, was higher than its theoretical value, and hence slip was not activated as intended at the design stage. The last two tests were conducted with half the slip resistance applied in the previous tests by reducing the preloading value by 50%. Connection slip was now activated in both tests and a second fuse for seismic energy dissipation was created as intended.

#### *7.4. Suggestions for future work*

As mentioned in Section 7.3, none of the tested joints reached their maximum moment of resistance, and no strength or stiffness degradation greater than 20% was observed in any of their moment-rotation curves. This leaves room for future work that may aim at attaining the full seismic performance profiles. It has been shown through the test results that the maximum rotation of the plastic hinge region, when its bolts were appropriately preloaded, could exceed the minimum rotation capacity threshold of 25mrad for DCM structures whilst maintaining all the joint components elastic, except the TCPs that were designed to be replaceable.

Suggestions for future work include the exact determination of the most suitable slip resistance of the proposed joint to achieve its optimal performance whilst meeting all the criteria of the adopted design philosophy, and then examining the rotational ductility of the plastic hinge region, especially for the joint with stiffened S235–OSH–TCPs and controlled bolt preloading, to check whether it exceeds 35mrad without having permanent deformations in the primary components of the joint. If this check is satisfied then the findings of the PhD work can be extended to be applied for the design of external diaphragm joints, with built-in replaceable links, between steel I-beams and CHS columns in high ductility class (DCH) structures as defined in BS EN 1998-1: 2004.

The future work suggested may be carried out through finite element (FE) analysis of the joint using a suitable software package such as ABAQUS. The FE models should use the measured geometry and the actual material properties of the joint components after converting the engineering stress-strain values, obtained from tensile coupon tests, into true stress-strain values. The results of the FE models

should be validated against the experimental results obtained in this project. The FE models may then be utilised to further investigate the joint performance and extend its applicability.

Moreover, the numerical investigations done by Sabbagh *et al.* (2013) showed that the energy dissipation mechanism of this joint may be extended to include a third fuse, which is yielding of the critical section of the I-beam. Although plastic deformations of the beam were not desired in this project, but their activation beyond the full plasticity of the tapered sections of the cover plates makes the joint configuration more redundant under severe earthquakes. Validated numerical models could be utilised to investigate this approach further.

Finally, this research may form with previous and future relevant studies a base for the preparation of a comprehensive, practical and efficient seismic design guidance for special joints between steel I-beams and tubular columns in moment-resisting frames in the future.

### *7.5. Scientific outcomes*

A poster about the experimental planning of this project was presented in March 2013 at the Young Researchers Conference organised by the Institution of Structural Engineers in London, and was awarded the joint-first prize in the posters category. A conference paper titled “Structural behaviour of external diaphragm connection between steel I-section beam and circular hollow section columns under cyclic loading” has been accepted for publication and will be presented in September 2014 at the seventh edition of the European Conference on Steel and Composite Structures (EuroSteel) in Naples, Italy, {Khador and Chan (2014)}. This paper covers the results of three tests from the experimental programme of this project and

investigates the influence of using stiffeners to TCPs and different bolts preloading values on the overall seismic performance of the joint. The full text of this paper and its extended abstract are included in Appendix E. In addition to that, an abstract has been submitted and accepted for the 15th International Symposium on Tubular Structures (ISTS15) to be held in Rio de Janeiro, Brazil in May 2015. The full-text paper to be submitted to this conference will focus on the effect of using different steel grades of TCPs and different bolt-holes sizes on the overall seismic performance of the joint. Finally, a journal paper is under ongoing preparation to be submitted to the Journal of Constructional Steel Research published by Elsevier; this paper will cover the whole experimental programme of this project and all its findings in details.

# References

AIJ (1990). Recommendations for the design and fabrication of tubular structures in steel. 3rd edition. *Architectural Institute of Japan (AIJ)*.

AIJ (1997). Recommendations for design and construction of concrete filled steel tubular structures. *Architectural Institute of Japan (AIJ)*.

AIJ (2001). Standard for structural calculation of steel reinforced concrete structures. *Architectural Institute of Japan (AIJ)*.

Alostaz, Y. M., and Schneider, S. P. (1996). Connections to concrete-filled steel tubes. Structural Engineering Series No. 613, University of Illinois at Urbana-Champaign.

Alostaz, Y. M., and Schneider, S. P. (1997). "Analytical behavior of connections to concrete-filled steel tubes". *Journal of Constructional Steel Research*, ISSN 0143-974X, Elsevier Science Limited, Vol. 40 (2), pp. 95-127.

ANSI/AISC 341-10 (2010). Seismic provisions for structural steel buildings. *American Institution of Steel Construction (AISC)*.



ANSI/AISC 360-10 (2010). Specification for structural steel buildings. *American Institution of Steel Construction (AISC)*.

Azizinamini, A., and Schneider, S. P. (2004). "Moment connections to circular concrete-filled steel tube columns". *Journal of Structural Engineering*, ISSN 0733-9445, American Society of Civil Engineers (ASCE), Vol. 130 (Special issue: Composite and hybrid structures), pp. 213-222.

Azuma, K., Kurobane, Y., and Makino, Y. (2000). "Cyclic testing of beam-to-column connections with weld defects and assessment of safety of numerically modelled connections from brittle fracture". *Engineering Structures*, ISSN 0141-0296, Elsevier Science Limited, Vol. 22 (12), pp. 1596-1608.

Bergmann, R., Matsui, C., Meinsma, C., and Dutta, D. (1995). *Design guide for concrete filled hollow section columns under static and seismic loading*. First Edition, CIDECT series 'Construction with hollow sections', No. 5, Germany.

BS EN 10025-1 (2004). Hot rolled products of structural steels – Part 1: General technical delivery conditions. *British Standards Institution (BSI)*.

BS EN 10034 (1993). Structural steel I and H sections – Tolerances on shape and dimensions. *British Standards Institution (BSI)*.

BS EN 10210-2 (2006). Hot finished structural hollow sections of non-alloy and fine grain steels – Part 2: Tolerances, dimensions and sectional properties. *British Standards Institution (BSI)*.

BS EN 1090-2:2008 (2008). Execution of steel structures and aluminium structures – Part 2: Technical requirements for the execution of steel structures. *British Standards Institution (BSI)*.

BS EN 1993-1-1 (2005). Eurocode 3: Design of steel structures – Part 1-1: General rules and rules for buildings. *British Standards Institution (BSI)*.

BS EN 1993-1-5 (2006). Eurocode 3: Design of steel structures – Part 1-5: Plated structural elements. *British Standards Institution (BSI)*.

BS EN 1993-1-8 (2005). Eurocode 3: Design of steel structures – Part 1-8: Design of joints. *British Standards Institution (BSI)*.

BS EN 1998-1 (2004). Eurocode 8: Design of structures for earthquake resistance – Part 1: General rules, seismic actions and rules for buildings. *British Standards Institution (BSI)*.

BS EN ISO 17640 (2010). Non-destructive testing of welds – Ultrasonic testing – Techniques, testing levels, and assessment. *British Standards Institution (BSI)*.

BS EN ISO 6892-1 (2009). Metallic materials - Tensile testing – Part 1: Method of test at ambient temperature. *British Standards Institution (BSI)*.

BS EN ISO 7500-1 (2004). Metallic materials. Verification of static uniaxial testing machines. Tension/compression testing machines. Verification and calibration of the force-measuring system. *British Standards Institution (BSI)*.

Chan, T. M., and Gardner, L. (2008). "Bending strength of hot-rolled elliptical hollow sections". *Journal of Constructional Steel Research*, ISSN 0143-974X, Elsevier Science Limited, Vol. 64 (9), pp. 971-986.

Chan, T. M., Gardner, L., and Law, K. H. (2010). "Structural design of elliptical hollow sections: a review". *Proceedings of the Institution of Civil Engineers - Structures and Buildings*, ISSN 0965-0911, ICE Publishing, Vol. 163 (6), pp. 391-402.

Chen, C. C., Lin, C. C., and Tsai, C. L. (2004). "Evaluation of reinforced connections between steel beams and box columns". *Engineering Structures*, ISSN 0141-0296, Elsevier Science Limited, Vol. 26 (13), pp. 1889–1904.

Cheng, C. T., Chan, C. F., and Chung, L. L. (2007). "Seismic behaviour of steel beams and CFT column moment-resisting connections with floor slabs". *Journal of Constructional Steel Research*, ISSN 0143-974X, Elsevier Science Limited, Vol. 63 (11), pp. 1479–1493.

Cheng, C. T., and Chung, L. L. (2003). "Seismic performance of steel beams to concrete-filled steel tubular column connections". *Journal of Constructional Steel Research*, ISSN 0143-974X, Elsevier Science Limited, Vol. 59 (3), pp. 405–426.

Chiew, S. P., Lie, S. T., and Dai, C. W. (2001). "Moment resistance of steel I-beam to CFT column connections". *Journal of Structural Engineering*, ISSN 0733-9445, American Society of Civil Engineers (ASCE), Vol. 127 (10), pp. 1164-1172.

ECCS (1986). Recommended testing procedure for assessing the behaviour of structural steel elements under cyclic loads. *European Convention for Constructional Steelwork (ECCS)*.

Elghazouli, A. Y. (2010). "Assessment of European seismic design procedures for steel framed structures". *Bulletin of Earthquake Engineering*, ISSN 1570-761X, European Association for Earthquake Engineering, Vol. 8 (1), pp. 65-89.

Elghazouli, A. Y., Málaga-Chuquitaype, C., Castro, J. M., and Orton, A.H. (2009). "Experimental monotonic and cyclic behaviour of blind-bolted angle connections". *Engineering Structures*, ISSN 0141-0296, Elsevier Science Limited, Vol. 31 (11), pp. 2540-2553.

FEMA-353 (2000). Recommended specifications and quality assurance guidelines for steel moment-frame construction for seismic applications. *Federal Emergency Agency Management (FEMA)*.

FEMA-355D (2000). State of the art report on connection performance. *Federal Emergency Agency Management (FEMA)*.

FEMA-355E (2000). Past performance of steel moment-frame buildings in earthquakes. *Federal Emergency Agency Management (FEMA)*.

FEMA-356 (2000). Prestandard and commentary for the seismic rehabilitation of buildings. *The American Society of Civil Engineers and the Federal Emergency Management Agency (FEMA)*.

Foolad Machine Company website. "Foolad Machine Co. – Rigid joint on HSS sections", from <http://www.fooladmachine.com>.

France, J. E., Davison, J. B., and Kirby, P. A. (1999). "Strength and rotational stiffness of simple connections to tubular columns using flowdrill connectors". *Journal of Constructional Steel Research*, ISSN 0143-974X, Elsevier Science Limited, Vol. 50 (1), pp. 15-34.

France, J. E., Davison, J. B., and Kirby, P. A. (1999a). "Moment-capacity and rotational stiffness of endplate connections to concrete-filled tubular columns with flowdrilled connectors". *Journal of Constructional Steel Research*, ISSN 0143-974X, Elsevier Science Limited, Vol. 50 (1), pp. 35-48.

Fukumoto, T., and Morita, K. (2005). "Elastoplastic behaviour of panel zone in steel beam-to-concrete filled steel tube column moment connections". *Journal of Structural Engineering*, ISSN 0733-9445, American Society of Civil Engineers (ASCE), Vol. 131 (12), pp. 1841-1853.

Fukumoto, T. (2005a). "Steel beam to concrete filled steel tube column moment connections in Japan". *International Journal of Steel Structures*, ISSN 1598-2351, Korean Society of Steel Construction, Vol. 5 (4), pp. 357-365.

Gardner, L., Chan, T. M., and Abela, J. M. (2011). "Structural behaviour of elliptical hollow sections under combined compression and uniaxial bending". *Advanced Steel Construction*, ISSN 1816-112X, Hong Kong Institute of Steel Construction, Vol. 7 (1), pp. 86-113.

Han, L. H., Wang, W. D., and Zhao X. L. (2008). "Behaviour of steel beam to concrete-filled SHS column frames: Finite element model and verifications". *Engineering Structures*, ISSN 0141-0296, Elsevier Science Limited, Vol. 30 (6), pp. 1647-1658.

Han, L. H., Wang, W. D., and Zhong T. (2011). "Performance of circular CFST column to steel beam frames under lateral cyclic loading". *Journal of Constructional Steel Research*, ISSN 0143-974X, Elsevier Science Limited, Vol. 67 (5), pp. 876–890.

Jiao, Y., Yamada, S., Kishiki, S., and Shimada, Y. (2011). "Evaluation of plastic energy dissipation capacity of steel beams suffering ductile fracture under various loading histories". *Earthquake Engineering & Structural Dynamics*, ISSN 1096-9845, John Wiley & Sons Limited, Vol. 40 (14), pp. 1553-1570.

Kang, C. H., Shin, K. J., Oh, Y. S., and Moon, T. S. (2001). "Hysteresis behaviour of CFT column to H-beam connections with external T-stiffeners and penetrated elements". *Engineering Structures*, ISSN 0141-0296, Elsevier Science Limited, Vol. 23 (9), pp. 1194-1201.

Khador, M., and Chan, T. M. (2014). "Structural behaviour of external diaphragm connection between steel I-section beam and circular hollow section columns under cyclic loading". *Proceedings of the 7th European Conference on Steel and Composite Structures (EuroSteel2014)*, Naples, Italy.

Kim, T., Stojadinovic, B., and Whittaker, A. S. (2004). "Seismic performance of US steel box column connections". *Proceedings of the 13th World Conference on Earthquake Engineering (13WCEE)*, Vancouver, B.C., Canada, Paper No. 981.

Kim, Y. J., Shin, K. J., and Kim, W. J. (2008). "Effect of stiffener details on behaviour of CFT column-to-beam connections". *International Journal of Steel Structures*, ISSN 1598-2351, Korean Society of Steel Construction, Vol. 8 (2), pp. 119-133.

Kumar, S. R. S., and Rao, D. V. P. (2006). "RHS beam-to-column connection with web opening – Experimental study and finite element modelling". *Journal of Constructional Steel Research*, ISSN 0143-974X, Elsevier Science Limited, Vol. 62 (8), pp. 739-746.

Kurobane, Y., Packer, J. A., Wardenier, J., and Yeomans, N. (2004). *Design guide for structural hollow section column connections*. First Edition, CIDECT series 'Construction with hollow sections', No. 9, Germany.

LabVIEW (2010). LabVIEW system design software. *National Instruments (NI)*.

Lee, S. L., Ting, L. C., and Shanmugam, N. E. (1993). "Use of external T-stiffeners in box-column to I-beam connections". *Journal of Constructional Steel Research*, ISSN 0143-974X, Elsevier Science Limited, Vol. 26 (2-3), pp. 77-98.

Liu, H., and Wang, Y.C. (2009). "A numerical study of the behaviour of steel beam to tubular column joints using reverse channel". *Proceedings of the 9th International*

*Steel Concrete Composite and Hybrid Structures (ASCCS 2009)*, Leeds, UK, ISBN 78-981-08-3194-3, pp. 619-624.

Mahin, S. A. (1998). "Lessons from steel buildings damaged by the Northridge earthquake". *Engineering Structures*, ISSN 0141-0296, Elsevier Science Limited, Vol. 20 (4-6), pp. 261-270.

Málaga-Chuquitaype, C., and Elghazouli, A. Y. (2010). "Behaviour of combined channel/angle connections to tubular columns under monotonic and cyclic loading". *Engineering Structures*, ISSN 0141-0296, Elsevier Science Limited, Vol. 32 (6), pp. 1600-1616.

McMullin, K. M., and Astaneh-Asl, A. (2003). "Steel semirigid column–tree moment resisting frame seismic behaviour". *Journal of Structural Engineering*, ISSN 0733-9445, American Society of Civil Engineers (ASCE), Vol. 129 (9), pp. 1243-1249.

Mesquita, A. B., Simões da Silva, L. A. P., and Jordão, S. (2009). "Experimental behaviour of I Beam – SHS column steel joints with hollo-bolts". *Proceedings of the 11th Nordic Steel Construction Conference (NSCC2009)*, Malmö, Sweden, ISBN 91-7127-058-2, pp. 230-237.

Mesquita, A. B., Simões da Silva, L. A. P., and Jordão, S. (2010). "Behaviour of I beam-SHS column steel joints with hollo-bolts – An experimental study". *Proceedings of the 13th International Symposium on Tubular Structures*, Hong Kong, China, ISBN 978-0-415-58473-9, pp. 17-25.



Miller, D. K. (1998). "Lessons learned from the Northridge earthquake". *Engineering Structures*, ISSN 0141-0296, Elsevier Science Limited, Vol. 20 (4-6), pp. 249-260.

Miura, K., Makino, Y., Kurobane, Y., Tanaka, M., Tokudome, K., and van der Vegte, G. J. (2001). "Testing of beam-to-RHS column connections without weld-access holes". *Proceedings of the 11th International Offshore and Polar Engineering Conference (ISOPE-2001)*, Stavanger, Norway, ISBN 1-880653-55-9, pp. 37-44.

Morino, S., and Tsuda, K. (2003). "Design and construction of concrete-filled steel tube column system in Japan". *Earthquake Engineering and Engineering Seismology*, ISSN The Society of Earthquake Engineering of the Republic of China, Vol. 4 (1), pp. 51-74.

NA to BS EN 1993-1-1 (2005). UK National Annex to Eurocode 3: Design of steel structures – Part 1-1: General rules and rules for buildings. *British Standards Institution (BSI)*.

NA to BS EN 1993-1-5 (2006). UK National Annex to Eurocode 3: Design of steel structures – Part 1-5: Plated structural elements. *British Standards Institution (BSI)*.

NA to BS EN 1993-1-8 (2005). UK National Annex to Eurocode 3: Design of steel structures – Part 1-8: Design of joints. *British Standards Institution (BSI)*.

NA to BS EN 1998-1 (2004). UK National Annex to Eurocode 8: Design of structures for earthquake resistance – Part 1: General rules, seismic actions and rules for buildings. *British Standards Institution (BSI)*.

Nakashima, M., Suita, K., Morisako, K., and Maruoka, Y. (1998). "Tests of welded beam-column subassemblies – Global behaviour". *Journal of Structural Engineering*, ISSN 0733-9445, American Society of Civil Engineers (ASCE), Vol. 124 (11), pp. 1236-1244.

Nishiyama, I., Fujimoto, T., Fukumoto, T., and Yoshioka, K. (2004). "Inelastic force-deformation response of joint shear panels in beam-column moment connections to concrete-filled tubes". *Journal of Structural Engineering*, ISSN 0733-9445, American Society of Civil Engineers (ASCE), Vol. 130 (2), pp. 244-252.

O'Brien, T. K., and Salpekar, S. A. (1993). Scale effects on the transverse tensile strength of graphite/epoxy composites. *Composite Materials: Testing and Design*. Camponeschi, E. T., Editor. ASTM, Philadelphia, United States of America, Vol. 11, pp. 23-52.

Park, J. W., Kang, S. M., and Yang, S. C. (2005). "Experimental studies of wide flange beam to square concrete-filled tube column joints with stiffening plates around the column". *Journal of Structural Engineering*, ISSN 0733-9445, American Society of Civil Engineers (ASCE), Vol. 131 (12), pp. 1866-1876.

Qin, Y., Chena, Z., Yang, Q., and Shang, K. (2014). "Experimental seismic behaviour of through-diaphragm connections to concrete-filled rectangular steel tubular columns". *Journal of Constructional Steel Research*, ISSN 0143-974X, Elsevier Science Limited, Vol. 93, pp. 32–43.

Rao, D. V. P., and Kumar, S. R. S. (2006). "RHS beam-to-column connection with web opening – Parametric study and design guidelines". *Journal of Constructional*

*Steel Research*, ISSN 0143-974X, Elsevier Science Limited, Vol. 62 (8), pp. 747-756.

Ricles, J. M., Peng, S. W., and Lu, L. W. (2004). "Seismic behaviour of composite concrete filled steel tube column-wide flange beam moment connections". *Journal of Structural Engineering*, ISSN 0733-9445, American Society of Civil Engineers (ASCE), Vol. 130 (2), pp. 223-232.

Ruiz-Teran, A. M., and Gardner, L. (2008). "Elastic buckling of elliptical tubes". *Thin-Walled Structures*, ISSN 0263-8231, Elsevier Science Limited, Vol. 46 (11), pp. 1304-1318.

Sabbagh, A. B., Chan, T. M., and Mottram, J. T. (2013). "Detailing of I-beam-to-CHS column joints with external diaphragm plates for seismic actions". *Journal of Constructional Steel Research*, ISSN 0143-974X, Elsevier Science Limited, Vol. 88, pp. 21–33.

Schneider, S. P., and Alostaz, Y. M. (1998). "Experimental behavior of connections to concrete-filled steel tubes". *Journal of Constructional Steel Research*, ISSN 0143-974X, Elsevier Science Limited, Vol. 45 (3), pp. 321-352.

Schneider, S. P., Kramer, D. R., and Sarkkinen, D. L. (2004). "The design and construction of concrete-filled steel tube column frames". *Proceedings of the 13th World Conference on Earthquake Engineering (13WCEE)*, Vancouver, B.C., Canada, Paper No. 252.

Shanmugam, N. E., and Ting, L. C. (1995). "Welded interior box-column to I-beam connections". *Journal of Structural Engineering*, ISSN 0733-9445, American Society of Civil Engineers (ASCE), Vol. 121 (5), pp. 824-830.

Shen , Z., Chen, Y., Wang, W., and Zhao, X. (2010). "Tubular structures in China: state of the art and applications". *Proceedings of the Institution of Civil Engineers - Structures and Buildings*, ISSN 0965-0911, ICE Publishing, Vol. 163 (6), pp. 417-426.

Shin, K. J., Kim, Y. J., and Oh Y. S. (2008). "Seismic behaviour of composite concrete-filled tube column-to-beam moment connections". *Journal of Constructional Steel Research*, ISSN 0143-974X, Elsevier Science Limited, Vol. 64 (1), pp. 118-127.

Shin, K. J., Kim, Y. J., Oh, Y. S., and Moon, T. S. (2004). "Behaviour of welded CFT column to H-beam connections with external stiffeners". *Engineering Structures*, ISSN 0141-0296, Elsevier Science Limited, Vol. 26 (13), pp. 1877-1887.

Ting, L. C., Shanmugam, N. E., and Lee, S. L. (1991). "Box-column to I-beam connections with external stiffeners". *Journal of Constructional Steel Research*, ISSN 0143-974X, Elsevier Science Limited, Vol. 18 (3), pp. 209-226.

TML (2012). *Strain gauges*. Tokyo Sokki Kenkyujo Co.,Ltd, pp. 56-57.

Tremblay, R., Filiatrault, A., Timler, P., and Bruneau, M. (1995). "Performance of steel structures during the 1994 Northridge earthquake". *Canadian Journal of Civil*

*Engineering*, ISSN 0315-1468, The Canadian Society for Civil Engineering, Vol. 22 (2), pp. 338-360.

Wang, J., Zhang, L., and Spencer Jr, B. F. (2013). "Seismic response of extended end plate joints to concrete-filled steel tubular columns". *Engineering Structures*, ISSN 0141-0296, Elsevier Science Limited, Vol. 49, pp. 876-892.

Wang, W. D., Han, L. H., and Uy, B. (2008). "Experimental behaviour of steel reduced beam section to concrete-filled circular hollow section column connections". *Journal of Constructional Steel Research*, ISSN 0143-974X, Elsevier Science Limited, Vol. 64 (5), pp. 493-504.

Wang, W. D., Han, L. H., and Zhao X. L. (2009). "Analytical behaviour of frames with steel beams to concrete-filled steel tubular column". *Journal of Constructional Steel Research*, ISSN 0143-974X, Elsevier Science Limited, Vol. 65 (3), pp. 497-508.

Wang, W., Chen, Y., Li, W., and Leon, R.T. (2011). "Bidirectional seismic performance of steel beam to circular tubular column connections with outer diaphragm". *Earthquake Engineering & Structural Dynamics*, ISSN 1096-9845, John Wiley & Sons Limited, Vol. 40, pp. 1063–1081.

Wang, W., Qian, X., and Yang, B. (2014). "Fracture in concrete-filled square hollow section to H-section joints under low-cycle loading". *Journal of Constructional Steel Research*, ISSN 0143-974X, Elsevier Science Limited, Vol. 101, pp. 363–372.

Wardenier, J., Kurobane, Y., Packer, J. A., van der Vegte, G. J., and Zhao, X. L. (2008). *Design guide for circular hollow section (CHS) joints under predominantly static loading*. Second Edition, CIDECT series 'Construction with hollow sections', No. 1, Germany.

Wardenier, J., Packer, J. A., Zhao, X. L., and van der Vegte, G. J. (2010). *Hollow sections in structural applications*. Second Edition, CIDECT, Geneva, Switzerland.

Wu, L., Chung, L., Tsai, S., Lu, C., and Huang, G. (2007). "Seismic behaviour of bidirectional bolted connections for CFT columns and H-beams". *Engineering Structures*, ISSN 0141-0296, Elsevier Science Limited, Vol. 29 (3), pp. 395-407.

Zhang, D., Gao, S., and Gong, J. (2012). "Seismic behaviour of steel beam to circular CFST column assemblies with external diaphragms". *Journal of Constructional Steel Research*, ISSN 0143-974X, Elsevier Science Limited, Vol. 76, pp. 155–166.

Ziemian, R. D. (2010). *Guide to stability design criteria for metal structures*. Sixth Edition, John Wiley & Sons, Hoboken, New Jersey, United States of America.

# *Appendix A*

## *LabVIEW Graphical Codes*

This appendix presents the LabVIEW block diagram, and its graphical code, designed for the experimental work of this research. The LabVIEW programme synchronised the outputs of the different instruments in a test with each other, logged them to a computer, applied the appropriate calibration factors to them, monitored the calibrated measurements on the front panel of the LabVIEW programme during testing, produced important plots on the front panel and finally recorded all the obtained data to a file saved on the test-computer. Figure A.1 illustrates the whole block diagram of the joint-test programme. Due to the complexity of this code, the main processes carried out in it were highlighted in Figure A.1 and detailed more clearly in Figures A.3 to A.6.

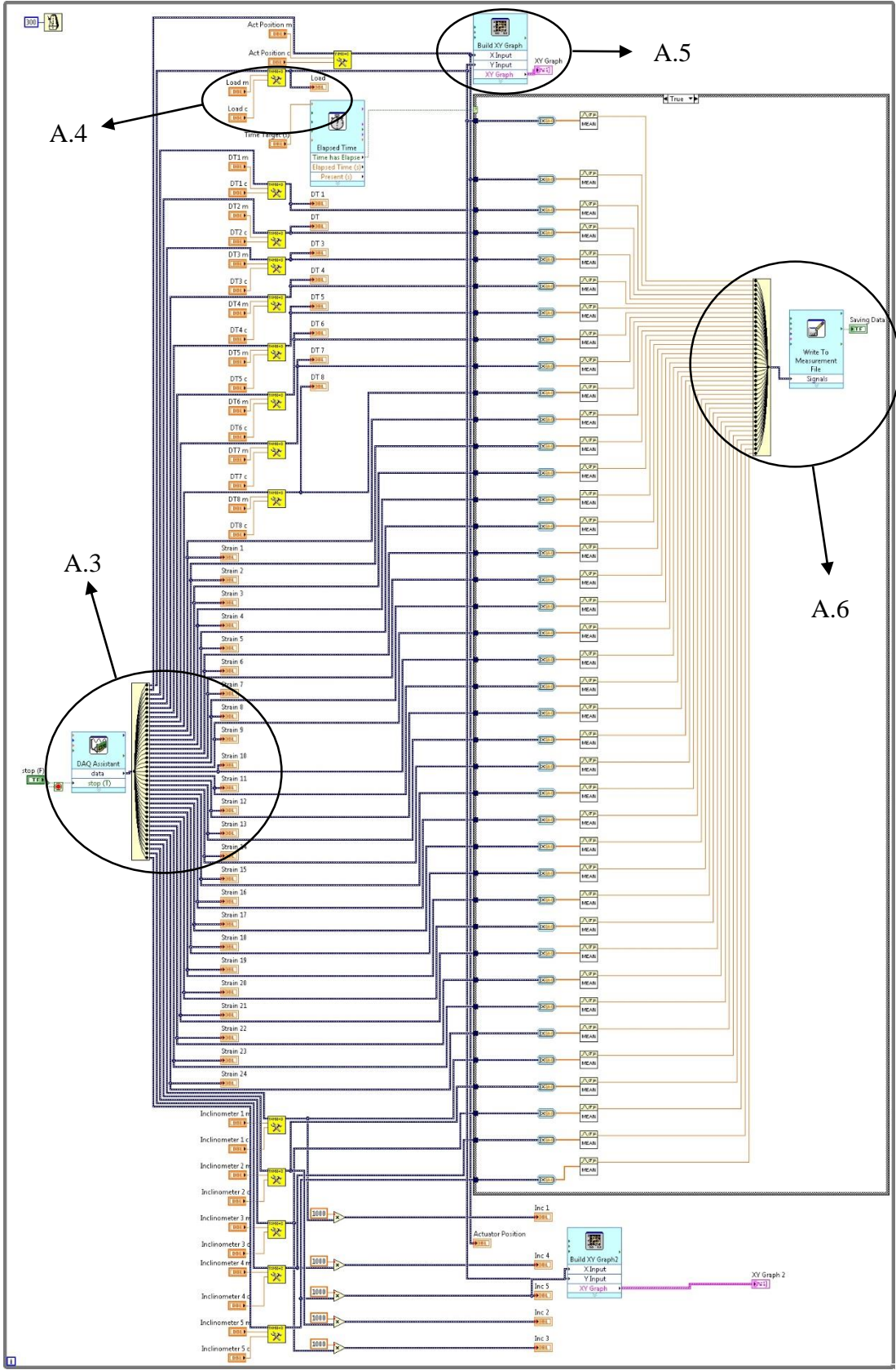
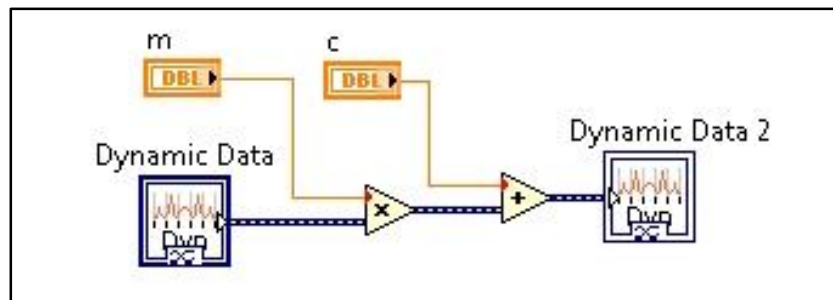


Figure A.1: Block diagram of the main joint-test programme in LabVIEW

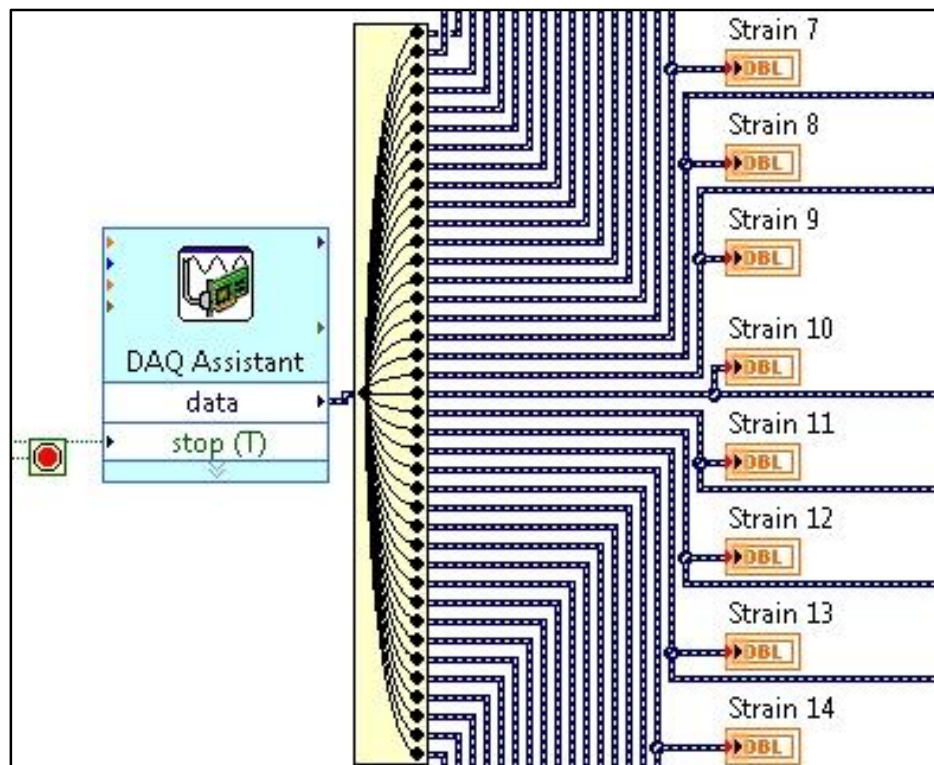


The yellow icons that can be noticed in Figure A.1 represent a sub-programme named “*Calibration*” built with LabVIEW to perform the calibration of an instrument measurement after inputting the values of its calibration factors ( $m$  and  $c$ ). The block diagram of the sub-programme “*Calibration*” is shown in Figure A.2.



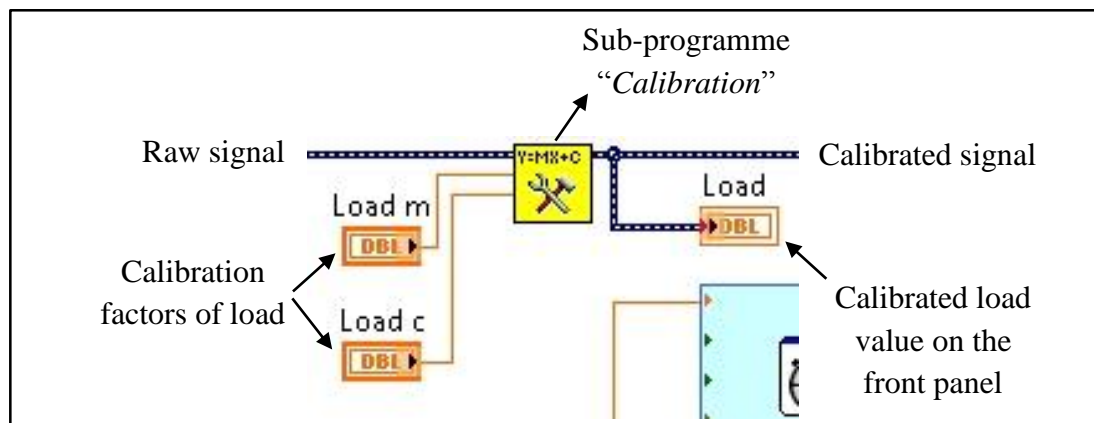
**Figure A.2:** Block diagram of the sub-programme “*Calibration*” in LabVIEW

Figure A.3 presents a detail from the main-test block diagram, and it highlights the data acquisition function that produced all the measurements signals obtained from the test instruments that were connected to the NI hardware.



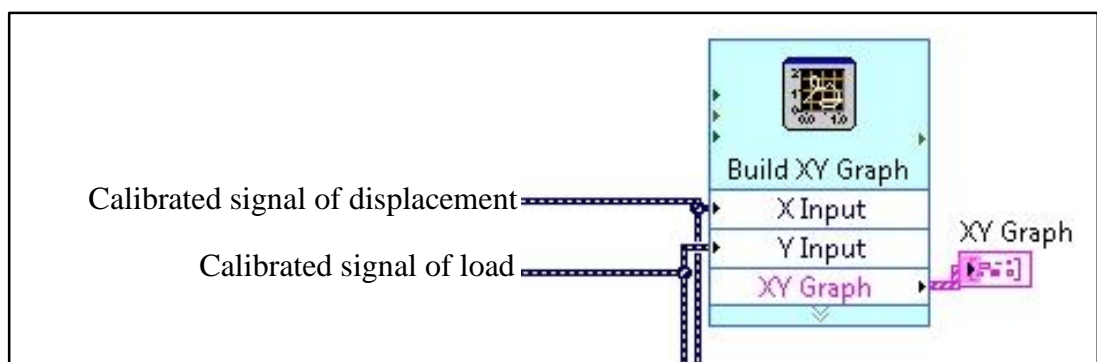
**Figure A.3:** Block diagram detail – Data acquisition function

Figure A.4 presents another detail from the main-test block diagram, which gives an example of recalling the sub-programme “Calibration” into the main-test code to apply the calibration factors (m and c) of an instrument, which is the actuator load cell in this detail, to its raw signal. The “Calibration” sub-programme was recalled for all other measurements except for the ones obtained from the strain gauges because they were calibrated automatically through the NI system.



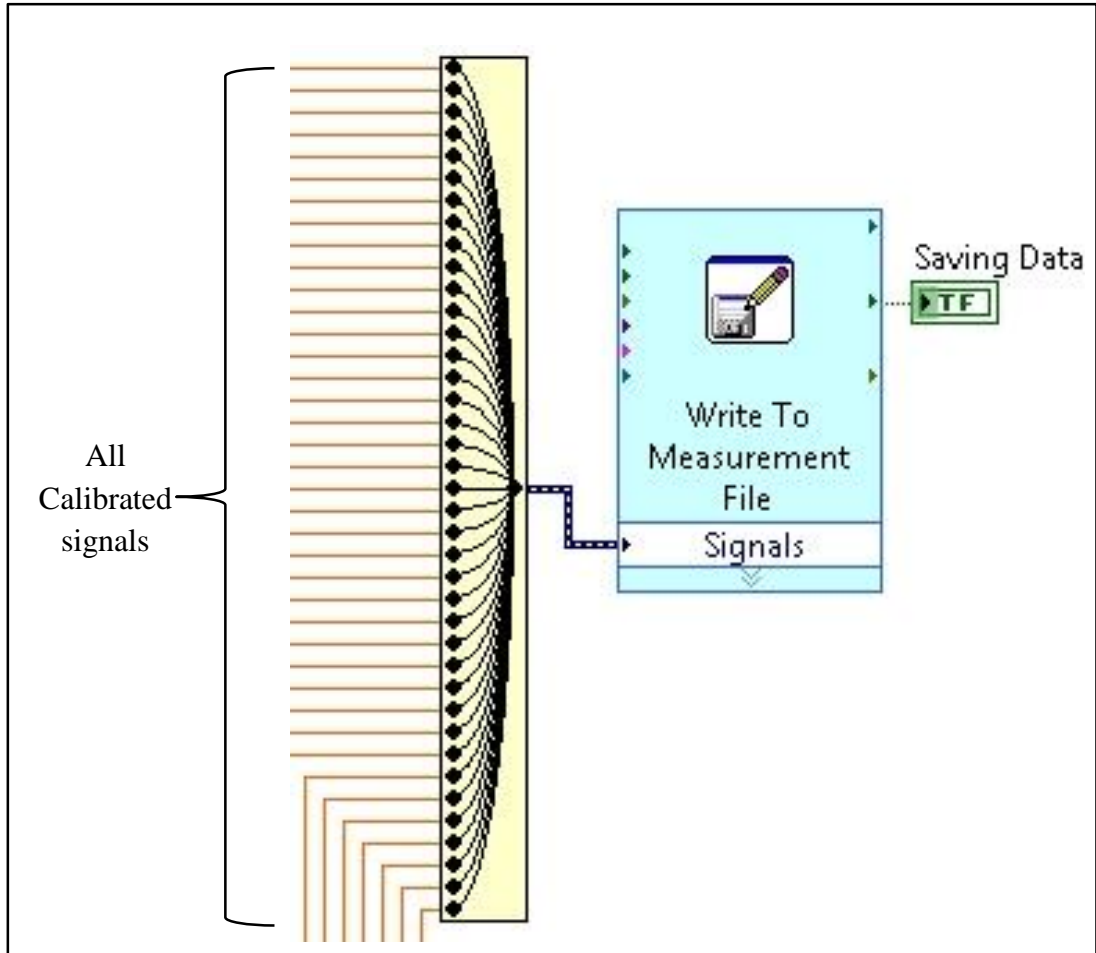
**Figure A.4:** Block diagram detail – Recalling the sub-programme “Calibration”

Figure A.5 presents one more detail from the main-test block diagram, and it shows how the plot of “Load vs. Actuator displacement” was produced on the front panel of LabVIEW to monitor its values during testing.



**Figure A.5:** Block diagram detail – Producing the “Load vs. Actuator displacement” plot on the front panel of LabVIEW

Figure A.6 illustrates the last highlighted detail from the main-test block diagram, and it shows how the values of the calibrated measurements of a test were written to a “Microsoft Excel” file saved on the hard drive of the test-computer.



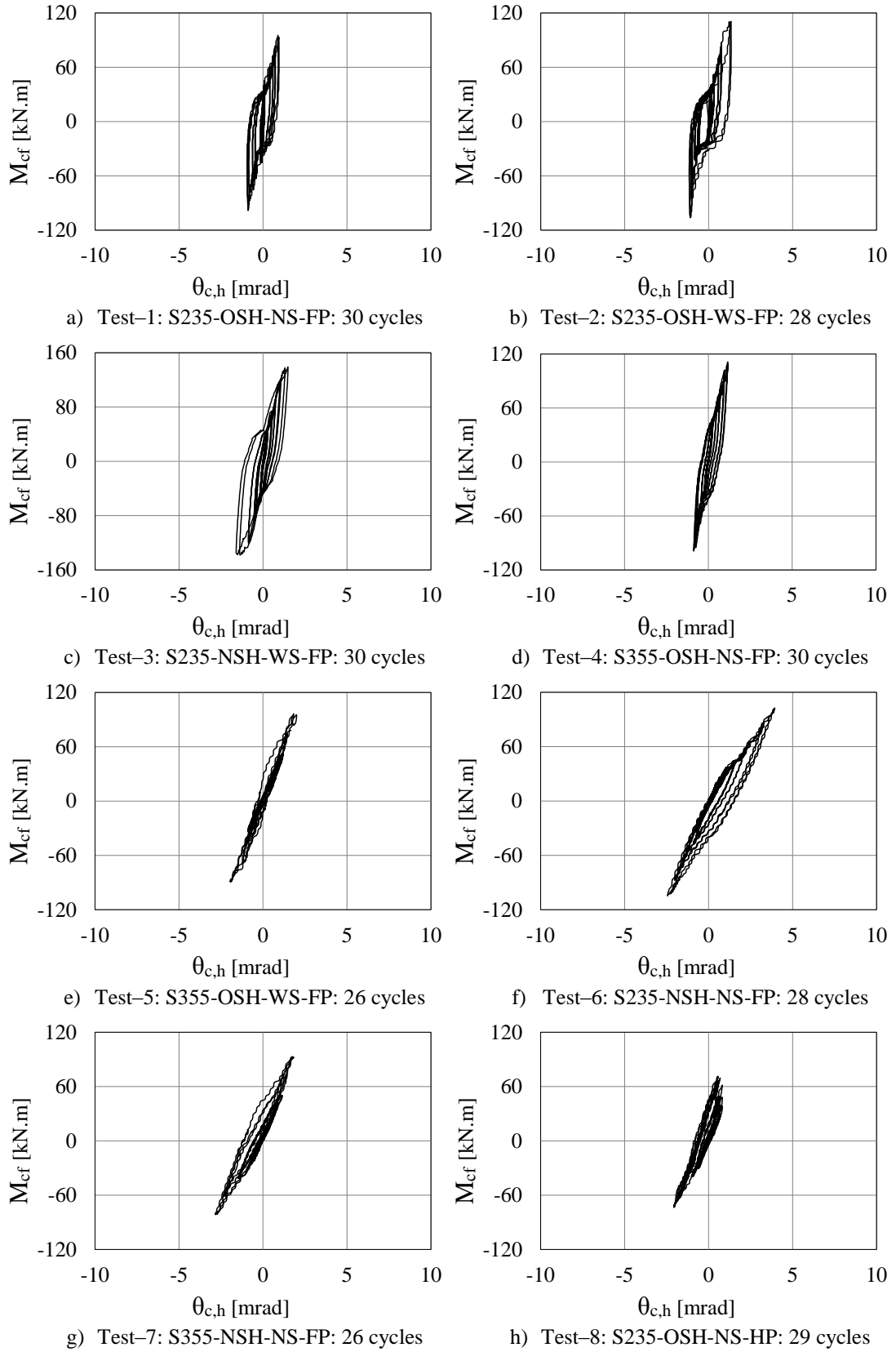
**Figure A.6:** Block diagram detail – Saving calibrated measurements to an Excel file

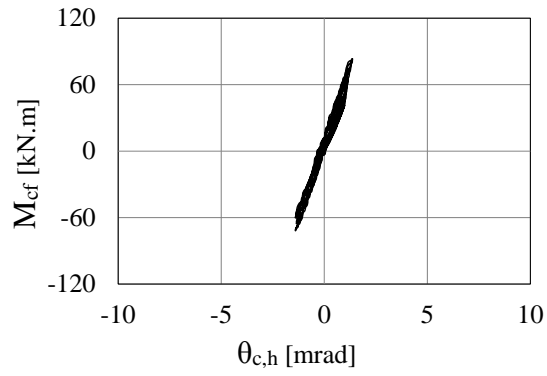
# *Appendix B*

## *Rotation of The Column Hinges*

This Appendix presents the rotation measurements of the column hinges  $\theta_{c,h}$  obtained using the displacement transducers DT-1 and DT-4 in the nine joint tests. Locations and details of the two transducers are described in Section 5.7.4.  $\theta_{c,h}$  was calculated by dividing the difference between the measurements of the displacement transducers DT-1 and DT-4 by the vertical distance of 2000mm between their bodies. However, DT-1 illustrated abnormal readings in Tests 1 and 2 due to the weakness of its attachments, which caused the transducer body to move slightly during testing. This affected the reliability of DT-1 measurements in Tests 1 and 2, and so  $\theta_{c,h}$  were calculated by doubling the measurements of DT-4 and then dividing them by 2000mm. The weak attachments of DT-1 were replaced in Tests 3-9 by stronger ones that guaranteed no movement of the transducer body, which subsequently produced reliable results. Moments calculated at the column face  $M_{cf}$  are plotted against  $\theta_{c,h}$  for the nine tests, as shown in the plots in Figure B.1.

Appendix B: *Rotation of The Column Hinges*





i) Test-9: S355-OSH-WS-HP: 30 cycles

**Figure B.1:** *Moment-rotation curves of the column hinges in Tests 1–9*

# *Appendix C*

## *Elastic Deformation of The I-beam*

This Appendix details the calculation of the relative elastic rotation of the I-beam between the sections at which INC-4 and INC-5 were mounted. The elastic rotations in this appendix were compared to those obtained in the nine tests, by means of subtracting the measurements of INC-4 from INC-5, and they were found to be very similar. This proved that the I-beam suffered elastic deformations only in the nine tests.

To simplify the calculation of the elastic rotational deformation of the I-beam, the latter was assumed to be a cantilever beam fixed at one end (at the connection) and subjected to a vertical load at the other end (the actuator), as shown in Figure C.1. The assumed cantilever has the same section, length and material properties of the I-beam. The elastic deformation of a cantilever at a certain section can be calculated using the equation C.1.

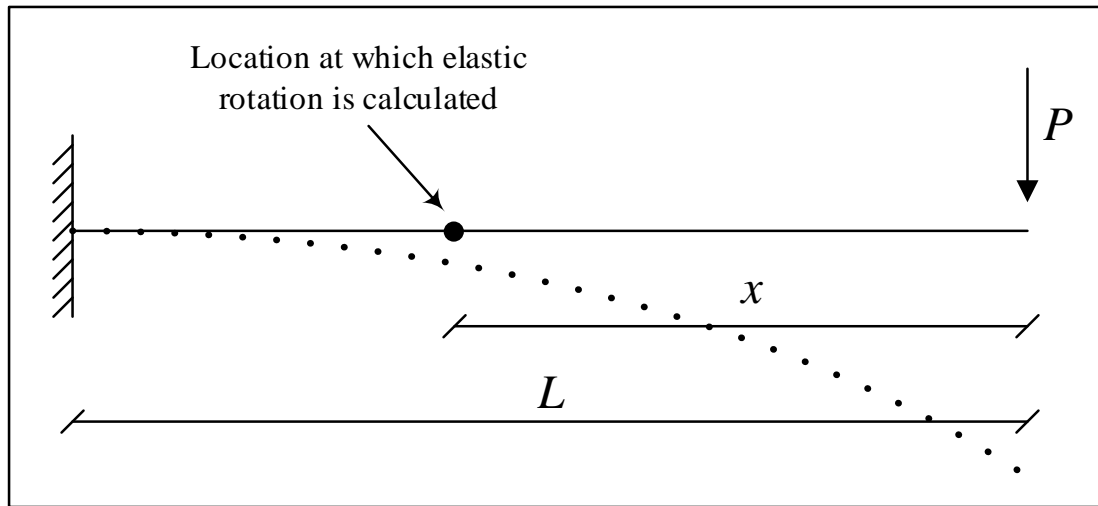


**Figure C.1:** Elastic rotation of a cantilever at a given section

$$\theta_{el} = P \times (L^2 - x^2) / (2 \times E \times I_y) \quad (C.1)$$

Where  $\theta_{el}$  here is the elastic rotation of the cantilever at a certain section,  $P$  is the vertical load acting on the cantilever free end (the actuator load),  $L$  is the length of the cantilever,  $x$  is the distance between the section at which rotation is calculated and the loading point,  $E$  is the Young modulus of the cantilever steel and  $I_y$  is the second moment of area of the cantilever about its major axis.

The only variable in Equation C.1 is “ $x$ ” whose value depends on the location of the cantilever section at which rotation is calculated. Equation C.1 was used to calculate the elastic rotation of the I-beam as a cantilever at the locations of INC-4 and INC-5 using the values ( $x = 1.63\text{m}$ ) and ( $x = 1.43\text{m}$ ) respectively. The relative elastic rotation between the two sections was obtained by subtracting the elastic rotations calculated at the location of INC-4 from those calculated at the location of INC-5.

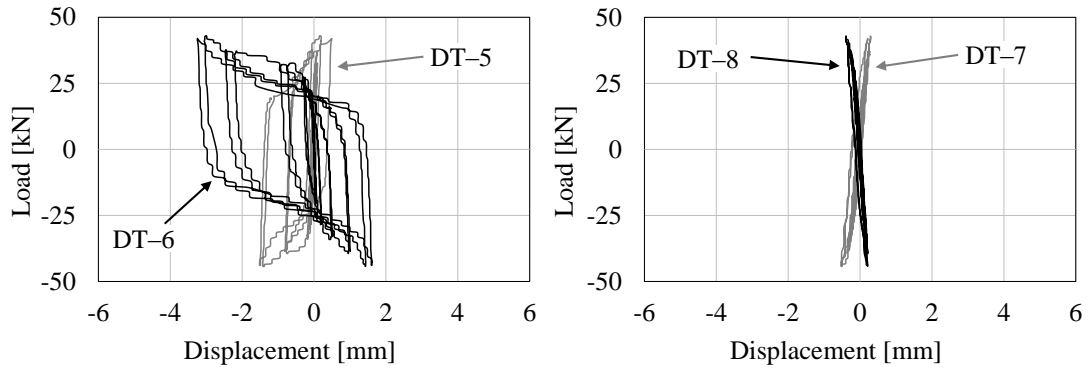


# *Appendix D*

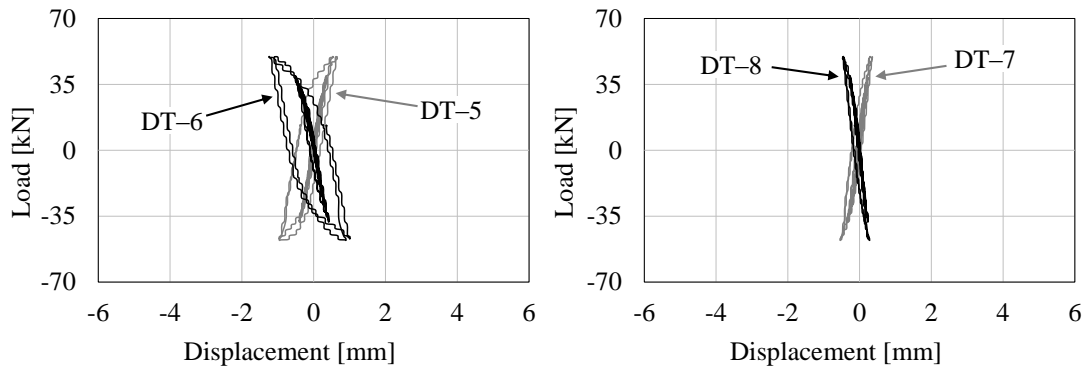
## *Connection Slip Measurements*

This Appendix presents the measurements of DT-5, DT-6, DT-7 and DT-8 in the nine tests. Locations and details of the four transducers are described in Section 5.7.4. DT-5 and DT-6 were used in all tests to measure the relative deformation and connection slip between the tapered cover plates and the diaphragm plates. Whereas DT-7 and DT-8 were used to measure the relative deformation and connection slip between the tapered cover plates and the I-section beam. Loads from the actuator load cell are plotted against the displacement measurements obtained from the displacement transducers DT-5, DT-6, DT-7 and DT-8 for the nine tests, as shown in the plots of Figure D.1. Connection slips were noticed in Test-8 and Test-9, which are presented in Figures D.1 (h) and D.1 (i). The preloading force acting on the TCPs bolts in these two tests was half the value recommended in BS EN 1993-1-8: 2005 for slip-resistant connections. No significant slippage was observed in Tests 1 to 7 in which bolts were fully preloaded to the recommended value in Eurocode 3: Part 1-8, although the connection slip resistance was designed to occur. This is due to the uncertainty about the real slip factor of the friction surfaces when the

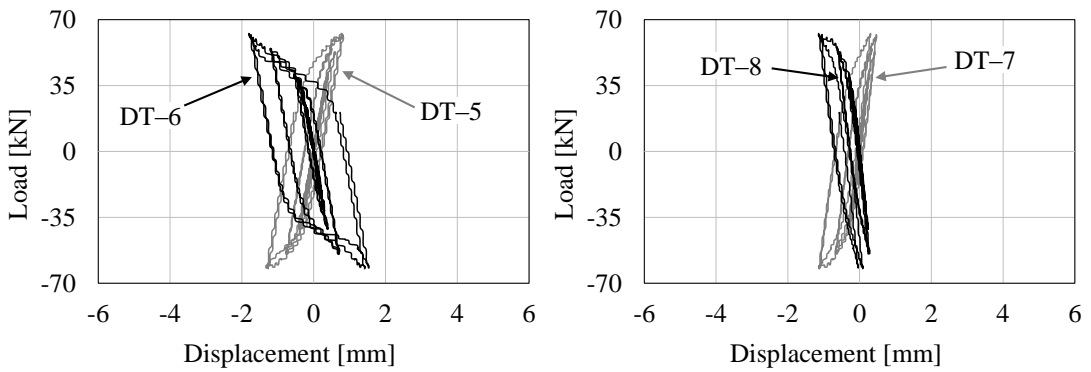
connection slip resistance was calculated theoretically and the uncertainty about the actual bolts preloading forces that were applied using a torque wrench.



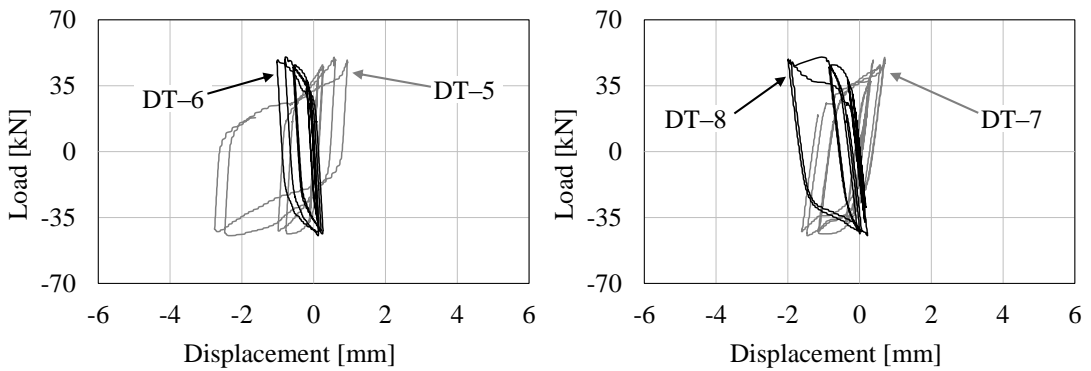
a) Test-1: S235-OSH-NS-FP: 30 cycles



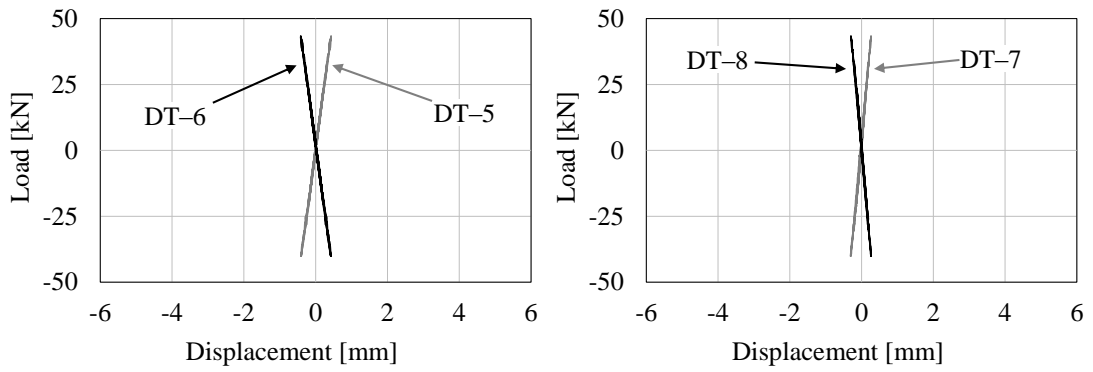
b) Test-2: S235-OSH-WS-FP: 28 cycles



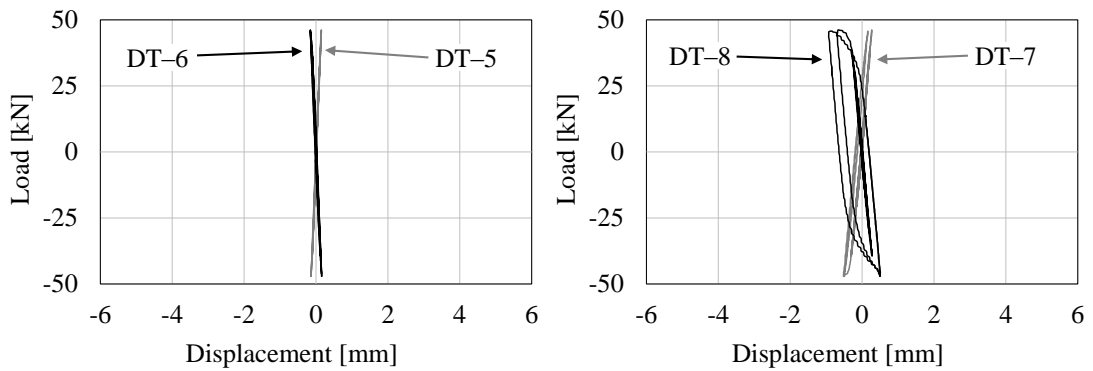
c) Test-3: S235-NSH-WS-FP: 30 cycles



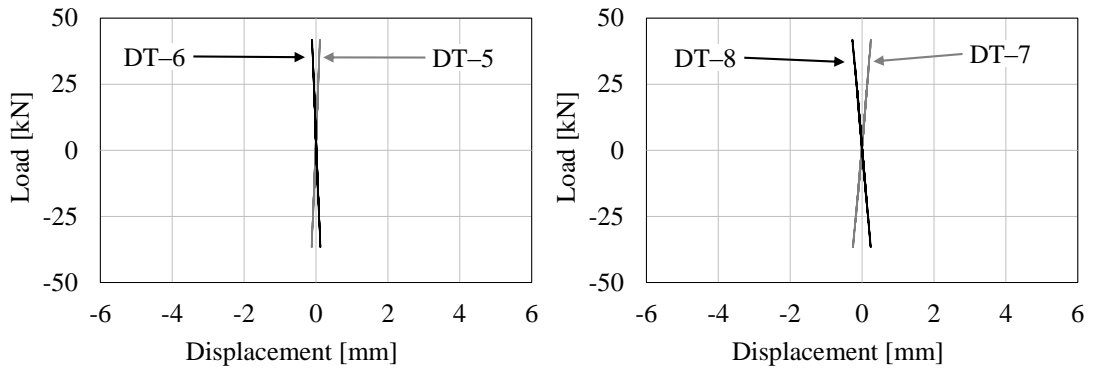
d) Test-4: S355-OSH-NS-FP: 30 cycles



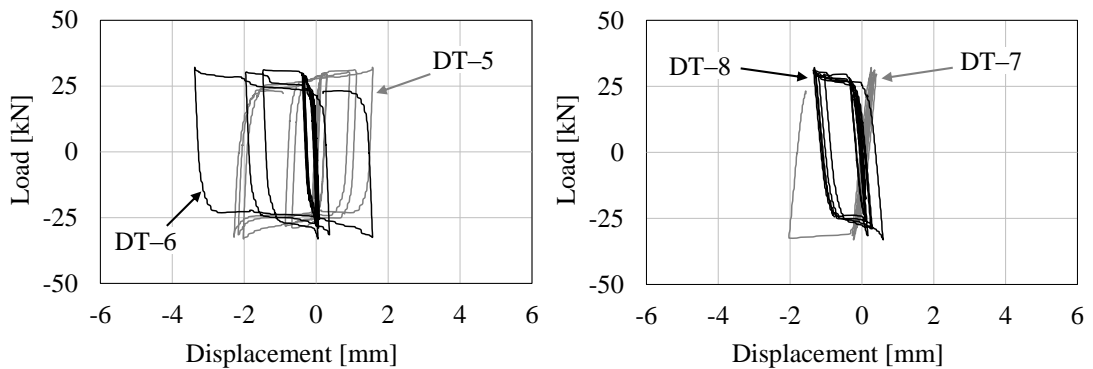
e) Test-5: S355-OSH-WS-FP: 26 cycles



f) Test-6: S235-NSH-NS-FP: 28 cycles



g) Test-7: S355-NSH-NS-FP: 26 cycles



h) Test-8: S235-OSH-NS-HP: 29 cycles

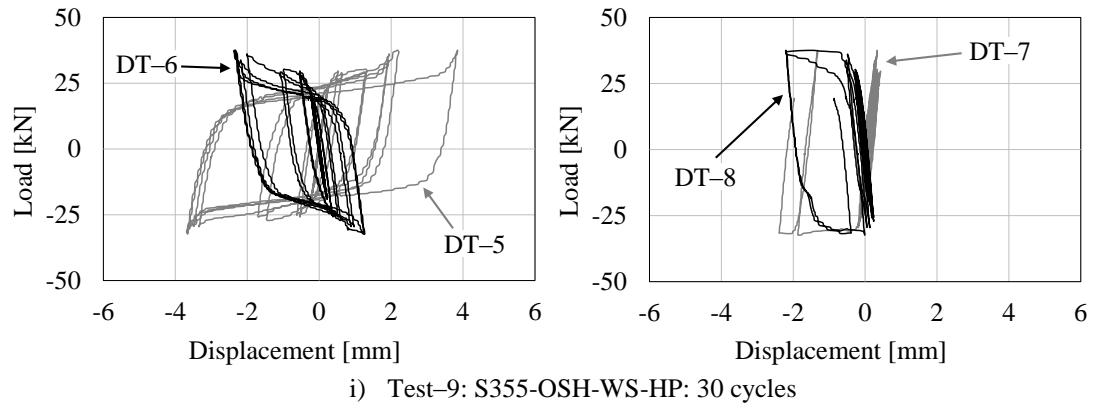


**Figure D.1:** Load–displacement curves for the DTs (5, 6, 7 and 8) in Tests 1–9

# *Appendix E*

## *EuroSteel-2014 Conference Paper*

This Appendix presents the conference paper and its extended abstract that have been submitted and accepted for publication at the seventh edition of the European Conference on Steel and Composite Structures (EuroSteel) to be held in Naples, Italy in September 2014. The conference paper is titled “Structural behaviour of external diaphragm connection between steel I-section beam and circular hollow section columns under cyclic loading”. This paper covers the results of three tests from the experimental programme of this project and investigates the influence of using stiffeners to TCPs and different bolts preloading values on the overall seismic performance of the joint. The full text of this conference paper and its extended abstract are presented next.

EUROSTEEL 2014, September 10-12, 2014, Naples, Italy

**STRUCTURAL BEHAVIOUR OF EXTERNAL DIAPHRAGM  
Connection between Steel I-Section Beam and Circular Hollow Section Columns  
under Cyclic Loading**

Majd Khador<sup>a</sup>, Tak-Ming Chan<sup>a</sup>

<sup>a</sup>University of Warwick, School of Engineering, UK  
[M.Khador@warwick.ac.uk](mailto:M.Khador@warwick.ac.uk), [T.M.Chan@warwick.ac.uk](mailto:T.M.Chan@warwick.ac.uk)

**INTRODUCTION**

Tubular columns own many special structural and architectural features that can make them more favourable than open-section columns in steel moment-resisting frames [1-2]. Different configurations for I-beam to tubular column connections have been investigated including through diaphragm, external diaphragm and through plate connections [2-5]. Alostaz and Schneider [6] investigated the use of external diaphragm plates welded to the outer circumference of a tubular column. When these connections were tested under cyclic loading, large distortion of the tube wall was noted around the connection area, and high stress concentrations were observed in the diaphragm plates leading to fracture in them and their weld. A numerical parametric study on a single-sided I-beam to CHS column joint under monotonic and cyclic loadings was carried out by Sabbagh et al. [7] to establish joint details that eliminate the structural deficiencies identified in the work of Alostaz and Schneider [6]. To avoid fracture in the I-beam flanges due to local buckling failure and to protect the primary members of the joint under seismic actions, a joint detailing was proposed which involved shifting the beam away from the column face, using tapered cover plates to connect the I-beam flanges to the diaphragm plates and bolting the I-beam web to a single-sided web stub plate welded to the column face. The tapered cover plates (TCPs) with oversized bolt holes were integrated in the joint to act as a sacrificial energy dissipation fuse by designing them to reach full plasticity before the I-beam reached its plastic bending resistance in order to create a multi-fuse energy dissipative mechanism in the joint under seismic actions. Bolt holes in the web stub plate were oversized with the maximum practical clearance, and the bolts were appropriately preloaded to allow slippage in the web connection to occur after the onset of the inelastic joint response. Yielding in TCPs was the main energy dissipation mechanism accompanied by bolts slippage and yielding in the beam's section located right after the connection as two extra energy dissipation fuses. In this paper, the work of Sabbagh et al.[7] is investigated experimentally; a series of full-scale laboratory experiments of the external diaphragm joint were conducted in the Structures Laboratory at the School of Engineering, University of Warwick, and selected results are presented herein.

**1 EXPERIMENTAL SET-UP AND DETAILS**

**1.1 Test specimens**

The proposed single-sided joint included two diaphragm plates (DPs) welded to the outer circumference of a circular hollow section column using complete joint penetration (CJP) welds and bolted to the I-beam flanges with two tapered cover plates (TCPs). A single-sided web stub (WS) plate was welded to the CHS column and bolted to the I-beam web with three M16 bolts of class 10.9. The specimens of the tests were identical except for their tapered cover plates that were bolted to the I-section beam from one end and to the diaphragms plates from the other end using 24×M22 bolts of class 10.9. The I-beam (UKB: 203×133×30, grade S355) was used in this joint and was designed to be 2m long. The CHS column (244.5×10, grade S355) with the height of 2m was used in all tests, and its boundary conditions were designed to be hinges. The arrangement and components of the beam to column joint after assembly are illustrated in Fig. 1.

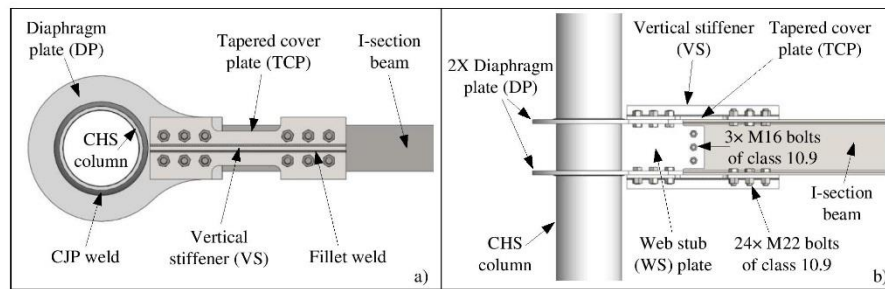


Fig. 1. Test specimen components a) Top view; b) Front view

The diaphragm plates' (grade S355) geometry shown in Fig. 2 was chosen efficiently to allow for a smooth stress flow around and into the CHS column to eliminate any stress concentration in them or distortion in the column web panel. The web connection (grade S355) was designed to transfer the shear forces from the I-beam to the column face efficiently. The bolt-holes in the web stub were oversized with 6mm clearance in accordance to the AISC standards [8], and bolts of the web connection were preloaded so that slip was activated after the occurrence of yield in the TCPs to eliminate any distortion in the web stub. The tapered cover plates were designed to act as a seismic energy dissipation fuse in the connection, and be the replaceable components of the connection whilst the rest of the joint components keep intact. Thus, it was crucial to understand the effect of using different types of TCPs on the overall cyclic performance of the connection under seismic actions. The pairs of TCPs used in the experimental work had the same geometry, shown in Fig. 2, but differed from each other on steel grade, size of the bolt-holes, use of stiffeners and value of the bolts' preloading force.

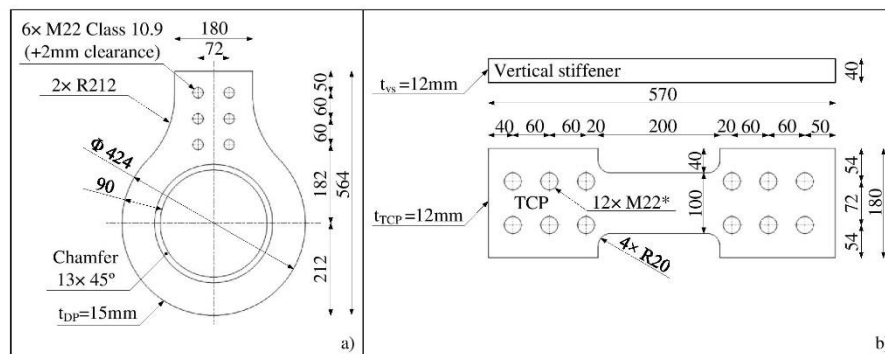


Fig. 2. Geometry of a) Diaphragm plate; b) Tapered cover plate and stiffener (all dimensions in [mm])

The reference used for tests' titling follows the format G-H-S-BP where G represents the steel grade of the TCPs; H is the size of the TCPs bolt-holes; S reflects the use of stiffeners in TCPs; and BP is the preloading force acting on the TCPs' bolts. The type of TCPs used in the reported test specimens is detailed in Table 1.

### 1.2 Material properties

Tensile coupon (TC) tests were carried out in the Material Laboratory at the University of Warwick in accordance with the British standard for tensile testing [9] to determine the actual material properties of the steel that composes the different components of the test specimens.

Table 1. Type of TCPs used in test specimens

Test number	Test title	Type of tapered cover plates (TCPs)			
		Steel grade	Size of bolt-holes	Use of stiffeners	Bolts preload force
1	S235-OSH-NS-FP	S235	Oversized	No	Full preload
2	S235-OSH-WS-FP	S235	Oversized	Yes	Full preload
3	S235-OSH-NS-HP	S235	Oversized	No	Half preload

### 1.3 Test layout

A test rig was designed and built in the Structures Laboratory at the University of Warwick to transfer the loads applied to test specimens to the strong floor safely. A 100kN hydraulic actuator, connected to a reaction frame, was used to apply vertical displacement-controlled loading at the specimen's I-beam. A loading mechanism including swivel hinges was designed to accommodate the large rotations expected in the connection whilst maintaining the verticality of the actuator. Two more hinges were designed and connected to the ends of the specimen's column to provide the column's boundary conditions assumed in the design stage. The schematic arrangement and a photograph of the test rig are shown in Fig. 3.

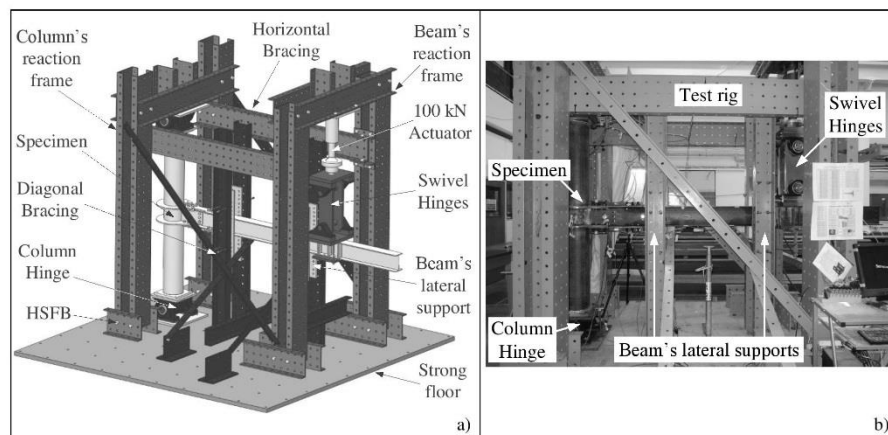


Fig. 3. Test rig a) Schematic arrangement; b) Laboratory photograph at the University of Warwick

### 1.4 Loading protocol

The loading protocol adopted for this experimental study was based on the AISC provisions [10] for qualifying beam-column moment joints in special and intermediate moment frames. The cyclic loading was conducted by controlling the vertical deflection of the beam's section located under the actuator. Fig. 4 shows the displacement-controlled loading protocol used in all tests.

### 1.5 Instrumentations

Electrical post-yield strain gauges were used at the expected locations of plastic hinges, stress concentration regions and other areas in the test specimen where strain levels should be monitored. Eight strain gauge displacement Transducers were installed horizontally at different locations of the test specimen to measure primary slips and displacements. Electronic inclinometers were also used in the tests to measure angle of rotation in five different locations of the specimen and calculate the accurate rotation of the connection. All instrumentations were calibrated prior to and after conducting the tests.



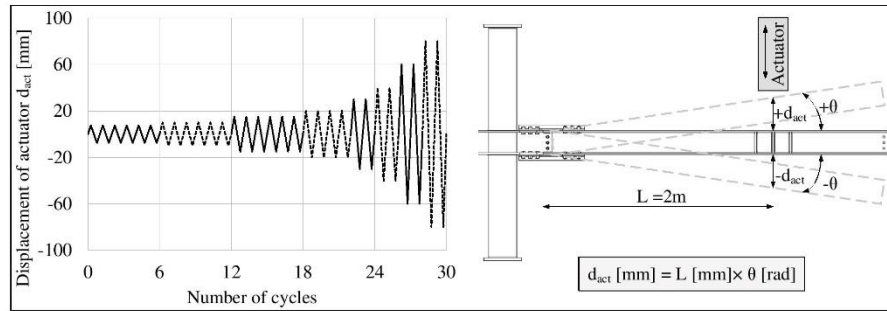


Fig. 4. Loading protocol

## 2 EXPERIMENTAL RESULTS AND OBSERVATIONS

### 2.1 Failure modes

The results of all tests revealed that yielding was limited to the reduced section areas of the TCPs and their stiffeners when applicable; whereas all the other joint components showed elastic response throughout testing.

### 2.2 Hysteretic response

The main response parameters obtained from three of the tests (Test–1, 2 and 3) are presented in Table 2, and their hysteresis plots are illustrated in Fig. 5. The moments of the connection  $M_{\text{connection}}$  were calculated at the beam's connected end and were then normalised by dividing them by the design elastic bending resistance of the beam  $M_{b,el,y} = 117.46$  kN.m in Fig. 5. Some of the tests were stopped before completing the loading program described in section 1.4 of this paper due to technical challenges related to the laboratory facilities. The number of completed cycles for each of the three tests discussed in this section is included in Table 2.

Table 2. Summary of results for cyclic tests 1, 2 and 3

Test number	Test title	Number of completed cycles	Maximum moment [kN.m]	Maximum rotation [mRad]	Dissipated energy [kN.m.Rad]
1	S235-OSH-NS-FP	30	88.1	21.1	12.76
2	S235-OSH-WS-FP	28	99.2	7.7	3.23
3	S235-OSH-NS-HP	29	65.9	25.8	12.76

Both pairs of tapered cover plates used in the specimens of Test–1 and Test–2 had the same steel grade (S235), same size of bolt holes (OSH) and same preloading force acting on their bolts (FP). The only difference between the two test specimens was the use of stiffeners for the TCPs in Test–2. Comparing the two tests results helped understand the influence of using TCPs' stiffeners on the overall hysteretic behaviour of the connection. As expected, it was found that the use of stiffeners resulted in a connection with higher stiffness and strength. The maximum  $M_{\text{connection}}/M_{b,el,y}$  ratios recorded at the end of cycle 28 in Test–1 and Test–2 were 67% and 84% respectively. Furthermore, comparing strain measurements in both tests revealed that there were higher stress demands on the I-beam and the diaphragm plates when the TCPs were stiffened. It was also found that the connection maximum rotation obtained at the end of cycle 28 in Test–1 was two times bigger than that at the end of cycle 28 in Test–2.

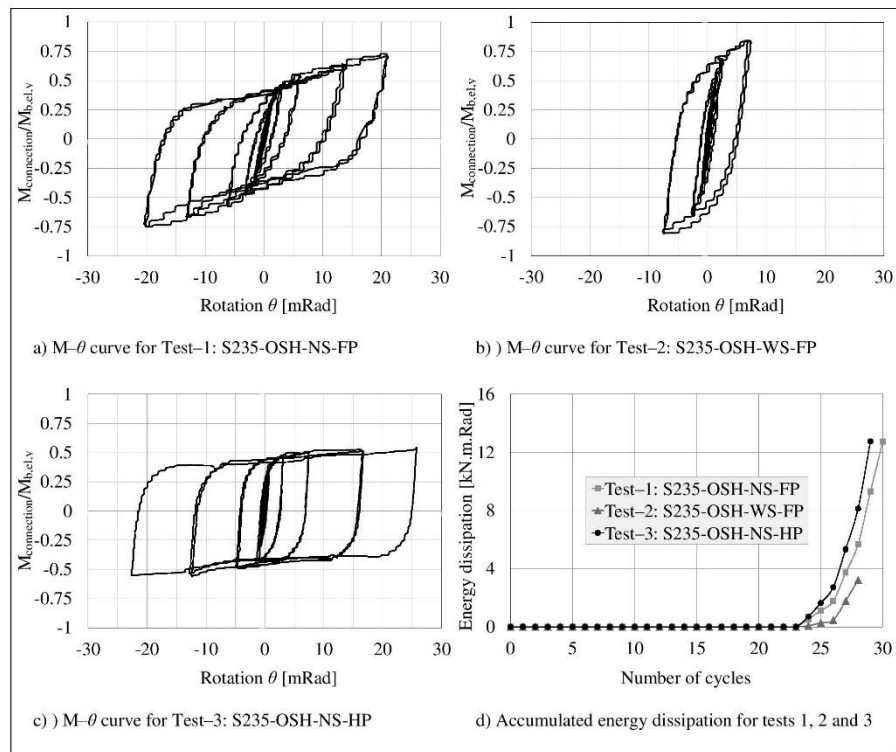


Fig. 5. Moment-rotation hysteresis and energy dissipation for the connections in tests 1, 2 and 3

Similarly, the results of Test-1 and Test-3 were compared together up to the end of cycle 29. Their TCPs were identical but differed only in the value of preloading force acting on their bolts. The maximum  $M_{\text{connection}}/M_{b,el,y}$  ratios recorded at the end of cycle 29 of Test-1 and Test-3 were 75% and 56% respectively. The relatively earlier activation of slip in the connection with half-preloaded bolts caused slightly less stress demands on the beam and DPs in comparison to the connection with fully-preloaded bolts although yielding in the TCPs occurred at the same moment value in both tests. Additionally, the maximum connection rotation obtained at the end of Test-3 was 20% higher than that at the end of cycle 29 in Test-1.

### 2.3 Energy dissipation

Accumulated energy dissipation values at the end of each loading cycle were obtained for all tests by calculating the areas enclosed by the moment-rotation hysteresis loops. Fig. 5 illustrates the actual accumulated energy dissipation values at the end of each cycle for tests 1, 2 and 3, and the total energy dissipation values at the end of these three tests are presented in Table 2. It can be seen from Fig. 5 that the difference in energy dissipation values between the three tests were negligible up to cycle 24 because yielding had not occurred yet and hence the dissipation values were very small. However, it is apparent in the following cycles that the absence of stiffeners in Test-1 led to higher energy dissipation than that in Test-2. Tests 1 and 3 showed similar energy dissipation behaviour up to cycle 25 during which slip was activated in the connection of Test-3 resulting in higher energy dissipation values than those achieved in Test-1 in all the subsequent cycles. This is because the slip activation created a new fuse for energy dissipation in addition to the existing one that is yielding in the TCPs.

### 3 CONCLUSIONS

Full-scale laboratory experiments were carried out on a series of external diaphragm connection to CHS column incorporating different types of tapered cover plates which were designed to act as replaceable links in the connection after seismic actions whilst the rest of the joint components keep intact. The results of three tests were reported in this paper highlighting the effect of using TCPs' stiffeners and controlled bolts preloading force on the overall hysteretic response of the connection and its energy dissipation. The results presented in this paper confirmed that the main energy dissipation fuse in these connections was yielding in the reduced section areas of the TCPs; and that stiffening TCPs resulted in a stronger connection but imposed higher stress demands on the beam and the diaphragm plates and dissipated less energy than the same connection with unstiffened TCPs. Reducing the preloading force acting on the TCP's bolts to half the value recommended in Eurocode 3: Part 1-8 [11] for slip-resistant connections created a second fuse for energy dissipation that was slip activation in the oversized bolt-holes of the connection, which subsequently led to higher rates of energy dissipation.

### 4 ACKNOWLEDGMENTS

The authors are grateful to the Engineering and Physical Science Research Council (EP/1020489/1) for the project funding and Damascus University for the doctoral scholarship awarded to the first author. Financial support from TATA Steel, the School of Engineering at the University of Warwick and the technical support from the Structures Laboratory at the University of Warwick are gratefully acknowledged. The authors wish also to thank Dr Alireza Bagheri Sabbagh for his advice and contribution to this research.

### REFERENCES

- [1] Wardenier J. P. J. A., Zhao X. -L., Vegte G.J. van der, 2010. *Hollow Sections in Structural Applications*, CIDECT, Switzerland.
- [2] Kurobane Y., Packer J.A., Wardenier J., Yeomans N., 2005. *Design Guide for Structural Hollow Section Column Connections*, First Edition, CIDECT, Germany.
- [3] Mesquita A.B., Simões da Silva L.A.P., Jordão S., 2009. "Experimental Behaviour of I Beam – SHS Column Steel Joints with Holo-bolts". *The Nordic Steel Construction Conference*, 2 September – 4 September, 2009, Malmö, Sweden, ISBN 978-82-91466-12-5, pp. 230-237.
- [4] Chan T.M., Gardner L., 2008. "Bending strength of hot-rolled elliptical hollow sections". *Journal of Constructional Steel Research*, ISSN 0143-974X, Elsevier Science Limited, Vol. 64 (9), pp. 971-986.
- [5] Wang W., Chen Y., Li W., Leon R.T., 2011. "Bidirectional seismic performance of steel beam to circular tubular column connections with outer diaphragm". *Earthquake Engng Struct. Dyn.*, ISSN 1096-9845, John Wiley & Sons Limited, Vol. 40, pp. 1063-1081.
- [6] Alostaz Y.M., Schneider S.P., 1996. "Analytical Behavior of Connections to Concrete-filled Steel Tubes". *Journal of Constructional Steel Research*, ISSN 0143-974X, Elsevier Science Limited, Vol. 4 (2), pp. 95-127.
- [7] Sabbagh A.B., Chan T.M., Mottram J.T., 2013. "Detailing of I-beam-to-CHS column joints with external diaphragm plates for seismic actions". *Journal of Constructional Steel Research*, ISSN 0143-974X, Elsevier Science Limited, Vol. 88, pp. 21-33.
- [8] *Specification for structural steel buildings*, 2010. American Institution of Steel Construction (AISC).
- [9] *Metallic materials - Tensile testing - Part 1: Method of test at ambient temperature*, 2009. British Standards Institution (BSI).
- [10] *Seismic provisions for structural steel buildings*, 2005. American Institution of Steel Construction (AISC).
- [11] *Eurocode 3: Design of steel structures – Part 1-8: Design of joints*, 2005. British Standards Institution (BSI).

EUROSTEEL 2014, September 10-12, 2014, Naples, Italy

**STRUCTURAL BEHAVIOUR OF EXTERNAL DIAPHRAGM  
Connection between Steel I-Section Beam and Circular Hollow Section Columns  
under Cyclic Loading**

Majd Khador<sup>a</sup>, Tak-Ming Chan<sup>a</sup>

<sup>a</sup>University of Warwick, School of Engineering, UK  
[M.Khador@warwick.ac.uk](mailto:M.Khador@warwick.ac.uk), [T.M.Chan@warwick.ac.uk](mailto:T.M.Chan@warwick.ac.uk)

**KEYWORDS:** Moment–rotation behaviour, external diaphragm connections, tubular columns, replaceable links, energy dissipation.

**ABSTRACT**

Tubular columns own many special structural and architectural features that can make them more favorable than open-section columns in steel moment-resisting frames. Different configurations for I-beam to tubular column connections have been investigated including through diaphragm, external diaphragm and through plate connections [1]. This paper in particular investigates experimentally the cyclic behavior of an external diaphragm connection between steel I-beam and circular hollow section column. The proposed joint [2] includes two diaphragm plates (DPs) welded to the outer circumference of the circular hollow section (CHS) column and bolted to the I-beam flanges with two tapered cover plates (TCPs). A web stub is welded to the column face and bolted to the I-beam web, see Fig. 1. The TCPs were integrated in the detailing of the joint to create a sacrificial energy dissipation mechanism, and were designed to act as replaceable links in the connection after seismic actions whilst the rest of the joint components keep intact. A series of laboratory experiments of the external diaphragm joint were conducted in the Structures Laboratory at the University of Warwick to investigate the energy dissipative performance of the proposed connection under cyclic loading. The reported three tests have the same joint arrangement and components except the TCPs that connect the DPs to the I-beam flanges. The reported three different types of TCPs were adopted to investigate the effect of

1. Using TCPs with/without stiffeners.
2. The value of the preloading force acting on the TCPs' Bolts.

The resulted hysteretic response and energy dissipation of three tests are reported in the full paper.

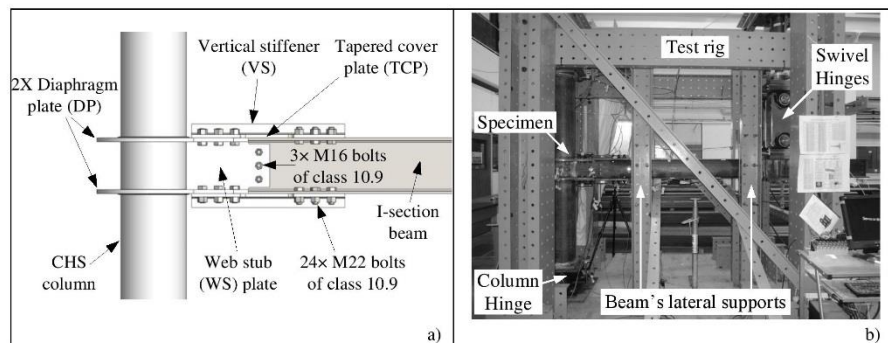


Fig. 1. a) Test specimen; b) Test rig

### CONCLUSIONS

The results of three tests were reported in this paper highlighting the effect of using TCPs' stiffeners and controlled bolts preloading force on the overall hysteretic response of the connection and its energy dissipation. The results presented in this paper confirmed that the main energy dissipation fuse in these connections was yielding in the reduced section areas of the TCPs; and that stiffening TCPs resulted in a stronger connection but imposed higher stress demands on the beam and the diaphragm plates and dissipated less energy than the same connection with unstiffened TCPs. Reducing the preloading force acting on the connection's bolts to half the value recommended in Eurocode 3: Part 1-8 [3] for slip-resistant connections created a second fuse for energy dissipation that was slip activation in the oversized bolt-holes of the connection, which subsequently led to higher rates of energy dissipation.

### ACKNOWLEDGMENTS

The authors are grateful to the Engineering and Physical Science Research Council (EP/1020489/1) for the project funding and Damascus University for the doctoral scholarship awarded to the first author. Financial support from TATA Steel, the School of Engineering at the University of Warwick and the technical support from the Structures Laboratory at the University of Warwick are gratefully acknowledged. The authors wish also to thank Dr Alireza Bagheri Sabbagh for his advice and contribution to this research.

### REFERENCES

- [1] Kurobane Y., Packer J.A., Wardenier J., Yeomans N., 2005. Design Guide for Structural Hollow Section Column Connections, First Edition, CIDECT, Germany.
- [2] Sabbagh A.B., Chan T.M., Mottram J.T., 2013. "Detailing of I-beam-to-CHS column joints with external diaphragm plates for seismic actions". Journal of Constructional Steel Research, ISSN 0143-974X, Elsevier Science Limited, Vol. 88, pp. 21-33.
- [3] Eurocode 3: Design of steel structures – Part 1-8: Design of joints, 2005. British Standards Institution (BSI).